

## **SCEE 2008 BOOK OF ABSTRACTS**

**The 7th International Conference on  
Scientific Computing in Electrical Engineering (SCEE 2008),  
September 28 – October 3, 2008,  
Helsinki University of Technology,  
Espoo, Finland**

**Editors: Janne Roos and Luis R.J. Costa**



TEKNILLINEN KORKEAKOULU  
TEKNISKA HÖGSKOLAN  
HELSINKI UNIVERSITY OF TECHNOLOGY  
TECHNISCHE UNIVERSITÄT HELSINKI  
UNIVERSITE DE TECHNOLOGIE D'HELSINKI



## **SCEE 2008 BOOK OF ABSTRACTS**

**The 7th International Conference on  
Scientific Computing in Electrical Engineering (SCEE 2008),  
September 28 – October 3, 2008,  
Helsinki University of Technology,  
Espoo, Finland**

**Editors: Janne Roos and Luis R.J. Costa**

This report contains abstracts of presentations given at the SCEE 2008 conference.

Distribution:

Helsinki University of Technology

Department of Radio Science and Engineering

P.O. Box 3000

FI-02015 TKK

Tel. +358 9 451 2261

Fax +358 9 451 2267

E-mail: ari.sihvola@tkk.fi

© 2008 Janne Roos, Luis R.J. Costa, SCEE, and TKK

ISBN 978-951-22-9557-9 (printed)

ISBN 978-951-22-9563-0 (electronic)

<http://lib.tkk.fi/Books/2008/isbn9789512295630.pdf>

urn:nbn:fi:tkk-012356

ISSN 1797-4364 (printed)

ISSN 1797-8467 (electronic)

Picaset Oy

Helsinki 2008

---

## Preface

SCEE is an international conference series dedicated to Scientific Computing in Electrical Engineering. It started as a national German meeting held in Darmstadt (1997) and Berlin (1998), both under the auspices of the Deutscher Mathematiker Verein. In 2000, the first truly international SCEE conference was organized in Warnemünde by the University of Rostock, Germany. In 2002, the 4th SCEE conference was jointly organized by the Eindhoven University of Technology and Philips Research Laboratories Eindhoven, The Netherlands. In 2004, the 5th SCEE conference took place in Capo D'Orlando, Italy, organized by Università di Catania and Consorzio Catania Ricerche. Most recently, in 2006, the 6th SCEE conference took place in Sinaia, Romania, organized by Politehnica University of Bucharest.

The 7th International Conference on Scientific Computing in Electrical Engineering (SCEE 2008) in Espoo, Finland, is organized by the Helsinki University of Technology (TKK); Faculty of Electronics, Communications and Automation (ECA); Department of Radio Science and Engineering (RAD); Circuit Theory Group. (SCEE 2008 web site: <http://www.ct.tkk.fi/scee2008/>).

The aim of the SCEE 2008 conference is to bring together scientists from academia and industry with the goal of intensive discussions on modeling and numerical simulation of electronic circuits and of electromagnetic fields. The conference is mainly directed towards mathematicians and electrical engineers. The SCEE 2008 conference has the following four main topics:

1. Computational Electromagnetics (CE),
2. Circuit Simulation (CS),
3. Coupled Problems (CP),
4. Mathematical and Computational Methods (CM).

The selection of abstracts in this book was carried out by the Program Committee; each abstract was reviewed by two or three reviewers. The authors of all accepted abstracts were invited to submit an extended full paper, which will be reviewed as well. The accepted full papers will be published in a separate post-conference book.

On behalf of the Local Organizing Committee, we would like to thank the invited speakers for graciously agreeing to participate in the conference, the authors of contributed abstracts for their well-written scientific texts, the members of the Program Committee for their efforts and time, and those of the Scientific Advisory Committee for their support. Also, we are grateful to the financial and material support received from our sponsors.

Finally, we would like to warmly welcome all participants to SCEE 2008.

Espoo, September 12, 2008

*Janne Roos*, SCEE 2008 chairman

*Luis Costa*, SCEE 2008 secretary

## Committees

### Local Organizing Committee

Dr. Janne Roos (*chairman*, TKK/RAD)  
Mr. Luis Costa (*secretary*, TKK/RAD)  
Prof. Martti Valtonen (TKK/RAD)  
Mr. Mikko Honkala (TKK/RAD)  
Mr. Jan Fagerström (TKK)  
Mr. Vesa Linja-aho (TKK)  
Ms. Jenni Tulensalo (TKK)  
Ms. Tuija Karviala (Congreszon)  
Ms. Katri Luomanpää (Congreszon)

### Program Committee

Prof. Gabriela Ciuprina (Politehnica University of Bucharest, Romania)  
Dr. Georg Denk (Qimonda, Germany)  
Prof. Michael Günther (University of Wuppertal, Germany)  
Dr. Jan ter Maten (NXP Semiconductors, The Netherlands)  
Dr. Bastiaan Michielsen (ONERA, France)  
Prof. Ursula van Rienen (University of Rostock, Germany)  
Prof. Vittorio Romano (University of Catania, Italy)  
Dr. Janne Roos (Helsinki University of Technology, Finland)  
Prof. Wil Schilders (TU Eindhoven & NXP Semiconductors, The Netherlands)  
Prof. Jan Sykulski (University of Southampton, United Kingdom)  
Prof. Thomas Weiland (TU Darmstadt & CST, Germany)

### Scientific Advisory Committee

Dr. Andreas Blaszczyk (ABB Corporate Research, Switzerland)  
Prof. Roland Freund (University of California, Davis, USA)  
Dr. Francois Henrotte (IEM RWTH, Germany)  
Prof. Ralf Hiptmair (ETH Zürich, Switzerland)  
Prof. Daniel Ioan (Politehnica University of Bucharest, Romania)  
Prof. Lauri Kettunen (Tampere University of Technology, Finland)  
Prof. Wolfgang Mathis (Leibniz Universität Hannover, Germany)  
Dr. Irina Munteanu (Computer Simulation Technology, Germany)  
Prof. Caren Tischendorf (Universität zu Köln, Germany)

---

## Sponsors

### Industrial sponsors

Nokia	<a href="http://research.nokia.com/">http://research.nokia.com/</a>
STMicroelectronics	<a href="http://www.st.com/">http://www.st.com/</a>
ABB	<a href="http://www.abb.com/">http://www.abb.com/</a>
Computer Simulation Technology (CST)	<a href="http://www.cst.com/">http://www.cst.com/</a>
Applied Wave Research (AWR)	<a href="http://www.awrcorp.com/">http://www.awrcorp.com/</a>
MunEDA	<a href="http://www.muneda.com/">http://www.muneda.com/</a>

### Other sponsors

Academy of Finland	<a href="http://www.aka.fi/en-gb/A/">http://www.aka.fi/en-gb/A/</a>
Helsinki University of Technology	<a href="http://www.tkk.fi/en/">http://www.tkk.fi/en/</a>
City of Espoo	<a href="http://english.espoo.fi/">http://english.espoo.fi/</a>
CoMSON Research Training Network	<a href="http://www.comson.org/">http://www.comson.org/</a>
Elektroniikkainsinöörien seura	<a href="http://www.eis.fi/">http://www.eis.fi/</a>



## Conference program

Sun 28.09.	Mon 29.09.	Tue 30.09.	Wed 01.10.	Thu 02.10.	Fri 03.10.
	09:00–09:45 Invited CE 1I	09:00–09:45 Invited CP 1Ia	09:00–09:45 Invited CE 2I	09:00–09:45 Invited CS 2I	09:00–09:45 Invited CM 2I
	09:45–10:15 Oral CE 1A	09:45–10:15 Oral CP 1A	09:45–10:15 Oral CE 2A	09:45–10:15 Oral CS 2A	09:45–10:15 Oral CM 2A
10:15–10:45 <b>Coffee break</b>					
	10:45–11:15 Oral CE 1B	10:30–11:15 Invited CP 1Ib	10:45–11:15 Oral CE 2B	10:45–11:15 Oral CS 2B	10:45–11:15 Oral CM 2B
	11:15–11:45 Oral CE 1C	11:15–11:45 Oral CP 1B	11:15–11:45 Oral CE 2C	11:15–11:45 Oral CS 2C	11:15–11:45 Oral CM 2C
	11:45–12:15 Oral CE 1D	11:45–12:15 Oral CP 1C	11:45–12:15 Oral CE 2D	11:45–12:15 Oral CS 2D	11:45–12:15 Oral CM 2D
	12:15–12:45 Short poster presentation 1	12:15–12:45 Short poster presentation 2	12:15–12:45 Oral CE 2E	12:15–12:45 Short poster presentation 3	12:15–12:45 Closing
12:45–14:00 <b>Lunch</b>					
	14:00–14:45 Invited CS 1I	14:00–14:45 Invited CM 1I	14:00–22:00  Excursion  &  Dinner	14:00–14:45 Invited CS 3I	
	14:45–15:15 Oral CS 1A	14:45–15:15 Oral CM 1A		14:45–15:15 Oral CS 3A	
15:15–15:30 <b>Coffee break</b>				<b>Coffee break</b>	
	15:30–16:00 Oral CS 1B	15:30–16:00 Oral CM 1B		15:30–16:00 Oral CS 3B	
16:00–18:00 Registration	16:00–16:30 Oral CS 1C	16:00–16:30 Oral CM 1C		16:00–16:30 Oral CS 3C	
	16:30–17:00 Oral CS 1D	16:30–17:00 Oral CM 1D		16:30–17:00 Oral CS 3D	
	17:00–18:00 Poster P1	17:00–18:00 Poster P2	17:00–18:00 Poster P3		
18:00–19:00 Opening session Invited CS 0I	Walk to Radisson SAS Hotel Espoo				
19:00–21:00 Welcome cocktail	18:45–21:00 Espoo city reception				

### Invited talks

- CS 0I Prof. Peter Benner (TU Chemnitz, Germany)  
*Advances in balancing-related model reduction for circuit simulation*
- CE 1I Dr. Sergey Yuferev (Nokia, Finland)  
*Challenges and approaches in EMC/EMI modeling of wireless devices*
- CS 1I Prof. Qi-Jun Zhang (Carleton University, Canada)  
*ANN/DNN-based behavioral modeling of RF/microwave components/devices and circuit blocks*
- CP 1Ia Dr. Wim Schoenmaker (MAGWEL, Belgium)  
*Evaluation of the EM coupling between microelectronic device structures using computational electrodynamics*
- CP 1Ib Prof. Ansgar Jüngel (TU Wien, Austria)  
*Thermal effects in coupled circuit-device simulations*
- CM 1I Dr. David Levadoux (ONERA, France)  
*New trends in the preconditioning of integral equations of electromagnetism*
- CE 2I Prof. Jan Hesthaven (Brown University, USA)  
*High-order discontinuous Galerkin methods for computational electromagnetics and uncertainty quantification*
- CS 2I Dr. Emira Dautbegovic (Qimonda, Germany)  
*Wavelets in circuit simulation*
- CS 3I Prof. Daniel Ioan (Politehnica University of Bucharest, Romania)  
*Parametric reduced-order models for passive integrated components coupled with their EM environment*
- CM 2I Dr. Galina Benderskaya (CST, Germany)  
*Numerical time integration in computational electromagnetics*

---

## Contents

<b>Preface</b> .....	iii
<b>Committees</b> .....	iv
<b>Sponsors</b> .....	v
<b>Conference program</b> .....	vi
<b>Invited talks</b> .....	vi
<hr/>	
<b>Session: CS 0</b>	
<hr/>	
CS 0I Advances in balancing-related model reduction for circuit simulation <i>Peter Benner</i> .....	3
<hr/>	
<b>Session: CE 1</b>	
<hr/>	
CE 1I Challenges and Approaches in EMC/EMI Modeling of Wireless Consumer Devices <i>Sergey Yuferev</i> .....	7
CE 1A Computation of Eigenmodes in Dispersive Materials <i>Bastian Bandlow, Rolf Schuhmann</i> .....	9
CE 1B Region-oriented BEM formulation for numerical computations of electric and magnetic fields <i>Andreas Blaszczyk</i> .....	11
CE 1C Tearing and Interconnecting Methods for Non-Elliptic Operators <i>Markus Windisch, Olaf Steinbach</i> .....	13
CE 1D Parametric Models of Transmission Lines Based on First Order Sensitivities <i>Alexandra Ștefănescu, Daniel Ioan, Gabriela Ciuprina</i> .....	15
<hr/>	
<b>Session: CS 1</b>	
<hr/>	
CS 1I ANN/DNN-based Behavioral Modeling of RF/Microwave Components/Devices and Circuit Blocks <i>Q.J. Zhang, Shan Wan</i> .....	19
CS 1A Model Order Reduction for Nonlinear IC models with POD <i>A. Verhoeven, M. Striebel, E.J.W. ter Maten</i> .....	21
CS 1B Model Order Reduction for Systems with Coupled Parameters <i>Lihong Feng, Peter Benner</i> .....	23

CS 1C	Model order and terminal reduction approaches via matrix decomposition and low rank approximation <i>André Schneider, Peter Benner</i> .....	25
CS 1D	Model order reduction for large resistance networks <i>Joost Rommes, Peter Lenaers, Wil H.A. Schilders</i> .....	27

---

**Session: P 1**

---

P 1.1	Integral equation method for magnetic modelling of cilia <i>Mihai Rebican, Daniel Ioan</i> .....	31
P 1.2	Electromagnetic modeling of 3D bodies in layered earths using integral equations <i>R. Grimberg, Adriana Savin, Rozina Steigmann, Alina Bruma, S.S. Udpa, Lalita Udpa</i>	33
P 1.3	Electromagnetic field diffraction on subsurface electrical barrier. Application to nondestructive evaluation <i>Adriana Savin, Rozina Steigmann, Alina Bruma, Raimond Grimberg</i> .....	35
P 1.4	Relativistic High Order Particle Treatment for Electromagnetic Particle-In-Cell Simulations <i>Martin Quandt, Claus-Dieter Munz, Rudolf Schneider</i> .....	37
P 1.5	A Simulation-Based Genetic Algorithm for Optimal Antenna Pattern Design <i>Yi-Ting Kuo, Yiming Li</i> .....	39
P 1.6	Probabilistic characterization of resonant EM interactions with thin-wires: variance and kurtosis analysis <i>O.O. Sy, J.A.H.M. Vaessen, M.C. van Beurden, B.L. Michielsen, A.G. Tijhuis</i> .....	41
P 1.7	Domain Partitioning Based Parametric Models for Passive On-chip Components <i>Gabriela Ciuprina, Daniel Ioan, Diana Mihalache, Ehrenfried Seebacher</i> .....	43
P 1.8	Parametric Reduced Compact Models for Passive Components <i>Diana Mihalache, Daniel Ioan, Gabriela Ciuprina, Alexandra Ștefănescu</i> .....	45
P 1.9	An Effective Technique for Modelling Nonlinear Lumped Elements Spanning Multiple Cells in FDTD <i>Luis R.J. Costa, Keijo Nikoskinen, Martti Valtonen</i> .....	47
P 1.10	Mixed-Derating of Three-Phase Distribution Transformer under Unbalanced Supply Voltage and Non-Linear Load Conditions Using Finite Element Method <i>Jawad Faiz, M. Ghofrani, B.M. Ebrahimi</i> .....	49
P 1.11	Design Optimization of Radial Flux Permanent Magnet Wind Generator for Highest Annual Energy Input and Lower Magnet Volumes <i>Jawad Faiz, M. Rajabi-Sebdani, B.M. Ebrahimi, M.A. Khan</i> .....	53
P 1.12	Finite-element discretization for analyzing eddy currents in the form-wound stator winding of a cage induction motor <i>M. Jahirul Islam, Antero Arkkio</i> .....	57

---

**Session: CP 1**

---

CP 1Ia	Evaluation of the electromagnetic coupling between microelectronic device structures using computational electrodynamics <i>Wim Schoenmaker, Peter Meuris</i> .....	61
CP 1A	Simulations of a electron-phonon hydrodynamical model based on the maximum entropy principle <i>V. Romano, C. Scordia</i> .....	67

CP 1Ib	Thermal Effects in Coupled Circuit-Device Simulations <i>Markus Brunk, Ansgar Jüngel</i> .....	69
CP 1B	Automatic Thermal Network Extraction and Multiscale Electro-Thermal Simulation <i>Massimiliano Culpò, Carlo de Falco, Georg Denk, Steffen Voigtmann</i> .....	71
CP 1C	Canonical Stochastic Electromagnetic Fields <i>B.L. Michielsen</i> .....	73

---

**Session: CM 1**


---

CM 1I	New trends in the preconditioning of integral equations of electromagnetism <i>David P. Levadoux</i> .....	77
CM 1A	A New Approach to Modeling Multi-Port Scattering Parameters <i>Sanda Lefteriu, Athanasios C. Antoulas</i> .....	79
CM 1B	Numerical and Mathematical Properties of Electromagnetic Surface Integral Equations <i>Pasi Ylä-Oijala, Matti Taskinen</i> .....	81
CM 1C	Nonlinear models for silicon semiconductors <i>Salvatore La Rosa, Giovanni Mascali, Vittorio Romano</i> .....	83
CM 1D	Hyperbolic PDAEs for semiconductor devices coupled with circuits <i>Giuseppe Alì, Giovanni Mascali, Roland Pulch</i> .....	85

---

**Session: P 2**


---

P 2.1	Consistent Initialization for Coupled Circuit-Device Simulation <i>Sascha Baumanns, Mónica Selva, Caren Tischendorf</i> .....	89
P 2.2	Heating of semiconductor devices in electric circuits <i>Markus Brunk, Ansgar Jüngel</i> .....	91
P 2.3	Surrogate Modeling of Low Noise Amplifiers Based on Transistor Level Simulations <i>Luciano De Tommasi, Dirk Gorissen, Jeroen Croon, Tom Dhaene</i> .....	93
P 2.4	On Local Handling of Inner Equations in Compact Models <i>Uwe Feldmann, Masataka Miyake, Takahiro Kajiwara, Mitiko Miura-Mattausch</i> .....	95
P 2.5	Transient Analysis of Nonlinear Circuits Based on Waves <i>Carlos Christoffersen</i> .....	97
P 2.6	Time-Domain Preconditioner for Harmonic Balance Jacobians <i>Mikko Honkala, Ville Karanko</i> .....	99
P 2.7	Evaluation of Oscillator Phase Transfer Functions <i>M.M. Gourary, S.G. Rusakov, S.L. Ulyanov, M.M. Zharov, B.J. Mulvaney, K.K. Gullapalli</i> .....	101
P 2.8	Quasiperiodic steady-state analysis of electronic circuits by a spline basis <i>Hans Georg Brachtendorf, Angelika Bunse-Gerstner, Barbara Lang, Siegmund Lampe</i> ..	103
P 2.9	Accurate Simulation of the Devil's Staircase of an Injection-Locked Frequency Divider <i>Tao Xu, Marissa Condon</i> .....	105
P 2.10	Nonlinear distortion in differential circuits with single-ended and balanced drive <i>Timo Rahkonen</i> .....	107
P 2.11	Speed-up techniques for time-domain system simulations <i>Timo Rahkonen</i> .....	109

P 2.12	Lookup-Table Based Settling Error Modeling in SIMULINK <i>Marko Neitola, Timo Rahkonen</i> .....	111
P 2.13	BRAM - Backward Reduced Adjoint Method <i>Z. Ilievski, W.H.A. Schilders, E.J.W. ter Maten</i> .....	113
P 2.14	Applications of Eigenvalue Inclusion Theorems in Model Order Reduction <i>E. Fatih Yetkin, Hasan Dağ</i> .....	115
P 2.15	Hierarchical Model-Order Reduction Flow <i>Mikko Honkala, Pekka Miettinen, Janne Roos, Carsten Neff</i> .....	117
P 2.16	Partitioning-based RL-in–RL-out MOR Method <i>Pekka Miettinen, Mikko Honkala, Janne Roos</i> .....	119
P 2.17	Nonlinear model order reduction based on trajectory piecewise linear approach: comparing different linear cores <i>Kasra Mohaghegh, Michael Striebel</i> .....	121
P 2.18	On Model Order Reduction for Perturbed Nonlinear Neural Networks with Feedback <i>Marissa Condon, Georgi G. Grahovski</i> .....	123

---

**Session: CE 2**

---

CE 2I	High-order discontinuous Galerkin methods for computational electromagnetics and uncertainty quantification <i>J.S. Hesthaven, T. Warburton, C. Chauviere, L. Wilcox</i> .....	127
CE 2A	Using Nudg++ to Solve Poisson’s Equation on Unstructured Grids <i>Christian R. Bahls, Gisela Pöplau, Ursula van Rienen</i> .....	129
CE 2B	From the Boundary Element DDM to Trefftz Finite Element Methods on Arbitrary Polyhedral Meshes <i>Dylan Copeland, Ulrich Langer, David Pusch</i> .....	131
CE 2C	Reduced Basis Method for Electromagnetic Field Computations <i>Jan Pomplun, Frank Schmidt</i> .....	133
CE 2D	Surface Integrated Field Equations Method for solving 3D Electromagnetic problems <i>Zhifeng Sheng, Patrick Dewilde</i> .....	135
CE 2E	A Novel Staggered Finite Volume Time Domain Method <i>Thomas Lau, Erion Gjonaj, Thomas Weiland</i> .....	137

---

**Session: CS 2**

---

CS 2I	Wavelets in circuit simulation <i>Emira Dautbegovic</i> .....	141
CS 2A	Hybrid Analysis of Nonlinear Time-Varying Circuits Providing DAEs with at Most Index 1 <i>Satoru Iwata, Mizuyo Takamatsu, Caren Tischendorf</i> .....	143
CS 2B	Convergence Issues of Ring Oscillator Simulation by Harmonic Balance Technique <i>M.M. Gourary, S.G. Rusakov, S.L. Ulyanov, M.M. Zharov, B.J. Mulvaney</i> .....	145
CS 2C	Stochastic Models for Analysing Parameter Sensitivities <i>Roland Pulch</i> .....	147
CS 2D	Simultaneous Step-size and Path Control for Efficient Transient Noise Analysis <i>Werner Römisch, Thorsten Sickenberger</i> .....	149

---

**Session: CS 3**


---

CS 3I	Parametric Reduced Order Models for Passive Integrated Components Coupled with their EM Environment <i>Daniel Ioan</i> .....	153
CS 3A	Stability of the Super Node Algorithm for EMC Modelling of ICs <i>M.V. Ugryumova, W.H.A. Schilders</i> .....	155
CS 3B	GABOR: Global-Approximation-Based Order Reduction <i>Janne Roos, Mikko Honkala, Pekka Miettinen</i> .....	157
CS 3C	Passivity-preserving balanced truncation model reduction of circuit equations <i>Tatjana Stykel, Timo Reis</i> .....	159
CS 3D	A new approach to passivity preserving model reduction <i>Roxana Ionutiu, Joost Rommes, Athanasios C. Antoulas</i> .....	161

---

**Session: P 3**


---

P 3.1	Analysis of a PDE Thermal Element Model for Electrothermal Circuit Simulation <i>Giuseppe Alì, Andreas Bartel, Massimiliano Culpo, Carlo de Falco</i> .....	165
P 3.2	Efficient simulation of large-scale dynamical systems using tensor decompositions <i>F. van Belzen, S. Weiland</i> .....	167
P 3.3	Magnetic Force Calculation applied to Magnetic Force Microscopy <i>Thomas Preisner, Michael Greiff, Josefine Freitag, Wolfgang Mathis</i> .....	169
P 3.4	EM Scattering Calculations using Potentials <i>Magnus Herberthson</i> .....	171
P 3.5	Simulation of large interconnect structures using a ILU-type preconditioner <i>D. Harutyunyan, W. Schoenmaker, W.H.A. Schilders</i> .....	173
P 3.6	Fast Linear Solver for Vector Fitting Method <i>M.M. Gourary, S.G. Rusakov, S.L. Ulyanov, M.M. Zharov, B.J.M. Mulvaney, B. Gu</i> .....	175
P 3.7	Evaluation of Domain Decomposition Approach for Compact Simulation of On-Chip Coupled Problems <i>Michal Dobrzynski, Jagoda Plata, Sebastian Gim</i> .....	177
P 3.8	A Novel Graphical Based Tool for Extraction of Magnetic Reluctances between On-Chip Current Loops <i>Sebastian Gim, Alexander Vasenev, Diana Mihalache, Alexandra Ștefănescu, Sebastian Kula</i> .....	179
P 3.9	Multiobjective Optimization Applied to Design of PIFA Antennas <i>Stefan Jakobsson, Björn Andersson, Fredrik Edelvik</i> .....	181
P 3.10	Space Mapping with Difference Method for Optimization <i>N. Serap Şengör, Murat Şimsek</i> .....	183
P 3.11	Modification of Space Mapping with Difference Method for Inverse Problems <i>Murat Şimsek, N. Serap Şengör</i> .....	185
P 3.12	Exploiting Model Hierarchy in Semiconductor Design using Manifold-Mapping <i>D.J.P. Lahaye, C. Drago</i> .....	187
P 3.13	An <i>hp</i> -Adaptive Strategy for the Solution of the Exact Kernel Curved Wire Pocklington Equation <i>D.J.P. Lahaye</i> .....	189

P 3.14 Sensitivity Analysis of Capacitance for a TFT-LCD Pixel  
*Ta-Ching Yeh, Hsuan-Ming Huang, Yiming Li* ..... 191

---

**Session: CM 2**

---

CM 2I Numerical Time Integration in Computational Electromagnetics  
*Galina Benderskaya, Oliver Sterz, Wolfgang Ackermann, Thomas Weiland* ..... 195

CM 2A Co-Simulation of Circuits Refined by 3-D Conductor Models  
*Sebastian Schöps, Andreas Bartel, Herbert De Gersem, Michael Günther* ..... 197

CM 2B Robust FETI solvers for multiscale elliptic PDEs  
*Clemens Pechstein, Robert Scheichl* ..... 199

CM 2C Functional Type A Posteriori Error Estimates for Maxwell's Equations  
*Antti Hannukainen* ..... 201

CM 2D Large-Scale Atomistic Circuit-Device Coupled Simulation of Intrinsic Fluctuations in  
 Nanoscale Digital and High-Frequency Integrated Circuits  
*Chih-Hong Hwang, Ta-Ching Yeh, Tien-Yeh Li, Yiming Li* ..... 203

**Author Index** ..... 205

---

**Session**

**CS 0**

---



# Advances in balancing-related model reduction for circuit simulation

Peter Benner

TU Chemnitz, Fakultät für Mathematik, 09107 Chemnitz, Germany [benner@mathematik.tu-chemnitz.de](mailto:benner@mathematik.tu-chemnitz.de)

**Summary.** We discuss methods related to balanced truncation for model reduction of linear systems. These methods are known to have good global approximation properties and to preserve important system properties. A computable error bound allows to choose the order of the reduced-order model adaptively. We will emphasize those aspects that make their application to models arising in circuit simulation a non-straightforward task. In recent years, these issues have been addressed by several authors. We will survey these developments and demonstrate that these techniques are now suitable for the large-scale, sparse systems encountered in circuit simulation.

## 1 Introduction

Model order reduction (MOR) is an ubiquitous tool in the design and analysis of integrated circuits (ICs) and circuit simulation in general. In many situations, only the use of MOR techniques allows the numerical simulation of the usually very large systems of ordinary differential and differential-algebraic equations used to describe (parts of) complex circuit layouts. MOR has been particularly successful in reducing the complexity of large linear subcircuits modeling parasitic effects of interconnect etc., and it is becoming an increasingly useful tool also in other areas of circuit design.

We consider linear descriptor systems

$$E\dot{x}(t) = Ax(t) + Bu(t), \quad y(t) = Cx(t), \quad (1)$$

with  $A, E \in \mathbb{R}^{n \times n}$ ,  $B \in \mathbb{R}^{n \times m}$ ,  $C \in \mathbb{R}^{p \times n}$  and corresponding transfer function  $G(s) = C(sE - A)^{-1}B$ , resulting from describing the input-to-output map  $u \rightarrow y$  in frequency domain.<sup>1</sup> One difficulty for balancing related model reduction methods arises from  $E$  being singular as it is usually the case in circuit simulation — a part of the talk and the full paper will be devoted to the advances made for resolving this issue.

The model reduction problem now consists of finding a reduced-order system,

$$\hat{E}\dot{\hat{x}}(t) = \hat{A}\hat{x}(t) + \hat{B}u(t), \quad \hat{y}(t) = \hat{C}\hat{x}(t), \quad (2)$$

of order  $r$ ,  $r \ll n$ , with the same number of inputs  $m$ , the same number of outputs  $p$ , and associated transfer function  $\hat{G}(s) = \hat{C}(s\hat{E} - \hat{A})^{-1}\hat{B}$ , so that for the same input function  $u \in L_2(0, \infty; \mathbb{R}^m)$ , we have  $y(t) \approx \hat{y}(t)$ .

## 2 Review of MOR in IC design

First attempts of employing MOR in circuit simulation used the so called *asymptotic waveform evaluation (AWE)* technique [6]. This is based on the following observation: for  $s_0 \notin \Lambda(A, E)$ , where  $\Lambda(A, E)$  denotes the set of generalized eigenvalues of the matrix pencil  $A - \lambda E$ , we can re-write the transfer function of (1) and expand it into a power (Laurent) series as follows:

$$\begin{aligned} G(s) &= C(I + (s - s_0)(s_0E - A)^{-1}E)^{-1} \\ &\quad \times (s_0E - A)^{-1}B \\ &= M_0 + M_1(s - s_0) + M_2(s - s_0)^2 + \dots \end{aligned}$$

For  $s_0 = 0$ , the coefficient matrices in the power series are given by  $M_j := C(A^{-1}E)^j A^{-1}B$  and are called *moments*.

As reduced-order model we can now use the  $r$ th Padé approximant  $\hat{G}$  to  $G$ , defined by the property  $G(s) = \hat{G}(s) + \mathcal{O}((s - s_0)^{2r})$ , i.e.,  $M_j = \widehat{M}_j$  for  $j = 0, \dots, 2r - 1$ . Thus, Padé approximation is based on *moment matching*. AWE now computes the moments explicitly and obtains the coefficients of the numerator and denominator polynomials of  $\hat{G}$  by solving a linear system of equations. It was soon observed that this procedure is numerically unstable as computing the moments can be interpreted as kind of a power iteration so that the computed moments become numerically linearly dependent quite fast.

A breakthrough for Padé approximation methods then was the observation that the moments need not be computed explicitly as moment matching is equivalent to projecting the state-space onto  $\mathcal{V} = \mathcal{K}(\tilde{A}, \tilde{B}, r)$ , along  $\mathcal{W} = \mathcal{K}(\tilde{A}^H, C^H, r)$ . Here,  $\tilde{A} = (s_0E - A)^{-1}E$ ,  $\tilde{B} = (s_0E - A)^{-1}B$ , and  $\mathcal{K}(M, b, \ell)$  denotes the *Krylov subspace*

<sup>1</sup> Note that frequently in the area of circuit simulation, different notation is used: there  $E, A$ , and  $C$  become  $C, G$ , and  $L^T$ , respectively. The notation used here is standard in systems theory.

$$\text{span}\{b, Mb, M^2b, \dots, M^{\ell-1}b\}.$$

Bi-orthogonal bases of these two (block-)Krylov subspaces can be computed via the unsymmetric (block, band) Lanczos method [2–4]. In addition, a realization of the reduced-order model is computed as a by-product of the unsymmetric Lanczos process. The computation of a reduced-order model based on the moment matching idea implemented as unsymmetric Lanczos process is called the *(matrix) Padé-via-Lanczos ((M)PVL) method* [2,3]. PVL is popular in circuit simulation and micro electronics as it can be applied without changes to descriptor systems with  $E$  singular which quite commonly arise in these applications.

*Padé-type methods* are also based on the moment matching property, but the approximations need not match the maximum possible number of moments. One such method is PRIMA [5] which employs the numerically stable Arnoldi process to compute an orthogonal bases of  $\mathcal{V}$  as above and performs an orthogonal projection onto  $\mathcal{V}$ . PRIMA has been a success story in MOR for circuit simulation as besides having moment-matching properties, it preserves stability and passivity of RLC circuit models.

Despite all the success with Padé(-type) approximation techniques based on the moment-matching properties of Krylov subspace methods, some major difficulties of this approach persist:

1. So far there exists in general no computable error estimate or bound for  $\|y - \hat{y}\|_2$ .
2. The reduced-order model provides a good approximation quality only locally.
3. The preservation of physical properties like stability or passivity can only be shown in very special cases; usually some post processing which (partially) destroys the moment matching properties, is required.

There are many recent advances with respect to items 1.–3. discussed in the recent literature, due to space limitations we can not discuss all these new developments here.

### 3 Balancing-related MOR

All the above problems of moment-matching methods are avoided when using balanced truncation (BT) or its relatives. Computable error bounds exist and come for free as by-product of the computational procedures for obtaining the reduced-order model. Stability of the linear system is preserved for all variants, other properties like passivity (which is important for passive devices) can be preserved, depending on which variant of BT is used. The methods have good global approximation properties and thus, the reduced-order model

can serve as surrogate for a large frequency range. In the simplest case of balanced truncation, the main computational task is the solution of the dual Lyapunov equations

$$\begin{aligned} AP + PA^T + BB^T &= 0, \\ A^TQ + QA + C^TC &= 0. \end{aligned} \quad (3)$$

The reduced-order model is then obtained by further manipulations from the solutions  $P, Q$  of (3). Other variants of BT replace the Lyapunov equations by algebraic Riccati equations which seems to be even more challenging from the computational point of view. It has been common belief until recently that BT-related methods are not applicable in circuit simulation due to the  $\mathcal{O}(n^3)$  complexity of usual matrix equation solvers. But advances in numerical linear algebra nowadays allow to compute solutions to those Lyapunov and Riccati equations arising in BT-related methods for linear system in circuit simulation at a computational cost that scales with the cost for solving linear systems of equations with coefficient matrix  $A + s_0E$ . Thus these methods can now be applied to systems of order  $\mathcal{O}(10^6)$ . Moreover, most of the difficulties resulting from a singular  $E$  matrix have now also been overcome. Many of these developments can already be found in [1] and references therein. In the talk and the full paper, we will survey the most important advances useful for MOR of linear systems in circuit simulation and will also highlight some recent improvements.

### References

1. P. Benner, V. Mehrmann, and D.C. Sorensen, editors. *Dimension Reduction of Large-Scale Systems*, volume 45 of *Lecture Notes in Computational Science and Engineering*. Springer-Verlag, Berlin/Heidelberg, Germany, 2005.
2. P. Feldmann and R.W. Freund. Efficient linear circuit analysis by Padé approximation via the Lanczos process. *IEEE Trans. Comput.-Aided Des. Integr. Circuits Syst.*, 14:639–649, 1995.
3. R. Freund. Model reduction methods based on Krylov subspaces. *Acta Numerica*, 12:267–319, 2003.
4. K. Gallivan, E. Grimme, and P. Van Dooren. Asymptotic waveform evaluation via a Lanczos method. *Appl. Math. Lett.*, 7(5):75–80, 1994.
5. A. Odabasioglu, M. Celik, and L.T. Pileggi. PRIMA: passive reduced-order interconnect macromodeling algorithm. In *Tech. Dig. 1997 IEEE/ACM Intl. Conf. CAD*, pages 58–65. IEEE Computer Society Press, 1997.
6. L.T. Pillage and R.A. Rohrer. Asymptotic waveform evaluation for timing analysis. *IEEE Trans. Comput.-Aided Design*, 9:325–366, 1990.

---

**Session**

**CE 1**

---



# Challenges and Approaches in EMC/EMI Modeling of Wireless Consumer Devices

Sergey Yuferev

Nokia Corp., Visiokatu 3, 33720 Tampere, Finland, [sergey.yuferev@nokia.com](mailto:sergey.yuferev@nokia.com)

**Summary.** The paper contains overview of key tasks in numerical modeling of EMC (Electromagnetic Compatibility) problems of mobile phones. Special focus is given to following questions: overcoming computational difficulties caused by multi-scale feature, representation of different types of EMI sources in numerical models using measured data and methods of validation of numerical results. Examples of numerical modeling of real problems are included in full version of the paper.

## 1 Introduction

With decreasing design circles in modern electronic industry, simulations play more and more important role as an alternative to traditional way of making prototypes and measurements. High frequency wireless consumer devices like mobile phones are becoming increasingly complex since they are actually combinations of other products such as cameras, sensors, radio, computers etc. At the same time, they are getting smaller so complying with EMC regulations is now challenging task. At least some of potential EMC problems can be predicted well before physical prototypes are built by application of numerical analysis at early design stage. Significant efforts have been recently made by IEEE EMC Society to develop standards and recommended practice of the use of computational packages for simulation of real EMC problems [1].

In spite of so obvious benefits, CAD simulation packages have not become yet everyday tools of EMC designers unlike antenna, thermal or signal integrity designers of wireless devices. Even now, EMC problems of wireless devices are frequently considered as "black magic area" where rigorous numerical analysis is impossible due to high complexity of the problems. In the present paper some key challenges in numerical analysis of EMC problems of wireless devices are discussed.

## 2 Tasks for EMC Simulations

EMC regulations are imposed as maximum acceptable values (limits) of the electromagnetic

field at certain distances from the product. Limiting values of the EM field parameters are also specified inside the phone around modules containing strong EM radiators (emission interoperability limits) and modules sensitive to excessive levels of the EM field (immunity interoperability limits). Compliance with interoperability limits ensures functioning of the device without noises and interferences, and, finally, effects on the product quality.

Obviously those limits are expressed in terms of absolute numbers and do not depend on conditions of neither measurements nor numerical modeling. Thus EMC simulation technology should also provide numerical solution in the form of absolute numbers to be compared with EMC standards and interoperability limits.

## 3 Multi-Scale Feature

Characteristic size of the device is about 5-10 cm whereas characteristic size of the PCB details is less than 1 mm. Difference between the characteristic dimensions is two orders of magnitude that leads to very serious computational problem, namely: to provide necessary resolution in simulation of the PCB details, the average size of the cell in computational mesh used by the software for three-dimensional electromagnetic simulations should be hundreds or even tens microns. Thus discretization of the computational space including the device by cells of this size leads to such a mesh that no one modern computer will be able to simulate such a device "as is" in reasonable time. This problem got the name of "multi-scale" feature is well known in computational electromagnetics [2].

Computational problems related with "multi-scale" features may be overcome using so-called multi-stage modeling: the problem is divided into sub-problems, each of them is analyzed by special software and the results are combined [3]. In the case of wireless devices like mobile phones, basic idea of this approach is separate numerical solution of Maxwell's equations in domain occupied by the printed circuit board and in rest of

the device. Realization of the idea can be done by iterations; each of them consists of the following two steps:

- a. The electromagnetic behavior of the printed circuit board is analyzed separately from the device (the device is ignored) and near field radiation of the board is calculated; then the electromagnetic field distribution around the board is transferred to the next iteration to be used as input data (equivalent source or boundary condition).
- b. Three-dimensional problem of the electromagnetic field distribution is solved everywhere inside the device excepting domain occupied by the printed circuit board: the PCB domain is eliminated from the numerical procedure and replaced by the field distribution at the interface (obtained at the previous iteration).

Main advantage of the described procedure is that cells for modeling the PCB and the device are not combined in the same mesh. Instead, computer grids for the PCB and device are used separately at different stages so the multi-scale problem is resolved and three-dimensional distribution of the electromagnetic field inside and outside the device can be simulated in wide range of frequencies. However, practical realization of the approach requires high level of compatibility between codes applied at steps a and b (files produced by one code should be used as input data in another one). Another issue requiring further investigation is convergence of the iterative procedure. Intuitively clear that convergence will depend on characteristic scales of the problem: size of device, size of PCB and distance between them. Full version of the paper contains analysis of conditions of applicability and numerical example.

## 4 Representation of EMC/EMI Sources

Main EMI sources in the wireless devices are antennas, RF modules located on the board and currents flowing in the PCB traces. Electromagnetic behaviour of most of them cannot be described without SPICE-like models. Rigorous consideration requires combination of 3D EM (device), 2.5D EM (PCB) and circuit simulations using real characteristics of RF ICs. Alternative approach is to approximate real sources by combinations of lumped ports and calibrate their parameters using measured data, for example - near field distribution over IC. Advantages, limitations and examples of both approaches are considered in full version of the paper.

## 5 Validations of Numerical Results

Mixing circuit (lumped) level, field level and even molecular level models may naturally lead to significant errors so the problem of validation of numerical results becomes central problem when new simulation approaches are developed. In the area of board level EMC problems neither analytical solutions nor estimations based on previous experience may be applied for validations so measurements are the only approach to obtain reference data. Full version of the paper is focused on the near/far fields and scattering parameters measurements, and methodologies to represent measured data in the form suitable for comparison with numerical results and EMC limits.

## References

1. A.L. Drozd. Progress on the development of standards and recommended practices for CEM computer modeling and code validation. In *Proceedings of 2003 IEEE International Symposium on Electromagnetic Compatibility*, pp.313-316, 8-22 Aug. 2003.
2. A. Yilmaz, M.L. Choi, J. Jin, E. Michielsson and A.C. Cangellaris. Multi-scale hybrid electromagnetic modeling and transient simulation of multilayered printed circuit boards. In *Proceedings of Progress in Electromagnetic Research Symposium (PIERS)*, 28-31 Mar. 2004.
3. B. Archambeault, O.M. Ramahi and C. Brench, *EMI/EMC Computational Modeling Handbook*. Kluwer Academic Publishers, 1998.

# Computation of Eigenmodes in Dispersive Materials

Bastian Bandlow and Rolf Schuhmann

Theoretische Elektrotechnik, Universität Paderborn, Warburger Str. 100, D-33098 Paderborn, Germany  
bandlow@tet.upb.de, schuhmann@tet.upb.de

**Summary.** In dispersive materials, the material properties depend on the operating frequency. Eigenvalue problems including dispersive materials occur when computing the dispersion relations of photonic crystal and metamaterial unit cells in the THz spectrum. One possible procedure for solving is a fixed point iteration, but we show, that a reformulation as polynomial eigenvalue problem is also possible.

## 1 Introduction

In Fig. 1 there is exemplarily shown a metamaterial unit cell consisting of two rectangular structures of silver and a dielectric spacing in between. The fundamental eigenmode of such a unit cell is the focus of our interest. Especially in the THz frequency range, noble metals show a dispersion of their dielectric constant which follows the Drude model [3]. Thus, solving for eigenmodes of electromagnetic structures can be a quite challenging task when frequency dispersive materials are involved. A first approach is to evaluate the frequency dependent material properties at a specific frequency and to perform a fixed point iteration over several frequencies which may converge to the desired eigenmode of interest. But since the dependency of the material parameters on the frequency is explicitly known, the problem can be reformulated leading to a polynomial eigenvalue problem (PEP) which can be solved in different ways.

## 2 Formulation

From Maxwell's equations we derive the eigenmode formulation for the electric field strength  $\underline{\mathbf{E}}$

$$\text{rot} \frac{1}{\mu} \text{rot} \underline{\mathbf{E}} = \underline{\omega}^2 \underline{\epsilon} \underline{\mathbf{E}}, \quad (1)$$

where

$$\mu = \mu_0 \mu_r \quad \underline{\epsilon} = \epsilon_0 \underline{\epsilon}(\underline{\omega}). \quad (2)$$

We refer the following results to a relative permeability of  $\mu_r = 1$ . The dependency on the frequency of the relative permittivity  $\underline{\epsilon}(\underline{\omega})$  is given for example by a general 2nd order model

$$\underline{\epsilon}(\underline{\omega}) = \epsilon_\infty - \frac{\beta_0 + i\underline{\omega}\beta_1}{\alpha_0 + i\underline{\omega}\alpha_1 - \underline{\omega}^2}, \quad (3)$$

with the real-valued parameters  $\epsilon_\infty$ ,  $\alpha_0$ ,  $\alpha_1$ ,  $\beta_0$  and  $\beta_1$ . Note that all underlined symbols are complex quantities. Then we insert equation (3) into equation (1) and formulate a PEP in  $\underline{\omega}$

$$(\underline{\omega}^4 A_4 + \underline{\omega}^3 A_3 + \underline{\omega}^2 A_2 + \underline{\omega} A_1 + A_0) \underline{\mathbf{E}} = 0 \quad (4)$$

$$A_4 = -\epsilon_\infty, \quad A_3 = i(\alpha_1 \epsilon_\infty + \beta_1),$$

$$A_2 = \epsilon_\infty \alpha_0 + \beta_0 + A_{cc},$$

$$A_1 = -i\alpha_1 A_{cc}, \quad A_0 = -\alpha_0 A_{cc},$$

$$A_{cc} = \text{rot} \frac{1}{\mu} \text{rot}.$$

Using the Finite Integration Technique (FIT) [4] this representation of the PEP can be transformed into a matrix-vector formulation in a straightforward manner

$$(\underline{\omega}^4 \mathbf{M}_{A_4} + \underline{\omega}^3 \mathbf{M}_{A_3} + \underline{\omega}^2 \mathbf{M}_{A_2} + \underline{\omega} \mathbf{M}_{A_1} + \mathbf{M}_{A_0}) \underline{\mathbf{e}} = 0, \quad (5)$$

where  $\underline{\mathbf{e}}$  is a large algebraic vector of the electric grid voltages.

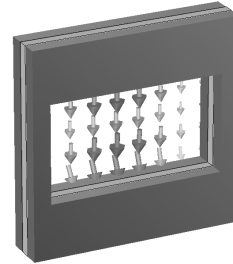


**Fig. 1.** Sample unit cell structure with two layers of Drude-dispersive silver and a spacing in between.

## 3 Strategies for Solving

### 3.1 Linearization of the PEP

A PEP can be linearized by the cost of multiplying the dimension of matrices by the order  $l$  of the polynomial, generating a generalized eigenvalue problem  $\mathbf{A}\mathbf{x} = \lambda\mathbf{B}\mathbf{x}$  of high dimension.

$$\mathbf{A} = \begin{bmatrix} 0 & \mathbf{I} & \cdots & 0 \\ \vdots & \vdots & \ddots & \vdots \\ \vdots & \vdots & \vdots & \mathbf{I} \\ -\mathbf{M}_{A_0} & -\mathbf{M}_{A_1} & \cdots & -\mathbf{M}_{A_{l-1}} \end{bmatrix}, \quad (6)$$

$$\mathbf{B} = \begin{bmatrix} \mathbf{I} & & & \\ & \ddots & & \\ & & \mathbf{I} & \\ & & & \mathbf{M}_{A_{l-1}} \end{bmatrix}$$

This approach leads to  $(l - 1)$  times additional eigenvalues which are not all solutions of the original PEP. Moreover, the system (6) is often known to be ill-conditioned [1].

### 3.2 Jacobi-Davidson for PEP

A promising approach was recently published in [2]. The PEP is kept in the form (5), the dimension is not blown up and a Jacobi-Davidson method is established. So far, we implemented the linearized harmonic Rayleigh-Ritz variant of the method in [2] which is intended to find one or more interior eigenvalues of the spectrum near a given estimation. Note, that the linearized harmonic Rayleigh-Ritz method fails to produce an exact eigenvalue, since only the linear part of a Taylor expansion is incorporated. Nevertheless, the obtained results are quite promising.

## 4 Numerical Example

As numerical example we choose a rectangular waveguide resonator. The resonator is filled homogeneously with a Drude-dispersive material, leading to a PEP of third order. The advantage of this rather simple setup is that the computation of the fundamental mode can be done for comparison purposes

1. analytically (including the lattice dispersion equation [4]),
2. using a fixed point iteration around  $\underline{\omega}$ ,
3. using the blown-up linearized approach,
4. using the JD approach.

### 4.1 Results

For the analytical solution we obtain the reference result

$$\underline{\omega}_{\text{analytical}} = 2\pi(24.49 \times 10^9 + 66.32 \times 10^3 i) \text{ s}^{-1}. \quad (7)$$

Note, that there is a factor  $10^6$  between real and imaginary part of the result.

For the first setup with full matrix-formulation we perform the fixed point iteration until the

residual is smaller than  $10^{-12}$ . We obtain a deviation to the analytical solution of

$$\frac{|\underline{\omega}_{\text{meshed, fixedpoint}} - \underline{\omega}_{\text{analytical}}|}{|\underline{\omega}_{\text{analytical}}|} = 3.38 \times 10^{-8}. \quad (8)$$

The blown-up linearized approach of equation (6) is solved by using Matlab's `eigs` and yields

$$\frac{|\underline{\omega}_{\text{meshed, linearized}} - \underline{\omega}_{\text{analytical}}|}{|\underline{\omega}_{\text{analytical}}|} = 1.07 \times 10^{-4}. \quad (9)$$

This rather poor accuracy is due to the bad condition of system (6). It can easily be improved by scaling and shifting the matrices in (6) which leads to

$$\frac{|\underline{\omega}_{\text{meshed, linearized, scaled}} - \underline{\omega}_{\text{analytical}}|}{|\underline{\omega}_{\text{analytical}}|} = 5.31 \times 10^{-8}. \quad (10)$$

The JD method based on linearized harmonic Rayleigh-Ritz method produces an approximation only which leads to a deviation of

$$\frac{|\underline{\omega}_{\text{meshed, JD}} - \underline{\omega}_{\text{analytical}}|}{|\underline{\omega}_{\text{analytical}}|} = 7.57 \times 10^{-4} \quad (11)$$

which is in the same order of magnitude as the blown up linearized approach without any additional preconditioning operations.

## 5 Summary

We have shown how to get a PEP from an electromagnetic structure containing some material following general 2nd order dispersive models. As a first result, This PEP can be solved using a Jacobi-Davidson method from [2]. Further details will be given in the full paper.

## References

1. Z. Bai, J. Demmel, J. Dongarra, A. Ruhe, and H. van der Vorst, editors. *Templates for the solution of Algebraic Eigenvalue Problems: A Practical Guide*. SIAM, Philadelphia, 2000.
2. Michiel E. Hochstenbach and Gerard L. G. Sleijpen. Harmonic and refined rayleigh-ritz for the polynomial eigenvalue problem. *Numerical Linear Algebra with Applications*, 15(1):35–54, 2008.
3. P. B. Johnson and R. W. Christy. Optical constants of the noble metals. *Phys. Rev. B*, 6(12):4370–4379, Dec 1972.
4. T. Weiland. Time domain electromagnetic field computation with finite difference methods. *International Journal of Numerical Modelling*, 9(4):295–319, 1996.

# Region-oriented BEM formulation for numerical computations of electric and magnetic fields

Andreas Blaszczyk

ABB Corporate Research, 5405 Baden-Daettwil, Switzerland [Andreas.Blaszczyk@ch.abb.com](mailto:Andreas.Blaszczyk@ch.abb.com)

**Summary.** The paper presents a concept of the region-oriented 3D formulation for the boundary element method (BEM) applied to computation of electric and magnetic fields. Basic equations are included. An example shows the advantages of the new formulation over the classical approach used for dielectric computation of high voltage power equipment.

## 1 Introduction

The calculation of electric fields based on the boundary element method became during last 10 years a defacto standard in design of high voltage devices [1, 2]. The fundamental advantage of the BEM approach is related to the fact that only surface mesh on boundaries of solid parts is needed. The modeling of so called “airbox” as well as the generation of solid mesh is not required, which significantly simplifies the discretization of complex models.

The classical formulation of the indirect BEM for electrostatic problems introduces a single layer of virtual charges (free and bound) located on surfaces of solid bodies [3]. The field and potential in arbitrary points can be computed as a superposition of all the charges. This approach provides a good accuracy for dielectric problems with typical values of the relative permittivity (in the range between 1 and 10). For values of material properties far beyond the typical range significant numerical errors may occur (see example in section 4).

In this paper the region-oriented formulation concept has been introduced to improve the numerical performance of the BEM approach. This type of formulation has been successfully applied in the charge simulation method in the 1990s [4, 5].

The concept of the region-oriented BEM can be also used for the computation of magnetic fields [6]. However in this abstract only the formulation and examples for electric fields are presented.

## 2 Concept

The basic concept is shown in Fig. 1. The model space has been divided into regions in which the field and potential is calculated based on a unique set of charges located on the region boundaries. Consequently, on boundaries between two regions a double layer of charges is defined while in triple points three different charge values are specified. In contrast to the region-oriented charge simulation the regions can consist of many domains with different material properties.

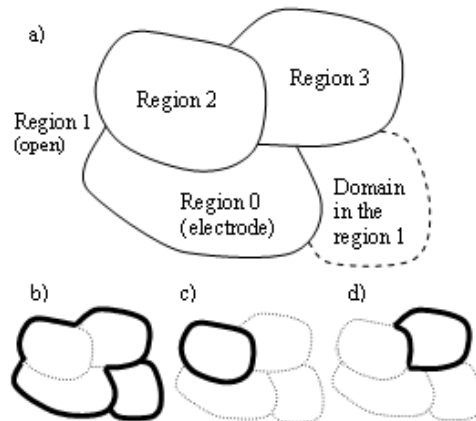


**Fig. 1.** Basic concept of the region-oriented formulation: (a) geometrical configuration (b), (c) and (d) charges assigned to regions 1, 2 and 3 respectively.

## 3 Formulation

In order to find the values of charges the following types of equations are formulated:

- fixed potential on electrodes boundaries in region  $k$ :

$$\sum_{j \in k} p_{ij} \cdot \sigma_{jk} + \Phi_{rk} = \Phi_i \quad (1)$$

- potential continuity on interfaces between regions – this equation is formulated for each region  $l$  that meets with region  $k$  at point  $i$ :

$$\sum_{j \in k} p_{ij} \cdot \sigma_{jk} + \Phi_{rk} = \sum_{j \in l} p_{ij} \cdot \sigma_{jl} + \Phi_{rl} \quad (2)$$

- electric displacement continuity at the boundary point  $i$  (one equation for all regions that meet at point  $i$ )

$$\sum_{k \in i} \varepsilon_k n_{ik} \sum_{j \in k} \nabla p_{ij} \cdot \sigma_{jk} = 0 \quad (3)$$

- flux (charge) compensation for closed regions:

$$\sum_{i \in k} n_{ik} \sum_{j \in k} \nabla p_{ij} \cdot \sigma_{jk} = 0 \quad (4)$$

where  $\varepsilon_k$  are electric permittivities and  $n_{ik}$  are normal vectors. The unknowns in (1)–(4) are charge densities  $\sigma_{ik}$  at collocation points  $i$  (mesh corner nodes) and reference potentials  $\Phi_{rk}$  (both assigned to region  $k$ ). The potential  $p_{ij}$  and field coefficients  $\nabla p_{ij}$  between the collocation point  $i$  and the integration points  $j$  are calculated in the same way as in the classical BEM approach [1, 3].

## 4 Example

Figure 2 shows an example of surge arrester. It consists of 3 sections of zinc oxide cylinders supported by porcelain tubes. In spite of a simple geometry this example makes some difficulties for the classical BEM approach because of high value of electric permittivity of the zinc oxide.

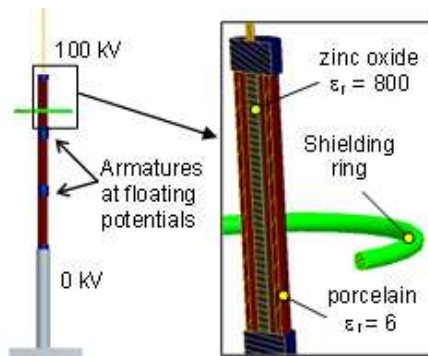


**Fig. 2.** Example of surge arrester. This example is used by IEC as a benchmark model for arrester calculations. For the benchmark configuration the whole arrangement is surrounded by a grounded cylinder with 8 m diameter.

The goal of designers is calculation of the potential distribution along the arrester axis for the purely capacitive case. In order to keep the properties of zinc oxide in linear range a uniform potential gradient is required for normal operation. The result in Fig. 3 shows significant differences between the classical and the region-oriented BEM approaches. The better accuracy of the region-oriented result could be achieved due to explicit formulation of potential continuity (2)

as well as the charge compensation for the high permittivity regions (4). In this way the result does not depend on precision of the numerical integration.

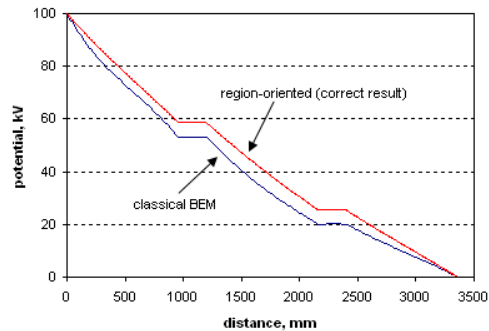


**Fig. 3.** Potential distribution along the axis of the surge arrester from Fig. 2.

## 5 Conclusion

The region-oriented BEM formulation is suitable for the calculation of electric fields in arrangements with extreme differences in material properties. The new approach provides a good foundation for handling of complex geometries as well as nonlinear and quasi-static problems. The details on numerical performance of this formulation will be presented in the extended version of this paper.

## References

1. N. De Kock, M. Mendik, Z. Andjelic and A. Blaszczyk. Application of 3D boundary element method in the design of EHV GIS components. *IEEE Magazine on Electrical Insulation.*, Vol.14, No. 3, pp. 17–22, May/June 1998
2. A. Blaszczyk, H. Ketterer and A. Pedersen. Computational electromagnetism in transformer and switchgear design: Current trends. SCEE 2000. *Lecture Notes on Computational Science and Engineering*, vol. 18, Springer Verlag, ISBN 3-540-42173-3, pp.55–62
3. Z. Andjelic, B. Krstajic, S. Milojkovic, A. Blaszczyk, H. Steinbigler and M. Wohlmuth. Integral methods for the calculation of electric fields. *Scientific Series of the International Bureau Research Center Juelich*, 1992 (ISBN 3-89336-084-0).
4. A. Blaszczyk and H. Steinbigler. Region-oriented charge simulation. *IEEE Trans. on Magnetics*, vol 30, no. 5, September 1994, pp. 2924–2927.
5. A. Blaszczyk. Computation of quasi-static electric fields with region-oriented charge simulation. *IEEE Trans. on Magnetics*, vol. 32. no. 3, May 1996, pp. 828–831.
6. A. Blaszczyk. Formulations based on region-oriented charge simulation for electromagnetics. *IEEE Trans. on Magnetics*, vol 36, no. 4, July 2000, pp. 701–704.

# Tearing and Interconnecting Methods for Non-Elliptic Operators

Markus Windisch and Olaf Steinbach

Institut für Numerische Mathematik markus.windisch@tugraz.at, o.steinbach@tugraz.at

**Summary.** Finite and boundary element tearing and interconnecting methods are well established domain decomposition solvers for elliptic operators. Contrary, for non-elliptic operators much less is known. Here we discuss some approaches for both the Helmholtz equation and the Maxwell system, to construct efficient related parallel solvers.

## 1 Introduction

The use of domain decomposition methods can have different reasons, for example jumping coefficients, the use of different methods on different subdomains, or just because of computational arguments, such as preconditioning. As a model problem we first consider the Helmholtz equation

$$\begin{aligned} -\Delta u(x) - \kappa^2 u(x) &= f(x) & \text{for } x \in \Omega, \\ \gamma_0 u(x) &= g(x) & \text{for } x \in \Gamma_D, \\ \gamma_1 u(x) &= \frac{\partial u}{\partial n}(x) = h(x) & \text{for } x \in \Gamma_N, \end{aligned}$$

where  $\partial\Omega = \Gamma_D \cup \Gamma_N$ .

## 2 Domain decomposition

We decompose the domain  $\Omega$  in several non-overlapping bounded and simply connected subdomains  $\Omega_i$ . If present,  $\Omega_0$  may denote the exterior of some bounded domain, in addition.

The interface and the skeleton of the domain decomposition are defined by

$$\begin{aligned} \Gamma_I &:= \bigcup_{i,j \in \mathcal{I}} \bar{\Gamma}_{ij} \setminus \Gamma_D, \\ \Gamma_S &:= \bigcup_{i \in \mathcal{I}} \Gamma_i = \Gamma_I \cup \partial\Omega. \end{aligned}$$

## 3 Steklov-Poincaré operator

The Dirichlet to Neumann map including the Steklov-Poincaré operator plays a key role in our analysis. Analytically it is just defined by the mapping of some Dirichlet data  $\gamma_0 u$  of a function which fulfills the Helmholtz equation to its

Neumann data  $\gamma_1 u$ . This operator is well defined and invertible as long the wave number  $\kappa$  is not a Dirichlet (resp. Neumann) eigenvalue of the Laplace operator (this is always the case, if the domain  $\Omega_i$  is small enough). There are different possibilities to discretize this operator, here we want to mention the approaches based on finite and boundary element methods. In the finite element approach one assembles the local stiffness matrices and eliminates all interior degrees of freedom to obtain

$$S := A_{\Gamma\Gamma} - A_{\Gamma I} A_{II}^{-1} A_{I\Gamma}.$$

In the boundary element framework we can realize the Steklov-Poincaré operator by the so-called symmetric representation

$$S := D_\kappa + \left(\frac{1}{2} + K'_\kappa\right) V_\kappa^{-1} \left(\frac{1}{2} + K_\kappa\right)$$

where  $V_\kappa$  is the single layer,  $K_\kappa$  is the double layer, and  $D_\kappa$  is the hypersingular potential operator.

## 4 Deduction of coupled systems

In this section we deduce different equivalent formulations of our problem. First we localize the partial differential equation.

Find  $u \in H^1(\Omega)$  such that

$$\begin{aligned} -\Delta u_i - \kappa_i^2 u_i &= 0 & \text{in } \Omega_i, \\ \gamma_1 u_i &= -\gamma_1 u_j & \text{on } \Gamma_{ij}, \\ \gamma_0 u &= g & \text{on } \Gamma_D, \\ \gamma_1 u &= h & \text{on } \Gamma_N, \end{aligned}$$

where  $u_i = u|_{\Omega_i}$ .

By using the local Steklov-Poincaré operator, it is possible to reduce the problem to functions defined on the boundary:

Find  $\gamma_0 u \in H^{1/2}(\Gamma_S)$  so that

$$\begin{aligned} S_i \gamma_0 u|_{\Gamma_i} + S_j \gamma_0 u|_{\Gamma_j} &= 0 & \text{on } \Gamma_{ij} \\ \gamma_0 u &= g & \text{on } \Gamma_D, \\ S_i \gamma_0 u &= h & \text{on } \Gamma_N \cup \Gamma_i. \end{aligned} \tag{1}$$

This system is the starting point of the algebraic approach in the next section.

For a second approach we introduce boundary functions for the local subdomains and the Neumann data  $\lambda \in H^{-1/2}(\Gamma)$  on the skeleton.

Find  $\gamma_0 u_i \in H^{1/2}(\Gamma_i), \lambda \in H^{-1/2}(\Gamma_S)$  such that

$$\begin{aligned} \mu_{ij} \cdot S_i \gamma_0 u_i &= \lambda && \text{on } \Gamma_{ij}, \\ \gamma_0 u &= g && \text{on } \Gamma_D, \\ \lambda &= h && \text{on } \Gamma_N, \\ \gamma_0 u_i &= \gamma_0 u_j && \text{on } \Gamma_{ij} \end{aligned} \quad (2)$$

with  $\mu_{ij} := \text{sign}(i - j)$ .

## 5 Algebraic approach

After discretizing (1) we end up with the algebraic system

$$S_h \underline{u} = \sum_{i=1}^p A_i^T S_{h,i} A_i \underline{u} = \sum_{i=1}^p A_i^T \underline{f}_i.$$

Here, one entry on an interface between two domains has the form

$$S_h[m, n] \bar{u}_n = \langle (S_i + S_j) u_n, \phi_m \rangle.$$

By splitting the degrees of freedom and enforcing the continuity again by an additional equation (this is done for the whole column), this leads to

$$\begin{aligned} \langle S_i u_{i,n}, \phi_m \rangle + \langle S_j u_{j,n}, \phi_m \rangle &= r h s_i + r h s_j, \\ u_{i,n} - u_{j,n} &= 0. \end{aligned}$$

By splitting the test function and reinforcing the continuity of the related Neumann data we end up with

$$\begin{aligned} \langle S_i u_{i,n}, \phi_{i,m} \rangle + \lambda &= r h s_i, \\ \langle S_j u_{j,n}, \phi_{j,m} \rangle - \lambda &= r h s_j, \\ u_{i,n} - u_{j,n} &= 0. \end{aligned}$$

By repeating these operations for all columns one finally obtains

$$\begin{pmatrix} S_{h,1} & & B_1^T \\ & \ddots & \vdots \\ & & S_{h,p} & B_p^T \\ B_1 & \dots & B_p & 0 \end{pmatrix} \begin{pmatrix} \mathbf{u}_1 \\ \vdots \\ \mathbf{u}_p \\ \boldsymbol{\lambda} \end{pmatrix} = r h s.$$

This is the same system which is usually deduced in the elliptic case, but we didn't use any minimization arguments as it is done in the elliptic case.

## 6 Continuous approach

A more analytical approach is based on system (2), the variational formulation of it is

$$\begin{aligned} &\sum_{ij} \int_{\Gamma_{ij}} (\gamma_0 u_i - \gamma_0 u_j) \mu(x) ds_x \\ &+ \int_{\Gamma_N \cap \Gamma_i} (S_i \gamma_0 u_i - h(x)) \cdot v_i ds_x \\ &+ \sum_{ij, i>j} \left( \int_{\Gamma_{ij}} (S_i \gamma_0 u_i - \lambda(x)) \cdot v_i ds_x \right. \\ &\left. + \int_{\Gamma_{ij}} (S_j \gamma_0 u_j + \lambda(x)) \cdot v_j ds_x \right) = 0. \end{aligned}$$

By introducing related bilinear forms we get the mixed formulation:

Find  $u \in \Pi_i H^{1/2}(\Gamma_i)$  and  $\lambda \in H^{-1/2}(\Gamma_S)$  such that

$$\begin{aligned} a(u, v) + b(v, \lambda) &= r h s \\ b(u, \mu) &= r h s \end{aligned}$$

where  $b(u, \mu)$  fulfills the BBL-condition. A Galerkin discretization will now lead to a similar system as above, but the connectivity matrices  $B_i$  have to be replaced by related mass matrices.

## 7 Alternative interface conditions

It is not always possible or practical to decompose the domain  $\Omega$  in domains  $\Omega_i$  such that each domain is small enough to avoid eigenvalues of the Laplace operator. Another way to avoid this critical eigenvalues are alternative interface conditions. One possible choice are Robin-type interface conditions. In the finite element case this approach was introduced in [1], in the case of boundary elements one has to find a way to treat the inverse of the single layer potential which also appears when solving Robin-type problems. At least in the case of the domain  $\Omega_0$  it is no problem to use the boundary element method (which is the favourable method for unbounded domains) also for Dirichlet or Neumann interfaces when using regularized boundary integral formulations, see [2].

Another possibility is to use interface conditions which are based on the representation formula, see [3]

## References

1. O. Cessenat and B. Despres. Application of an ultra weak variational formulation of elliptic PDEs to the two-dimensional Helmholtz problem. *SIAM J. Numer. Anal.*, 35(1):255–299 (electronic), 1998.
2. S. Engleder and O. Steinbach. Modified boundary integral formulations for the Helmholtz equation. *J. Math. Anal. Appl.*, 331(1):396–407, 2007.
3. R. Hiptmair. Boundary element methods for eddy current computation. In *Boundary element analysis*, volume 29 of *Lect. Notes Appl. Comput. Mech.*, pages 213–248. Springer, Berlin, 2007.

# Parametric Models of Transmission Lines Based on First Order Sensitivities

Alexandra Ștefănescu, Daniel Ioan, and Gabriela Ciuprina

Politehnica University of Bucharest, Electrical Engineering Dept., Numerical Methods Lab., Spl. Independentei 313, 060042, Romania [lmn@lmn.pub.ro](mailto:lmn@lmn.pub.ro)

**Summary.** One of the major goals in designing transmission lines is to handle variability. This paper proposes a method to parameterize the p.u.l. parameters of TL models w.r.t. the geometric parameters, subject to large or small variations. Examples of such variations are either due to design or technology (process or lithography), respectively. The accuracy of the simplest first order models is studied and validated experimentally for both affine and rational variability models.

## 1 Introduction

While short interconnects have simple circuit models (e.g. a lumped capacitance), interconnects longer than the wave length are critical for a proper functionality of the designed system. In this case the extracted model has to consider also the effect of the distributed parameters. Fortunately, in most cases, the long interconnects have the same cross-sectional geometry along their extension. If not, they may be decomposed in straight parts connected together by junction components. The former are represented as transmission lines, while the latter are modeled as common passive 3D components.

This paper focuses on the variability of the numerical extracted models for interconnects with respect to the geometric parameters. Such an approach represents one of the issues of the research carried out within the European project FP6/IST/Chameleon [1].

## 2 Parametric Models Based on First Order Sensitivities

The parameter variability is computed using the first order Taylor series expansion. This needs the computation of the derivatives of the device characteristics with respect to the design parameters [2]. Let  $y$  be the device characteristic which depends on the design parameters  $(p_1, p_2, \dots, p_n)$ . The quantity  $y$  may be, for instance the real or the imaginary part of the device admittance at a given frequency. The parameter variability is

thus completely described by the real function  $y : S \rightarrow \mathbb{R}$ , defined over the design space  $S$ , a subset of  $\mathbb{R}^n$ . Denoting by  $p_0 = (p_{01}, p_{02}, \dots, p_{0n})$  the nominal values of the design parameters and by  $y_0 = y(p_0)$ , the device characteristic for the nominal set of parameter, if  $y$  is smooth enough then its truncated Taylor series expansion is the best polynomial approximation in the vicinity of the expansion point  $p_0$ . The first order truncation of the Taylor series is the affine function:

$$y(p_1, p_2, \dots, p_n) = y_0 + \sum_{k=1}^n S_{pk}(p_k - p_{0k}), \quad (1)$$

where  $S_{pk} = \frac{\partial y}{\partial p_k}(p_0)$  are the first order absolute sensitivities, defined as partial derivatives of the device characteristics, with respect to the design parameters, computed for the nominal values of the parameters. This definition is valid not only for real valued characteristics, but also when  $y$  is a complex number, a vector or a matrix.

## 3 Results

The test consists of a microstrip (MS) transmission line having one Aluminum conductor embedded in a  $\text{SiO}_2$  layer. The line has a rectangular cross-section, parameterized by the parameters  $p_2$  and  $p_3$  (Fig. 1). Its position is parameterized by  $p_1$ . The return path is on the grounded surface placed at  $y = 0$ . The nominal values used are:  $x_{max} = 20\mu\text{m}$ ,  $h_2 = 10\mu\text{m}$ ,  $h_3 = 5\mu\text{m}$ ,  $h_0 = 1\mu\text{m}$ ,  $p_1 = 1\mu\text{m}$ ,  $p_2 = 0.67\mu\text{m}$ ,  $p_3 = 3\mu\text{m}$ ,  $\sigma_{Al} = 3.3\text{MS}/\text{m}$ ,  $\epsilon_{r-\text{SiO}_2} = 3.9\text{F}/\text{m}$ .

For the nominal case, by using dFIT + dELOB, at low frequencies, the following values are obtained:

$$\begin{aligned} R &= 18.11\text{k}\Omega/\text{m} & L &= 322\text{nH}/\text{m} \\ C &= 213\text{pF}/\text{m} \end{aligned} \quad (2)$$

At high frequencies, the per unit length resistance and inductance are frequency dependent, and they can be computed for instance with the method described in [3].

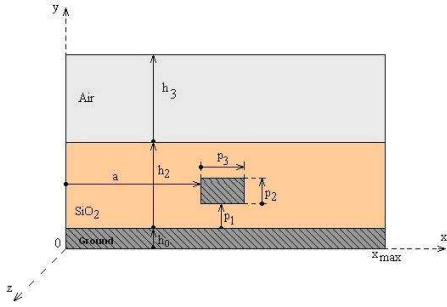


Fig. 1. Stripline parameterized conductor

### A. Affine or Rational Models for One Parameter Case

The first order sensitivities are essential for the analysis of the parameter variability in the time domain. In order to evaluate the error introduced by the first order TS expansion, let us consider only one parameter ( $n = 1$ ). The variability model based on (1) defines an *affine* or *additive* model (A) since each new parameter considered adds a contributing term to the sum.

The affine models for the p.u.l. parameters considered are first order truncation of the Taylor Series:

$$X = X_0(1 + S_p^X \delta p) \quad (3)$$

where  $X$  is either  $R$ ,  $L$  or  $C$ . The *rational* models are first order Taylor series approximations of the inverse quantity,  $1/X$ :

$$X = \frac{X_0}{(1 + S_p^{\frac{1}{X}} \delta p)} \quad (4)$$

where it can be easily shown that the reverse relative sensitivity is  $S_p^{\frac{1}{X}} = -S_p^{X_0}$ . The sensitivities are computed using the CHAMY software [1], by the differential method (DM) applied to the state space equations [2].

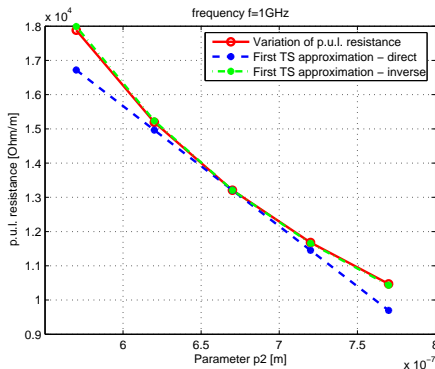


Fig. 2. Reconstruction of the per unit length  $R$  at 1GHz, from TS first order expansion

Figure 2 illustrates the effect of variation of parameter  $p_2$  between  $0.57\mu\text{m}$  and  $0.77\mu\text{m}$ . As

expected, the reverse approximation of  $R$  is better than the direct Taylor series approximation. Using this graph, the validity range for an imposed accuracy can be identified.

### B. Models for Multi Parametric Case

For the example considered above, in order to extend its validity domain a rational model (R) can be used:

$$X = \frac{X_0(1 + S_{p1}^X \delta p_1)}{(1 + S_{p2}^{\frac{1}{X}} \delta p_2)(1 + S_{p3}^{\frac{1}{X}} \delta p_3)} \quad (5)$$

where nominal values of per length parameters are given by (2). A multi - parametric model can be obtained by multiplication of affine models for several parameters (model M):

$$X = X_0 \prod_{k=1}^n (1 + S_{pk}^X \delta p_k) \quad (6)$$

while the additive (affine) models A are

$$X = X_0(1 + \sum_{k=1}^n S_{pk}^X \delta p_k) \quad (7)$$

First order multi - variable model is obtained by addition of variations along several directions. The main difference between A and M models are the "cross terms", which are neglected in the A model. In the full paper we will address this issue, being a completion to [4].

The paper analyzes variability models for TL structures considering the dependency of p.u.l. parameters w.r.t. geometric parameters, at a given frequency. A symbolic approach will also be considered in a future research. As an alternative to the affine dependence, a rational approximation of first order is proposed.

## References

1. CHAMELEON-RF site: [www.chameleon-rf.org](http://www.chameleon-rf.org)
2. G. Ciuprina, D. Ioan, D. Niculae, J. F. Villena, L. M. Silveira Parametric models based on sensitivity analysis for passive components *Intelligent Computer Techniques in Applied Electromagnetics Studies in Computational Intelligence* vol. 119, pp. 17-22, Springer, 2008.
3. D. Ioan, G. Ciuprina, S. Kula, Reduced Order Models for HF Interconnect over Lossy Semiconductor Substrate *Proceedings of the 11th IEEE Workshop on Signal Propagation on Interconnects, May 2007*, pp.233-236
4. A. Ștefănescu, G. Ciuprina, D. Ioan, Models for Variability of Transmission Line Structures *Proceedings of the 12th IEEE Workshop on Signal Propagation on Interconnects, May 2008*

---

**Session**

**CS 1**

---



# ANN/DNN-based Behavioral Modeling of RF/Microwave Components/Devices and Circuit Blocks

Q.J. Zhang and Shan Wan

Dept. of Electronics, Carleton University, 1125 Colonel By Dr., Ottawa, Canada K1S 5B6  
 qjz@doe.carleton.ca, swan@doe.carleton.ca

**Summary.** This paper provides a tutorial overview of ANN/DNN for RF and microwave modeling and design. We will describe neural network structures suitable for representing high-speed/high-frequency behaviors in components and circuits, ANN training exploiting RF/microwave device and circuits data, formulation of ANN/DNN for passive and active device modeling, and behavioral modeling of nonlinear circuit blocks, and use of ANN/DNN models for high level RF/microwave simulation and design optimization.

## 1 Introduction

Artificial neural networks (ANNs) have gained recognition as an emerging vehicle in enhancing the effectiveness of computer-aided modeling and design of RF and microwave circuits and systems [1–6]. ANNs can be trained to learn electromagnetic/circuit behaviors from component data. Trained ANNs can be used in high-level circuit and system simulation and optimization providing accuracy and/or speed advantages in design. The learning capabilities of ANN can be used for enhancing the existing CAD models of passive and active components [7], and thereby extending our ability of describing component behaviors to be even closer towards reality. ANNs can be used to improve speed, accuracy and flexibility of microwave modeling and CAD. This is made possible because of their established network structures, universal approximation property, and the ability to integrate with circuit knowledge. ANNs have been applied to modeling and design of microstrip and CPW circuits, multilayer interconnects, embedded passive components, printed antennas, semiconductor devices, filters, amplifiers and so on. Further advances in embedding microwave information into neural networks lead to new knowledge-based methods for robust electrical modeling [8]. There are increased initiatives for integration of neural network capabilities into circuit design and test processes. For example, recent reports include embedding neural networks in circuit optimization, statistical design, global modeling, computational electromag-

netics, measurement standards, and nonlinear circuits and system level design. Automatic model generation algorithms allow systematic and computerized model creation, complimenting existing human based approaches in developing RF and microwave models [9]. The development of an advanced ANN structure, called dynamic neural network (DNN) [10, 11], is one of the major recent directions where dynamic behavior of nonlinear circuits is modeled by ANN-learning of circuit input-output data.

## 2 Tutorial Overview of Methodology and Application

This paper will describe the fundamentals of using ANN/DNN for RF and microwave modeling and design, and highlight its recent applications. The major topics will be ANN structures, ANN training, formulation of ANN for RF/microwave modeling, and use of ANN models for RF/microwave design. Several ANN structures will be described, including multiplayer perceptron (MLP), radial basis function (RBF) networks, knowledge-based neural networks (KBNN), recurrent neural networks (RNN) and dynamic neural networks (DNN). The knowledge based neural networks combine conventional empirical/equivalent models with ANN to achieve accurate model with less training data. Several methods for knowledge based networks will be highlighted such as different method, prior-knowledge-input method, space mapped neural network method, and KBNN method. By establishing relationships between buffered history of input-output signals, or set of time-derivatives of input-output signals, the RNN and DNN can represent the dynamic relationship between input and output signals in circuit blocks. Formulations of RNN and DNN for behavioral modeling of nonlinear devices and circuit blocks will be presented. We also introduce automated model generation algorithms (AMG) which perform ANN training including selection of training samples and neural network size adjustment. An adaptive sam-

pling algorithms are used during the training process to decide how many training data is needed, and how the data should be distributed/sampled in the training space. The neural network size (such as the number of hidden neurons) is determined during the training process according to a set of under-learning and over-learning criteria. The AMG algorithm aims to achieve required model accuracy with minimum amount of training data. Application examples such as fast parametric modeling of EM structures, modeling of semiconductor devices, behavioral modeling of high-speed driver/receiver buffers, behavioral modeling of power amplifiers will be presented. Examples of applying the ANN/DNN models in circuit simulation will be presented.

## References

1. Q.J. Zhang and K.C. Gupta. *Neural Networks for RF and Microwave Design*. Artech House, Boston, Massachusetts, 2000.
2. Q.J. Zhang, K.C. Gupta and V.K. Devabhaktuni. Artificial neural networks for RF and microwave design: from theory to practice. *IEEE Trans. Microwave Theory Tech.*, 51:1339-1350, 2003.
3. J.E. Rayas-Sanchez. EM-based optimization of microwave circuits using artificial neural networks: the state-of-the-art. *IEEE Trans. Microwave Theory Tech.*, 52:420-435, 2004.
4. X. Ding, V.K. Devabhaktuni, B. Chattaraj, M.C.E. Yagoub, M. Doe, J.J. Xu and Q.J. Zhang. Neural network approaches to electromagnetic based modeling of passive components and their applications to high-frequency and high-speed nonlinear circuit optimization. *IEEE Trans. Microwave Theory Tech.*, 52:436-449, 2004.
5. Y. Fang, M.C.E. Yagoub, F. Wang and Q.J. Zhang. A new macromodeling approach for nonlinear microwave circuits based on recurrent neural networks. *IEEE Trans. Microwave Theory Tech.*, 48:2335-2344, 2000.
6. H. Zaabab, Q. Zhang and M. Nakhla. A neural network modeling approach to circuit optimization and statistical design. *IEEE Trans. Microwave Theory Tech.*, 43:1349-1358, 1995.
7. L. Zhang, J.J. Xu, M. Yagoub, R. Ding and Q.J. Zhang. Efficient analytical formulation and sensitivity analysis of neuro-space mapping for nonlinear microwave device modeling. *IEEE Trans. Microwave Theory Tech.*, 53:3752-3767, 2005.
8. F. Wang and Q.J. Zhang. Knowledge-based neural models for microwave design. *IEEE Trans. Microwave Theory Tech.*, 45:2333-2343, 1997.
9. V.K. Devabhaktuni, B. Chattaraj, M.C.E. Yagoub and Q.J. Zhang. Advanced microwave modeling framework exploiting automatic model generation, knowledge neural networks and space mapping. *IEEE Trans. Microwave Theory Tech.*, 51:1822-1833, 2003.
10. J.J. Xu, M.C.E. Yagoub, R. Ding and Q.J. Zhang. Neural-based dynamic modeling of nonlinear microwave circuits. *IEEE Trans. Microwave Theory Tech.*, 50:2769-2780, 2002.
11. Y. Cao, R.T. Ding and Q.J. Zhang. State-space dynamic neural network technique for high-speed IC applications: modeling and stability analysis. *IEEE Trans. Microwave Theory Tech.*, 54: 2398-2409, 2006.

# Model Order Reduction for Nonlinear IC models with POD

A. Verhoeven<sup>1</sup>, M. Striebel<sup>2,3</sup>, and E.J.W. ter Maten<sup>3,4</sup>

<sup>1</sup> VORtech Computing, Delft, The Netherlands [Arie.Verhoeven@vortech.nl](mailto:Arie.Verhoeven@vortech.nl)

<sup>2</sup> Technical University Chemnitz, Chemnitz, Germany [michael.striebel@mathematik.tu-chemnitz.de](mailto:michael.striebel@mathematik.tu-chemnitz.de)

<sup>3</sup> NXP Semiconductors, Eindhoven, The Netherlands [Jan.ter.Maten@nxp.com](mailto:Jan.ter.Maten@nxp.com)

<sup>4</sup> Technische Universiteit Eindhoven, The Netherlands

**Summary.** Reduced order modelling of large nonlinear system is of large importance for industry. Despite the linear case where great progress is being recorded, methodologies for nonlinear problems is only beginning to develop. Approaches based on linearisation are promising. We present a technique based on singular value decomposition that keeps the nonlinear characteristic and yet avoids the need to evaluate the nonlinear functions describing the complete system.

## 1 Introduction

The development of fail-safe circuit designs relies heavily on computer simulations. The demand for short time-to-market circles requires both accurate and fast algorithms.

Model Order Reduction (MOR) aims at accelerating the process of simulation by streamlining the models to be treated in such a way that the basic characteristics of interest are conserved.

Due to the ever increasing refinement in modelling physical effects in circuit design, network equations exhibit a more and more nonlinear characteristic.

As the packaging density and therefore the complexity of network models is increasing, too, reduced order modelling of large nonlinear systems is of large practical importance for industry.

For linear RLC circuits there exist already quite a lot of MOR techniques [1]. However, corresponding techniques for nonlinear problems is only beginning to develop.

## 2 Pojection Based Nonlinear MOR

In general an electrical network is described by the nonlinear differential-algebraic equation of the form

$$\frac{d}{dt}[q(x(t))] + j(x(t)) + Bu(t) = 0, \quad (1)$$

where  $x(t) \in \mathbb{R}^n$  represents the unknown vector of circuit variables at time  $t$ ;  $q, j : \mathbb{R}^n \rightarrow \mathbb{R}^n$  describe the contribution of reactive and nonreactive elements, respectively.  $B \in \mathbb{R}^{n \times n}$  distributes the input  $u(t) \in \mathbb{R}^m$ .

Projection based MOR techniques use Petrov-Galerkin projection to obtain a order reduced model for (1) of the form

$$\frac{d}{dt}[W^T q(Vz)] + W^T j(Vz) + W^T Bu = 0, \quad (2)$$

where  $W, V \in \mathbb{R}^{n \times r}$ . The original state can be obtained by  $x = Vz$ . With  $r \ll n$  it is clear that the order of (2) is much smaller than the size of the original system (1).

But, using any implicit integration scheme, e.g., a Backward Differentiation Formula (BDF), to solve (2) numerically on some discrete time scale  $\{t_0, t_1, \dots\}$  necessitates the Jacobians

$$W^T \cdot \frac{\partial}{\partial x} q(x(t_i)) \cdot V \quad \text{and} \quad W^T \cdot \frac{\partial}{\partial x} j(x(t_i)) \cdot V, \quad (3)$$

evaluated at  $x(t_i) = Vz(t_i)$  for  $i = 1, 2, \dots$ . Clearly, still the complete functions  $q$  and  $j$  have to be evaluated. Furthermore, matrix-vector products have to be evaluated and the Jacobians most likely become dense. Actually, except from the lower dimension, no reduction is achieved.

### 2.1 Adapted POD

To overcome these problems, we suggest to adapt the POD approach such that only a few components of  $q$  and  $j$  have to be determined i.e., evaluated.

We assume that we have a benchmark solution  $\tilde{x}(t)$  of (1) to some input  $u(t)$  and a matrix  $X \in \mathbb{R}^{n \times N}$  of  $N$  snapshots. We determine the eigenvalue decomposition of the correlation matrix

$$W = \frac{1}{N} X X^T = \frac{1}{N} U \Sigma \Sigma^T U^T. \quad (4)$$

Here the matrix  $U \in \mathbb{R}^{n \times n}$  is orthonormal. The product  $\Sigma \Sigma^T \in \mathbb{R}^{n \times n}$  is a positive real diagonal matrix, and therefore we can write  $\Sigma \Sigma^T = \Gamma^2$  for a real positive diagonal matrix  $\Gamma \in \mathbb{R}^{n \times n}$ . In contrast to POD we introduce the orthogonal matrix  $L = U \Gamma \in \mathbb{R}^{n \times n}$ , such that  $W = \frac{1}{N} L L^T$ .

We perform a projection of (1):

$$\frac{d}{dt}[L^T q(Ly)] + L^T j(Ly) + L^T Bu = 0, \quad (5)$$

with  $x = Lu$ . We approximate  $L \approx LP_r^T P_r$  and  $L^T \approx L^T P_g^T P_g$  where  $P_r \in \{0,1\}^{r \times n}$  and  $P_g \in \{0,1\}^{g \times n}$  select the  $r$  and  $g$  columns of  $L$  and  $L^T$  with largest norm, respectively. That means,  $L$  and  $L^T$  are replaced by matrices where all but the  $r$  and  $g$ , respectively, most dominant columns are set to zero.

After multiplication of (5) with  $P_r$ , i.e. truncation according to the  $r$  most dominant singular values of  $X$  and proper scaling we arrive at the reduced system of order  $r \ll n$

$$\frac{d}{dt}[W_{rg}\bar{q}(U_r z)] + W_{rg}\bar{j}(U_r z) + B_r u = 0, \quad (6)$$

with reduced state  $z(t) \in \mathbb{R}^r$ ,  $U_r \in \mathbb{R}^{n \times r}$  containing the  $r$  most dominant columns of  $U$  like in classical POD,  $W_{rg} = U_r^T P_g^T \in \mathbb{R}^{r \times g}$  and  $B_r = U_r^T B \in \mathbb{R}^{r \times m}$ . The state vector of the full systems can be recovered by  $x(t) = U_r z(t)$ .

We stress that the principal reduction takes place in the nonlinear functions  $\bar{q}(\cdot) = P_g q(\cdot) \in \mathbb{R}^g$  and  $\bar{j} = P_g j(\cdot) \in \mathbb{R}^g$ , meaning that instead of the complete functions, just  $g \ll n$  components have to be evaluated.

## 2.2 Trajectory PieceWise Linear approach

The basic idea of the Trajectory PieceWise Linear approach (TPWL, [2, 3]) is to replace the nonlinear problem (1) with a convex linear combination of linear systems which are reduced by means of some linear MOR techniques:

$$\sum_{i=1}^s w_i(z) \cdot [V_r^T C_i V_r \dot{z} + V_r^T G_i V_r z + V_r^T B_i u(t)] = 0,$$

where the weights  $w_i(z) \geq 0$  with  $\sum w_i(z) = 1$  determine, which of the local linear subsystems that arise from linearisation of (1) around a typical trajectory are contributing to the dynamics close to the current state.

## 3 Numerical Results

We consider the academic diode chain model shown in Fig. 1 with 300 nodes. The current traversing a diode with potential  $V_a$  and  $V_b$  at the input- and output-node, respectively is described by the nonlinear equation

$$q(V_a, V_b) = \begin{cases} I_s (e^{\frac{V_a - V_b}{V_T}} - 1) & \text{if } V_a - V_b > 0.5 \\ 0 & \text{otherwise} \end{cases}$$

The voltage source is described by

$$u(t) = \begin{cases} 20 & \text{if } t \leq 10\text{ns} \\ 170 - 15 \cdot 10^9 \cdot t & \text{if } 10\text{ns} < t \leq 11\text{ns} \\ 5 & \text{if } t > 11\text{ns} \end{cases}$$

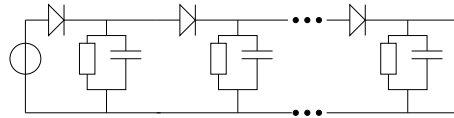


Fig. 1. Testcircuit: Diode chain

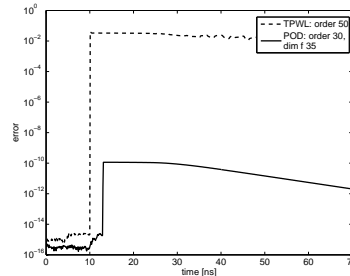


Fig. 2. Relative errors for TPWL and POD

Table 1. Comparison of adapted POD and TPWL

Method	r	g	Extr. time	Sim. time
Original	302	0		79s
TPWL	50		202s	2.4s
adapt. POD 30		35	107 s	10.2s

Figure 2 shows the relative error and Table 1 reflects the time needed to extract and resimulate a reduced model. This clearly shows that POD approach still is a promising approach for MOR of nonlinear problems.

*Acknowledgement.* This work is funded by the Marie-Curie projects O-MOORE-NICE! and COMSON.

## References

1. A. Antoulas. *Approximation of Large-Scale Dynamical Systems*, Advances in Design and Control 6, SIAM, 2005
2. M. J. Rewieński. A Trajectory Piecewise-Linear Approach to Model Order Reduction of Nonlinear Dynamical Systems. Ph.D. thesis, Massachusetts Institute of Technology, USA, 2003.
3. T. Voß, R. Pulch, J. ter Maten, A. El Guennoui. Trajectory piecewise linear approach for nonlinear differential-algebraic equations in circuit simulation. *Scientific Computing in Electrical Engineering. Mathematics in Industry.*, G. Ciuprina, D. Ioan (editors), Vol. 11, Springer, pp. 167-174, 2007.

# Model Order Reduction for Systems with Coupled Parameters

Lihong Feng and Peter Benner

Mathematics in Industry and Technology, Faculty of Mathematics, Chemnitz University of Technology,  
D-09107 Chemnitz, Germany [lihong.feng@mathematik.tu-chemnitz.de](mailto:lihong.feng@mathematik.tu-chemnitz.de),  
[benner@mathematik.tu-chemnitz.de](mailto:benner@mathematik.tu-chemnitz.de)

**Summary.** We consider parametric model order reduction of systems with parameters which are non-linear functions of the frequency parameter  $s$ . Such systems result from, for example, the discretization of electromagnetic systems with surface losses [3]. Since the parameters are functions of the frequency  $s$ , they are highly coupled with each other. We see them as individual parameters when we implement model order reduction. By analyzing existing parametric model order reduction methods for computing the projection matrix  $V$ , we show the applicability of each method and propose an optimized method for the parametric system considered in this paper.

## 1 Problem Description

The transfer function of the parametric systems considered here takes the form

$$H(s) = sB^T(s^2I_n - 1/\sqrt{s}D + A)^{-1}B, \quad (1)$$

where  $A, D$  and  $B$  are  $n \times n$  and  $n \times m$  matrices, respectively, and  $I_n$  is the identity of suitable size. To apply parametric model order reduction to (1), we first expand  $H(s)$  into a power series. Using a series expansion about an expansion point  $s_0$ , and defining  $\sigma_1 := \frac{1}{s^2\sqrt{s}} - \frac{1}{s_0^2\sqrt{s_0}}$ ,  $\sigma_2 := \frac{1}{s^2} - \frac{1}{s_0^2}$ ,  $G := I - \frac{1}{s_0^2\sqrt{s_0}}D + \frac{1}{s_0^2}A$ , we get:

$$\begin{aligned} H(s) &= sB^T(s^2I - 1/\sqrt{s}D + A)^{-1}B \\ &= \frac{1}{s}B^T(I - \frac{1}{s^2\sqrt{s}}D + \frac{1}{s^2}A)^{-1}B \\ &= \frac{1}{s}B^T(G - \sigma_1D + \sigma_2A)^{-1}B \\ &= \frac{1}{s}B^T(I - \sigma_1G^{-1}D + \sigma_2G^{-1}A)^{-1}G^{-1}B \\ &= \frac{1}{s}B^T[I - (\sigma_1G^{-1}D - \sigma_2G^{-1}A)]^{-1}G^{-1}B \\ &= \frac{1}{s}B^T \sum_{i=0}^{\infty} (\sigma_1G^{-1}D - \sigma_2G^{-1}A)^i G^{-1}B. \end{aligned} \quad (2)$$

We may use the three different parametric model reduction methods below to compute a projection matrix  $V$  (which is independent of  $s$ ) from (2) and get the reduced-order transfer function

$$\hat{H}(s) = s\hat{B}^T(s^2I_r - 1/\sqrt{s}\hat{D} + \hat{A})^{-1}\hat{B},$$

where  $\hat{A} = V^TAV$ ,  $\hat{B} = V^TB$ , etc., and  $V$  is an  $n \times r$  projection matrix with  $V^TV = I_r$ . To simplify notation, in the following we use  $B_M := G^{-1}B$ ,  $M_1 := G^{-1}D$ , and  $M_2 := -G^{-1}A$ .

Notice that (1) is also discussed in [3], where only conventional non-parametric model order reduction method is considered. The generated projection matrix  $V$  is dependent on a particular value of  $s$ :  $s_0$ , which may cause large error for other values of  $s$  which are far away from  $s_0$ . All methods presented in this paper are parametric model order reduction methods. The basic difference of parametric model reduction from non-parametric model reduction is that the computed projection matrix  $V$  is independent of any special value of  $s$ , which produces a reduced model with evenly distributed small error.

## 2 Different Methods of Computing Projection matrix $V$

### 2.1 Directly Computing $V$

A simple and direct way for obtaining  $V$  is to compute the coefficient matrices in the series expansion

$$\begin{aligned} H(s) &= \frac{1}{s}B^T[B_M + (M_1B_M\sigma_1 + M_2B_M\sigma_2) \\ &\quad + (M_1^2B_M\sigma_1^2 + (M_1M_2 + M_2M_1)B_M\sigma_1\sigma_2 \\ &\quad + M_2^2B_M\sigma_2^2) + (M_1^3B_M\sigma_1^3 + \dots) + \dots], \end{aligned} \quad (3)$$

by direct matrix multiplication and orthogonalize these coefficients to get the matrix  $V$  [1]. After the coefficients  $B_M, M_1B_M, M_2B_M, M_1^2B_M, (M_1M_2 + M_2M_1)B_M, M_2^2B_M, M_1^3B_M, \dots$  are computed, the projection matrix  $V$  can be obtained by

$$\text{range}\{V\} = \text{orthogonalize}\{B_M, M_1B_M, \dots, (M_1M_2 + M_2M_1)B_M, \dots\} \quad (4)$$

Unfortunately, the coefficients quickly become linearly dependent due to numerical instability. In the end, the matrix  $V$  is often so inaccurate that it does not possess the expected theoretical properties.

### 2.2 Recursively Computing $V$

The series expansion (3) can also be written into the following formulation:

$$H(s) = \frac{1}{s} [B_M + (\sigma_1 M_1 + \sigma_2 M_2) B_M + \dots + (\sigma_1 M_1 + \sigma_2 M_2)^i B_M + \dots] \quad (5)$$

Using (5), we define

$$\begin{aligned} R_0 &= B_M, \\ R_1 &= [M_1, M_2] R_0, \\ &\vdots \\ R_j &= [M_1, M_2] R_{j-1}, \\ &\vdots \end{aligned} \quad (6)$$

We see that  $R_0, R_1, \dots, R_j, \dots$  include all the coefficient matrices in the series expansion (5). Therefore, we can use  $R_0, R_1, \dots, R_j, \dots$  to generate the projection matrix  $V$ :

$$\text{range}\{V\} = \text{colspan}\{R_0, R_1, \dots, R_m\}. \quad (7)$$

Here,  $V$  can be computed by employing the recursive relations between  $R_j$ ,  $j = 0, 1, \dots, m$  combined with the modified Gram-Schmidt process [2].

### 3 Optimized Method of Computing Projection Matrix $V$

Note that the coefficients  $M_1 M_2 B_M$  and  $M_2 M_1 B_M$  are two individual terms in (6), which are computed and orthogonalized sequentially within the modified Gram-Schmidt process. Observing that they are actually both coefficients of  $\sigma_1 \sigma_2$ , they can be combined together as one term during the computation as in (4). Based on this, we develop an algorithm which can compute  $V$  in (4) by a modified Gram-Schmidt process. By this algorithm, the matrix  $V$  is numerically stable which guarantees the accuracy of the reduced-order model. Furthermore, the size of the reduced-order model is smaller than that of the reduced-order model derived by (7). The improved algorithm is well suited for the parametric system from computational electromagnetics considered in this paper. Its performance will be illustrated using an industrial test example.

*Acknowledgement.* This research is supported by the Alexander von Humboldt-Foundation and by the research network *SyreNe — System Reduction for Nanoscale IC Design* within the program *Mathematics for Innovations in Industry and Services* (Mathematik für Innovationen in Industrie und Dienstleistungen) funded by the German Federal Ministry of Education and Science (BMBF).

### References

1. L. Daniel, O.C. Siong, L.S. Chay, K.H. Lee, and J. White. A multiparameter moment-matching

model-reduction approach for generating geometrically parameterized interconnect performance models. *IEEE Trans. Comput.-Aided Des. Integr. Circuits Syst.*, 22(5):678–693, 2004.

2. L. Feng and P. Benner. A robust algorithm for parametric model order reduction. *In Proc. Appl. Math. Mech.*, 2008 (to appear).
3. T. Wittig, R. Schuhmann, and T. Weiland. Model order reduction for large systems in computational electromagnetics. *Linear Algebra Appl.*, 415(2-3):499–530, 2006.

# Model order and terminal reduction approaches via matrix decomposition and low rank approximation

André Schneider and Peter Benner

Technische Universität Chemnitz, Fakultät für Mathematik, 09107 Chemnitz, Germany  
 andre.schneider@mathematik.tu-chemnitz.de, peter.benner@mathematik.tu-chemnitz.de

**Summary.** We discuss methods for model order reduction (MOR) of linear systems with many inputs and outputs, arising in the modeling of linear (sub) circuits with a huge number of nodes and a large number of terminals, like power grids. Our work is based on the approaches SVDMOR and ESVDMOR proposed in recent publications. In particular, we discuss efficient numerical algorithms for their implementation. Only using efficient tools from numerical linear algebra techniques, these methods become applicable for truly large-scale problems.

## 1 Introduction

One issue in MOR for VLSI design is the reduction of parasitic linear sub circuits. These circuits form substructures in the design of ICs and contain linear elements with little or no influence on the result of the simulation. In some applications, the structure of these parasitic linear sub circuits has recently changed in the following sense. So far, the number of elements in these sub circuits was significantly larger than the number of connections to the whole circuit, the so called pins or terminals. This assumption is no longer valid in all cases. Circuits with a lot of elements need an extra power supply network, so called power grids. In clock distribution networks, the clock signal is distributed from a common point to all the elements that need it for synchronization. For simulating these circuits new methods are needed. We want to introduce an efficient algorithm handling this problem.

## 2 SVDMOR and ESVDMOR

Recent studies have shown that we can make use of a large degree of correlation between the plurality of input and output terminals. We use the singular value decomposition (SVD) based method SVDMOR [2, 8] as well as an extended version of SVDMOR, the so called ESVDMOR [4–6, 8], which is the foundation for our work and will be explained in the following.

### 2.1 Extended-SVDMOR

We assume that the linear system to be reduced has the following transfer function in frequency domain:

$$H(s) = L(sC + G)^{-1}B, \quad (1)$$

with  $C, G \in \mathbb{R}^{n \times n}$ ,  $B \in \mathbb{R}^{n \times m_{in}}$ , and  $L \in \mathbb{R}^{m_{out} \times n}$ . We assume that there is a difference between the number of inputs  $m_{in}$  and the number of outputs, here  $m_{out}$ . Consider the  $i$ -th block moment of (1)

$$\mathbf{m}_i = \begin{bmatrix} m_{1,1}^i & m_{1,2}^i & \cdots & m_{1,m_{in}}^i \\ m_{2,1}^i & m_{2,2}^i & \cdots & m_{2,m_{in}}^i \\ \vdots & \vdots & \ddots & \vdots \\ m_{m_{out},1}^i & m_{m_{out},2}^i & \cdots & m_{m_{out},m_{in}}^i \end{bmatrix}, \quad (2)$$

where  $\mathbf{m}_i$  is a  $m_{out} \times m_{in}$  matrix. The ESVDMOR approach uses the information of these moments to create a decomposition of (1) and consequently a new internal transfer function  $H_r(s)$ ,

$$H(s) \approx \hat{H}(s) = V_{O,r_o} \underbrace{L_r(G + sC)^{-1}B_r}_{:=H_r(s)} V_{I,r_i}^T. \quad (3)$$

The matrices  $L_r$  and  $B_r$  are approximations of  $L$  and  $B$  computed with the help of the SVD, which also generates  $V_{O,r_o}$  and  $V_{I,r_i}^T$ . Note that  $r_i$  and  $r_o$  are the numbers of the reduced virtual input and output terminals. This terminal reduced transfer function is now reduced to  $\tilde{H}_r(s)$  by a well known established MOR method, e. g., balanced truncation or Krylov subspace methods. At the end we get a very compact terminal and reduced order model

$$H(s) \approx V_{O,r_o} \tilde{H}_r(s) V_{I,r_i}^T. \quad (4)$$

Note that SVDMOR can be considered as a special of ESVDMOR, using only one moment, e. g.,  $\mathbf{m}_0$  and one SVD.

### Drawbacks and solutions

For very large sub circuits the (E)SVDMOR approaches are not suitable because of using the

SVD. Therefore we combine the (E)SVD MOR approach with cheaper matrix decomposition methods, like the truncated SVD (TSVD), which just computes the singular values and the corresponding singular vectors we need. Also other ideas to cheaply compute a truncated SVD-like decomposition like [1, 3, 7] can be used here.

To perform the TSVD we do not compute the moments in (2) explicitly. This would be numerically unstable and too expensive. The TSVD can be computed, e.g., with the implicit restarted Arnoldi method as implemented in the MATLAB function `svds` or with the Jacobi-Davidson SVD [3]. Thus, we only need to provide a function applying  $\mathbf{m}_i$  to a vector. We will give more details of this approach in the full paper.

### 3 Numerical Results

The spectrum of the singular values of the moment used for computing the SVD is essential for this kind of MOR, so we firstly concentrate on this issue. Figure 1 shows the decrease of the singular values of a circuit with 3916 nodes and 1905 terminals, provided by NEC Labs in St. Augustin, Germany. We can see, that there are about 130 significant singular values. That means, after the reduction we have 130 virtual input and output pins instead of 1905 terminals originally. The rel-

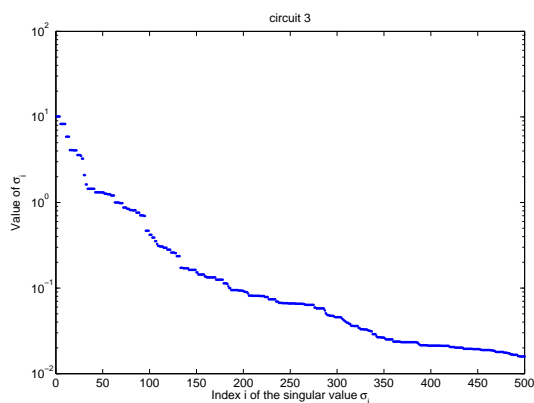


**Fig. 1.** Range of the largest 500 singular values of *circuit3*.

ative approximation error for a circuit with 141 nodes and 70 terminals is shown in Figure 2. We reduced to just one virtual terminal and we can see that the error is sufficiently small up to the Gigahertz range which is enough for the application behind this problem.

*Acknowledgement.* The work reported in this paper was supported by the German Federal Ministry of Education and Research (BMBF), grant no. 03BEPAE1.

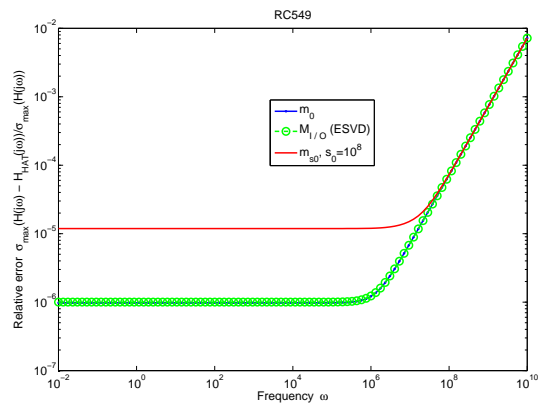


**Fig. 2.** Relative error  $\epsilon_{rel}$  of *RC549* with the help of SVD MOR ( $\mathbf{m}_0$ ,  $\mathbf{m}_{s0}$ ) and ESVD MOR ( $M_{I/O}$ ).

Responsibility for the contents of this publication rests with the authors.

### References

1. M. W. Berry, S. A. Pulatova, and G. W. Stewart. Algorithm 844: Computing sparse reduced-rank approximations to sparse matrices. *ACM Trans. Math. Softw.*, 31(2):252–269, 2005.
2. P. Feldmann and F. Liu. Sparse and efficient reduced order modeling of linear subcircuits with large number of terminals. In *ICCAD '04: Proceedings of the 2004 IEEE/ACM International conference on Computer-aided design*, pages 88–92, Washington, DC, USA, 2004. IEEE Computer Society.
3. M. E. Hochstenbach. A Jacobi–Davidson type SVD method. *SIAM J. Sci. Comput.*, 23(2):606–628, 2001.
4. P. Liu, S. X. D. Tan, H. Li, Z. Qi, J. Kong, B. McGaughy, and L. He. An efficient method for terminal reduction of interconnect circuits considering delay variations. In *ICCAD '05: Proceedings of the 2005 IEEE/ACM International Conference on Computer-Aided Design*, pages 821–826, Washington, DC, USA, 2005. IEEE Computer Society.
5. P. Liu, S. X. D. Tan, B. Yan, and B. McGaughy. An efficient terminal and model order reduction algorithm. *Integr. VLSI J.*, 41(2):210–218, 2008.
6. P. Liu, S.X.-D. Tan, B. Yan, and B. Mcgaughy. An extended SVD-based terminal and model order reduction algorithm. In *Proceedings of the 2006 IEEE International, Behavioral Modeling and Simulation Workshop*, pages 44–49, 2006.
7. M. Stoll. A Krylov-Schur approach to the truncated SVD. *Submitted to SIAM J. Sci. Comput.*, 2008.
8. S. Tan and L. He. *Advanced Model Order Reduction Techniques in VLSI Design*. Cambridge University Press, New York, NY, USA, 2007.

# Model order reduction for large resistance networks

Joost Rommes<sup>1</sup>, Peter Lenaers<sup>2</sup>, and Wil H.A. Schilders<sup>1</sup>

<sup>1</sup> NXP Semiconductors, HTC 37, 5656 AE Eindhoven, The Netherlands [Joost.Rommes@NXP.com](mailto:Joost.Rommes@NXP.com), [Wil.Schilders@NXP.com](mailto:Wil.Schilders@NXP.com). Supported by O-MOORENICE! (MCA FP6 MTKI-CT-2006-042477).

<sup>2</sup> Mathematics for Industry, Eindhoven University of Technology, P.O.Box 513, 5600 MB, Eindhoven, The Netherlands [PLenaers@gmail.com](mailto:PLenaers@gmail.com)

**Summary.** Electro Static Discharge analysis is time consuming due to the increasing size of resistance networks. We propose an algorithm for the reduction of large resistance networks to much smaller equivalent networks. Experiments show reduction and speed-ups up to a factor 10.

## 1 Introduction

Electro Static Discharge (ESD) analysis [4] requires knowledge on how fast electrical charge on the pins of a package can be discharged. In many cases, the discharge is done through the power network and the substrate, which both are resistive. Diodes are used to protect transistors on a chip against peak charges. The discharge paths, that consist of very large resistance networks connected through diodes, must be of low resistance to allow for sufficient discharge.

In order to analyze the discharge behavior, designers are interested in the path resistance between all IC-pins. To this end, the substrate and resistance network are modeled by resistors. The resulting resistive network may contain up to millions of resistors, hundreds of thousands of internal nodes, and thousands of external nodes (nodes with connections to diodes). Simulation of such large networks within reasonable time is not possible, and including such networks in full system simulations may be even unfeasible. Hence, there is need for much smaller networks that accurately or even exactly describe the resistive behavior of the original network, but allow for fast analysis.

In this paper we describe a new approach for the reduction of large resistance networks. We show how insights from graph theory, numerical linear algebra, and matrix reordering algorithms can be used to construct an equivalent network with the same number of external nodes, but much less internal nodes and resistors. This equivalent reduced network exactly describes the behavior of the original network. The approach is illustrated by numerical results.

## 2 Properties of resistance networks

A resistance network consists of internal nodes, external nodes (or terminals), and resistors. Figure 1 shows a simple resistance network with external nodes  $Z$  (the input node),  $A$ ,  $B$ , and  $C$  (the output nodes), and internal nodes  $X$  and  $Y$  (there are five resistors). Of interest are the path resistances from  $Z$  to  $A$ ,  $B$ , and  $C$ . This small exam-

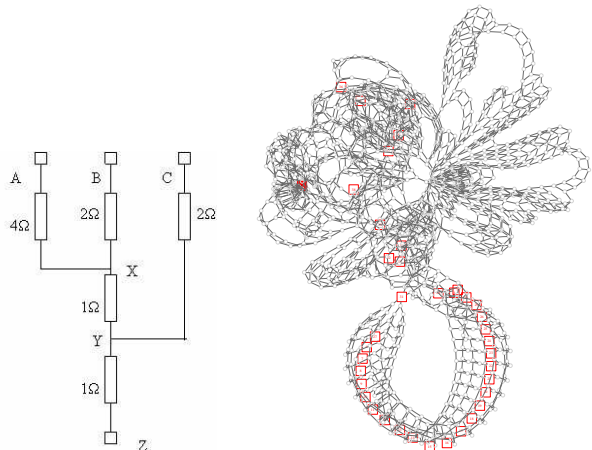


**Fig. 1.** Simple resistance network (left) with external nodes  $Z$ ,  $A$ ,  $B$ , and  $C$ , and realistic network (right, squares are external nodes). Of interest are the path resistances between external nodes.

ple is purely for illustrational purposes; in real-life applications the number of nodes and resistors is much larger. In the following it will be assumed that the network has  $n > 0$  internal nodes,  $m > 0$  external nodes, and  $r > 0$  resistors.

### 2.1 Mathematical formulation

Using Ohm's Law for resistors and Kirchhoff's Current Law [2], the electrical behavior of a resistance network can be described by

$$\mathbf{i} = Y \cdot \mathbf{v}, \quad (1)$$

where  $\mathbf{i}, \mathbf{v} \in \mathbb{R}^N$  and  $Y \in \mathbb{R}^{N \times N}$  (with  $N = n + m$ ) contain the unknown inflowing currents, node voltages, and conductances, respectively.

We distinguish between internal and external nodes:

$$\begin{bmatrix} \mathbf{i}_e \\ \mathbf{i}_i \end{bmatrix} = \begin{bmatrix} Y_{ee} & Y_{ei} \\ Y_{ei}^T & Y_{ii} \end{bmatrix} \begin{bmatrix} \mathbf{v}_e \\ \mathbf{v}_i \end{bmatrix},$$

where  $\mathbf{i}_e, \mathbf{v}_e \in \mathbb{R}^m$  and  $\mathbf{i}_i, \mathbf{v}_i \in \mathbb{R}^n$  correspond to external and internal nodes, respectively, and  $Y$  is partitioned accordingly. Note that  $\mathbf{i}_i = 0$  since currents can only be injected in external nodes.

All diagonal elements of  $Y$  are strictly positive and all off-diagonal elements are negative or zero. The conductance matrix  $Y = (y_{ij})$  is symmetric and (after grounding) positive-definite ( $\mathbf{x}^T Y \mathbf{x} > 0$  for all  $\mathbf{x} \in \mathbb{R}^n$ ). In most of the applications, the conductance matrix  $Y$  is very sparse, typically having  $O(1)$  nonzeros per row.

The impedance matrix  $Z$  can be obtained by inverting  $Y$ :  $Z = Y^{-1}$ . For large networks this is not possible due to memory and CPU limitations, and it is neither necessary since usually only specific elements are needed: the path resistances, for instance, can be found on the diagonal of  $Z$ .

## 2.2 Problem formulation

The problem is: given a large resistance network described by (1), find an equivalent network with (a) the same external nodes, (b) exactly the same path resistances between external nodes, (c)  $\hat{n} \ll n$  internal nodes, and (d)  $\hat{r} \ll r$  resistors.

Simply eliminating all internal nodes will lead to an equivalent network that satisfies conditions (a)–(c), but violates (d): for large numbers  $m$  of external nodes, the number of resistors  $\hat{r} = m^2/2$  in the dense reduced network is in general much larger than the number of resistors in the sparse original network ( $r = O(n)$ ), leading to increased memory and CPU requirements.

## 3 Improved approach

Knowing that eliminating all internal nodes is not an option, we use concepts from matrix reordering algorithms such as AMD [1] and BBBD [5], usually used as preprocessing step for LU-factorization, to determine which nodes to eliminate. The fill-in reducing properties of these methods also guarantee sparsity of the reduced network. For related work, see [6].

The first step is to bring the conductance matrix  $Y$  into Balanced Border Block Diagonal (BBBD) form [1, 3, 5], see Figure 2. In this form, the matrix consists of two parts: the main body  $A_{11}$  and the border blocks  $A_{12}$ ,  $A_{21} = A_{12}^T$  and  $A_{22}$ . The blocks  $A_{ij}$  can be partitioned into sub-blocks  $B_{kl}$ . The second step is to eliminate the internal nodes in block  $A_{11}$ . Since the ordering is

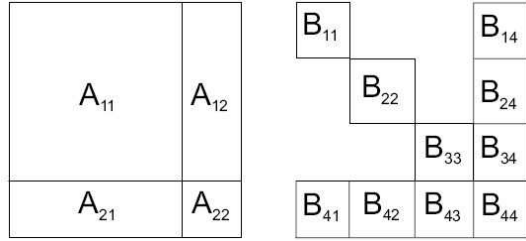


Fig. 2. Matrix in BBBD-form (left) with subblocks.

chosen to minimize fill-in, the resulting reduced matrix is sparse. Finally, the reduced conductance matrix can be realized as an reduced resistance network that is equivalent to the original network.

## 4 Numerical results and conclusions

Initial results for realistic resistance networks are shown in Table 1. The number of nodes is reduced by a factor  $> 10$  and the number of resistors by a factor  $> 3$ . As a result, the computing time for calculating path resistances is 10 times smaller.

Table 1. Results of reduction algorithm

	Network I		Network II	
	Original	Reduced	Original	Reduced
#nodes	5558	516	99112	6012
#resistors	8997	1505	161183	62685
CPU time	10 s	1 s	67 hrs	7 hrs

By using insights from matrix reordering algorithms, the proposed algorithm can reduce large resistance networks to small equivalent networks, that allow for faster simulation and can efficiently be used in Electro Static Discharge analysis. Further improvements are under development.

## References

1. P. R. Amestoy, T. A. Davis, and I. S. Duff. An Approximate Minimum Degree Ordering Algorithm. *SIAM J. Matrix Anal. Appl.*, 17(4):886–905, 1996.
2. L. O. Chua and P. Lin. *Computer aided analysis of electric circuits: algorithms and computational techniques*. Prentice Hall, first edition, 1975.
3. I. S. Duff, A. M. Erisman, and J. K. Reid. *Direct methods for sparse matrices*. Oxford: Clarendon Press, 1986.
4. J. M. Kolyer and D. Watson. *ESD: From A To Z*. Springer, 1996.
5. A. I. Zečević and D. D. Šiljak. Balanced decompositions of sparse systems for multilevel prallel processing. *IEEE Trans. Circ. Syst.-I:Fund. Theory and Appl.*, 41(3):220–233, 1994.
6. Q. Zhou, K. Sun, K. Mohanram, and D. C. Sorensen. Large power grid analysis using domain decomposition. In *Proc. Design Automation and Test in Europe*, pages 27–32, 2006.

---

**Session**

**P 1**

---



# Integral equation method for magnetic modelling of cilia

Mihai Rebican and Daniel Ioan

University Politehnica of Bucharest, Splaiul Independentei 313, Bucharest, Romania mrebican@yahoo.com

**Summary.** The paper presents an original and accurate method to model the magnetic behavior of the cilia. The method is based on Maxwell equation, formulated as integral equations for the magnetization.

## 1 Introduction

Micro-Fluidics is the science and technology of manipulating and analysing fluid flow in structures of sub-millimetre dimensions. The availability of micro-fluidics technology is essential for the development of advanced products in a variety of application areas, the most important of which is the biomedical field.

Many industrial research groups are studying ways of micro-fluidic manipulation. A method of fluid manipulation technology in micro-fluidics systems, inspired by nature is based on cilia. This approach enables effective local fluid manipulation, and the possibility to generate complex flow patterns.

The movement of the artificial cilia can be actively controlled, preferably using a magnetic field or an electrical field.

In this paper, an original, accurate and very fast method to model the magnetic behavior of the cilia is proposed. The method is based on the integral equations of the magnetic field, in term of the magnetization.

## 2 Integral equations method

Starting from Maxwell equations, the integral equation for the magnetization is:

$$\mathbf{M} + \frac{\chi}{4\pi} \int_{\Omega_2} \frac{\mathbf{R} \nabla \mathbf{M}}{R^3} dv = \chi \mathbf{H}_0 + \mathbf{M}_p. \quad (1)$$

Let us consider the cilium divided in  $n$  elements (1D finite elements), each being uniformly magnetised along the cilium direction (Fig. 1). Using this assumption, the integral equation (1) becomes a linear system of  $n$  equations [1]:

$$M_j + \frac{\chi g \Delta z}{4\pi} \sum_{i=1}^n \left[ \frac{(M_i - M_{i-1}) \cos(\Delta\beta_i/2)}{a_{ij} \sqrt{(\Delta z/2)^2 + a_{ij}^2}} \right] =$$

$$= \chi H_0 + M_p, \quad j = 1, n. \quad (2)$$

Figure 2 shows the magnetic flux density along a righth cilium, discretized in 10 finite elements. The cilium ( $\mu_r = 100$ ) is situated into an uniform magnetic field ( $B_0 = 10\text{mT}$ ), oriented along the cilium. The cilium has a paralelipipedic geometry ( $100 \times 20 \times 2 \mu\text{m}$ ).

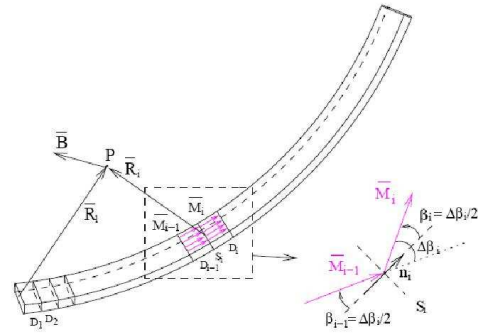


**Fig. 1.** Discretization of the cilium for the magnetic field computation

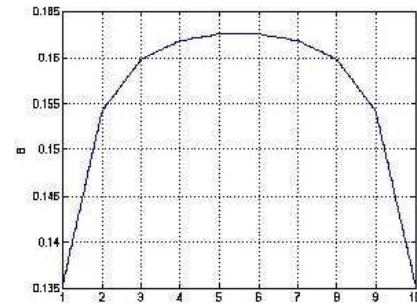


**Fig. 2.** Magnetic field along a right cilium situated in a uniform magnetic field

## References

1. D. Ioan, I.F. Hăntilă, M. Rebican, and C. Constantin. FLUXSET Sensor Analysis Based on Non-linear Magnetic Wire Model of the Core. In *Electromagnetic Nondestructive Evaluation (II)*, pages 160–169. IOS Press, Amsterdam, 1998.



# Electromagnetic modeling of 3D bodies in layered earths using integral equations

R. Grimberg<sup>1</sup>, Adriana Savin<sup>1</sup>, Rozina Steigmann<sup>1</sup>, Alina Bruma<sup>1</sup>, S.S. Udpa<sup>2</sup>, and Lalita Udpa<sup>2</sup>

<sup>1</sup> National Institute of Research and Development for Technical Physics, Iasi, Romania

grimberg@phys-iasi.ro, asavin@phys-iasi.ro, steigmann@phys-iasi.ro, abruma@phys-iasi.ro

<sup>2</sup> Michigan State University, East Lansing, MI, USA udpa@egr.msu.edu, udpal@egr.msu.edu

Consider a 3D body in an n-layered host. The total electric and magnetic fields as functions of position  $\vec{r}$  for an  $e^{j\omega t}$  time dependence obey Maxwell's equation

$$\begin{aligned} -\nabla \times \vec{E} &= \hat{z}\vec{H} + \vec{M}_i \\ \nabla \times \vec{H} &= \vec{J} + \vec{J}_i \end{aligned} \quad (1)$$

where  $\vec{J} = \hat{y}\vec{E}$  is the total current density,  $\hat{y} = \sigma + j\omega\epsilon$  is the admittivity,  $\hat{z} = j\omega\mu$  at any point and  $\vec{J}_i$  and  $\vec{M}_i$  are impressed electric and magnetic source current,  $\sigma$ ,  $\epsilon$  and  $\mu$  are conductivity, permittivity and permeability.

In our model, the 3D body is replaced by an equivalent scattering current distribution. The total fields  $(\vec{E}, \vec{H})$  in any layer are hence decomposed into an incident set  $(\vec{E}_i, \vec{H}_i)$  due to  $\vec{J}_i$  and  $\vec{M}_i$  and scattered set  $(\vec{E}_S, \vec{H}_S)$  contributed by the body.

The scattered fields can be expressed as

$$\begin{aligned} \int_V \vec{G}_l^E(\vec{r}|\vec{r}') \vec{J}_S(\vec{r}') d\vec{r}' \\ \vec{H}_S(\vec{r}) = \int_V \vec{G}_l^H(\vec{r}|\vec{r}') \vec{J}_S(\vec{r}') d\vec{r}' \end{aligned} \quad (2)$$

The quantities  $\vec{G}_l^E(\vec{r}|\vec{r}')$  and  $\int_V \vec{G}_l^H(\vec{r}|\vec{r}')$  are 3x3 dyadic Green's functions relating a vector field at  $\vec{r}'$  in layer l to a current element at in layer j, including l=j. A matrix solution of (2) can be found using the method of collocation with pulse subsection basis functions [1].

The body is approximated by N rectangular prismatic cells, each of dimensions  $M_{Xn}\Delta_n \times M_{Yn}\Delta_n \times M_{Zn}\Delta_n$ , where  $M_{Xn}$ ,  $M_{Yn}$  and  $M_{Zn}$  are positive integers and  $\Delta_n$  is the size of a cubic sub cell in cell n. Over each cell, the body conductivity and total electric field are presumed constant.

The total electric field at the center of cell m due to all N cells is approximated by

$$\vec{E}(\vec{r}_m) = \vec{E}_i(\vec{r}_m) + \sum_{n=1}^N (\sigma_n - \sigma_j) \vec{G}_l^E(\vec{r}_m|\vec{r}_n) \vec{E}(\vec{r}_n) \quad (3)$$

in which the electric Green's dyadic function for a rectangular prism of current is

$$\vec{G}_l^E(\vec{r}_m|\vec{r}_n) = \int_{V_n} \vec{G}_l^E(\vec{r}_m|\vec{r}') d\vec{r}' \quad (4)$$

Calculation of  $\vec{G}_l^E(\vec{r}_m|\vec{r}_n)$  from  $\vec{G}_l^E(\vec{r}|\vec{r}')$  for the matrix elements requires same care. When the in homogeneity does not cut across layer interfaces, l=j. Each cell in this case is coupled to every other cell by a Green's function compared of a primary on free space component and a reflected component

$$\vec{G}_l^E(m, n) = {}^P\vec{G}_l^E(m, n) + {}^S\vec{G}_l^E(m, n) \quad (5)$$

Each matrix element is given by a summation over the cubic subcells. If the body cuts across layer interfaces cells in different layers are coupled only by secondary electric Green's function.

An efficient evaluation of the dyadic Green's functions is necessary to avoid prohibitive computer time. The primary solutions are analytic expressions and present no problems, but the secondary Green's function requires Hankel transformation of complicated kernel functions. Following the procedure described above, the forward problem was solved for the situations:

- the incident field is created by planar rectangular coil with 1m outer side, 0.004X0.006mm<sup>2</sup> transversal section of conductor, 0.006 step and 10turns, current density 10<sup>8</sup>A/m<sup>2</sup> and frequency 10kHz.
- scattering electric field was determined by using one array 5X5 rectangular coil sensors
- 3D body conductive sphere with 1m diameter, 10<sup>6</sup> S/m electric discretized in 5<sup>3</sup> cells, the center of sphere is at 10m under the surface of soil

*Acknowledgement.* This paper is partially supported by the Romanian Ministry of Education, Research and Youth under Excellence Research Program CEEEX under contracts: 9 I 03 / 06.10.2005 nEDA, Grant no.706/CNCSIS.

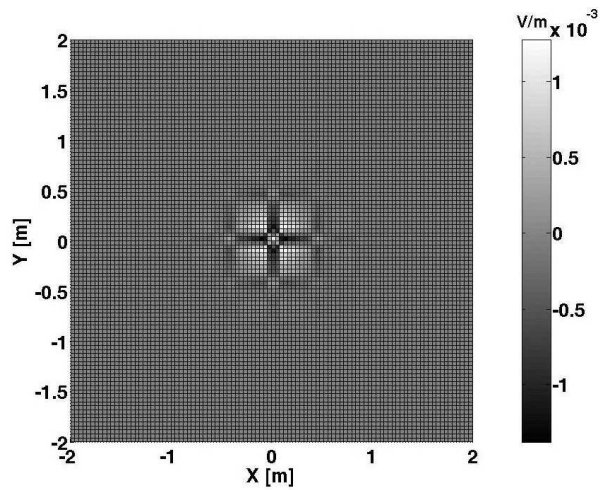


Fig. 1. The image of a conductive sphere

## References

1. R.F. Herrington. *Field computation by moment methods*, McMillan, NY, 1968
2. R.Grimberg , L.Udpa, SS Udpa. Electromagnetic transducer for the determination of soil condition, accepted for publication in *International Journal for Applied Electromagnetics and Mechanics*

# Electromagnetic field diffraction on subsurface electrical barrier. Application to nondestructive evaluation

Adriana Savin, Rozina Steigmann, Alina Bruma, and Raimond Grimberg

National Institute of Research and Development for Technical Physics, Iasi, Romania [asavin@phys-iasi.ro](mailto:asavin@phys-iasi.ro), [steigmann@phys-iasi.ro](mailto:steigmann@phys-iasi.ro), [abruma@phys-iasi.ro](mailto:abruma@phys-iasi.ro), [grimberg@phys-iasi.ro](mailto:grimberg@phys-iasi.ro)

Consider a half-space conductor which contains a deep dielectric barrier whose edge lies a depth  $h$  below the surface of the conductor. The boundary condition for scattered magnetic field on the surface of the conductor will match by introducing an image of the barrier (Figure 1).

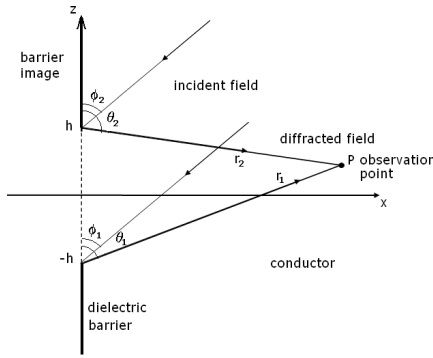


Fig. 1. Problem geometry

The incident magnetic field in each conducting half-space is

$$\Psi^{(i)} \sim \begin{cases} -e^{-jkz} & z < 0 \\ -e^{jkz} & z > 0 \end{cases} \quad (1)$$

The diffracted field, which is determined by a generalization of Fermat's principles, has the form [1]

$$\Psi^{(S)}(0, z) \sim \begin{cases} -e^{-jkz}, & z < -h \\ -e^{jkz}, & z > h \end{cases} \quad (2)$$

$$\frac{\partial \Psi^{(S)}(0, z)}{\partial x} = 0, \quad |z| < h$$

The diffraction functions for the lower and upper edges,  $K_1$  and  $K_2$  respectively are defined as follows

$$\begin{aligned} K_1(r_1, \theta_1, \varphi_1) &= \\ &= -\frac{e^{jkr_1}}{2} [w(\sqrt{2jkr_1} \cos \frac{1}{2}(\theta_1 + \varphi_1)) + \\ &+ w(\sqrt{2jkr_1} \cos \frac{1}{2}(\theta_1 - \varphi_1))] \\ K_2(r_2, \theta_2, \varphi_2) &= \\ &= -\frac{e^{jkr_2}}{2} [w(-\sqrt{2jkr_2} \cos \frac{1}{2}(\theta_2 + \varphi_2)) + \\ &+ w(\sqrt{2jkr_2} \cos \frac{1}{2}(\theta_2 - \varphi_2))] \end{aligned} \quad (3)$$

where  $w$  is the Fadeeva's function [2].

The single scattered field is

$$\psi_S^{(S)} = \psi_{1S}^{(S)} + \psi_{2S}^{(S)} \quad (4)$$

where

$$\begin{aligned} \psi_{1S}^{(S)} &= e^{jkh} K_1(r_1, \theta_1, 0) \\ \psi_{2S}^{(S)} &= e^{jkh} K_2(r_2, \theta_2, \pi) \end{aligned} \quad (5)$$

The multiple scattering may be treated systematically in the following manner. There are four distinct "types" of multiply scattered field, tabulated in Table 1.

Table 1. Types of multiple scattered field

type	Initial scattering at edge number	Scattering at each edge		Final scattering at edge number
		Lower edge 1	Upper edge 2	
A	1	n+1	n	1
B	1	n	n	2
C	2	n	n+1	2
D	2	n	n	1

The sum over all scattered fields can be written as follows

$$\begin{aligned} \psi_n^{(S)} &= -e^{jkh} K_1(2h, 0, 0) [1 - K_1(2h, 0, 0)] \cdot \\ &\cdot [K_1(r_1, \theta_1, 0) - K_2(r_2, \theta_2, \pi)] \cdot \\ &\cdot \sum_{n=1}^{\infty} K_1^{2n-2}(2h, 0, 0) \end{aligned} \quad (6)$$

The multiply scattered field has the same spatial form as the simply scattered field. The total scattered field is simply the sum of the simply and multiply scattered fields. The sum over all scattered fields can be written as follows

$$\psi^{(S)} = \psi_S^{(S)} + \psi_n^{(S)} = (1 + M) \psi_S^{(S)} \quad (7)$$

where

$$\begin{aligned} M &= \frac{-K_1(2h, 0, 0)}{1 + K_1(2h, 0, 0)} = \frac{e^{2jkh} w(\sqrt{4jkh})}{1 - e^{2jkh} w(\sqrt{4jkh})} \\ w(z) &= e^{-z^2} \operatorname{erfc}(-jz) \end{aligned} \quad (8)$$

If the electrical conductivity of the conducting half-space is  $\sigma$  and the relative magnetic permeability is  $\mu_r=1$  (amagnetic conductor), the standard penetration depth is defined as

$$\delta = \sqrt{\frac{2}{\omega\mu\sigma}} \quad (9)$$

where  $\omega$  is the angular frequency of the incident field and  $\mu = \mu_r\mu_0$ .

The contour plot of real and imaginary component of the total magnetic field, for which multiple scattering has been taken into account, on the dielectrically barrier placed at 4mm below the surface of an aluminium alloy 4032T6 half space at 10kHz, the frequency of the incident electromagnetic field are presented in Figure 2 and respective Figure 3.

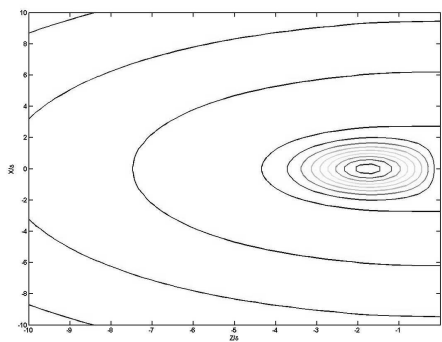


**Fig. 2.** Real component of the total magnetic field on the subsurface dielectric barrier

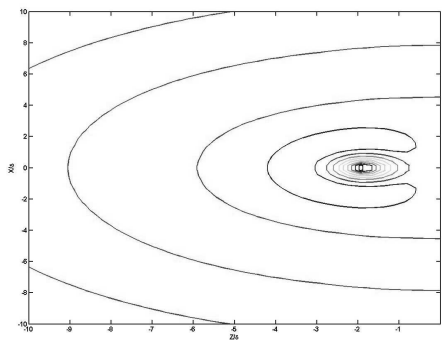


**Fig. 3.** Imaginary component of the total magnetic field on the subsurface dielectric barrier

*Acknowledgement.* This paper is partially supported by the Romanian Ministry of Education, Research and Youth under Excellence Research Program CEEEX under contracts: 9 I 03 / 06.10.2005 nEDA and 6110/2005 SINERMAT; Grant no.586/CNCSIS and PNII -71-016/2007 MODIS.

## References

1. J.von Blodel. *Electromagnetic field*, Sec.Ed., IEEE Press Series on Electromagnetic Wave Theory, NY, 2007
2. M. Abramowitz, I. Stegun. *Handbook of Mathematical Functions: with Formulas, Graphs, and Mathematical Tables* , National Bureau of Standards,1964
3. R. Grimberg, A.Savin, E.Radu, O.Mihalache. Nondestructive Evaluation of the Severity of Discontinuities in Flat Conductive Materials Using the Eddy Current Transducer with Orthogonal Coils. *IEEE Trans on Mag.* 36, 1, (2000), 299-307

# Relativistic High Order Particle Treatment for Electromagnetic Particle-In-Cell Simulations

Martin Quandt<sup>1</sup>, Claus-Dieter Munz<sup>1</sup>, and Rudolf Schneider<sup>2</sup>

<sup>1</sup> Institut für Aerodynamik und Gasdynamik, Universität Stuttgart [quandt@iag.uni-stuttgart.de](mailto:quandt@iag.uni-stuttgart.de), [munz@iag.uni-stuttgart.de](mailto:munz@iag.uni-stuttgart.de)

<sup>2</sup> Forschungszentrum Karlsruhe, Institut für Hochleistungsimpuls und Mikrowellentechnik [rudolf.schneider@ihm.fzk.de](mailto:rudolf.schneider@ihm.fzk.de)

**Summary.** A recently developed high order field solver for the complete Maxwell equations provides all informations needed by a new relativistic particle push method based on a truncated Taylor series expansion up to the desired order of convergence. The capability of this approach is compared with other classic schemes for different numerical experiments.

## 1 Abstract

The deeper physical understanding of systems like microwave devices and pulsed plasma thrusters requires the numerical modeling and simulation of highly rarefied plasma flows. Mathematically, the description of such flows demand a kinetic formulation which is established by the time-dependent Boltzmann equation. An attractive numerical approach to tackle this complex non-linear problem consists in a combination of the Particle-in-Cell (PIC) and Direct Simulation Monte Carlo (DSMC) methods extended by a PIC-based Fokker-Planck model which are coded in the hybrid PIC/DSMC simulation program named PicLas [1]. In this code the DSMC module accommodates the charged-neutral and neutral-neutral particle interactions as well as the plasma chemistry. The new developed Fokker-Planck solver [5] takes into account the long range intra- and inter-species charged particle Coulomb collisions. Finally, the Maxwell-Vlasov module allows the self-consistent simulation of charged particles in electro-magnetic fields. Note, the proposed high order particle (HIOP) treatment is an essential part in the latter building block of the PicLas code.

In essence, the operating mode of the Maxwell-Vlasov solver is as follows: at each time step the electromagnetic fields are obtained by the numerical solution of the full set of the nonstationary Maxwell equations, where different kind of methods like finite volume or discontinuous Galerkin schemes of free selectable order of convergence are applied [3, 4]. Note, that the Maxwell part of this solver comprises additionally a purely hyper-

bolic divergence correction mechanism [2] to ensure the constrain of charge conservation during the simulation. Subsequently, these fields are interpolated to the actual locations of the charged plasma particles which are then pushed according the Lorentz force and redistributed in phase space according to the usual laws of dynamics. Afterwards, the particles have to be located with respect to the computational grid in order to assign the contribution of each charge to the changed charge and current density to the nodes of the mesh. These densities are the sources for the Maxwell equations for the subsequent iteration cycle which finally guarantee a self-consistent computation of the interaction of the electromagnetic fields with the charged plasma particles.

To sustain the high order of the Maxwell-Vlasov module, we introduce a new particle treatment based on a Taylor series expansion of the phase space variables in time up to the desired order of the field solver, where high order time derivatives of the electro-magnetic fields occur. To replace these derivatives by known spatial derivatives of the fields given by the Maxwell solver, we apply a Cauchy-Kovalevskaya procedure to the Lorentz force equation. To demonstrate the capability and reliability of the HIOP procedure different numerical simulations are performed. The results are compared with those obtained from the classic second order Boris Leap-Frog scheme. The achieved effective order of convergence is also tested for non-relativistic as well as relativistic cases and listed in charts.

*Acknowledgement.* We gratefully acknowledge the Landesstiftung Baden-Württemberg for funding the present project for two years up to September 2006. Furthermore, the authors would like to thank the Deutsche Forschungsgemeinschaft for financial support of this work.

## References

1. D. Petkow, M. Fertig, T. Stindl, M. Auweter-Kurtz, M. Quandt, C.-D. Munz, S. Roller, D. D'Andrea and R. Schneider, *Development of a 3-Dimensional, Time Accurate Particle Method for Rarefied Plasma Flows*, AIAA-2006-3601, Proceedings of the 9th AIAA/ASME Joint Thermophysics and Heat Transfer Conference, San Francisco, USA, 2006
2. C.-D. Munz, P. Omnes, R. Schneider, E. Sonnendrücker and U. Voß, *Divergence correction techniques for Maxwell solvers based on a hyperbolic model*, J. Comput. Phys., 2000
3. J.S. Hesthaven and T. Warburton, *Nodal high-order methods on unstructured grids* J. Comput. Phys., 181:186-221, 2002
4. T. Schwartzkopff, F. Lörcher, C.-D. Munz, and R. Schneider, *Arbitrary High Order Finite-Volume Methods for Electromagnetic Wave Propagation* Computer Physics Communications, 2006
5. D. D'Andrea, C.-D. Munz and R. Schneider, *Modeling of Electron-Electron Collisions for Particle-In-Cell Simulations*, **FZKA 7218** Research Report, Forschungszentrum Karlsruhe – in der Helmholtz-Gemeinschaft, 2006

# A Simulation-Based Genetic Algorithm for Optimal Antenna Pattern Design

Yi-Ting Kuo and Yiming Li<sup>1</sup>

National Chiao Tung University, 1001 Ta-Hsueh Rd., Hsinchu 300, Taiwan <sup>1</sup>ymli@faculty.nctu.edu.tw

**Summary.** In this paper, a simulation-based optimization method for the design of antenna pattern in mobile broadcasting, multi-bandwidth operation and the 802.11a WLAN is presented. A simulation-based genetic algorithm (GA) is advanced for the antenna design automation with requested specifications. The corresponding cost function in optimization is evaluated by external numerical electromagnetic (EM) solver, and the communication of the GA and EM solver is provided on our unified optimization framework (UOF). Our preliminary numerical results confirm the robustness and efficiency of the proposed simulation-based optimization method.

## 1 Introduction

A trend of portable device integration has risen last decade due to the massive growth of wireless communications, and products are expected to have multiple wireless service. However, how to adjust the geometry to get the best design is a state-of-art and needs more experience through trial-and-error process. Recently, the optimization scheme, genetic algorithm (GA), is considered to be a efficiency approach to optimize the antenna to satisfy requested specifications and make design procedure fully automatic. However, the notch and slit-loaded entries provide extra resonant frequencies and introduce new band into original antenna [1, 2]. Hence, to make GA more flexible in planer antenna design optimization, we provide a new approach to optimize the planer antenna.

In this work, we implement an optimization method to enhance the receiving and transmitting abilities of the given antenna with GA and numerical simulation. Based on our experience and technique of using GA to optical proximity correction (OPC) [3] and transistor model parameter extraction [4], we for the first time advance the idea of pattern correction in OPC for antenna design optimization. The proposed method partitions the edges of the antenna into some sections (small segments) and then those sections can be shifted in the normal direction of the edges to improve the return loss of the antenna. This novel approach can extend the geometry without limited boundaries and can construct geometry without specific form. The involved simulator solves Maxwell's equations by finite element method.

Maxwell's equations govern the performance in electric and magnetic fields and the simulated results are applied to evaluate the new generated antenna.

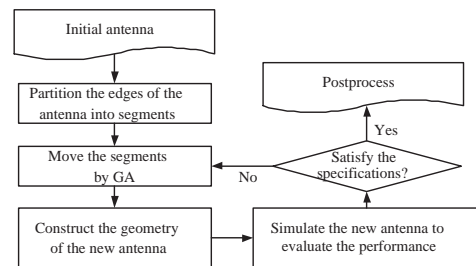


**Fig. 1.** A flowchart for the proposed optimization approach in antenna design.

## 2 The Intelligent Methodology

As a designer drew a blueprint of an antenna for the specific purpose, a fine tune process should be performed repeatedly for further improvement. We already know the geometry of the antenna affects its performance. However, the major difficulty is how the antenna shape affects its performance. For an antenna designer, when one fine tunes the shape, it is just like making a wild guess. To automate the search for the optimized antenna shape in an efficient way, GA is a good candidate of optimization methods in the simulation-based procedure. There are several components in the GA, such as problem definition, encoding method, fitness evaluation, selection method, crossover procedure, and mutation scheme have to be performed for an evolutionary process. Figure 1 shows the flowchart of the proposed optimization approach. During the procedure, the original antenna shape is divided into small segments. The movements of those segments are then optimized with respect to the calculated results using GA. Then the GA is applied to correct the antenna shape and outputs a new geometry of antenna. To evaluate the cost function in GA, the external EM solver is used to simulate the new antenna. This procedure will stop till the all specifications are satisfied by the optimized antenna. Figure 2 shows the geometry and the partitioned segments for a specified antenna shape. We have implemented this optimization proce-

ture in the developed unified optimization framework (UOF) [5]. We notice that UOF has already provided an efficient way in optical proximity correction problem using a simulation-based optimization scheme [3].

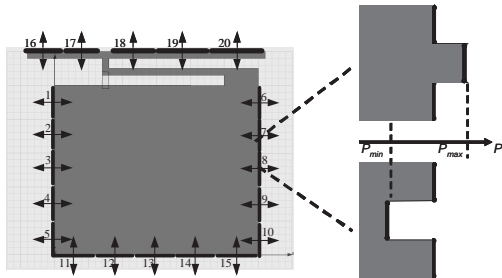


**Fig. 2.** The original geometry of examined antenna and the partitioned segments. The black rectangular frame near the top line is the contact for input excitation.

### 3 Results and Discussion

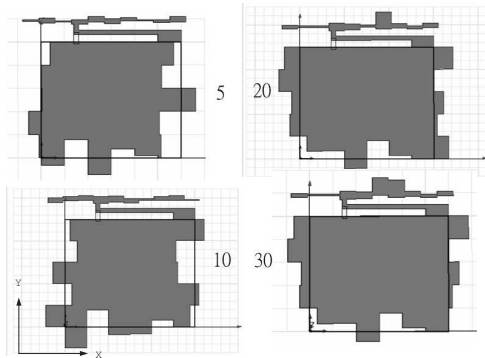


**Fig. 3.** Obtained antenna patterns in the GA procedure with 5, 10, 20, and 30 evolutionary generations.

Figure 2 shows the original shape of the examined antenna. The studied structure is a Z-shaped antenna and has radiation elements and ground plane on the same plane. As shown in Fig. 2, the top line is the ground plane, the bottom rectangle represents the radiation element, and the segments 1-20 are the partitions for evolution. The dual operating frequencies are set to 2.6 and 4.9 GHz, where the return loss of the original antenna are about -14 and -10 dB, respectively. The frequency 2.6 GHz is referred as the "S-band" used for mobile broadcasting and the frequency 4.9 GHz is used by the 802.11a WLAN protocol. Our target is to improve the return loss for both operating frequencies 2.6 and 4.9 GHz. Apply GA to search the better antenna patterns automatically, the antenna patterns in some generations are shown in Fig. 3. Figure 4 shows the corresponding return losses for the antenna patterns in each generation. The number on the subplots in Fig. 3 represents the number of generations in GA procedure. Figure 4 shows that the return loss of the second band has been improved as the number of generations increases. When the antenna pattern generated by GA satisfies the de-

sign specifications, it will be the optimized pattern. The return loss on the frequencies of 2.6 and 4.9 GHz is down to -20 dB for the optimized antenna which has a significant improvement.

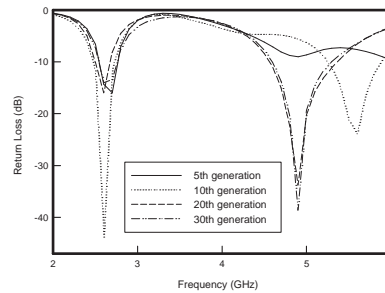


**Fig. 4.** The return losses corresponding to generations of antenna patterns in GA procedure.

### 4 Conclusion

In this paper, simulation-based optimization method for the design of antenna has been presented. GA works well for the antenna design automation on our UOF [5] and communicated with an external numerical EM solver. This method minimizes the return loss under the frequencies 2.6 and 4.9 GHz. Improved return loss is observed, and the effect of this method for the optimized configuration is examined and discussed. Furthermore, UOF also has capability to connect with other external software through the script file, which can generate the antenna geometry. We believe that this optimization method can benefit the RF antenna design applied for mobile broadcasting and the 802.11a WLAN.

*Acknowledgement.* This work was supported in part by Taiwan National Science Council (NSC) under Contract NSC-96-2221-E-009-210.

### References

1. F. Castellana, F. Bilotti, and L. Vegni. Automated dual band patch antenna design by a genetic algorithm based numerical code. *IEEE Antennas and Propagation Society International Symposium*, 4:696–699, 2001.
2. F. J. Villegas, T. Cwik, Y. Rahmat-Samii, and M. Manteghi. A parallel electromagnetic genetic-algorithm optimization (EGO) application for patch antenna design, *IEEE Transaction on Antennas and Propagation*, 52:2424–2435, 2004.
3. S.-M. Yu and Y. Li. A computational intelligent optical proximity correction for process distortion compensation of layout mask in subwavelength era, *10th International Workshop on Computational Electronics*, 179–180, 2004.
4. Y. Li and Y.-Y Cho. An automatic parameter extraction technique for advanced CMOS device modeling using genetic algorithm, *Microelectron. Eng.*, 84:206–272, 2007.
5. Y. Li, S.-M. Yu and Y.-L. Li. Application of a unified optimization framework to electronic design automation, *Mathematics and Computers in Simulation*, To appear.

# Probabilistic characterization of resonant EM interactions with thin-wires: variance and kurtosis analysis

O.O. Sy<sup>1</sup>, J.A.H.M. Vaessen<sup>1</sup>, M.C. van Beurden<sup>1</sup>, B.L. Michiels<sup>2</sup>, and A.G. Tijhuis<sup>1</sup>

<sup>1</sup> Eindhoven University of Technology, Den Dolech 2, 5600 MB, Eindhoven, The Netherlands o.o.sy@tue.nl, j.a.h.m.vaessen@tue.nl, m.c.v.beurden@tue.nl, a.g.tijhuis@tue.nl

<sup>2</sup> ONERA, 2, av E. Belin, 31055 Toulouse Cedex, France bastiaan.michielsen@onera.fr

**Summary.** A probabilistic characterization of random electromagnetic interactions affected by resonances is presented. It hinges on the analysis of the variance and the kurtosis. It is illustrated by the case of a randomly undulating thin wire over a plane.

## 1 Introduction

Interactions between electronic devices and electromagnetic sources in their environment are of prime importance in EMC models for design or maintenance studies. The range of validity of these models depends on their ability to accurately represent an ensemble of configurations.

For non-resonant systems, the study of a few configurations provides a good picture of the overall interaction. However, for resonant phenomena, a stochastic approach yields a more suitable quantitative and qualitative model. Stochastic methods are frequently used in fields as diverse as rough-surface scattering problems [1] and Mode-stirred-Chamber theory [2]. In EMC, random models have been applied to undulating thin-wire setups modeled by transmission-line theory, or by integral equations [3]. In all these cases the aim is to quantify the uncertainty of the response parameters or observables, by their average and variance. Although these statistics provide bounds for the observable, they do not inform on the presence of extreme values beyond these bounds.

This paper proposes to characterize stochastically, the voltage induced at the port of randomly-undulating thin-wire setups affected by resonances. In addition to the average and the variance, the fourth-order moment, or *kurtosis*, is computed by quadrature. The kurtosis measures the likelihood of presence of extreme events. It is often used in financial-risk analysis to foretell bankruptcy [4].

## 2 Deterministic configuration

The scattering configuration consists of a scattering device and the incident field. The scatterer is a perfectly electrically conducting (PEC) wire  $S_{\alpha}$  containing a port region, and, located over a PEC ground plane, as shown in figure 1.

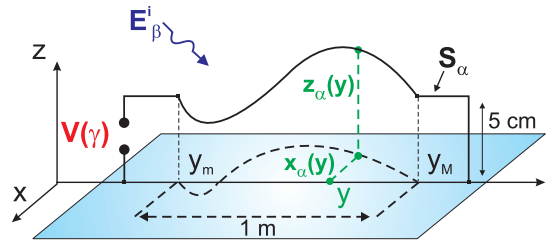


**Fig. 1.** undulating thin-wire over a PEC plane

The vector  $\alpha$  contains all the parameters controlling the geometry of  $S_{\alpha}$ . The parameters of the incident field  $E_{\beta}^i$ , such as its direction of propagation or its amplitude, form the vector  $\beta$ . Therefore the vector  $\gamma = \alpha \oplus \beta$  contains all information needed to define the configuration. The coupling itself is observed through the voltage  $V_e(\gamma)$  induced at the port. It follows by first solving a frequency-domain electric-field integral equation (EFIE) depending on  $S_{\alpha}$ , then performing a duality product between the solution and  $E_{\beta}^i$  [3].

## 3 Random parameterization

An ensemble  $\Omega_{\gamma}$  of configurations is considered. Computing  $V_e(\gamma)$  for each element  $\gamma$  of  $\Omega_{\gamma}$  can be very costly numerically. Instead, the variations of  $\gamma$  in  $\Omega_{\gamma}$  are viewed as random according to a *known* distribution  $p_{\gamma}$ . The voltage  $V_e(\gamma)$  thus becomes a random variable, with statistical moments, such as its mean  $\mathbb{E}[V_e]$  and its standard deviation  $\sigma[V_e]$ , defined as

$$\mathbb{E}[V_e] = \int_{\Omega_{\gamma}} V_e(\gamma') p_{\gamma}(\gamma') d\gamma', \quad (1)$$

$$\sigma[V_e] = \sqrt{\mathbb{E}[|V_e|^2] - |\mathbb{E}[V_e]|^2}, \quad (2)$$

where  $\sigma[V_e]$  measures the spread of  $V_e$  around  $\mathbb{E}[V_e]$ . Extreme values of  $V_e$ , at least  $4\sigma$  away from  $\mathbb{E}[V_e]$ , are accounted for by the *kurtosis*  $\kappa[|V_e|]$  which is a dimensionless moment defined as

$$\kappa [|V_e|] = \mathbb{E} \left[ \left( \frac{|V_e| - \mathbb{E}[|V_e|]}{\sigma [|V_e|]} \right)^4 \right] \geq 0. \quad (3)$$

Gaussian random variables, which have 97% of their values within  $2\sigma$  of their average, have a kurtosis of 3. Thus, the higher the value of  $\kappa [|V_e|]$  above 3, the more peak values of  $V_e$  are present. Since all the statistical moments are integrals over a known integrand depending on  $V_e(\gamma)$ , and the same support  $\Omega_\gamma$ . They can be computed by quadrature rules, which are cautiously chosen, to efficiently handle the dimension of  $\Omega_\gamma$  [3].

## 4 Results

With reference to figure 1, a roughly undulating thin wire is studied with a geometry defined as

$$x\alpha(y) = \alpha_1 \sin(3\pi y), \quad (4)$$

$$z\alpha(y) = 5 + \alpha_2 \sin(9\pi y) \quad \text{in cm} \quad (5)$$

$\alpha_1$  and  $\alpha_2$  being independent and uniformly distributed in  $\Omega_{\alpha_1} = \Omega_{\alpha_2} = [-5; 5]$  cm. The incident field is a vertically-polarized plane-wave with an amplitude of  $1 \text{ V.m}^{-1}$ , and propagating in the direction  $\theta_i = 45^\circ$ ,  $\phi_i = 0^\circ$ . Figure 2 depicts  $\sigma [|V_e|]$  and  $\kappa [|V_e|]$ .

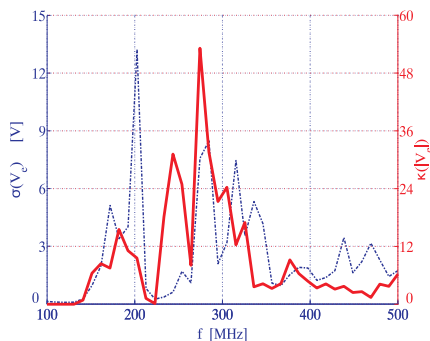


**Fig. 2.**  $\sigma [|V_e|]$  (dotted line) and  $\kappa [|V_e|]$  vs frequency

The graph of  $\sigma [|V_e|]$  shows several peaks which indicate an increased uncertainty of  $V_e$ , that can be caused by a generalized spread  $V_e$ , or, by a few very large samples of  $V_e$ . The mitigation of these two cases is possible thanks to  $\kappa [|V_e|]$ , which is generally consistent with  $\sigma [|V_e|]$ . However, between 230 MHz and 260 MHz, although  $V_e$  is concentrated around  $\mathbb{E}[V_e]$  ( $\sigma [|V_e|] \leq 2V$ ), extreme samples are present ( $\kappa [|V_e|] \geq 15$ ). The opposite situation is observed between 330 MHz and 350 MHz. To confirm these observations, 1000 samples have been computed for the frequencies specified in Table 1. These samples are then normalized as follows

$$V_n = \frac{V_e - \mathbb{E}[V_e]}{\sigma [|V_e|]}, \quad (6)$$

**Table 1.** Results at given frequencies

	$\sigma [ V_e ]$	$\kappa [ V_e ]$
$f_1 = 120 \text{ MHz}$	0.126 V	0.001
$f_2 = 223 \text{ MHz}$	0.613 V	31
$f_3 = 346 \text{ MHz}$	4.169 V	4.3

thus allows for comparisons between different frequencies, as in figure 3. The concentric circles result from the normalization of circles centered at  $\mathbb{E}[V_e]$  and with radii equal to multiples of  $\sigma [|V_e|]$ . Figure 3 confirms the predictions based on the analysis of  $\sigma [|V_e|]$  and  $\kappa [|V_e|]$ .

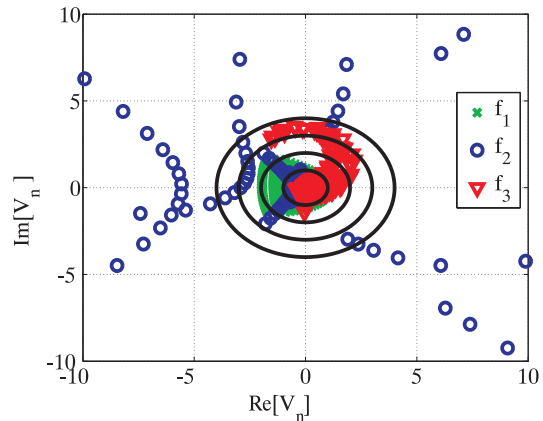


**Fig. 3.** Normalized Samples  $V_n$  for  $f_1$ ,  $f_2$  and  $f_3$

More results will be shown at the conference for setups with multiple undulating thin wires, under deterministic and random incident fields.

## 5 Conclusion

The method presented in this abstract shows how the efficient computation of the kurtosis can yield valuable statistical information. The kurtosis, informs qualitatively on the ability of the variance to accurately represent stochastic electromagnetic interactions hindered by resonances.

*Acknowledgement.* This work is funded by the Dutch Ministry of Economic Affairs, in the Innovation Research Program (IOP) number EMVT 04302.

## References

1. G. S. Brown. Simplifications in the stochastic fourier transform approach to random surface scattering. *IEEE TAP*, AP-33(1):48–55, 1985.
2. D.A. Hill. Plane wave integral representation for field in reverberation chambers. *IEEE Trans. EMC* 40(3):209–217, 1998.
3. Sy O.O. et. al. Probabilistic study of the coupling between deterministic electromagnetic fields and a stochastic thin-wire over a pec plane. In *ICEAA (pp. 1-4). Torino, Italy, 2007.*
4. B. Mandelbrot R.L. Hudson. *The (Mis)behaviour of Markets*. Profile Business, 2004.

# Domain Partitioning Based Parametric Models for Passive On-chip Components

Gabriela Ciuprina<sup>1</sup>, Daniel Ioan<sup>1</sup>, Diana Mihalache<sup>1</sup>, and Ehrenfried Seebacher<sup>2</sup>

<sup>1</sup> Politehnica University of Bucharest, Electrical Engineering Dept., Numerical Methods Lab., Spl. Independentei 313, 060042, Bucharest, Romania [lmn@lmn.pub.ro](mailto:lmn@lmn.pub.ro)

<sup>2</sup> Austriamicrosystems, A 8141 Schloss Premstaetten, Austria  
[ehrenfried.seebacher@austriamicrosystems.com](mailto:ehrenfried.seebacher@austriamicrosystems.com)

**Summary.** Models for passive integrated components that take into consideration the variability of their design can be obtained by partitioning the computational domain into sub-domains, by using the electromagnetic circuit element formulation. The sub-models can be interconnected afterwards to obtain a global parametric model that can be simulated or reduced. The sub-models can be treated independently either from the point of view of the variability, or from the point of view of electromagnetic field formulation.

## 1 Introduction

The design of the next-generation of integrated circuits is challenged by an increased number of difficulties since electromagnetic field effects at high frequencies are too relevant to be neglected. In this respect, one of the issues of the European research project CHAMELEON-RF was to develop methodologies and tools able to simulate RF blocks up to 60 GHz by taking the electromagnetic (EM) coupling and variability into account ([www.chameleon-rf.org](http://www.chameleon-rf.org)). In this framework, the concept of magnetic terminals ("hooks" or "connectors") was used for the first time, to describe the interaction of on-chip components with their environment [2]. These magnetic hooks are special boundary conditions that allow the extension of the electric circuit element (ECE) to the electromagnetic circuit element (EMCE). Such an EMCE allows the connection to an external magnetic circuit, and thus inductive coupling effects between the device and its environment can be considered. Details on the implementation of these concepts when using the Finite Integration Technique (FIT) are given in [1].

This paper shows how domain partitioning (DP) can be further exploited: on the one hand by taking into account the variability, and on the other hand by using simplified models for sub-domains in which the full-wave (FW) electromagnetic field formulation is not strictly required.

## 2 Parametric Models Obtained by Domain Partitioning

The EM field effects at high frequencies are quantified by Maxwell equations in FW regime. By applying FIT to discretize these equations in the case of the EMCE formulation, a parametric semi-state space model can be obtained

$$\mathbf{C}(\mathbf{p}) \frac{d\mathbf{x}}{dt} + \mathbf{G}(\mathbf{p})\mathbf{x} = \mathbf{B}\mathbf{u}, \quad (1)$$

$$\mathbf{y} = \mathbf{L}\mathbf{x}, \quad (2)$$

where  $\mathbf{u} = [\mathbf{u}_e, \mathbf{u}_m, \mathbf{y}]^T$  is the state space vector, consisting of electric voltages  $\mathbf{u}_e$  defined on the electric grid, magnetic voltages  $\mathbf{u}_m$  defined on the magnetic grid and output quantities  $\mathbf{y}$ . Only two matrices are affected by the parameters  $\mathbf{p}$ .

The simplest way to analyze the parameter variability is to compute first order sensitivities, which are derivatives of the device characteristic with respect to the design parameters. The computation of sensitivities of matrices is straightforward in FIT, since the assembling of sensitivities is similar to the assembling of matrices, the only difference being that only the affected cells add contributions to the sensitivities matrices  $\partial\mathbf{C}/\partial p_k$ ,  $\partial\mathbf{G}/\partial p_k$ . Such parametric mod-

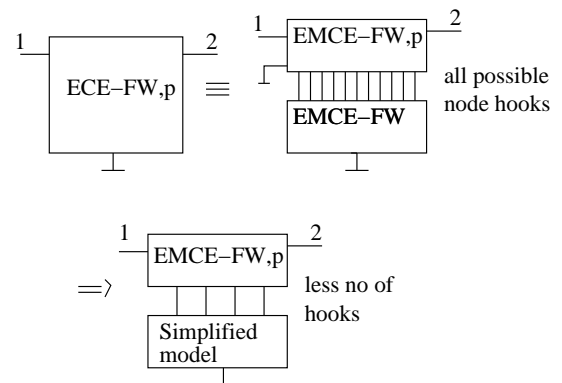


**Fig. 1.** Domain partitioning of complex models: parameters affect only some submodels while simplified formulations can be used for other submodels.

els are useful for a variety of available parametric model order reduction procedures, and that is why, a standard for parametric representation of systems has been defined [3].

By means of electric and/or magnetic terminals the EMCE parametric models can be coupled, or the analysis of a more complex device can be divided into sub-parts that can be modeled independently. The latter idea is illustrated in Fig. 1 and numerical results are given in the next section.

### 3 Numerical results and conclusions

The effectiveness of the proposed methodology was tested at first on a simple test, consisting of two U-shape conductors, placed above a silicon substrate. This domain was decomposed in two parts: a bottom part (the substrate), the rest being the top part. Table 1 gives the complexity of the models obtained by DP and coupling of sub-models. The reference taken is the result obtained by using FW models and node-hooks on the cut. It can be noticed that for the substrate the FW formulation can be substituted with a simpler one, a magnetostatic formulation (MS), case in which the size of the bottom model decreases about 6 times. Figure 2 shows the parameter (conductor width) impact at 60 GHz, obtained for the parametric model obtained.

**Table 1.** Uncoupled test - complexity of models obtained by coupling.

Model	Top size	Bottom size	Model size	Rel. error
FW-top FW-bot	(5466;129)	(5351;127)	(10817;2)	0
FW-top EQS+MS bot	(5466;129)	(1152;72)+ (950;55)= (2102;127)	(7569;2)	5e-4
FW top MS bot	(5394;57)	(950;55)	(6344;2)	3e-3

The real test aimed consists of two coupled inductors, as shown in Fig. 3. Each spiral coil have five metal turns, one terminal grounded and the other excited by means of corresponding pads. The test structure is surrounded by a ground ring. Its domain was decomposed in three parts, the top part (air) and the bottom part (Si) while the middle part, which contain the coils is modeled with FW. Results are shown in Fig. 4. Also the coils width is considered variable and the influence on the result is analysed.

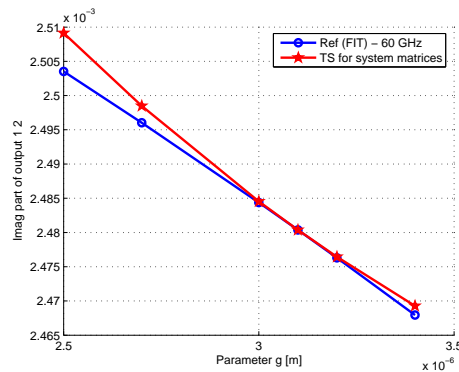


**Fig. 2.** Parameter impact at 60 GHz.

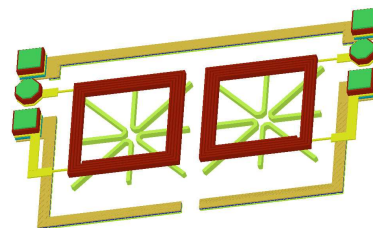


**Fig. 3.** CHRF benchmark no 202 - two coupled inductors.

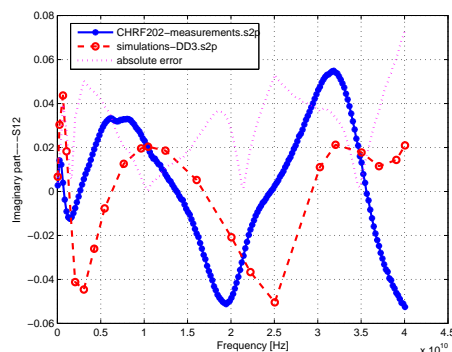


**Fig. 4.** Comparison between measurements from AMS and simulations for CHRF 202.

The full paper will describe in detail the modelling methodology and will prove its usefulness.

### References

1. G. Ciuprina, D. Ioan, and D. Mihalache. Magnetic hooks in the finite integration technique: a way towards domain decomposition. In *Proceedings of CEFEC*. Greece, 2008.
2. D. Ioan, W. Schilders, G. Ciuprina, N. Meijs, and W. Schoenmaker. Models for integrated components coupled with their em environment. *COMPEL Journal*, 27(4):820–829, 2008.
3. L.M. Silveira et al. Report on parametric model order reduction techniques. Technical report, FP6/Chameleon-RF deliverable D1.3a, 2007. Available at <http://www.chameleon-rf.org/>.

# Parametric Reduced Compact Models for Passive Components

Diana Mihalache, Daniel Ioan, Gabriela Ciuprina, and Alexandra Ștefănescu

Politehnica University of Bucharest, Electrical Engineering Dept., Numerical Methods Lab., Spl. Independentei 313, 060042, Romania [lmn@lmn.pub.ro](mailto:lmn@lmn.pub.ro)

**Summary.** This paper describes a technique for extraction of electromagnetic models for passive integrate components, considering the variability of their design (physical and geometrical) parameters.

## 1 Introduction

Actual fabrication of physical devices is prone to the variation of certain circuit parameters due to deliberate adjustment of the process or random deviations inherent to this manufacturing. This variability leads to a dependence of the circuit extracted elements on several parameters which can have either electrical or geometrical background. After the extraction stage a parametric system is obtained, often represented as a state-space system in its descriptor form. Finally, a compact circuit has to be obtained.

Such an approach was the goal work of the frame of the FP6 / IST / Chameleon European project [1], which referred to developing methodologies and prototype tools for a comprehensive and highly accurate analysis of complete next-generation nanoscale functional IC blocks that will operate at RF frequencies of up to 60 GHz.

The problem of parametric model extraction is formulated in mathematical terms. In order to allow the consistent coupling between devices with EM field effects and electric circuits, special boundary conditions called EMCE (Electromagnetic Circuit Element) are used [2]. For nominal cases the reduction procedure based on Vector Fitting (VFIT) [3] and circuit synthesis based on Differential Equation Method (DEM) [4] were very successful. The paper investigates if they can be applied to parametric extraction as well.

## 2 Numerical Example

The study case consist of two rectangular, spiral coils with five metal turns, each coil having one grounded terminal and the other one excited. The parametric model was obtained with the coarsest grid and it included one parameter: the design parameter  $d$  - the distance between the coils. The values of the varying parameter are  $14\mu\text{m}$  and

$56\mu\text{m}$ . Figure 1 shows the layout of the coupling of two spiral inductors. The benchmark is symmetrically w.r.t. their terminals  $S_{11} = S_{22}$  and  $S_{12} = S_{21}$ .

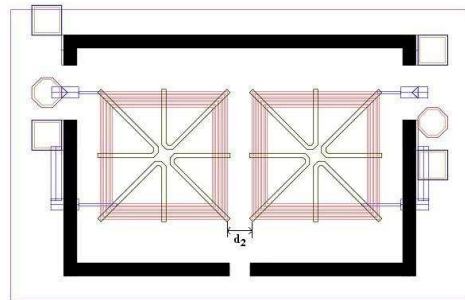


**Fig. 1.** CHRf 202 benchmarks layout ( $d=56\mu\text{m}$ )

In order to estimate the size of the reduced compact model, VFIT procedure followed by DEM procedure was used for the experimental data available for both cases. Reduced models of order 8 have been obtained for both cases, with a relative error between measurements and reduced order of 1%.

Since the order is the same, both circuits have identical topologies but different values for the parameters.

Also, numerical tests showed that the variation of the output characteristic w.r.t. the parameters is almost linear, especially at low frequencies. That is why, this paper will investigate if a parametric circuit can be obtained starting from the two reduced circuits obtained from VFIT+DEM.

Since VFIT procedure starts from impedance or admittance characteristics, the first thing to do is see how far are S parameters computed from averaged Z or averaged Y, to average value of S. Results are given in fig. 2 and the relative errors computed as:

$$err = rms\|X - Xref\|_{-F}/max\|Xref\|_{-F}$$

are:

$$err(S_m, S_{mZ}) = 0.124\%$$

$$err(S_m, S_{mY}) = 0.120\%$$

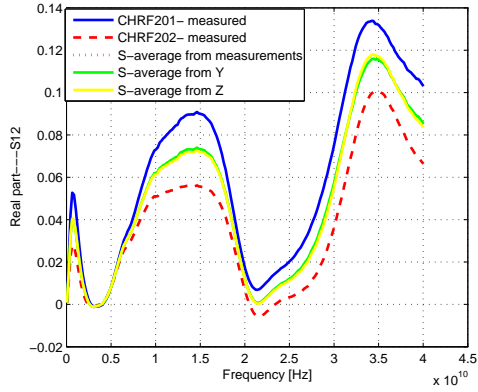


**Fig. 2.** Measurements vs. Average characteristic - S parameter

This preliminary result shows that parametric compact models can be obtained by combining compact models from two simulations, when the variation of the interest quantity w.r.t. the parameter is linear.

*Acknowledgement.* The authors wish to acknowledge that the measurements have been carried out in the frame of FP6/IST/Chameleon European project with support of Austria Micro Systems [www.austriamicrosystems.com](http://www.austriamicrosystems.com).

## References

1. Chameleon RF Project site: [www.chameleon-rf.org](http://www.chameleon-rf.org).
2. Daniel Ioan, Wil Schilders, Gabriela Ciuprina, Nick van der Meijs, Wim Schoenmaker. Models for integrated components coupled with their EM environment. *COMPTEL*, vol. 27, 820–829, 2008
3. Gustavsen and A. Semlyen. Rational Approximation of Frequency Domain Responses by Vector Fitting. *IEEE Trans. Power Delivery*, 14(3), 1052–1061, 1999.
4. T. Palenius and Janne Roos. Comparison of reduced-order interconnect macromodels for time-domain simulation. *IEEE Trans. Microwave Theory and Techniques*, 52(9), 2240–2250, 2004.

# An Effective Technique for Modelling Nonlinear Lumped Elements Spanning Multiple Cells in FDTD

Luis R.J. Costa, Keijo Nikoskinen, and Martti Valtonen

Dept. of Radio Science and Engineering, Faculty of Electronics, Communications and Automation, Helsinki University of Technology, Finland {luis.costa, keijo.nikoskinen, martti.valtonen}@tkk.fi

**Summary.** A technique for modelling lumped elements spanning multiple cells in FDTD is presented. The technique is applied to produce a stable LE-FDTD diode model that works well far beyond normal operational voltage ranges. Simulation results are in good agreement with those obtained with the circuit simulator Aplac and those in the literature [1].

## 1 Introduction

Simulating complex electronic systems often requires lumped elements to be embedded in electromagnetic field simulators. This was accomplished in [1] in a 3D finite-difference time domain (FDTD) simulation for the passive elements, the resistive voltage source, and the diode, each spanning one cell, and the transistor spanning two cells. The lumped element–FDTD (LE-FDTD) method, as this technique is called, requires an iteration routine to solve the transcendental equations resulting in the diode and transistor models due their exponential current-voltage relation. The one-celled resistive voltage source LE-FDTD model was extended in [2] to span multiple cells using a linear equation solver to update the electric field in the region occupied by the source. The authors presented a model for the resistive voltage source that does away with the need for a linear equation solver [3]. The method, suitably modified, turns out to be an effective technique for modelling nonlinear lumped elements, like the diode, spanning multiple cells without needing to solve a system of equations, making the implementation simpler. The strongly nonlinear diode, however, requires iteration to obtain a stable model over a very wide voltage range.

## 2 Modelling Technique

The LE-FDTD method splits the current density term in Ampère’s circuital law into the conduction current density  $\mathbf{J}_c = \sigma \mathbf{E}$  of the lossy medium and the current density  $\mathbf{J}_l$  due to the lumped element. The FDTD method evaluates the  $\mathbf{E}$  field at time  $n$  and the  $\mathbf{H}$  field at  $n + 1/2$  [4]:

$$\oint_C \mathbf{H}^{n+\frac{1}{2}} \cdot d\mathbf{l} = \int_S \left( \varepsilon \frac{\partial \mathbf{E}^{n+\frac{1}{2}}}{\partial t} + \sigma \mathbf{E}^{n+\frac{1}{2}} + \mathbf{J}_l^{n+\frac{1}{2}} \right) \cdot d\mathbf{s}, \quad (1)$$

where  $\mathbf{E}^{n+\frac{1}{2}}$  is computed semi-implicitly as the average  $(\mathbf{E}^{n+1} + \mathbf{E}^n)/2$ . In the following, a  $z$ -directed lumped element current is assumed, without loss of generality, and (1) is discretised in the standard manner, with some short-hand notation introduced at the same time, to derive the update equation for  $E_z$ . So, the left-hand side of (1), the current due to the circulating magnetic field, is

$$\begin{aligned} \mathcal{I}_z|_{i,j,k} &= (H_y|_{i+\frac{1}{2},j,k+\frac{1}{2}}^{n+\frac{1}{2}} - H_y|_{i-\frac{1}{2},j,k+\frac{1}{2}}^{n+\frac{1}{2}}) \Delta y \\ &\quad - (H_x|_{i,j+\frac{1}{2},k+\frac{1}{2}}^{n+\frac{1}{2}} - H_x|_{i,j-\frac{1}{2},k+\frac{1}{2}}^{n+\frac{1}{2}}) \Delta x, \quad (2) \end{aligned}$$

so that the update equation for the  $E_z$  field is

$$\begin{aligned} E_z|_{i,j,k+\frac{1}{2}}^{n+1} &= \left( \frac{1 - \frac{\sigma \Delta t}{2\varepsilon}}{1 + \frac{\sigma \Delta t}{2\varepsilon}} \right) E_z|_{i,j,k+\frac{1}{2}}^n + \left( \frac{\frac{\Delta t}{\varepsilon}}{1 + \frac{\sigma \Delta t}{2\varepsilon}} \right) \\ &\quad \times \left\{ \frac{\mathcal{I}_z|_{i,j,k}}{\Delta_x \Delta_y} - \frac{I_l}{\Delta_x \Delta_y} \right\} \quad (3) \end{aligned}$$

The position indices of  $\varepsilon$  and  $\sigma$  are omitted for compactness and must be added by the reader.

The voltage of the lumped element, connected across multiple cells, as shown in Fig. 1a, is

$$\begin{aligned} V_l^{n+\frac{1}{2}} &= - \sum_{m=a}^b \frac{E_z|_{i,j,m}^{n+1} + E_z|_{i,j,m}^n}{2} \Delta z \\ &= - \sum_{m=a}^b \left\{ \frac{2}{1 + \frac{\sigma \Delta t}{2\varepsilon}} E_z|_{i,j,k+\frac{1}{2}}^n + \frac{\frac{\Delta t}{\varepsilon} \frac{\mathcal{I}_z}{\Delta_x \Delta_y}}{1 + \frac{\sigma \Delta t}{2\varepsilon}} \right\} \frac{\Delta z}{2} \\ &\quad + I_l \sum_{m=a}^b \frac{\Delta z}{2 \Delta_x \Delta_y} \frac{\Delta t}{\varepsilon (1 + \frac{\sigma \Delta t}{2\varepsilon})}. \quad (4) \end{aligned}$$

Above,  $E_z|_{i,j,k+\frac{1}{2}}^{n+1}$  is substituted using (3). Denoting

$$R_g = \sum_{m=a}^b \frac{\Delta z}{2 \Delta_x \Delta_y} \frac{\Delta t}{\varepsilon (1 + \frac{\sigma \Delta t}{2\varepsilon})}, \quad (5)$$

(which is the grid resistance seen by the lumped element) dividing both sides of (4) by  $R_g$ , and denoting the first summation on the right-hand side of (4) divided by  $R_g$  as  $I_{EM}$ , results in

$$\frac{V_1^{n+\frac{1}{2}}}{R_g} = I_{EM} + I_1, \quad (6)$$

which is Kirchhoff's current law for the circuit in Fig. 1b.  $I_{EM}$  is the current due to the FDTD grid.

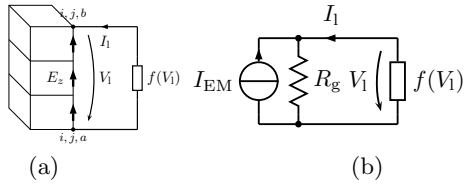


**Fig. 1.** (a) Lumped element connected across three cells and (b) the circuit equivalent of Eq. (6).

For a linear element,  $V_1$  is found directly from the circuit in Fig. 1b and put into (6) to obtain its current, which is then plugged into (3) to get the LE-FDTD model. This was done in [3] for the resistive voltage source. For nonlinear elements, however,  $V_1$  must be found with Newton-Raphson iteration, for example, since otherwise the simulation can be rendered unstable – the stability is very sensitive to the parameters used.

**Diode:** A simple diode model is given by

$$I_d = I_s \left( e^{\frac{q}{kT} V_d} - 1 \right), \quad (7)$$

where  $I_s$  is the saturation current,  $q$  is the electron charge,  $k$  is Boltzmann's constant, and  $T$  is the temperature in Kelvin. The diode voltage  $V_d$  is found from Fig. 1b using Newton-Raphson iteration, typically in two to four iterations, after which (6) gives the diode current  $I_d (= -I_1)$  that is then plugged into (3). Alternatively, (7) is used to compute  $I_d$ .

To test this model, the microstrip circuit in Fig. 2a was simulated. The microstrip had width  $6\Delta_x$ , length  $30\Delta_y$ , and substrate height  $3\Delta_z$ , its characteristic impedance is  $50\Omega$ . The FDTD space was  $64 \times 50 \times 12$ , terminated in a first-order Mur boundary condition, with  $\Delta_x = 0.4064$  mm,  $\Delta_y = 0.4233$  mm and  $\Delta_z = 0.265$  mm. The source resistance  $R_s = 50\Omega$  and frequency of the sinusoid excitation was 2 GHz. The simulation was run for 2286 time steps using a 10 V and 2.5 kV peak voltage to test the stability of the diode model. At 2.6 kV the simulation became unstable, but the instability formed in the Newton-Raphson iteration, which was implemented without any time-step control. A more sophisticated time-step control will further extend the working range of this diode model. The simulation results are compared with those obtained with the circuit simulator APlac and are seen to be in good agreement. At 200 MHz, the 10 V peak voltage yields the result obtained by [1], whose model is reported to be stable using a peak voltage of 15 V.

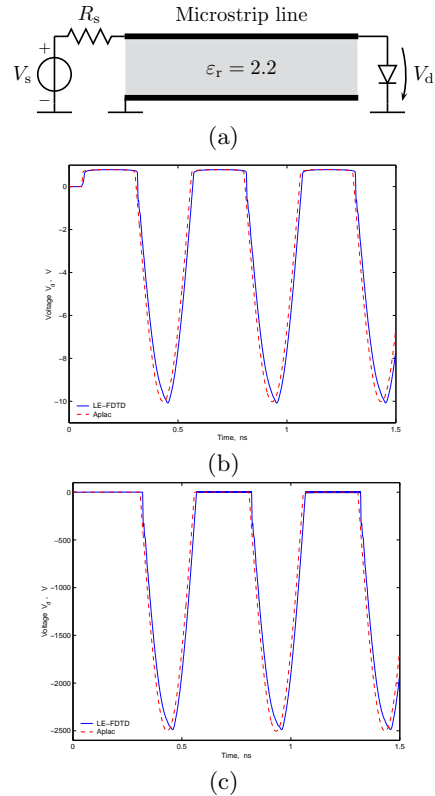


**Fig. 2.** (a) Microstrip test circuit used to verify the diode model. (b) Diode voltage when source peak voltage is 10 V and (c) 2.5 kV. The simulation results are compared with those obtained with APlac.

### 3 Conclusion

A technique for modelling lumped elements spanning multiple cells in FDTD is presented. The technique yields a novel diode model that is stable even far beyond useful operational voltages. The model produces simulation results that are in agreement with those produced by the circuit simulator APlac.

### References

1. M. Picket-May, A. Taflove, and J. Baron. FD-TD modeling of digital signal propagation in 3-D circuits with passive and active loads. *IEEE Trans. Microwave Theory and Tech.*, MTT-42(8):1514–1523, August 1994.
2. J. Xu, A.P. Zhao, and A.V. Räsänen. A stable algorithm for modeling lumped circuit source across multiple FDTD cells. *IEEE Microwave and Guided Wave Letters*, 7(9):308–310, September 1997.
3. L. J. Costa, K. Nikoskinen, and M. Valtonen. Models for the LE-FDTD resistive voltage source spanning multiple cells. In *Proceedings of the 2007 European Conference on Circuit Theory and Design, ECCTD 2007*, pages 671–674, August 26-30 2007.
4. A. Taflove and S.C. Hagness. *Computational Electrodynamics: the Finite-Difference Time Domain Method*. 2nd edition, Artech House, Boston, 2000.

# Mixed-Derating of Three-Phase Distribution Transformer under Unbalanced Supply Voltage and Non-Linear Load Conditions Using Finite Element Method

Jawad Faiz, M. Ghofrani, and B.M. Ebrahimi

Department of Electrical and Computer Engineering University of Tehran, North Kargar Avenue, Tehran, Iran ebrahimibm@ut.ac.ir

**Summary.** In this paper, a three-phase, three-legged 20/0.4 KV, 50 KVA distribution transformer is analyzed under unbalanced supply voltage in the presence of non-linear load. The transformer is modeled using time stepping finite element method (TSFEM), considering all geometrical and physical characteristics. Performance of the modeled transformer under unbalanced supply voltage and non-sinusoidal load conditions has been studied individually. Then the effect of unbalanced supply voltage in the presence of non-sinusoidal load current on the transformer performance is analyzed. It is shown that non-linear load causes the winding losses to increase considerably while the core loss approximately remains constant. According to IEEE standards and other papers, distribution transformers are needed to be derated under non-linear load conditions to prevent the insulation fatigue and the decrease of transformers life time. It is also shown that unbalanced supply voltage increases the core and copper losses simultaneously due to an increase in the amplitude of harmonic components. So the distribution transformers should be mix-derated in order to account for both winding losses and core losses increments.

## 1 Introduction

COMMON sources of harmonics in industrial electrical systems are rectifiers, dc motor drives, uninterruptible power supplies, and arc furnaces. With the ever-increasing use of these non-linear loads, transformers are exposed to the higher load losses, early fatigue of insulation, premature failure and reduction of the useful life. Therefore, distribution transformers should be derated according to IEEE C57-110 or other methods under non-sinusoidal load currents [1-2]. Another undesirable phenomenon that occurs in electrical power systems is the voltage unbalancy. Electrical trains, non-uniform distribution of loads on three phases of the power system and non-equal spacing of the transmission lines in non-transposed lines are the most common reasons of unbalanced voltage occurrence[3]. Unbalanced voltage leads to an increase in core loss as well as winding loss. So the studying of distribution transformer performance

under the simultaneous presence of unbalanced supply voltage and non-sinusoidal load currents could be of great interest. Since the transformer operates under various harmonic frequencies, the frequency dependent parameters of transformer, winding skin effect and magnetic core nonlinearity must be taken into account. Using Finite Element Method (Opera-2D) satisfies all these criteria with an acceptable accuracy.

## 2 Modeling of transformer using time stepping finite element method

Calculating the magnetic field distribution within the transformer is essential for transformer analysis. FEM is able to calculate the magnetic field distribution within the transformer from geometrical dimensions and magnetic parameters of the transformer. Other quantities of the transformer such as the induced voltage waveform, magnetic flux density and forces exerted on the windings can be determined knowing the magnetic field distribution [4]. Two-dimensional finite element method solves the following Poisson equation in order to evaluate and analyze the magnetic flux distribution:

$$\frac{\partial}{\partial x}(\Re \frac{\partial A}{\partial x}) + \frac{\partial}{\partial y}(\Re \frac{\partial A}{\partial y}) = -\frac{ni}{S_e} \quad (1)$$

where  $A$  is the magnetic potential vector,  $\Re$  is the core sheets reluctivity,  $n$  is the number of winding turns and  $S_e$  is the cross-section of the conductors. The principal equation of the electric circuits is presented as follows:

$$V_s = R_s i + L_s \frac{di}{dt} \quad (2)$$

where  $V_s$  is the input voltage of the transformer,  $R_s$  and  $L_s$  are the resistance and inductance of the supply. The matrix form of (1) and (2) is

$$[K][A] + [M] \frac{\partial}{\partial t}[A] - [C][i] = 0 \quad (3)$$

$$[D]^T \frac{\partial}{\partial t}[A] + [L] \frac{\partial}{\partial t}[i] + [R][i] = [u] \quad (4)$$

where  $[A]$  and  $[i]$  are the magnetic potential and current vectors,  $[K]$ ,  $[M]$ ,  $[C]$ ,  $[D]$ ,  $[L]$  and  $[R]$

are the vector of coefficients and  $[U]$  is the input vector. Now a non-linear equation must be introduced that links the FE magnetic equations to the electric circuit equations. This equation is

$$[P][A \ E \ i]^T + [Q]\frac{\partial}{\partial t}[A \ E \ i]^T = [S] \quad (5)$$

where  $[P]$  and  $[Q]$  are the coefficients vector and  $[S]$  is the transformer input vector. Solution of (5) gives magnetic potential vector  $[A]$  and transformer current  $[i]$ .

Having obtained parameter  $A$  from (5), distribution of flux density can be calculated in the core as follows:

$$B = \nabla \times A \quad (6)$$

### 3 Effects of nonlinear loads on distribution transformer performance

The non-linear modeled load is a six-pulsed power electronic converter. The current of this converter is of  $6k \pm 1$  harmonic orders ( $k$  is an integer). Non-sinusoidal load currents increase the winding eddy current losses and  $RI^2$  losses of the transformer, while the core loss approximately remains constant. Table I summarizes the transformer loss calculations for linear load and three different cases of non-linear loads using FEM.

**Table 1.** Performance of distribution transformer for non-linear load conditions

Load	THD <sub>I</sub> (%)	$P_{Cu}(w)$	$P_{Ec}(w)$
Linear	-	1199	46.76
Non-linear (case1)	18.22%	1238.85	90.8
Non-linear (case2)	23.01%	1262.5	115.97
Non-linear (case3)	28.32%	1295.2	168.8

### 4 Effects of unbalanced voltage on distribution transformer performance

For analyzing performance of the transformer under the unbalanced voltage condition, three different cases of unbalanced supply voltage are considered. FEM results show that core loss and winding copper loss increase considerably while the winding eddy current losses have a slight accretion.

**Table 2.** Table II: Performance of distribution transformer for unbalanced (U) voltage conditions

Supply	Phase(a-b-c)	$P_{Core}(w)$	$P_{Cu}(w)$	$P_{Ec}(w)$
Balanced	0%-0%-0%	210	1199	46.76
U(case1)	0%-5%-7.5%	228.9	1272.1	50
U(case2)	0%-7.5%-10%	256.18	1477.12	53
U(case3)	0%-10%-12.5%	270.2	1624	53.2

### 5 Effects of simultaneous presence of unbalanced voltage and non-linear load conditions on distribution transformer performance

Distribution transformer performance under individually applied unbalanced voltage or non-linear load condition has been studied using FEM. It is shown that the distribution transformer needs to be derated considering the winding eddy current losses increase under the non-sinusoidal load condition. Unbalanced supply voltage in the presence of the non-linear load adds to the amplitude of harmonic components and increases the core loss as well as the winding losses. In order to consider the effect of both core and winding eddy current losses on the transformer performance, the transformer should be mix-derated. Transformer mixed-derating requires the precise calculation of the losses under the simultaneous presence of unbalanced voltage and non-sinusoidal load current. The given transformer is modeled under unbalanced supply voltage using FEM and a six-pulsed power electronic converter is connected to the external circuit as the transformer load. Table III and Table IV summarize the results of transformer simulation under the above mentioned conditions.

**Table 3.** Table III: Performance of distribution transformer for simultaneous presence of unbalanced voltage (UV) and non-linear load (NL) conditions (three different cases of unbalanced voltage)

UV & NL	THD <sub>I</sub> (%)	Phase(a-b-c)	$P_{Core}(w)$	$P_{Cu}(w)$	$P_{Ec}(w)$
Case1	28.32%	0%-5%-7.5%	230	1310	170
Case2	28.32%	0%-7.5%-10%	260.2	1480	172
Case3	28.32%	0%-10%-12.5%	276	1730	180

**Table 4.** Table IV: Performance of distribution transformer for simultaneous presence of unbalanced voltage (UV) and non-linear load (NL) conditions (three different cases of non-linear load)

UV & NL	THD <sub>I</sub> (%)	Phase(a-b-c)	$P_{Core}(w)$	$P_{Cu}(w)$	$P_{Ec}(w)$
Case1	18.22%	0%-5%-7.5%	229	1245	100
Case2	23.01%	0%-5%-7.5%	229.8	1270	120
Case3	28.32%	0%-5%-7.5%	230	1310	170

### 6 Spectrum analysis of distribution transformer

Fig. 1 presents the frequency spectrum of the transformer secondary voltage for two different cases: 1) balanced supply voltage and linear load. 2) Unbalanced supply voltage and non-linear load.

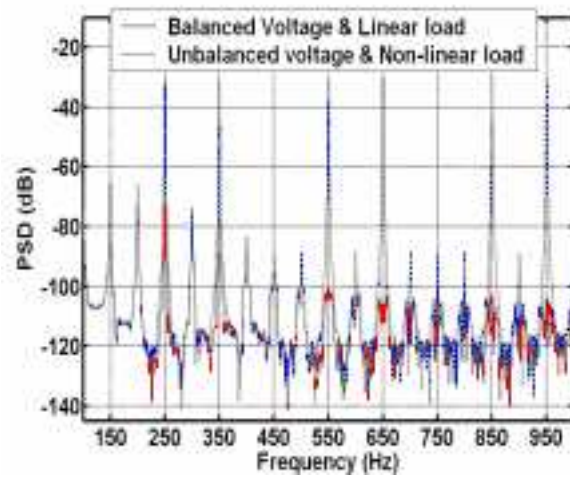


**Fig. 1.** Fig. 1. Normalized plots of the line voltage spectra of a transformer under balanced voltage-linear load and unbalanced voltage-non-linear load with 5<sup>th</sup>, 7<sup>th</sup>, 11<sup>th</sup>, 13<sup>th</sup>, 17<sup>th</sup>, 19<sup>th</sup> harmonics

## References

1. ANSI/IEEE C57.110/D7, "Recommended practice for establishing transformer capability when supplying non-sinusoidal load currents," IEEE, NY, Feb. 1998.
2. M.A.S. Masoum and E.F. Fuchs, "Derating of anisotropic transformers under nonsinusoidal operating conditions," *Elect. Power energy Syst.*, vol. 25, pp. 1–12, 2003.
3. A.V. Jouanne, B. Banerjee, "Assessment of Voltage Unbalance", *IEEE Trans. Power Delivery*, Vol. 16, No. 4, October 2001, pp. 782–790.
4. Vector Field Software Documentation, 2005.



# Design Optimization of Radial Flux Permanent Magnet Wind Generator for Highest Annual Energy Input and Lower Magnet Volumes

Jawad Faiz<sup>1</sup>, M. Rajabi-Sebdani<sup>2</sup>, B.M. Ebrahimi<sup>2</sup>, and M.A. Khan<sup>3</sup>

<sup>1</sup> University of Tehran and Iran Academy of Sciences, Tehran, Iran [jfaiz@ut.ac.ir](mailto:jfaiz@ut.ac.ir)

<sup>2</sup> Department of Electrical and Computer Engineering, University of Tehran, Tehran, Iran

<sup>3</sup> Department of Electrical Engineering, University of Cape Town, Cape Town, South Africa

**Summary.** This paper presents a multi-objective optimization method to maximize annual energy input (AEI) and minimize permanent magnet (PM) volume in use. For this purpose, the analytical model of the machine is utilized. Effects of generator specifications on the annual energy input and PM volume are then investigated. Permanent magnet synchronous generator (PMSG) parameters and dimensions are then optimized using genetic algorithm incorporated with an appropriate objective function. The results show an enhancement in PMSG performance. Finally 2D time stepping finite element method (2D TSFE) is used to verify the analytical results. Comparison of the results validates the optimization method.

## 1 Analytical design

The power captured by a wind turbine from the incident wind can be expressed as:

$$P_{\text{shaft}} = \frac{1}{2} \rho_{\text{air}} \pi R^2 U^3 C_p, \quad (1)$$

where  $\rho_{\text{air}}$  is the density of air at the height of the turbine hub and  $C_p$  is the dimensionless power co-efficient or aerodynamic efficiency of the turbine which is a function of the tip speed ratio ( $\lambda$ ) at which the turbine is operating. This ratio is defined as the ratio of blade tip speed to wind speed, and can be expressed as:

$$\lambda = \frac{\omega_r R}{U} \quad (2)$$

Equations (1) and (2) can be used to determine an expression for the torque applied to the turbine shaft, which can be expressed as:

$$T_{\text{shaft}} = \frac{P_{\text{shaft}}}{\omega_r} = \frac{1}{2} \rho_{\text{air}} \pi R^3 U^2 C_T \quad (3)$$

where  $C_T = C_p / \lambda$  is the torque coefficient of the turbine.

The power captured by a wind turbine and turbine shaft speed for a PMSG is shown in Fig. 1. Generator output power can be expressed as follows:

$$P_{\text{gen}} = \eta_{\text{gen}} P_{\text{shaft}} \quad (4)$$

That power shaft is maximized when [1]:

$$\frac{dP_{\text{gen}}}{d\omega_r} = 0 \quad (5)$$

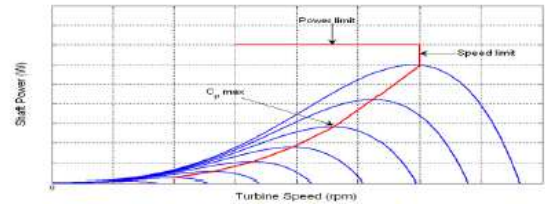


**Fig. 1.** Variation of shaft power with turbine speed

or

$$\frac{dP_{\text{gen}}}{d\omega_r} = \frac{dP_{\text{gen}}}{d\lambda} \cdot \frac{d\lambda}{d\omega_r} = 0 \quad (6)$$

It is necessary to note that

$$\frac{d\lambda}{d\omega_r} \neq 0 \rightarrow \frac{dP_{\text{gen}}}{d\lambda} \neq 0 \quad (7)$$

So, the peak power shaft can be found as follows:

$$\frac{dP_{\text{gen}}}{d\omega_r} = 0 \leftrightarrow \frac{dP_{\text{gen}}}{d\lambda} = 0 \rightarrow \frac{dC_p(\beta, \lambda)}{d\lambda} = 0 \quad (8)$$

With defined  $C_p$ , the maximization  $P_{\text{gen}}$  and  $P_{\text{shaft}}$  will be defined. The apparent power of a radial-flux machine at the air-gap can be written in terms of the main dimensions of the machine as follows:

$$S_g = \frac{1}{2} \pi^2 \cdot K_{w1} \cdot D^2 \cdot \ell \cdot n_s SML_{pk} \cdot SEL_{pk} \quad (9)$$

where  $K_{w1}$  is the fundamental winding factor,  $n_s$  is the rotational speed in rps,  $SML_{pk}$  and  $SEL_{pk}$  are the peak values of the specific magnetic and electric loadings of the machine. The output electrical power of a radial-flux generator can be related to its apparent airgap power by the following expression:

$$P_{\text{gen}} = 3V_a I_a \cos \phi = 3 \frac{E_f}{\varepsilon} I_a \cos \phi \quad (10)$$

where:

$$E_f = \sqrt{2} \pi f N_{ph} k \omega_1 \phi_p \quad (11)$$

where  $\phi_p$  is the flux per pole due to the fundamental space harmonic component of the excitation flux density distribution,  $f$  is the frequency and  $N_{ph}$  is the number of turns per phase. The product  $D^2 \ell$ , which is proportional to the rotor volume of a radial-flux machine, determines its output torque capability. This product can be determined by combining (10) and (11) as follows:

$$D^2 \ell = \frac{\varepsilon P_{\text{gen}}}{0.5 \pi^2 K_{w1} n_s SML_{pk} SEL_{ok} \cos \phi} \quad (12)$$

## 2 Optimization algorithm

Some of the typical dimensions of PMSG are selected as design variables where values are determined through an optimization procedure. In this paper, design variables are axial length, remanent flux density of the PMs, specific electric loading, efficiency, power factor, terminal voltage and wind speed. To have a more realistic design, some constraints are applied to design variables listed in Table 2. The pole pairs, rated frequency, number of blades, the main fixed specifications in the design procedure are (250 rpm), 50 Hz and 3 respectively. The operating frequency range for small PM wind generators is reported as typically: 30-80Hz. Thus, the nominal frequency of the generator at rated wind speed is chosen to be within the range 45-65Hz.

**Table 1.** Design constraints

Parameter	Minimum Value	Maximum Value
Terminal Voltage	180 V	240 V
Axial Length	0.04 m	0.08 m
Output power	1625 W	3800 W
Frequency	45 Hz	65 Hz
Number of pole pairs	4	24
SEL	10000 A/m	40000 A/m
Efficiency	80%	100%
Remnant of flux density	0.8 T	1.4 T
Wind speed	7 m/s	13 m/s

To obtain an optimal design considering, terminal voltage, power factor and PM volume, the three objective functions are defined as follows:

$$J_z(x_1, \dots, x_n) = \frac{AEI(x_1, \dots, x_n)^m}{VPM(x_1, \dots, x_n)^n} \quad (13)$$

where  $x_1, x_2, \dots, x_n$  are design variables. As seen in (11) the importance of the terminal voltage, power factor and PM volume are adjusted by power coefficients. Maximization for  $J_z$  fulfils simultaneously three objectives of the optimization. Such as objective function provides a higher degree of freedom is selecting appropriate design variables. The results of optimization are summarized in Table 2.

**Table 2.** Specification of intial and optimal designed generator

Parameters	Original PMSG	Proposed Opt. Design
Output power (W)	1625	1785
No. of turns per phase	370	816
Shaft torque (N.m)	112.4922	74.0794
Remnant of flux dens. (T)	1.17	1.1512
Axial length (m)	0.0665	0.0581
Current dens. (A/mm <sup>2</sup> )	2.037	0.9336
Pole pairs	4	12
Rotor speed (rpm)	157	250
No. of turbine blade	12	3
frequency (Hz)	10.47	50
Wind speed (m/s)	10	8.62
Ef (V)	72.89	247.0602
Annual energy capture (Wh)	1.4756e+007	1.9911e+07
Efficiency	87.86	92.03
Volume of PM (m3)	18.272e-005	14.824e-005

## 3 Time stepping finite element analysis

The first step in prediction and analysis of the PMSG is the precise modeling of the motor. The motor is modeled taking into account the non-linearity of the ferromagnetic materials and the physical conditions of the motor components. The local total current density ( $\mathbf{J}$ ) is:

$$\mathbf{J} = J_0 - j\omega\mathbf{A} \quad (14)$$

where  $J_0 = \sigma E_0$  is the current density due to the supply voltage and  $\mathbf{A}$  is the magnetic potential vector. The total current in a conductor having cross-section  $\Omega_b$  is:

$$\int_{\Omega_b} \mathbf{J} \cdot d\mathbf{s} = \int_{\Omega_b} (J_0 - j\omega\sigma\mathbf{A}) d\xi \quad (15)$$

where  $\omega$  is the angular frequency,  $\sigma$  is the electrical conductivity of conductor and  $\xi$  is the cross-section of the conductor. Since  $E_0$  is constant over the entire conductor cross section then:

$$I = J_0 \int_{\Omega_b} d\xi - j\omega \int_{\Omega_b} (\sigma\mathbf{A}) d\xi \quad (16)$$

where  $I$  is the total current of the conductor. For every circuit:

$$\nu_s = R_{\text{ext}}i + L_{\text{ext}} \frac{di}{dt} + E_s \quad (17)$$

where  $\nu_s$  is the impressed voltage,  $i$  is the phase current,  $R_{\text{ext}}$  is the stator phase resistance and  $L_{\text{ext}}$  is the end winding inductance and:

$$E_s = l_m \sum_{i=1}^N \pm E_i \quad (18)$$

where  $l_m$  is the length of the FE region,  $Z_{\text{ext}}$  is the external circuit impedance and  $N$  is the number of turns. By the following definition:

$$\nu_s = \frac{V_s}{l_m}, Z_e = \frac{Z_{\text{ext}}}{l_m} \quad (19)$$

The following can be obtained:

$$\nu_s = \sum_{i=1}^N \pm E_i + Z_e i \quad (20)$$

The matrix form of (20) is as follow:

$$[V_s] = [D]^T [E] + [Z_{\text{ext}}] [I_b] \quad (21)$$

By combining the above equations, the following general system is obtained:

$$\begin{bmatrix} A \\ \frac{E_s}{j\omega} \\ \frac{I_b}{j\omega} \end{bmatrix} = \begin{bmatrix} [S] + j\omega\sigma_{xy} [T] & -j\omega\sigma_z [C] & [0] \\ -j\omega\sigma_z [C] & -j\omega\sigma_z [\Omega_b] & -j\omega [D] \\ [0] & -j\omega [D] & -j\omega [Z_{\text{ext}}] \end{bmatrix}^{-1} \begin{bmatrix} 0 \\ 0 \\ -\nu_s \end{bmatrix} \quad (22)$$

where  $[I_b]$  is the circuit vector (number of circuits multiplied by 1),  $[E_s]$  is the bar voltage vector (number of bars multiplied by 1),  $[D]$  is the connection matrix of the bar (number of circuits multiplied by the number of bars),  $[\Omega_b]$  is the diagonal matrix of the cross-section of the bar (number of the bars multiplied by 1),  $[Z_{\text{ext}}]$  is the diagonal external impedance matrix and  $\nu_s$  is the circuit voltage vector (number of circuits multiplied by 1). Fig. 2 shows the optimized excitation voltage compared with the voltage of the original generator.

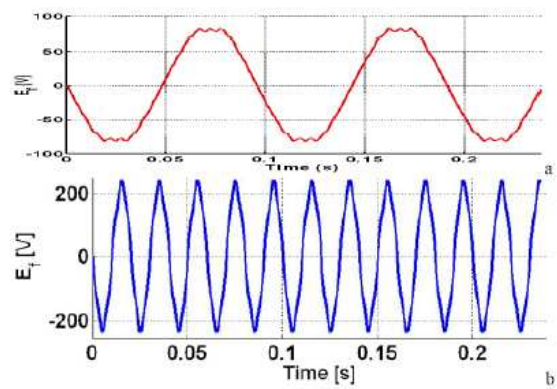


**Fig. 2.** Variation of excitation voltage with time, (a) original PMSG and (b) propose optimal design

## References

1. J. Clerk Maxwell. *A Treatise on Electricity and Magnetism*, 3rd ed., vol. 2. Oxford: Clarendon, 1892, pp. 68-73.



# Finite-element discretization for analyzing eddy currents in the form-wound stator winding of a cage induction motor

M. Jahirul Islam and Antero Arkkio

Department of Electrical Engineering, Helsinki University of Technology, Finland jahirul.islam@tkk.fi, antero.arkkio@tkk.fi

**Summary.** For the computation of the eddy-current loss in the form-wound multi-conductor stator winding accurately, finite element discretization (FED) is an important issue. The stator bars of the studied motor must be discretized detailed enough to compute the eddy-current effects accurately. Two main supply conditions of a cage induction motor, sinusoidal and PWM, are considered.

## 1 Introduction

The finite element analysis (FEA) is one of the most popular and reliable methods to consider eddy-currents in the form-wound multi-conductor stator windings. To model the eddy currents in the stator winding with FEA, all the stator bars connected in series and parallel should be considered. As a result, finite element discretization (FED) of every bar is an essential requirement [1].

In an induction motor, high-frequency harmonics are generated from the internal and external sources. When the supply of the motor is taken from grid, the source is almost sinusoidal. The harmonics are generated from the internal sources due to the complex geometry of electrical motor. The eddy-current loss can be reduced by lifting up the stator coils from the air-gap since those harmonics mainly stay close to the air-gap [2]. Due to the requirement of the speed control of electrical motor, the application of frequency converter supply has increased in recent decades. The supply from the frequency converter is strongly non-sinusoidal and contains a set of additional harmonics (external source) [3]. The presence of these high-frequency components means that the skin depth becomes shorter [4]. To consider the eddy-current effects of those high-frequency components accurately, the FED should be detailed enough. A more detailed discretization means an increase in the number of equations to be solved. As a result, the computational complexity and time is increased.

The main objective of this work is to study the accuracy of the FED for the eddy-current loss computation in the form-wound stator winding of a

cage induction motor. The following two conditions are considered for the study:

1. The motor is supplied from a sinusoidal voltage source
2. The motor is supplied from a pulse-width-modulated (PWM) voltage source.

## 2 Methods

To model the eddy current losses, time stepping finite element analysis has been used in which the backward Euler method is used for time discretization. The circuit equations of the cage rotor, stator phase and stator bars are strongly coupled with the electromagnetic field equations and the total system of equation is solved altogether [1-3], [5]. The stator resistive loss in the slot embedded stator bars after considering the eddy-current loss is

$$P_{sb} = \frac{Q_s l_e}{\sigma} \sum_{j=1}^{Q_b^s} \int_{\Omega} \eta_i^s \mathbf{J}^2 d\Omega \quad (1)$$

where the current density in the stator bar  $i$  is  $\mathbf{J} = -\sigma \frac{\partial \mathbf{A}}{\partial t} + \sigma \frac{u_i^s \mathbf{e}_z}{l_e}$ ,  $Q_s$  is the number of symmetry sectors,  $l_e$  is the length of the slot embedded stator bars,  $\sigma$  is the conductivity,  $\Omega$  is the cross sectional area of a stator bar,  $\eta_i^s$  is the parameter for correspondence between the points the equation is applied and the stator bar  $i$ ,  $\mathbf{A}$  is the vector potential,  $u_i^s$  is the potential difference of the stator bar  $i$  and  $\mathbf{e}_z$  is the unit vector in the  $z$  direction.

The eddy-current loss arises due to the uneven current distribution in the bars [6]. This causes the effective bar resistance to exceed its DC value. This effective resistance is defined as the AC resistance [1]. The eddy factor ( $k_{\text{eddy}}$ ) is defined as

$$k_{\text{eddy}} = \frac{P_{sb}}{i^2 R_{DC}} = \frac{i^2 R_{AC}}{i^2 R_{DC}} = \frac{R_{AC}}{R_{DC}} \quad (2)$$

## 3 Results

A 3-phase, 50 Hz, 690 V, delta-connected, 1250 kW cage induction machine with double layer

winding is studied [1-3]. The number of rotor slots is adjusted to reduce the symmetry sector. A bar is that part of a strand that is embedded in a slot. The bars are connected in series in a particular strand. Each effective turn consists of three copper strands connected in parallel. There are six effective turns in a slot. Therefore, there are 18 bars in a slot. The height of a bar is 3.2 mm and width is equal to 10.6 mm [1-3]. To study the accuracy of the FED, the number of finite elements is increased from 4 to 48 successively. Based on the number of FED layers, the discretization in the direction of bar height can be divided into three cases. Fig. 1 presents the finite-element discretization for all the three cases. For case A, there is only one layer over the height. In a similar way, by making two and three layer FED over the bar height leads to case B and C. For each cases, the number of finite elements is increased by making more subdivisions in the bar width. Second-order isoparametric triangular finite elements have been used to simulate the electrical machine. Fig. 2 presents the eddy-current effects ( $\frac{R_{AC}}{R_{DC}} - 1$ ) as a function of the number of elements in a stator bar. The results have been computed when the motor is supplied from a sinusoidal or a PWM voltage source.

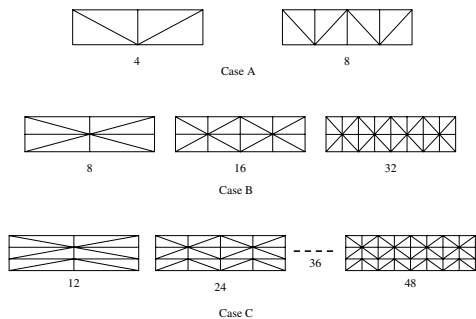


Fig. 1. Finite-element discretization of a bar.

## 4 Discussion

For the sinusoidal supply, the eddy-current effects ( $k_{\text{eddy}} - 1$ ) remains almost constant for the cases A, B and C (Fig. 2). Fine discretization seems just to increase the computational complexity and time. For this supply, the main component for the eddy-current loss in the stator winding is leakage flux that passes from one stator tooth to another. The frequency of this component is equal to the fundamental.

When the motor is supplied from a PWM voltage source, a single layer FED (case A) is not accurate

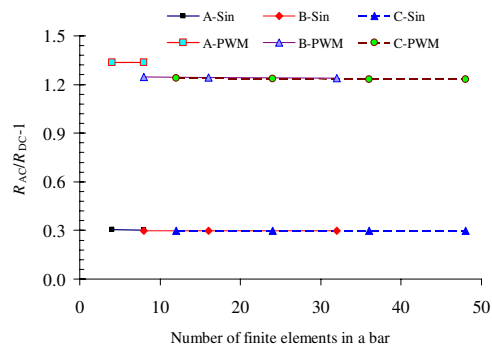


Fig. 2. Eddy-current effects ( $\frac{R_{AC}}{R_{DC}} - 1$ ) are presented as a function of the number of elements in a bar for sinusoidal and PWM supply.

enough (Fig. 2). The PWM supply injects higher harmonics to the supply. The high-frequency flux passes circumferentially from one stator tooth to another. The two and three layer FEDs result in almost identical losses.

For the sinusoidal supply, case A, where the number of finite elements is 4, and for the PWM supply, case B, where the number of elements is 8, compromises regarding the computational complexity and accuracy.

## References

1. M. J. Islam, J. Pippuri, J. Perho and A. Arkkio. Time-harmonic finite-element analysis of eddy currents in the form-wound stator winding of a cage induction motor, *IET Electric Power Application*, vol. 1, issue 5, September 2007, pp. 839-846.
2. M. J. Islam and A. Arkkio. Time-stepping finite element analysis of eddy currents in the form-wound stator winding of a cage induction motor supplied from a sinusoidal voltage source, *IET Electric Power Application*, In press.
3. M. J. Islam and A. Arkkio. Effects of pulse-width-modulated supply voltage on eddy currents in the form-wound stator winding of a cage induction motor, Under review.
4. A. D. Podoltsev, I. N. Kucheryavaya and A. B. Levedev. Analysis of effective resistance and eddy-current losses in multiturn winding of high-frequency magnetic components, *IEEE Transactions on Magnetics*, vol. 39, issue 1, January 2003, pp. 539-848.
5. I. Yatchev, A. Arkkio and A. Niemenmaa. *Eddy-current losses in the stator winding of cage induction motors*, Laboratory of Electromechanics, Helsinki University of Technology, Report 47, Finland 1995, p. 34.
6. A. Konrad. Integrodifferential finite element formulation of two-dimensional steady-state skin effect problems, *IEEE Transactions on Magnetics*, vol. 18, Issue 1, January 1982, pp. 284-292.

---

**Session**

**CP 1**

---



# Evaluation of the electromagnetic coupling between microelectronic device structures using computational electro-dynamics

Wim Schoenmaker and Peter Meuris

MAGWEL NV Martelarenplein 13, B-3000 Leuven, Belgium [wim@magwel.com](mailto:wim@magwel.com), [peter@magwel.com](mailto:peter@magwel.com)

**Summary.** Electromagnetic coupling between devices in an microelectronic layout can become a serious design concern. In this paper, the problem of electromagnetic coupling is addressed from field computational point of view. Approximation schemes are justified by evaluating dimensionless parameters in the set up of the field equations and scale considerations of devices.

## 1 Introduction

With the use of increasing frequency ranges, electromagnetic coupling becomes more pronounced design concern because induced electric fields are proportional to rate of change of the magnetic induction. However, not only the pace of time variations are determining for including electromagnetic coupling but also the problem scale and the intensity of the currents that are responsible for the induced fields must be considered. An overall picture of scaling arguments is presented in section 2 which is valuable for computational considerations. Once we note from scale considerations that electromagnetic coupling terms represent a non-negligible contribution to the full system of equations, we move on to the solution of these equations. In section 3, we review and update of the approach that was proposed some years ago by the author and co-workers [1–3]. We will refer to this approach as ‘computational electro-dynamics’. At several occasions we were inquired if this method is equivalent to the method based on Nedelec’s edge elements [4]. To the best of our knowledge, we believe it is not. The main difference being that we do not refer to test functions at all. Our method is more related to finite-integration techniques (FIT). Scale considerations are not only an issue for deciding if some terms in the full system of Maxwell equation and constitutive laws can be neglected. When discussing the coupling of devices, it is also important to realize that different devices can have an intrinsic or geometrical scales that differ orders of magnitude. In such scenarios the coupled problem is most easily split in computational domains. Computational

electrodynamics gives rather straightforwardly a series of prescriptions for matching the interface conditions of the various domains.

Electromagnetic coupling of microelectronic devices is an RF issue and is most conveniently measured using s-parameters. In section 4, we present our method to compute these matrix elements. In fact, s-parameter extraction is a straightforwardly achieved as a post-processing of the results of a computational electro-dynamics problem with the appropriate setting of the boundary conditions.

In section 5 we will present a few of coupled problems, that we have addressed recently.

## 2 Scaling rules the Maxwell equations

The use of scale arguments is definitely not new to the field of computing in electromagnetic modeling. Well-known approximations are the so-called EQS (electro-quasi static) and MQS (magneto-quasi static) approximations. Approximations can be put in a different perspective by considering the scaling step that is necessary when converting the full set of equations to dimensionless equations before computing can start. For our present argument it suffices to consider insulators and metals only. Semiconductors can be easily added.

$$\mathbf{J}_c = \sigma \mathbf{E} \quad (1)$$

$$\mathbf{D} = \varepsilon_0 \varepsilon_r \mathbf{E} \quad (2)$$

$$\mathbf{H} = \frac{1}{\mu_0 \mu_r} \mathbf{B} \quad (3)$$

$$\mathbf{B} = \nabla \times \mathbf{A} \quad (4)$$

$$\mathbf{E} = -\nabla V - \frac{\partial \mathbf{A}}{\partial t} \quad (5)$$

Consider the Maxwell equation is the potential formulation. The Poisson equation is used to solve the scalar field in insulators and semiconducting regions and the current-continuity equation is used in metals to find the scalar potential there. The electric system is :

$$\begin{aligned}\nabla \cdot [\varepsilon (\nabla V + i\omega \mathbf{A})] + \rho &= 0 \\ \nabla \cdot [(\sigma + i\omega\varepsilon) (\nabla V + i\omega \mathbf{A})] &= 0\end{aligned}\quad (6)$$

The Maxwell-Ampere equation is :

$$\nabla \times \left( \frac{1}{\mu} \nabla \times \mathbf{A} \right) - (\sigma + i\omega\varepsilon) (-\nabla V - i\omega \mathbf{A}) = 0 \quad (7)$$

This system must be completed with a gauge condition

$$\nabla \cdot \mathbf{A} + i\omega\xi\varepsilon\mu V = 0 \quad (8)$$

We introduced a parameter  $\xi$  that allows us to slide over different gauge conditions. Now let  $L$  be the 'natural' length scale of the problem that is considered. For example  $L = 1\mu\text{m}$ . Furthermore, let  $T$ , be the natural time scale. For example  $T = 10^{-9}$  sec. It is possible to reformulate the equations (6, 7) in *dimensionless* variables  $V$  and  $\mathbf{A}$  and the set of equations is controlled by two dimensionless variables,  $K$  and  $\nu$ .

$$\begin{aligned}\nabla \cdot [\varepsilon_r (\nabla V + i\omega \mathbf{A})] + \rho &= 0 \\ \nabla \cdot [(\sigma + i\omega\varepsilon_r) (\nabla V + i\omega \mathbf{A})] &= 0\end{aligned}\quad (9)$$

and

$$\begin{aligned}\nabla \times \left( \frac{1}{\mu_r} \nabla \times \mathbf{A} \right) - K\omega^2 (\varepsilon_r - i\nu) \mathbf{A} \\ - i\omega K (\varepsilon_r - i\nu) \nabla V = 0\end{aligned}\quad (10)$$

The constants  $K = \varepsilon_0\mu_0 L^2/T^2$  and  $\nu = \sigma T/\varepsilon_0$ . Note that for  $\sigma = 10^4$  S/m, we obtain  $K\nu = 10^{-5}$ . This number enters into the Maxwell-Ampere equation and suggests that in this scenario the magnetic sector is negligible. However, one can easily find cases with metallic conductances of  $10^7$  S/m, that magnetic effects are important.

### 3 Discretization

In our earlier work, we presented a discretization method that decided for each variable where on the grid it belongs. It was concluded that the geometrical and physical meaning of variables plays a key role. For instance, a scalar variable, e.g. the Poisson potential,  $V$ , is a number assigned to each space location and for computational purpose, it discretized value should be assigned to the nodes of the grid. On the other hand the vector potential  $\mathbf{A}$  is a vector variable of the same character as  $\nabla V$  and should therefore be assigned to the links of the computational grid. The conversion of continuous variables to discrete variables on the computation grid has also consequences for the particular discretization route that is followed when implementing discrete versions of the Maxwell equations. Gauss' law is discretized by considering the

elementary volumes around the nodes of the grid and next perform an integration of Gauss' law over the volume cell. The flux assigned to each segment of the enclosing surface is assumed to be constant which allows for expressing this (constant) flux in terms of the node variables and link variables. This scheme has been the key to the success of the simulation of the semiconductor devices. The Scharfetter-Gummel formulation of the discretized currents can be set up following above approach. Since links variables are essentially different from node variables, we expect that the discretization of the Maxwell-Ampere equation has to be done taking this geometrical aspect into account. Whereas it was quite 'natural' to regards node variables as a representative of some volume element, in the same way we consider a link variable representing some area element. Thus to each link is associated an area element and in order to discretize the Maxwell-Ampere equation on a grid we now apply Stokes' law to arrive at the discretized equations.

Once that we have found the way to discretize the Maxwell equations, we proceed with expanding then into a small signal analysis. This means that each variable is written as a time-independent part and an harmonic part.

$$X = X_0 + X_1 e^{i\omega t} \quad (11)$$

If we apply boundary conditions of a similar form and collect terms independent of  $\omega$  and terms proportional to  $e^{i\omega t}$  and omit terms proportional to  $X_1^2$  then we obtain a system of equations for the phasors  $X_1$ .

Of particular interest is the treatment of the spurious modes in the fields. These modes can be eliminated by selecting a 'gauge tree' in the mesh, adding a ghost field to the equation system or apply a projection method while iterating towards the solution. However, we can also apply a gauge condition and construct discrete operators that resemble a continuous operator as close as possible including having a semi-definite spectrum. Using a two-fold application of Stokes' law, the term  $\nabla \times \left( \frac{1}{\mu_r} \nabla \times \mathbf{A} \right)$  appears in the discretized formulation as a collection of closed-loop circulations. By subtracting a discretized version of  $\nabla (\nabla \cdot \mathbf{A})$  we arrive at a operator that resembles  $-\nabla^2 \mathbf{A}$ . However, since  $\mathbf{A}$  is a vector field, the latter can only have meaning in terms of the foregoing expressions. The discretization of the first term in (7) can be illustrated as shown in Fig. 1.

### 4 S-parameters

In order to determine the S matrix, a rather straightforward procedure is followed. For that

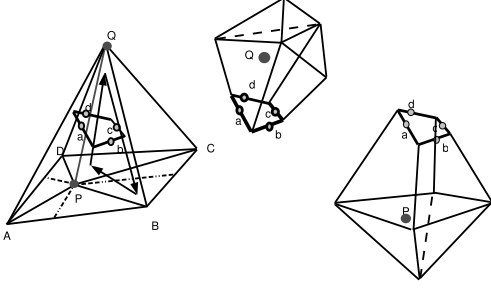


**Fig. 1.** Discretized version of the regularized curl-curl operator acting on a vector field.

purpose a collection of ports is needed and each port consists of two contacts. A contact is defined as a collection of nodes that are electrically identified. A rather evident appearance of a contact is a surface segment on the boundary of the simulation domain. A slightly less trivial contact consists of two or more of these surfaces on the boundary of the simulation domain. The nodes that are found on these surface are all having the same electrical potential. Therefore, although there may be many nodes assigned to a single contact, all these nodes together generate only one potential variable to the system of unknowns. Of course, when evaluating the current entering or leaving the contact, each node in the contact contributes to the total contact current. Assigning prescribed values for the contact potential can be seen as applying Dirichlet's boundary conditions to these contact. This is a familiar technique in technology CAD. Outside the contact regions, Neumann boundary conditions are applied. Unfortunately, since we are now dealing with the full system of Maxwell equations, providing boundary conditions for the scalar potential will not suffice. We also need to provide boundary conditions for the vector potential. Last but not least, since the the set of variable  $V$  and  $\mathbf{A}$  are not independent, setting a boundary condition for one variable has an impact on the others. Moreover, the choice of the gauge condition also participates in the appearance of the variables and their relations. A convenient set of boundary conditions is given by the following set of rules :

- contact surface:  $V = V|_c^i$ . To each contact area is assigned a prescribed potential value.
- outside the contact area on the simulation domain :  $\mathbf{D}_n = 0$ . There is no electric field component in the direction perpendicular to the surface of the simulation domain.
- For the complete surface of the simulation domain, we set  $\mathbf{B}_n = 0$ . There is no magnetic

induction perpendicular to the surface of the simulation domain.

We must next translate these boundary condition to restriction on  $\mathbf{A}$ . Let us start with the last one. Since there is no normal  $\mathbf{B}$ , we may assume that the vector potential has only a normal component on the surface of the simulation domain. That means that the links at the surface of the simulation domain do not generate a degree of freedom. It should be noted that more general options exist. Nevertheless, above set of boundary conditions provide the minimal extension of the TCAD boundary conditions if vector potentials are present.

In order to evaluate the scattering matrix, say of an N-port system, we iterate over all ports and put a voltage difference over one port and put an impedance load over all other ports. Thus the potential variables of the contacts belonging to all but one port, become degrees of freedom that need to be evaluated. The following variable are required to understand the scattering matrices, where  $Z_0$  is a real impedance that is usual taken to be 50 Ohms.

$$a_i = \frac{V_i + Z_0 I_i}{2\sqrt{Z_0}} \quad (12)$$

$$b_i = \frac{V_i - Z_0 I_i}{2\sqrt{Z_0}} \quad (13)$$

The variables  $a_i$  represent the voltage waves incident on the ports labeled with index  $i$  and the variables  $b_i$  represent the reflected voltages at ports  $i$ . The scattering parameters  $s_{ij}$  describe the relationship between the incident and reflected waves.

$$b_i = \sum_{j=1}^N s_{ij} a_j \quad (14)$$

The scattering matrix element  $s_{ij}$  can be found by putting a voltage signal on port  $i$  and place an impedance of  $Z_0$  over all other ports. Then  $a_j$  is zero by construction, since for those ports we have that  $V_j = -Z_0 I_j$ . Note that  $I_j$  is defined positive if the current is ingoing. In this configuration  $s_{ij} = b_i/a_j$ . In a simulation setup, we may put the input signal directly over the contacts that correspond to the input port. This would imply that the input load is equal to zero. The s-parameter evaluation set up is illustrated in Fig. 2.

## 5 Applications

Using the solver based on computational electrodynamics, we are able to compute the s-parameters

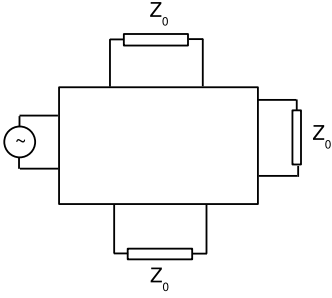


**Fig. 2.** Set up of the s-parameter evaluation: 1 port is excited and all others are floating.

by setting up a field simulation of the full structure. This allows us in detail to study the physical coupling mechanisms. As an illustration, we consider two inductors which are positioned on a substrate layer separated with a distance of 14 micron. This structure was processed and characterized and the s-parameters were obtained. It is quite convenient to study a compact model parameters to obtain a quick picture of the behaviour of the structure. For this device a convenient variable is the 'gain', which corresponds to the ratio of the injected injected power and the delivered power over an output impedance [5].

$$G = \frac{P_{in}}{P_{out}} \quad (15)$$

The structure is shown in Fig. 3 and a three-dimensional view using editEM (MAGWEL) is shown in Fig. 4.

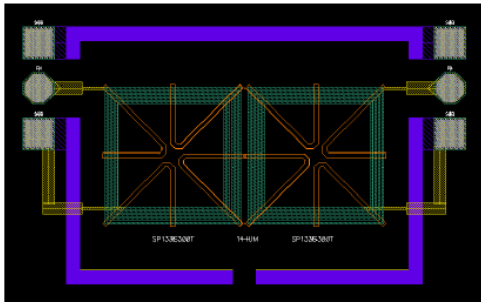


**Fig. 3.** View on the coupled spiral inductor using the Virtuosa design environment.

When computing the s-parameters, we put the signal source on one spiral (port 1) and place 50 Ohm impedance over the contacts of the second spiral (port 2). The  $s_{11}$ -parameter is shown in Fig. 5 and the  $s_{12}$ -parameter is shown in Fig. 6.

Finally, the gain plot is shown in Fig. 7. This results shown here have been obtained without any calibration of the material parameters. The silicon is treated 'as-is'. This means that the substrate and the eddy current suppressing n-wells are dealt with as doped silicon.

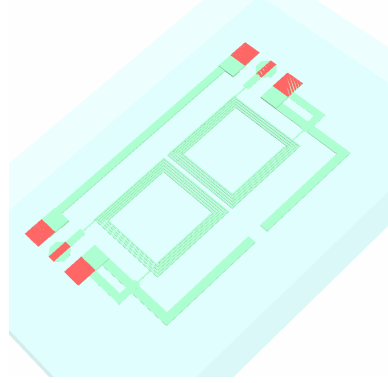


**Fig. 4.** View on the coupled spiral inductor using the MAGWEL structure editor editEM.

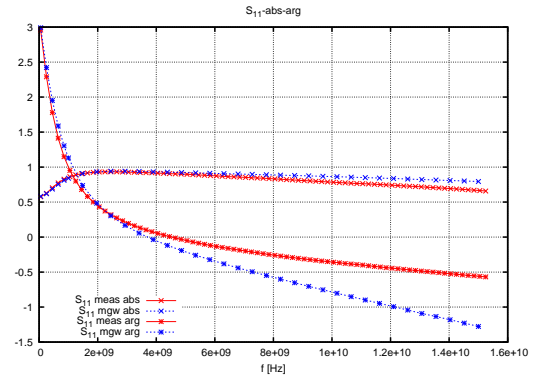


**Fig. 5.** Comparison of the experiment and simulation results for  $s_{11}$ .

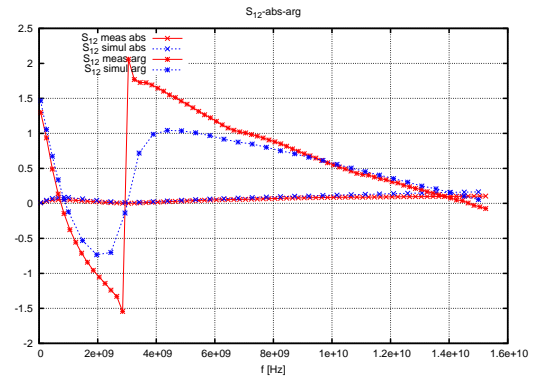


**Fig. 6.** Comparison of the experiment and simulation results for  $s_{12}$ .

## 6 conclusions

In this paper we presented a version of computational electrodynamics which is based on the scalar and vector potential formulation. Whereas the finite-integration technique deals directly with the field intensity quantities  $\mathbf{E}$  and  $\mathbf{B}$ , our formulation deals with the more fundamental gauge fields. It should be emphasized that the field quantities are derived variables and one that the potentials have been computed, all other variables are obtained by 'post-processing'. Our approach

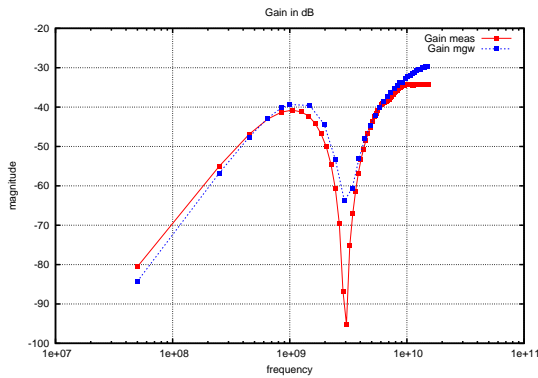


**Fig. 7.** Comparison of the experimental and simulation results for the gain.

is a discrete implementation of the geometrical interpretation of electrodynamics [6]. According to this interpretation, the field intensities correspond to the curvature and the potentials are connections in the geometrical sense. The practical capabilities of our method are comparable to other field solvers that focus directly on the fields  $\mathbf{E}$  and  $\mathbf{B}$ , with one exception: if the potential are needed in the evaluation of the constitutive relations then our method has a clear advantage. This happens if the true semiconductor modeling is needed and one can not mimic the semiconductor with moderately conductive material. Another area of application is the unified solving of quantum problems and magnetic induction problems. Our approach will be an excellent starting points. We have shown with a realistic application that the method is capable of producing fairly good results. The deviations at higher frequency are an indication that adaptive meshing methods are mandatory.

*Acknowledgement.* This work was performed in the EU funded projects CODESTAR and CHAMELEON-RF. The authors the numerous stimulating discussions with the partners in this project.

## References

1. P. Meuris, W. Schoenmaker and W. Magnus Strategy in electromagnetic interconnect modeling. *IEEE Trans. on CAD of Integr. Syst.*, 20:739-752, 2001
2. W. Schoenmaker, Peter Meuris "Electromagnetic Interconnects and Passives Modeling: Software Implementation Issues Software Implementation Issues. *IEEE Trans. on CAD of Integr. Syst.*, 21:534-543, 2002
3. W. Schoenmaker, W. Magnus and P. Meuris Ghost Fields in Classical Gauge Theories *Phys. Rev. Lett.*, 21:181602-1 - 181602-4, 2002
4. J.F. Lee, D.K. Sun and Z.J. Cendes. Tangential vector finite elements for electromagnetic field

computation. *IEEE Transactions on Magnetics*, 27:4032-4035, 1991

5. A. M. Niknejad and R. G. Meyer Analysis, Design and Optimization of Spiral Inductors and Transformers for Si RF ICs. *IEEE Journ. of Solid-State Circuits*, 33:1470-1481, 1998.
6. T. Frankels. *The Geometry of Physics* Cambridge University Press, Cambridge, UK, 1997



# Simulations of a electron-phonon hydrodynamical model based on the maximum entropy principle

V. Romano<sup>1</sup> and C. Scordia<sup>2</sup>

<sup>1</sup> Department of Mathematics and Computer Science, University of Catania, Italy [romano@dmi.unict.it](mailto:romano@dmi.unict.it),

<sup>2</sup> University of Wuppertal [scordia@dmi.unict.it](mailto:scordia@dmi.unict.it)

**Summary.** Recently a hydrodynamical and energy-transport models have been formulated based on the maximum entropy principle for the coupled phonon-electron system in silicon in order to cope with the effects of heating of the crystal lattice. Here the simulations of some standard devices are presented in order to asses the validity of the model.

## 1 Introduction

At macroscopic level, several heuristic models for the thermal effects in the crystal lattice have been proposed. They are represented by the crystal lattice energy balance equation and differ for the proposed form of thermal conductivity and energy production, e.g. [1–5]. A critical review can be also found in [6].

Recently, a consistent hydrodynamical model for charge carriers has been developed starting from the moment system associated with the transport equations, obtaining the closure relations with the maximum entropy principle (hereafter MEP) [7–11]. The same approach has been adopted in [12] for the electron-phonon system, obtaining also an energy-transport and a drift-diffusion model under appropriate scalings.

The electrons are described with the 8-moment system as in [7–9]. The phonons are considered as two populations: acoustic and non polar optical. The non-polar optical phonons are described with a Bose-Einstein distribution while the acoustic ones are described by the MEP distribution function in the 9-moment approximation already introduced in [13].

The simulations of some benchmark devices are presented and compared with those obtained with the standard models existing in the literature. The numerical discretization has been performed along the guide lines reported in [14, 15].

## 2 The model

The kinetic description of the electron-phonon system is based on the Boltzmann equations for

electrons distribution  $f$  and phonons distributions, both acoustic and non-polar optical,  $g^{(ac)}$ ,  $g^{(no)}$ , coupled to the Poisson electron for the electric potential

$$\frac{\partial f}{\partial t} + v^i(\mathbf{k}) \frac{\partial f}{\partial x^i} - \frac{eE^i}{\hbar} \frac{\partial f}{\partial k^i} = \mathcal{C}[f, g^{(ac)}, g^{(no)}], \quad (1)$$

$$\frac{\partial g^{(ac)}}{\partial t} + \frac{\partial \omega^{(ac)}}{\partial q^i} \frac{\partial g^{(ac)}}{\partial x^i} = S^{(ac)}[g^{(ac)}, g^{(no)}, f], \quad (2)$$

$$\frac{\partial g^{(no)}}{\partial t} = S^{(no)}[g^{(ac)}, g^{(no)}, f], \quad (3)$$

$$E_i = -\frac{\partial \phi}{\partial x_i}, \quad \epsilon \Delta \phi = -e(N_D - N_A - n). \quad (4)$$

$\mathbf{k}$  and  $\mathbf{q}$  are the wave vectors of electrons and phonons respectively.  $\mathbf{E}$  is the electric field and  $e$  the elementary charge. The non polar optical phonons are assumed to be described by the Bose-Einstein distribution.

The direct solution of the system (1)-(4) is a daunting computational task and requires long CPU times, not yet suitable for CAD purposes.

By considering the 8-moment model for electron and the 9-moment model for phonons of the previous sections, the following complete set of macroscopic balance equations is obtained

$$\frac{\partial n}{\partial t} + \frac{\partial (nV^i)}{\partial x^i} = 0, \quad (5)$$

$$\frac{\partial (nP^i)}{\partial t} + \frac{\partial (nU^{ij})}{\partial x^i} + neE^i = nC_p^i, \quad (6)$$

$$\frac{\partial (nW)}{\partial t} + \frac{\partial (nS^j)}{\partial x^i} + neV_k E^k = nC_W, \quad (7)$$

$$\frac{\partial (nS^i)}{\partial t} + \frac{\partial (nF^{ij})}{\partial x^i} + neE_j G^{ij} = nC_W^i, \quad (8)$$

$$\frac{\partial u}{\partial t} + Q_k = P_u, \quad (9)$$

$$\frac{\partial p_i}{\partial t} + \frac{1}{3} \frac{\partial u}{\partial x_i} + \frac{\partial N_{(jk)}}{\partial x_k} = P_i, \quad (10)$$

$$\frac{\partial N_{(ij)}}{\partial t} + \frac{\partial M_{(ij)k}}{\partial x_k} = P_{(ij)}. \quad (11)$$

$n$ ,  $P^i$ ,  $W$  and  $S^i$  are the electron density, average crystal momentum and average energy-flux while  $u$ ,  $p_i$  and  $N_{(ij)}$  are the phonon energy, average momentum and deviatoric part of the average flux of momentum.

In (9)-(11) each term is given by the sum of the contribution of the acoustic and the non-polar optical phonons.

Since the number of unknowns exceeds the number of equations, closure relations must be introduced. The maximum entropy principle (hereafter MEP) gives a systematic way for obtaining constitutive relations on the basis of information theory. It has been used in [12] to close the previous electron-phonon system as in [7-9].

All the coefficients depend on the electron energy  $W$  and crystal temperature  $T_L$ . Their analytical expressions are explicitly given and related to the scattering parameters (see [12] for more details).

In particular the energy phonon production terms can be written as

$$P_u = -nC_W, \quad (12)$$

that is the opposite of the electron production.

In Fig. 1 we plot the energy relaxation time defined as  $\tau_W = -\frac{W - \frac{3}{2}k_B T_L}{nC_W^{(e)}}$  versus the electron energy, for different values of the crystal temperature from 300° K to 330° K.

Under an appropriate scaling the following crystal energy balance equation is derived

$$\rho c_V \frac{\partial T_L}{\partial t} - \text{div} [k(T_L) \nabla T_L] = H, \quad (13)$$

where  $\rho$  is the silicon density,  $k(T_L)$  the thermal conductivity,

$$H = -nC_W + c^2 \text{div} \left( \tau_R n c_{11}^{(p)} \mathbf{V} + \tau_R n c_{12}^{(p)} \mathbf{S} \right) \quad (14)$$

with  $n c_{ij}^{(p)}$  related to the phonon production terms.

Equation 13 generalizes the models proposed in [1-5].

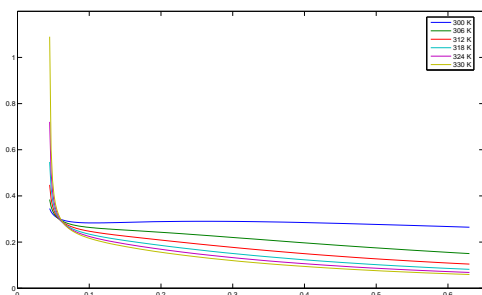


**Fig. 1.** energy relaxation time versus the electron energy, for different values of the crystal temperature from 300° K to 330° K

*Acknowledgement.* The authors acknowledge the financial support by the EU Marie Curie RTN project

**COMSON** grant n. MRTN-CT-2005-019417. V.R. acknowledges also the contribution by M.I.U.R. (PRIN 2007 *Equazioni cinetiche e idrodinamiche di sistemi collisionali complessi*), the P.R.A. University of Catania (ex 60 %).

## References

1. S. P. Gaur and D. H. Navon, *Two-dimensional carrier flow in a transistor structure under non-isothermal conditions*, IEEE trans. Electron. Devices, **ED-23** 50-57, 1976.
2. D. K. Sharma and K. V. Ramanathan, *Modeling thermal effects on MOS I-V characteristics*, IEEE Electron. Device Lett., **EDL-4**, 362-364, 1983.
3. M. S. Adler, *Accurate calculations of the forward drop and power dissipation in thyristors*, IEEE Trans. Electron. Devices, **ED-25**, 16-22, 1979.
4. A. Chrysosafis and W. Love, *A computer-aided analysis of one dimensional thermal transient in n-p-n power transistors*, Solid-State-Electron., **22**, 249-256, 1978.
5. G. Wachuka, *Rigorous thermodynamic treatment of heat generation and conduction in semiconductor device modeling*, IEEE Trans. on Computer-Aided Design, **9** 1141-1149 (1990).
6. S. Selberherr, *Analysis and simulation of semiconductor devices*, Wien - New York, Springer-Verlag, 1984.
7. A.M. Anile, V. Romano, *Non parabolic band transport in semiconductors: closure of the moment equations*, Continuum Mech. Thermodyn., 1999, 11: 307-325
8. V. Romano, *Non parabolic band transport in semiconductors: closure of the production terms in the moment equations*, Continuum Mech. Thermodyn., 2000, 12: 31-51
9. V. Romano, *Non parabolic band hydrodynamical model of silicon semiconductors and simulation of electron devices*, Mathematical Methods in the Applied Sciences **24** 439 (2001).
10. E. T. Jaynes, *Information theory and statistical mechanics*, Physical Review, Vol. 106, Nr. 4, 620 (1957).
11. N. Wu, *The maximum entropy method*, Springer-Verlag Berlin Heidelberg, 1997
12. V. Romano and M. Zwierz, *Electron-phonon hydrodynamical model for semiconductors*, preprint (2008).
13. W. Dreyer, H. Struchtrup, *Heat pulse experiment revisited*, Continuum Mech. Thermodyn., 1993, 5: 3-50
14. V. Romano, *2D simulation of a silicon MES-FET with a non-parabolic hydrodynamical model based on the maximum entropy principle*, Journal of Computational Physics 176 70 (2002).
15. V. Romano, *2D numerical simulation of the MEP energy-transport model with a finite difference scheme*, J. Comp. Physics 221 439-468 (2007).

# Thermal Effects in Coupled Circuit-Device Simulations

Markus Brunk<sup>1</sup> and Ansgar Jüngel<sup>2</sup>

<sup>1</sup> Norwegian University of Science and Technology, Department of Mathematical Sciences, 7491 Trondheim, Norway; markus.brunk@math.ntnu.no,

<sup>2</sup> Vienna University of Technology, Institute for Analysis and Scientific Computing, Wiedner Hauptstr. 8-10, 1040 Wien, Austria; juengel@anum.tuwien.ac.at

**Summary.** A coupled semiconductor-circuit model including thermal effects is proposed. The semiconductor device is modeled by the energy-transport equations, and the electric circuit is described by the network equations from modified nodal analysis. The resulting system of nonlinear partial differential-algebraic equations is solved by mixed finite elements in space and the BDF2 method in time. Numerical results for a rectifying circuit and a high-pass filter including a laser diode are presented.

## 1 Introduction

In industrial application, complex semiconductor device models are usually substituted by circuits of basic network elements resulting in simpler compact models. Such a strategy was advantageous up to now since integrated circuit simulations were possible without computationally expensive device simulations. Parasitic effects and high frequencies in the circuits, however, require one to take into account a very large number of basic elements and to adjust carefully a large number of parameters in order to achieve the required accuracy. Moreover, device heating cannot be easily modeled by this approach. Therefore, it is preferable to model those semiconductor devices which are critical for the parasitic effects by semiconductor transport equations.

We include the device model into the network equations directly and employ the energy-transport equations to model the electron temperature. A coupled model including the lattice temperature is work in preparation. As the device model is described by partial differential equations, and the network equations are given by differential-algebraic equations, this results in a *coupled system of nonlinear partial differential-algebraic equations*.

The (scaled) energy-transport equations consist of conservation laws for the electron density  $n$  and electron energy density  $w$ ,

$$n_t - \operatorname{div} J_n = -R(n, p),$$

$$w_t - \operatorname{div} J_w = -J_n \cdot \nabla V + W(n, T) - \frac{3}{2}TR(n, p),$$

with constitutive relations for the particle current density  $J_n$  and the energy current density  $J_w$ , derived from the semiconductor Boltzmann equation:

$$J_n = \mu_n \left( \nabla n - \frac{n}{T} \nabla V \right),$$

$$J_w = \frac{3}{2} \mu_n (\nabla(nT) - n \nabla V),$$

where  $R(n, p)$  denotes the generation-recombination term,  $p$  is the hole density, which is computed from the drift-diffusion equations,  $W(n, T)$  is the relaxation-time term, and  $\mu_n$  the (scaled) electron mobility [3]. The equations are coupled to the Poisson equation for the electric potential  $V$ :

$$\lambda^2 \Delta V = n - p - C(x),$$

where  $\lambda$  is the scaled Debye length and  $C(x)$  the doping concentration. The equations are supplemented by initial conditions for  $n$  and  $w$  and appropriate boundary conditions (see [1, 2] for details).

## 2 Numerical approximation

The energy-transport model is discretized in one space dimension by mixed-hybrid finite elements of Marini-Pietra type. These elements instead of standard Raviart-Thomas elements are employed since this guarantees the M-matrix property of the global stiffness matrix, even in the presence of zeroth-order terms.

The network equations as well as the parabolic equations are discretized in time by the 2-stage backward difference formula (BDF2) since this scheme allows one to maintain the M-matrix property. Then the semidiscretized equations are approximated by the mixed finite-element method, and static condensation is applied to reduce the number of variables. The final nonlinear discrete system is solved by Newton's method.

For a large applied bias, we observe strong gradients of the temperature at the boundary. Employing Robin boundary conditions for the

electron density and energy density instead of standard Dirichlet conditions help to avoid the boundary layer [1].

### 3 Numerical results

First, we consider a rectifying circuit containing four  $pn$  diodes (see Figure 1). Each of the diodes have the length  $0.1 \mu\text{m}$  and a maximal doping of  $10^{22} \text{m}^{-3}$ . The voltage source is given by  $v(t) = U_0 \sin(2\pi\omega)$  with  $U_0 = 5 \text{V}$  and  $\omega = 10 \text{GHz}$ .

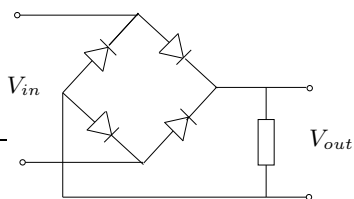


Fig. 1. Rectifier circuit.

The current through one of the diodes is presented in Figure 2. The figure clearly shows the rectifying behavior of the circuit. The largest current is obtained from the drift-diffusion (DD) model since we have assumed a constant electron mobility such that the drift is unbounded with respect to the modulus of the electric field. The stationary energy-transport (ET) model is not able to catch the capacitive effect at the junction.

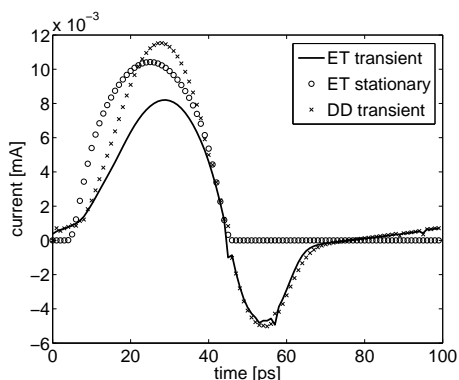


Fig. 2. Current through a  $0.1 \mu\text{m}$  diode in a  $10 \text{GHz}$  circuit.

Second, we consider a laser and photo diode as part of a small circuit (see Figure 3). The laser diode is biased with a digital input signal with bias  $3 \text{V}$  and frequency  $5 \text{GHz}$ . The photo diode receives the transmitted signal and is coupled to a high-pass filter only passing frequencies larger than the cutoff frequency. The filter consists of

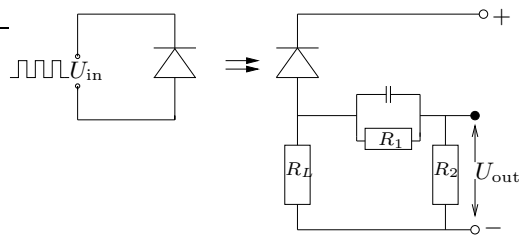


Fig. 3. Photo diode with a high-pass filter.

the photo diode, a capacitor, and three resistors. The photo diode is reversely biased with  $0.2 \text{V}$ .

The output of the high-pass filter is shown in Figure 4 for stationary and transient device simulations. The results for the high-pass output voltage differ significantly as the frequency is too large to be resolved by the stationary model.

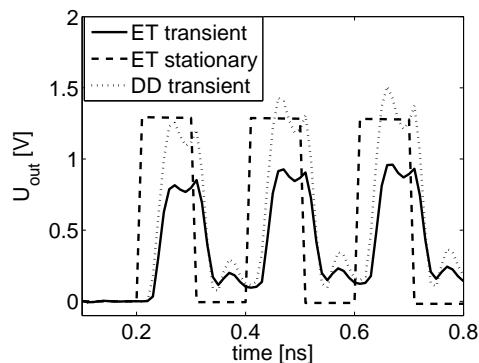


Fig. 4. Output of the high-pass filter for a  $5 \text{GHz}$  digital input signal with bias  $3 \text{V}$ .

*Acknowledgement.* The authors acknowledge partial support from the German Federal Ministry of Education and Research (BMBF), grant 03JUNAVN, and from the FWF Wissenschaftskolleg “Differential equations”.

### References

1. M. Brunk and A. Jüngel. Numerical coupling of electric circuit equations and energy-transport models for semiconductors. *SIAM J. Sci. Comput.* 30 (2008), 873-894.
2. M. Brunk and A. Jüngel. Simulation of thermal effects in optoelectronic devices using coupled energy-transport and circuit models. To appear in *Math. Models Meth. Appl. Sci.*, 2008.
3. A. Jüngel. *Quasi-hydrodynamic Semiconductor Equations*. Birkhäuser, Basel, 2001.

# Automatic Thermal Network Extraction and Multiscale Electro-Thermal Simulation

Massimiliano Culpo<sup>1</sup>, Carlo de Falco<sup>2</sup>, Georg Denk<sup>3</sup>, and Steffen Voigtmann<sup>3</sup>

<sup>1</sup> Bergische Universität Wuppertal [culpo@math.uni-wuppertal.de](mailto:culpo@math.uni-wuppertal.de),

<sup>2</sup> Dublin City University [carlo.defalco@dcu.ie](mailto:carlo.defalco@dcu.ie)

<sup>3</sup> Qimonda AG Munich [georg.denk@qimonda.com](mailto:georg.denk@qimonda.com), [steffen.voigtmann@qimonda.com](mailto:steffen.voigtmann@qimonda.com)

**Summary.** A strategy to perform coupled electro-thermal simulations is presented. The electrical behaviour of each circuit element is modeled by standard compact models with an added temperature node. Mutual heating is accounted for by a 2-D or 3-D diffusion reaction PDE which is coupled to the electrical network by enforcing instantaneous energy conservation. A suitable spatial discretization scheme is adopted which allows efficient meshing of large domains with details at a much smaller scale.

## 1 Introduction

In this communication, we present a tool to automatically extract a thermal network model for a CHIP level electro-thermal simulation. Starting from layout geometry and CHIP material data, it produces an  $n$ -port thermal device model, possibly non-linear, that can be coupled to the electrical circuit network via an extra temperature node in the electrical device compact models. Compared to other similar tools [2, 3], our tool does not work by fitting the parameters of a given network of 0D thermal resistors and capacitors but rather it produces a full 2D or 3D discretization of the heat equation on the whole CHIP and transforms it into a form which is amenable for coupling to a standard circuit simulator. If the material properties are assumed to be independent from the temperature, the resulting model is linear and the number of state variables may be reduced by means of standard Model Order Reduction techniques.

## 2 Electro-Thermal Network Model

Below we briefly outline how the model for the thermal network is computed and how it is coupled to the rest of the system. We will refer to the case of transient simulation, but the model we produce can be used in DC, AC and Harmonic Balance simulations as well. The global system of equation describing our circuit is constructed following the well known MNA approach:

$$\sum_{i=1}^{N_{el}} (J_{ik} (R_i^e \mathbf{e}, R_i^\theta \boldsymbol{\theta}, \mathbf{r}_i) + A_{ik}^E \dot{\mathbf{r}}_i) = 0 \quad (1a)$$

$$f_{il} (R_i^e \mathbf{e}, R_i^\theta \boldsymbol{\theta}, \mathbf{r}_i) + A_{il}^I \dot{\mathbf{r}}_i = 0 \quad (1b)$$

where in (1a)  $k = 1, \dots, N_{nodes}$  while in (1b)  $i = 1, \dots, N_{el}$ ;  $l = 1, \dots, N_{intvar}(i)$ . Here the number of elements and nodes in the circuit are denoted with  $N_{el}$  and  $N_{nodes}$ , respectively, while the number of internal variables describing the  $i$ -th element of the network will be  $N_{intvar}(i)$ ,  $\mathbf{e}(t)$  represents the set of unknown voltages,  $\boldsymbol{\theta}(t)$  the set of unknown temperatures,  $\mathbf{r}_i(t)$  the  $i$ -th element internal variables. Furthermore  $R_i^e$  and  $R_i^\theta$  are the electrical and thermal incidence matrix associated with element  $i$ , respectively, and  $A_{ik}^E$  and  $A_{il}^I$  are the coefficients of the differential term. The solution of (1) requires, at each time step, the resolution of a system of non-linear algebraic equations which is usually solved via Newton iterations. At each step of the Newton method the full jacobian matrix and the residual of the complete system are built assembling together the element matrices  $J_{ik, R_i^e \mathbf{e}}$ ,  $J_{ik, R_i^\theta \boldsymbol{\theta}}$ ,  $f_{il, R_i^e \mathbf{e}}$ ,  $f_{il, R_i^\theta \boldsymbol{\theta}}$ ,  $A_{ik}^E$  and  $A_{il}^I$  and the element residuals  $J_{ik}$ ,  $f_{il}$ . For electrical devices the latter represent essentially the currents and charges at the device contacts and the former the conductance and inductance and capacitance matrices. For the  $n$ -port thermal element, the local residual and matrices represent the net joule power in each device and its derivative with respect to each device temperature. The following sections describe how these quantities are computed.

### 2.1 Thermal network model

For sake of simplicity in this section we assume the distributed thermal network to be the element numbered as 1 in the circuit netlist. Let  $\Omega$  be the whole CHIP domain,  $\Omega_q$  the  $q$ -th active region on  $\Omega$ ,  $p_q$  the Joule power per unit Area on  $\Omega_q$  and  $\theta_k$  the temperature at the  $k$ -th external pin. Denote with  $J_{1k}$  the power flux entering the device from node  $k$  and with  $T(x, t)$  the temperature at a

point  $x \in \Omega$  at the time point  $t$ . If  $\Omega_q$  is connected to pin  $k$ :

$$J_{1k} = \int_{\Omega_q} p_q d\Omega_q = p_q |\Omega_q|$$

while, at the external boundary:

$$J_{1k} = \int_{\partial\Omega} \frac{T - \theta_k}{R} d\gamma$$

where  $R$  is the CHIP to ambient thermal resistance. The above equations must be complemented by constitutive relations of the form:

$$f_{1q} = \theta_k - \frac{1}{|\Omega_q|} \int_{\Omega_q} T(x, t) d\Omega_q = 0$$

for each active region  $\Omega_q$ , assuming  $\theta_k$  to be the temperature node connected to  $\Omega_q$  in the netlist. The temperature  $T$  is the solution of the following PDE boundary value problem:

$$\begin{aligned} c_v \dot{T} + \operatorname{div}(-\kappa(T) \nabla T) - r &= 0 \text{ in } \Omega \\ -\kappa(T) \frac{\partial T}{\partial n} &= \frac{T - \theta_{\text{ext}}}{R} \text{ on } \partial\Omega \end{aligned} \quad (2)$$

where  $r = p_q$  in  $\Omega_q$  and zero otherwise,  $\theta_{\text{ext}}$  is the temperature of the pin attached to the external boundary of  $\Omega$ .

## 2.2 Space discretization

The method of Patches of Finite Elements (PFE) [1] allows us to discretize the heat equation (2) on a set of unstructured triangulations  $\mathcal{T}_{hq}$  each covering the subdomain  $\Omega_q$  that are allowed to communicate with each other via a coarser triangulation  $\mathcal{T}_H$  covering the whole CHIP domain  $\Omega$ . By allowing  $\mathcal{T}_{hq}$  to completely overlap with  $\mathcal{T}_H$  this method allows to simulate characteristics of equation (2) that appear at completely different scales (CHIP scale/device scale) without imposing too many requirements on meshing software as the coarse mesh step  $H$  and the finer mesh step  $h$  can be completely unrelated.

Briefly the PFE method can be described as follows. Let  $V_{hq}$  be the standard piecewise linear conforming finite element function space on the triangulation  $\mathcal{T}_{hq}$  and  $V_H$  the space of piecewise linear conforming finite element functions defined on  $\mathcal{T}_H$ . The PFE discretization reads:

find  $T_{Hh} \in V_{Hh}$  such that

$$a(T_{Hh}, v_{Hh}) = (f, v_{Hh}) \quad \forall v_{Hh} \in V_{Hh}$$

with

$$V_{Hh} \equiv \left( V_H + \sum_q V_{hq} \right)$$

where  $a(\cdot, \cdot)$  is the bilinear form representing the weak form of the differential operator in (2),  $(\cdot, \cdot)$  is a scalar product in  $V_{Hh}$  and the known function  $f$  accounts for the source term  $r$  as well as for the boundary fluxes and the terms containing  $T$  evaluated at previous times. Notice that the sum above is not a direct sum, therefore forming a basis of  $V_{Hh}$  requires some extra care.

## 3 Workflow for Electro-thermal Simulation

Below we summarize the expected workflow using the tool we presented for a coupled electro-thermal simulation:

- In designing the IC the thermally active regions are defined by adding an extra mask layer to the layout
- A 2D or 3D mesh of the IC layout is formed automatically
- A passive thermal element is attached to the temperature nodes of the circuit elements, ambient temperature is set via additional temperature sources
- The full system can be simulated by a standard circuit simulator, producing as extra output the average temperature in each device as well as the full multidimensional temperature field in the IC

## 4 Acknowledgments

The first author was supported by the European Commission in the framework of the CoMSON RTN project. The second author was supported by the Mathematics Applications Consortium for Science and Industry in Ireland (MACSI) under the Science Foundation Ireland (SFI) mathematics initiative.

## References

1. Roland Glowinski, Jiwen He, Jacques Rappaz, and Joël Wagner. Approximation of multi-scale elliptic problems using patches of finite elements. *C. R. Math. Acad. Sci. Paris*, 337(10):679–684, 2003.
2. P.M. Iqic, P.A. Mawby, M.S. Towers, and S. Batcup. Dynamic electro-thermal physically based compact models of the power devices for device and circuit simulations. *Semiconductor Thermal Measurement and Management, 2001. Seventeenth Annual IEEE Symposium*, pages 35–42, 2001.
3. V. Szekeley, A. Poppe, A. Pahi, A. Csendes, G. Hajas, and M. Rencz. Electro-thermal and logi-thermal simulation of vlsi designs. *VLSI Systems, IEEE Transactions on*, 5(3):258–269, Sep 1997.

# Canonical Stochastic Electromagnetic Fields

B.L. Michielsen

ONERA, 2 avenue Édouard Belin, Toulouse, France [Bastiaan.Michielsen@onera.fr](mailto:Bastiaan.Michielsen@onera.fr)

**Summary.** The interaction between electromagnetic fields and material systems is often subject to uncontrolled fluctuations. As an alternative to trying to model this by choosing a number of “representative” cases, we propose methods to directly compute statistics from a stochastic field model. An important statistic is the standard deviation which depends on the covariance operator of the stochastic field. In this paper, we show the existence of stochastic fields such that the covariance operator is natural in a sense made precise below.

## 1 Introduction

In this paper, we are concerned with the problem of uncertainty in the modelling of the interaction between electromagnetic fields and systems. From the physical point of view this interaction is represented for by “observables” on an incident electromagnetic field. If the incident field is not exactly controlled, deterministic models are not the most appropriate. In particular, if we limit our simulations to some interaction configurations, which we think “representative,” we can easily miss the effects of resonant coupling for particular incidences. A more comprehensive way to handle uncertainty is to model the interaction problem as a problem to statistically characterise observables on stochastic fields.

In order to allow for an immediate interpretation of our considerations, we briefly present the particular case of the Thévenin model for a linear multi-port system

$$V = \mathcal{V} + Z * I$$

où  $V, I, \mathcal{V} \in C(\mathbb{R}, \mathbb{R}^n)$  are  $\mathbb{R}^n$ -valued functions of time representing the port-voltages, the port-currents and the open-port voltages, or Thévenin sources, respectively. The Thévenin sources are defined through distributions on the fields (integral representations). For example,  $\mathcal{V} = \langle J_P, E \rangle = \int_P E$ , where  $P$  is a curve defining a port. Now, we are interested in the time covariance of such observable functions of time. Supposing that the average field is zero, we get in the general case ( $\overline{X}$  is the time reversal of  $X$ ),

$$\mathbb{E}(V(t_1)V(t_2)) = \mathbb{E}(\langle \overline{J_{P,t_1}}, E \rangle \langle \overline{J_{P,t_2}}, E \rangle)$$

Introducing  $C_E$ , the covariance operator of the stochastic field  $E$ , we get

$$\mathbb{E}(V(t_1)V(t_2)) = \langle \overline{J_{P,t_1}}, C_E(\overline{J_{P,t_2}}) \rangle$$

This expression motivates the search for covariance operators of stochastic fields. However, in this paper we consider the inverse problem of finding a field such that the covariance operator is a known and “natural” operator. This is a development analogous to a time-harmonic analysis presented before (see [1]).

## 2 Basic field theory

The heart of our reasoning consists of a pair of integral relations between causal and anti-causal solutions of the Maxwell equations

$$\begin{aligned} dH - \varepsilon_0 \partial_t * E &= *J \\ dE + \mu_0 \partial_t * H &= 0 \end{aligned}$$

We can derive integral relations between two different electromagnetic states, i.e., solutions of Maxwell’s partial differential equations, by means of Stokes’ theorem on a cylindrical domain  $D \times T \subset \mathbb{R}^3 \times \mathbb{R}$ .

$$\begin{aligned} \int_{D \times \{t_1\}} (\mu_0 H^a \wedge *H^b + \varepsilon_0 E^a \wedge *E^b) \\ = - \int_{D \times T} (E^a \wedge *J^b + E^b \wedge *J^a) \end{aligned} \quad (1)$$

where we used the vanishing of the integral over  $\partial D \times T$  for large enough  $D$ . Observe that when one of the two states is in fact an anti-causal state, say  $\overline{J^c}, \overline{E^c}, \overline{H^c}$  (we use the over-line to indicate time-reversal), the domain of integration can be chosen such that also the contribution of the  $D \times \partial T$  integrals vanish (see Fig. 1). This leads to

$$0 = \int_{D \times T} (E^a \wedge *\overline{J^c} + \overline{E^c} \wedge *J^a) \quad (2)$$

If we choose the time interval  $T = (t_0, t_1)$  such that  $\text{supp}(J^a)$  does not intersect  $D \times T$ , we get a third integral relation

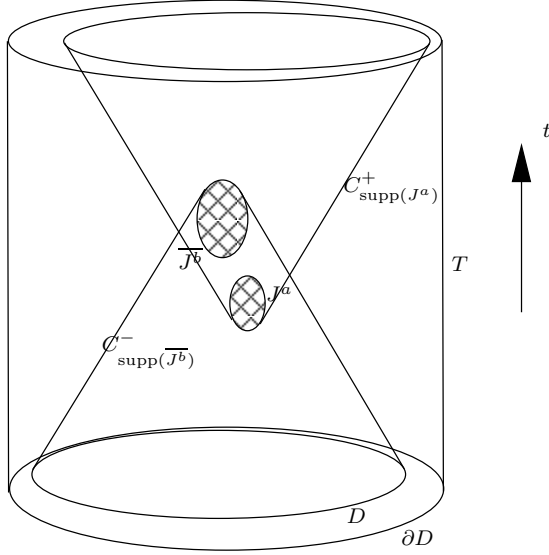


**Fig. 1.** Illustration of a causal and an anti-causal light cone bundle

$$\int_{D \times \{t_0\}} (\mu_0 H^a \wedge * \overline{H^c} + \varepsilon_0 E^a \wedge * \overline{E^c}) = - \int_{D \times T} E^a \wedge * \overline{J^c} \quad (3)$$

Making the substitutions  $J^c = \overline{J^b}$  (and thus  $\overline{J^c} = J^b$ ) and  $\overline{E^c} = \overline{E(\overline{J^b})} = E^{ac}(J^b)$  (the anti-causal solution for a given  $J^b$ ) we get for (3)

$$\int_{D \times \{t_0\}} (\mu_0 H^a \wedge * H^{ac}(J^b) + \varepsilon_0 E^a \wedge * E^{ac}(J^b)) = - \int_{D \times T} E^a \wedge * J^b \quad (4)$$

whereas adding (2), with the same substitutions, to (1) gives

$$\int_{D \times \{t_1\}} (\mu_0 H^a \wedge * H^b + \varepsilon_0 E^a \wedge * E^b) = - \int_{D \times T} C(J^b) \wedge * J^a \quad (5)$$

where  $C(J) = E(J) - E^{ac}(J)$  is the electric field propagator anti-symmetrised with respect to time reversal, i.e.,

$$\overline{C(J)} = -C(\overline{J})$$

This operator  $C$  can be shown to define a natural energy emission correlation operator.

### 3 Observables on canonical stochastic time-domain fields

We shall now consider the general problem of two observables,  $A$  and  $B$ , defined by electric current distributions,  $J^a$  and  $J^b$  respectively. We

consider the values of these observables on a stochastic electromagnetic field. The covariance of the stochastic values of these observables is then given by

$$\mathbb{E}(AB) = \langle \overline{J^a}, C_E(\overline{J^b}) \rangle$$

Comparing this with (5), leads to the idea to define a stochastic field such that its covariance operator be proportional to the emission correlation operator.

In order to achieve that, we define a direct sum Hilbert space  $\mathcal{H}$ , with scalar product

$$\langle \psi^a, \psi^b \rangle_{\mathcal{H}} = \int_{\mathbb{R}^3} (\varepsilon_0 E^a \wedge * E^b + \mu_0 H^a \wedge * H^b)$$

where  $E$  and  $H$  are the two components of  $\psi \in \mathcal{H}$ . On this space a probability measure exists of which the covariance operator is proportional to the metric. That means that a stochastic distribution exists  $\psi = (e_0, h_0)$  such that

$$\forall f, g \in \mathcal{H} \quad \mathbb{E}(\langle \psi, f \rangle \langle \psi, g \rangle) = \sigma^2 \langle f, g \rangle_{\mathcal{H}}$$

Now, using (4) we derive (explaining the details exceeds the limits of this summary),

$$\int_{D \times T} C_{E_0}(\overline{J^a}) \wedge * \overline{J^b} = \sigma^2 \int_{D \times T} C(\overline{J^a}) \wedge * \overline{J^b} \quad (6)$$

where  $E_0$  is the electric field corresponding to the stochastic distribution on  $D \times \{t_0\}$ . Because the two distributions  $J^a$  and  $J^b$  can be chosen arbitrarily, we obtain

$$C_{E_0} = \sigma^2 C$$

So,  $\sigma^2 C$  is the electric field covariance operator of  $(E_0, H_0)$  the Maxwellian field with initial values  $(e_0, h_0)$  (the stochastic distribution defined by the specific probability measure on  $\mathcal{H}$ ).

### 4 Conclusion

In this proposal, we have outlined the electromagnetic theory for the definition of a canonical stochastic electromagnetic field with a known covariance operator. In the final paper, we shall give the mathematical details and show the computation of the auto-covariance of induced Thévenin sources in linear interconnect systems placed in such a canonical stochastic field.

### References

1. Bas Michiels and Cécile Fiachetti. Covariance operators, green functions and canonical stochastic fields. *Radio Science*, 40(5):1–12, 2005.

---

**Session**

**CM 1**

---



# New trends in the preconditioning of integral equations of electromagnetism

David P. Levadoux<sup>1,2</sup>

<sup>1</sup> ONERA, Chemin de la Hunière, 91 761 Palaiseau, France david.levadoux@onera.fr

<sup>2</sup> University Paris XI, Laboratory of Mathematics, 91405 Orsay, France

The pertinence of integral equation methods for solving scattering Maxwell problems in harmonic regime requires no further proof. Using them in combination with a rapid multipole algorithm and an iterative solver makes them efficient and precise methods that can solve problems involving hundreds of thousands of unknowns. But the efficiency of iterative methods depends on the conditioning of the linear systems, so it is absolutely crucial to have either high-performance preconditioners or intrinsically well-conditioned integral formulations. It is in this field, a strategic one because necessary for solving very large calculation configurations, that the electromagnetism and radar department of ONERA has been conducting fundamental research for the past few years [2].

The main research theme, begun in 1998, is based on a generalized combined source integral equation (GCSIE) [4]. The master idea is to find a way to incorporate information on the solution that can be extracted beforehand in the integral formalism using the means offered by asymptotic theories (physical and/or mathematical). Thus the GCSIE equation depends on the choice of an operator whose purpose is to approximate the admittance of the diffracting body as best as possible. In the limit case where this approximation is exact, the integral operator to be inverted becomes the identity. We thus try to construct approximations of the admittance such that the operator underlying the equation appears as a mathematically controllable perturbation (*e.g.* compact) of the identity. When the GCSIE is discretized, we arrive at a linear system that is by essence well conditioned. From a theoretical viewpoint, this formalism is now well understood [1], as one of its foremost features is that it has no resonance frequency. As for experimental results, we point out for example that the Channel cavity (Fig. 1, right) modeling an aircraft air intake was processed at 7 GHz (300,000 unknowns) with the GCSIE in half as much computation time as is needed in production with a classical equation (Fig. 2).

A second research theme concerns the construction of non-standard preconditioners. Contrary to the preconditioners commonly used in industry, which are often algebraic and consequently leave out the mathematical properties of the equation from which the linear system derives, we construct analytical preconditioners from the parametrix (pseudo-inverse) of the equation. The result is new preconditioners, each dedicated to a given equation. The preconditioner of the CFIE, for example, gives encouraging results. Furthermore, the theoretical consequences of this work have established an original proof of the numerical convergence of the CFIE equation [3] which was still recently an open problem.

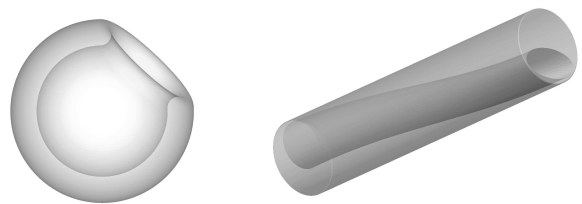


**Fig. 1.** *Translucent view of the spherical cavity and Channel used for the tests.*

## References

1. F. Alouges, S. Borel, and D. P. Levadoux. A stable well-conditioned integral equation for electromagnetic scattering. *J. Comp. Appl. Math*, 204:440–451, July 2007.
2. D. P. Levadoux. Stable integral equations for the iterative solution of electromagnetic scattering problems. *C. R. Physique*, 7(5):518–532, 2006.
3. D. P. Levadoux. Some preconditioners for the CFIE equation of electromagnetism. *Math. Meth. Appl. Sci.*, 2008, to appear.
4. D. P. Levadoux and B. L. Michielsen. An efficient high-frequency boundary integral equation. *Antennas and Propagation Society International Symposium*, 2:1170–1173, Orlando, FL, USA, July 11–16 1999.

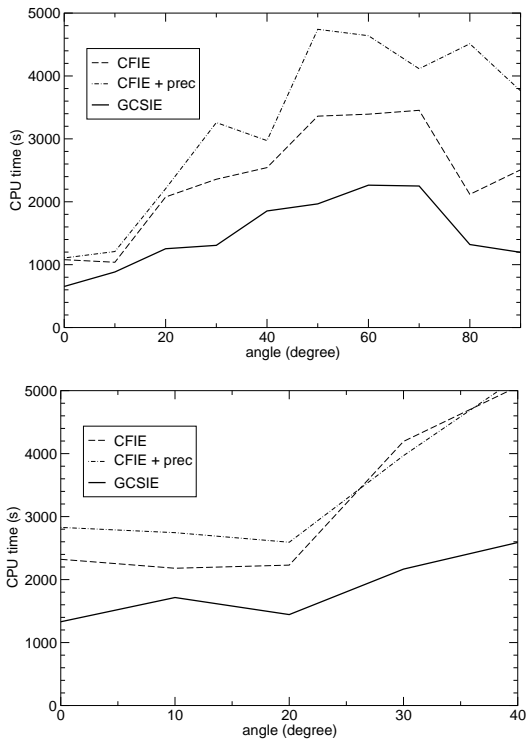


**Fig. 2.** Solution times as a function of the angle of presentation of the target. Top: spherical cavity at 2.8 GHz with 264,186 unknowns. Bottom: Channel at 7 GHz with 309,711 unknowns.

# A New Approach to Modeling Multi-Port Scattering Parameters

Sanda Lefteriu and Athanasios C. Antoulas

Rice University, 6100 Main Street, Houston, TX, 77005, USA [Sanda.Lefteriu@rice.edu](mailto:Sanda.Lefteriu@rice.edu), [aca@rice.edu](mailto:aca@rice.edu)

**Summary.** This paper addresses the issue of interpolating frequency response data by means of a linear dynamical system (macromodel). The proposed algorithm adaptively chooses the measurements to be used in building the system by minimizing the error in the singular values. Our method is suited for devices with a large number of ports due to the fact that data matrices are collapsed into vectors by taking appropriate linear combinations of the rows or columns.

## 1 Introduction and Motivation

The problem of building a system which approximates given frequency response measurements of a device is known as the *rational interpolation problem* and has been studied thoroughly (see [1] for a survey). This is related to the construction of state-space models of linear dynamical systems which are consistent with the data. Previous work includes several optimization methods [2], as well as the well-known vector fitting method [4].

Current applications in electromagnetic devices require a model of reasonable dimensions which approximates the response accurately in the desired frequency range. In this paper we present a novel approach for generating stable and passive macromodels of devices with a large number of ports, for which only a set of frequency-domain measurements (S-parameters) are available. Vector fitting and optimization-based methods are prohibitively expensive for this kind of devices. The proposed algorithm is based on a system-theoretic tool developed in [5]. It constructs the model by adaptively choosing measurements from the set of available ones to minimize the difference between the singular values of the data matrix and those of the transfer function of the intermediate model. The performance is compared to the popular vector fitting (VF) method in terms of the computational time needed to generate a model and the accuracy of the fit. Our technique proves to be both faster and more accurate.

## 2 Describing the Algorithm

The proposed algorithm constructs a macromodel of order  $k$  by building the state-space matrices

$\mathbf{E}, \mathbf{A} \in \mathbb{R}^{k \times k}$ ,  $\mathbf{B} \in \mathbb{R}^{k \times N_p}$ ,  $\mathbf{C} \in \mathbb{R}^{N_p \times k}$ ,  $\mathbf{D} = \mathbf{0}_{N_p \times N_p}$  such that the transfer function  $\mathbf{H}(s) = \mathbf{C}(s\mathbf{E} - \mathbf{A})^{-1}\mathbf{B} + \mathbf{D}$  of the system, when evaluated at the  $N_s$  available frequency samples, approximates the S-parameter matrix measured at the same frequency  $\omega_i$ :  $\mathbf{H}(j\omega_i) \approx \mathbf{S}_i \in \mathbb{C}^{N_p \times N_p}$

Our approach is based on the theory of *tangential interpolation*. The key and novel tools are the *Loewner matrix* together with the *shifted Loewner matrix* associated with the data. For details and proofs, we refer to [5].

We generate random vectors  $\mathbf{r}_i \in \mathbb{R}^{N_p \times 1}$ , set  $\mathbf{l}_i = \mathbf{r}_i^T \in \mathbb{R}^{1 \times N_p}$  (where  $(\cdot)^T$  stands for transposition) and, for each sample  $j\omega_i$ , we collapse the  $N_p \times N_p$  S-parameter matrix to a vector ( $\mathbf{w}_i = \mathbf{S}_i \mathbf{r}_i$  and  $\mathbf{v}_i = \mathbf{l}_i \overline{\mathbf{S}_i}$ , where  $\overline{(\cdot)}$  stands for complex conjugation). This idea makes the method suitable for devices with a large number of ports.

The right interpolation data is chosen as

$$\Lambda = \text{diag} [j\omega_1, \dots, j\omega_{N_s}] \in \mathbb{C}^{N_s \times N_s}, \quad (1)$$

$$\mathbf{R} = [\mathbf{r}_1, \dots, \mathbf{r}_{N_s}] \in \mathbb{R}^{N_p \times N_s}, \quad (2)$$

$$\mathbf{W} = [\mathbf{w}_1, \dots, \mathbf{w}_{N_s}] \in \mathbb{C}^{N_p \times N_s}, \quad (3)$$

while the left interpolation data is constructed as

$$\mathbf{M} = \text{diag} [-j\omega_1, \dots, -j\omega_{N_s}] \in \mathbb{C}^{N_s \times N_s}, \quad (4)$$

$$\mathbf{L} = [\mathbf{l}_1, \dots, \mathbf{l}_{N_s}]^T \in \mathbb{R}^{N_s \times N_p}, \quad (5)$$

$$\mathbf{V} = [\mathbf{v}_1, \dots, \mathbf{v}_{N_s}]^* \in \mathbb{C}^{N_s \times N_p}. \quad (6)$$

Afterwards, the Loewner and shifted Loewner matrices are built as follows for  $m, n = 1, \dots, N_s$

$$\mathbb{L}_{mn} = \frac{\mathbf{v}_m \mathbf{r}_n - \mathbf{l}_m \mathbf{w}_n}{\mu_m - \lambda_n}, \quad (7)$$

$$\sigma \mathbb{L}_{mn} = \frac{\mu_m \mathbf{v}_m \mathbf{r}_n - \lambda_n \mathbf{l}_m \mathbf{w}_n}{\mu_m - \lambda_n} \quad (8)$$

In practice, the number of measurements  $N_s$  is much larger than the order of the minimal realization of the underlying system, so the pencil  $(\sigma \mathbb{L}, \mathbb{L})$  is singular. In the case of noise-free measurements, the underlying system is obtained by projecting out the singular part, to obtain the regular part of the pencil. In our method, this singularity is overcome by using only selected measurements chosen adaptively.

The algorithm starts by selecting  $N_p$  measurements from the  $N_s$  available and constructing a system of order  $N_p$  by building the matrices  $\mathbf{A}$ ,  $\mathbf{M}$ ,  $\mathbf{R}$ ,  $\mathbf{L}$ ,  $\mathbf{W}$ ,  $\mathbf{V}$ ,  $\mathbb{L}$  and  $\sigma\mathbb{L}$  as presented in (1)-(8) and setting  $\mathbf{E}$  as  $-\mathbb{L}$ ,  $\mathbf{A}$  as  $-\sigma\mathbb{L}$ ,  $\mathbf{B}$  as  $\mathbf{V}$ ,  $\mathbf{C}$  as  $\mathbf{W}$  and  $\mathbf{D}$  as  $\mathbf{0}$ . We assess the error between the current interpolant and the data by computing, at each frequency sample, the difference between the  $N_p$  singular values of the S-parameter data matrices and the  $N_p$  singular values of the transfer function of the intermediary model evaluated at that particular frequency. For each singular value, the next measurement is chosen where the maximum error occurs. At the next step, a system of order  $2 \times N_p$  is constructed and the error in the singular values is computed again. The next set of  $N_p$  measurements will be picked according to the same criterion and the procedure continues until the desired accuracy or the desired order of the reduced model has been reached.

### 3 Numerical Example

The data set was provided by CST Ltd and it comes from a 14-port device. For each one of the 1001 frequency samples in the range 6MHz to 6GHz, a matrix of dimension  $14 \times 14$  with complex entries is given.

There were two error measures employed: the  $\mathcal{H}_\infty$ -norm of the error system defined as

$$\mathcal{H}_\infty \text{ error} = \max_{i=1 \dots N_s} \max_{k=1 \dots N_p} \sigma_1(\mathbf{S}_i - \mathbf{H}(j\omega_i))$$

and the  $\mathcal{H}_2$ -norm of the error system normalized with respect to the number of samples and the number of ports of the device as used in [3, 4]

$$\mathcal{H}_2 \text{ error} = \frac{1}{2\pi} \sqrt{\frac{\Delta\omega}{N_s N_p^2} \|\mathbf{S}_i - \mathbf{H}(j\omega_i)\|_F^2}$$

where  $\Delta\omega = \omega_{i+1} - \omega_i$ , for  $i = 1, \dots, N_s - 1$  (assuming equally spaced frequency samples).

Tables 1 and 2 compare the proposed algorithm with vector fitting. They show that our method is faster and yields better approximants for the same order of the desired system.

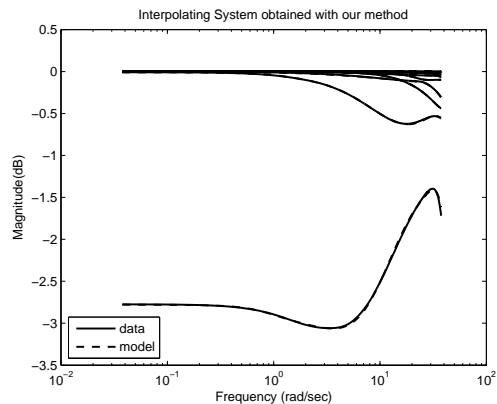
**Table 1.** Results obtained with our method

Order	Time (s)	$\mathcal{H}_\infty$ error	$\mathcal{H}_2$ error
14. 3=42	2.04	$5.7 \times 10^{-2}$	$7.81 \times 10^{-5}$
14. 4=56	3.35	$1.17 \times 10^{-2}$	$1.34 \times 10^{-5}$
14. 5=70	5.39	$1.04 \times 10^{-2}$	$8.1 \times 10^{-6}$
14. 6=84	8.01	$1.02 \times 10^{-2}$	$7.81 \times 10^{-6}$

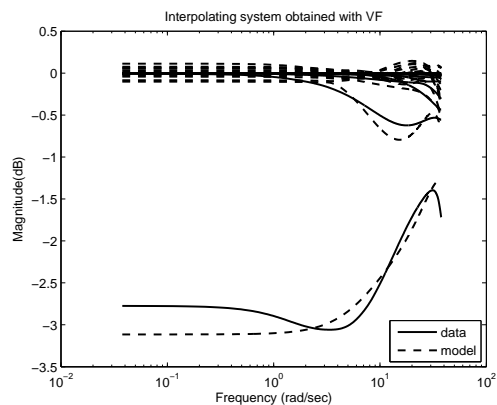
**Table 2.** Results obtained with VF

Order	Time (s)	$\mathcal{H}_\infty$ error	$\mathcal{H}_2$ error
14. 3=42	7.23	$1.97 \times 10^{-1}$	$1.01 \times 10^{-3}$
14. 4=56	8.92	$7.96 \times 10^{-2}$	$3.23 \times 10^{-4}$
14. 5=70	11.31	$3.65 \times 10^{-2}$	$1.25 \times 10^{-4}$
14. 6=84	13.51	$2.04 \times 10^{-2}$	$4.89 \times 10^{-5}$

Figures 1(a) and 1(b) present the response of the order  $k = 56$  interpolating system obtained with the proposed algorithm and vector fitting, respectively. They support the errors presented in the tables.



(a) Order 56 system obtained with our method



(b) Order 56 system obtained with vector fitting

**Fig. 1.** Comparison of our method and vector fitting against the data; plots have a logarithmic frequency axis scaled by  $10^9$ .

### References

1. A. C. Antoulas. *Approximation of Large-Scale Dynamical Systems*. SIAM, Philadelphia, 2005.
2. C. P. Coelho, J. R. Phillips, and L. M. Silveira. Optimization based passive constrained fitting. In *Proc. IEEE/ACM International Conference on Computer-Aided Design (ICCAD'02)*, pages 775–780, 2002.
3. Ioan D. and Ciuprina G. Reduced order models of on-chip passive components and interconnects, workbench and test structures. In Worst H. v. d. and Schilders W., editors, *Reduced Order Modeling*. Springer, 2008.
4. B. Gustavsen and A. Semlyen. Rational approximation of frequency domain responses by vector fitting. *IEEE Transactions on Power Delivery*, 14:1052–1061, 1999.
5. A. J. Mayo and A. C. Antoulas. A framework for the solution of the generalized realization problem. *Linear Algebra and Its Applications*, 405:634–662, 2007.

# Numerical and Mathematical Properties of Electromagnetic Surface Integral Equations

Pasi Ylä-Oijala and Matti Taskinen

Department of Radio Science and Engineering, Helsinki University of Technology, Finland  
 pasi.yla-oijala@tkk.fi, matti.taskinen@tkk.fi

**Summary.** Properties of electromagnetic surface integral operators, equations and formulations are investigated. It is shown that the two fundamental numerical properties, accuracy of the solution and convergence of an iterative solver, seems to be almost opposite properties. Reasons and remedies for this problem are discussed.

## 1 Introduction

The surface integral equation method is an efficient numerical technique for solving time-harmonic electromagnetic field problems. By using surface integral representations the original boundary value problem for Maxwell's equations can be transformed onto another equivalent problem of solving equivalent sources from surface integral equations. The method essentially reduces the dimensionality of the problem by one and can straightforwardly deal with unbounded domains.

Because discretization of an integral equation leads to a dense system matrix, the traditional surface integral equation methods are limited to rather small scale problems. Recently so called fast methods [1] have been developed to significantly enlarge the size of the problems that can be solved with integral equation methods. Many of the fast integral equation solvers, like the multilevel fast multipole algorithm (MLFMA), are based on the iterative solution of the matrix equation. In practical problems the bottleneck in the simulations can be the poor convergence of the iterative solution.

Recently, new surface integral equation formulations giving rise to better conditioned matrix equations and more efficient iterative solutions have been developed [2], [3]. However, many of these new formulations lead to lower solution accuracy. The fundamental problem with the electromagnetic surface integral equations seems to be that the solution accuracy and the convergence of iterative methods are almost opposite properties [4]. In this paper, reasons and remedies for the this problem are discussed and the properties of the surface integral operators, equations and formulations are studied.

## 2 Surface Integral Equations

Consider time-harmonic (time-factor  $e^{-i\omega t}$ ) electromagnetic scattering by a bounded and homogeneous object  $D$  in a homogeneous medium. Let  $\varepsilon_{o/i}, \mu_{o/i}$  denote the constant electromagnetic parameters outside (o) and inside (i) the object.

For a given primary field  $\mathbf{E}^p, \mathbf{H}^p$  the task is to find the secondary fields  $\mathbf{E}_{o/i}^s, \mathbf{H}_{o/i}^s$  so that they satisfy Maxwell's equations and the radiation conditions at the infinity and the total fields satisfy boundary conditions on the surface  $S$ .

Using the surface integral representations

$$\mathbf{E} = \frac{-1}{i\omega\varepsilon} (\nabla\nabla \cdot + k^2) \mathcal{S}(\mathbf{J}) - \nabla \times \mathcal{S}(\mathbf{M}) \quad (1)$$

$$\mathbf{H} = \frac{-1}{i\omega\mu} (\nabla\nabla \cdot + k^2) \mathcal{S}(\mathbf{M}) + \nabla \times \mathcal{S}(\mathbf{J}) \quad (2)$$

the above-mentioned boundary value problem can be reformulated as surface integral equations. Here  $\mathbf{J} = \mathbf{n} \times \mathbf{H}$ ,  $\mathbf{M} = -\mathbf{n} \times \mathbf{E}$  and  $\mathcal{S}$  is the *single-layer operator*

$$\mathcal{S}(\mathbf{F})(\mathbf{r}) = \int_S G(\mathbf{r}, \mathbf{r}') \mathbf{F}(\mathbf{r}') dS(\mathbf{r}') \quad (3)$$

with the homogeneous space Green's function

$$G(\mathbf{r}, \mathbf{r}') = \frac{e^{ik|\mathbf{r}-\mathbf{r}'|}}{4\pi|\mathbf{r}-\mathbf{r}'|} \quad (4)$$

and the wavenumber  $k = \omega\sqrt{\varepsilon\mu}$ .

From (1) and (2) two different types of surface integral equations can be derived:

1. Tangential **T-equations** are obtained by operating with  $-\mathbf{n} \times \mathbf{n} \times$  to (1) - (2) on  $S$ .
2. Rotated tangential **N-equations** are obtained by operating with  $\mathbf{n} \times$  to (1) - (2) on  $S$ .

By properly combining these equations, derived separately for both the primary and secondary fields, and inside and outside the object, and by applying the boundary conditions on the surface, several alternative surface integral formulations can be obtained.

### 3 Properties of Integral Operators

Consider a linear surface integral operator  $\mathcal{A}$

$$\mathcal{A}(\mathbf{F})(\mathbf{r}) = \int_S K(\mathbf{r}, \mathbf{r}') \mathbf{F}(\mathbf{r}') dS(\mathbf{r}'). \quad (5)$$

Here  $K$  is the *kernel* of  $\mathcal{A}$  satisfying

$$|K(\mathbf{r}, \mathbf{r}')| \leq \frac{C}{|\mathbf{r} - \mathbf{r}'|^{2-c}} \quad (6)$$

with  $C > 0$ . Depending on the value of the coefficient  $c$ ,  $K$  and  $\mathcal{A}$  have different properties:

1. If  $c > 0$   $K$  is *weakly singular* and operator  $\mathcal{A}$  is a *smoothing operator*.
2. If  $c \leq 0$   $K$  is *hyper-singular* and operator  $\mathcal{A}$  is a non-smoothing operator.

For a mathematical point of view the nicest properties has a Fredholm's integral equation of the second kind, i.e., a compact operator plus the identity operator. Because the derivatives in (1) and (2) increase the singularity of the kernel, in electromagnetics the surface integral operators are compact only in very rare cases.

### 4 Discretization and Results

In practical implementations the used numerical methods (discretization) plays also an important role in determining the properties of the equations. For example, with Galerkin's method and divergence conforming functions the hyper-singular integral operator  $\nabla \nabla \cdot \mathcal{S}$  can be regularized and reduced onto a operator with a weakly singular kernel.

Next the properties of the electromagnetic surface integral equations are studied by considering planewave scattering from a metallic (perfectly conducting, PEC) cube. The problem is formulated using a combined field integral equation (CFIE) defined as a combination of T electric field integral equation (T-EFIE) and N magnetic field integral equation (N-MFIE)

$$\text{CFIE} := \frac{\alpha}{\eta_o} \text{T-EFIE} + (1 - \alpha) \text{N-MFIE}. \quad (7)$$

Here  $0 \leq \alpha \leq 1$  is a coupling coefficient and  $\eta_o = \sqrt{\mu_o/\varepsilon_o}$ . Equation (7) is discretized with Galerkin's method using low order divergence conforming vector functions defined on planar triangles. Figures 1 and 2 show the solution (backscattered radar cross section) and the number of GMRES iterations with different discretization densities as functions of  $\alpha$ .

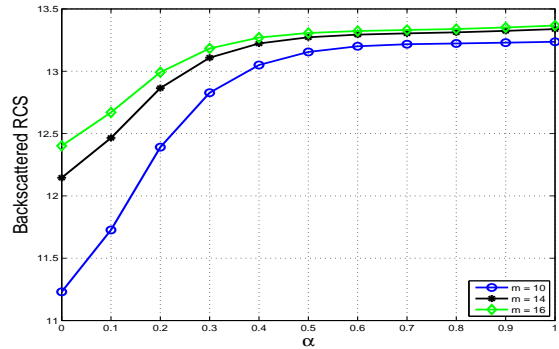


**Fig. 1.** Backscattered RCS for a  $\lambda \times \lambda \times \lambda$  PEC cube.  $m$  is the number of subdivisions on the edges.

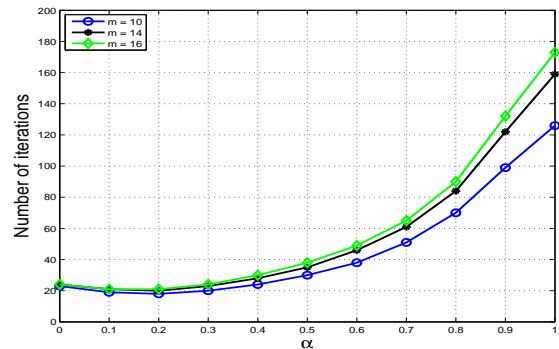


**Fig. 2.** Number of GMRES iterations for a  $\lambda \times \lambda \times \lambda$  PEC cube with stopping criterion  $10^{-6}$ .

The results show that the solution accuracy and convergence of the iterative solver behave almost opposite as functions of  $\alpha$  and mesh density. CFIE (7) with  $\alpha = 0$  is an integral equation of the second kind containing an operator with a hyper-singular kernel and the identity operator, whereas with  $\alpha = 1$ , the equation is of the first kind containing the single-layer operator, i.e., a smoothing operator, only. Hence, the existence of a smoothing/non-smoothing operator improves/decreases the solution accuracy, but decreases/improves the iteration convergence.

### References

1. W.C. Chew, J.-M. Jin, E. Michielssen and J. Song, *Fast and Efficient Algorithms in Computational Electromagnetics*. Artech House, Boston, 2001.
2. P. Ylä-Oijala, M. Taskinen and S. Järvenpää, Surface integral equation formulations for solving electromagnetic scattering problems with iterative methods, *Radio Science*, 40:RS6002, 2005.
3. M. Taskinen and P. Ylä-Oijala, Current and charge integral equation formulation, *IEEE Trans. Antennas Propag.*, 54:58–67, 2006.
4. P. Ylä-Oijala, M. Taskinen and S. Järvenpää, Analysis of surface integral equations in electromagnetic scattering and radiation problems, *Eng. Analysis Boundary Elements*, 32:196–209, 2008.

# Nonlinear models for silicon semiconductors

Salvatore La Rosa<sup>1</sup>, Giovanni Mascali<sup>2</sup>, and Vittorio Romano<sup>1</sup>

<sup>1</sup> Dipartimento di Matematica e Informatica, Università di Catania, viale A. Doria 6, 95125 Catania, Italy  
larosa@dmi.unict.it, romano@dmi.unict.it

<sup>2</sup> Dipartimento di Matematica, Università della Calabria and INFN-Gruppo c. Cosenza, 87036 Cosenza, Italy  
g.mascali@unical.it

**Summary.** Exact closures are obtained of the 8-moment and the 9-moment models for silicon semiconductors based on the maximum entropy principle. The validity of these models is assessed by numerical simulations of some test problems.

## 1 Introduction and mathematical model

Modern electronic devices require increasingly accurate models of charge transport in semiconductors in order to describe high-field phenomena such as hot electron propagation, impact ionization and heat generation.

Moreover, in many applications in optoelectronics, it is necessary to describe the transient interaction of electromagnetic radiation with carriers in complex semiconductor materials. In those cases the characteristic times are of the order of the electron momentum or the energy flux relaxation times. These are some of the main reasons of the necessity of developing models which incorporate a number of moments of the distribution function higher than those in the drift-diffusion and the energy transport models.

These extended models, generally called hydrodynamical models, are usually derived from the infinite hierarchy of the moment equations of the Boltzmann transport equation by suitable truncation procedures. One of the most successful among these procedures is that based on the Maximum Entropy Principle (MEP), see [1] for a complete review both for Si and GaAs semiconductors.

The models comprise the balance equations of electron density, energy density, average velocity, energy flux and possibly also of higher scalar and vector moments which do not have an immediate physical interpretation. These equations are coupled to the Poisson equation for the electric potential. Apart from the Poisson equation, the system is hyperbolic in the physically relevant region of the field variables.

The MEP approach leads to a constrained optimization problem which is handled by resort-

ing to the Lagrangian multipliers method. Recently [2], this problem has been solved numerically without resorting to asymptotic procedures. In this way the model is expressed in terms of the Lagrangian multipliers and the constitutive relations are given by integral expressions that do not allow an efficient numerical tabulation but require the use of suitable quadrature formulas in the half space.

In [2], we assessed the validity of the 8-moment model and we showed that the full nonlinear MEP model (hereafter NLMEP) is more accurate than the semi-linear MEP one (hereafter SLMEP). However, we found that for devices with a channel length smaller than 0.3 microns in some regions of the devices there is a loss of integrability of the fully nonlinear MEP distribution function, see Figure 1. This probably happens because the moments cross the boundary of the region of realizability as already known in classical gas dynamics. In this paper we tackle the problem to determine how the region of realizability changes by adding a further scalar moment. The model is given by the following system of balance equations

$$\frac{\partial n}{\partial t} + \frac{\partial(nV^i)}{\partial x^i} = 0, \quad (1)$$

$$\frac{\partial(nV^i)}{\partial t} + \frac{\partial(nU^{ij})}{\partial x^j} + neE_j H^{ij} = nC_{V^i}, \quad (2)$$

$$\frac{\partial(nW)}{\partial t} + \frac{\partial(nS^i)}{\partial x^i} + neV_i E^i = nC_W, \quad (3)$$

$$\frac{\partial(nS^i)}{\partial t} + \frac{\partial(nF^{ij})}{\partial x^j} + neE_j G^{ij} = nC_{S^i}. \quad (4)$$

$$\frac{\partial(nW_2)}{\partial t} + \frac{\partial(nS_2^i)}{\partial x^i} + 2neE_i S^i = nC_{W_2}, \quad (5)$$

where  $e$  is the absolute value of the electron charge and  $\mathbf{E}$  the electric field. The macroscopic quantities, which are involved in the balance equations, are related to the electron distribution function  $f(\mathbf{x}, \mathbf{k}, t)$  by the definitions

$$n = \int_{\mathbb{R}^3} f d\mathbf{k}, \quad \text{electron density,}$$

$$V^i = \frac{1}{n} \int_{\mathbb{R}^3} f v^i d\mathbf{k}, \quad \text{average electron velocity,}$$

$$W = \frac{1}{n} \int_{\mathbb{R}^3} \mathcal{E}(k) f d\mathbf{k}, \quad \text{average electron energy,}$$

$$W_2 = \frac{1}{n} \int_{\mathbb{R}^3} \mathcal{E}^2(k) f d\mathbf{k}, \quad \text{average electron energy square,}$$

$$S^i = \frac{1}{n} \int_{\mathbb{R}^3} f v^i \mathcal{E}(k) d\mathbf{k}, \quad \text{energy flux,}$$

$$S_2^i = \frac{1}{n} \int_{\mathbb{R}^3} f v^i \mathcal{E}^2(k) d\mathbf{k}, \quad \text{flux of the electron energy square,}$$

$$U^{ij} = \frac{1}{n} \int_{\mathbb{R}^3} f v^i v^j d\mathbf{k}, \quad \text{velocity flux,}$$

$$H^{ij} = \frac{1}{n} \int_{\mathbb{R}^3} \frac{1}{\hbar} f \frac{\partial}{\partial k_j} (v^i) d\mathbf{k},$$

$$F^{ij} = \frac{1}{n} \int_{\mathbb{R}^3} f v^i v^j \mathcal{E}(k) d\mathbf{k}, \quad \text{flux of the energy flux,}$$

$$G^{ij} = \frac{1}{n} \int_{\mathbb{R}^3} \frac{1}{\hbar} f \frac{\partial}{\partial k_j} (\mathcal{E} v^i) d\mathbf{k},$$

$$C_{V^i} = \frac{1}{n} \int_{\mathbb{R}^3} \mathcal{C}[f] v^i d\mathbf{k}, \quad \text{velocity production,}$$

$$C_W = \frac{1}{n} \int_{\mathbb{R}^3} \mathcal{C}[f] \mathcal{E}(k) d\mathbf{k}, \quad \text{energy production,}$$

$$C_{S^i} = \frac{1}{n} \int_{\mathbb{R}^3} \mathcal{C}[f] v^i \mathcal{E}(k) d\mathbf{k}, \quad \text{energy flux production,}$$

$$C_{W_2} = \frac{1}{n} \int_{\mathbb{R}^3} \mathcal{C}[f] \mathcal{E}^2(k) d\mathbf{k}, \quad \text{electron energy square production.}$$

The numerical simulations will give information about the integrability region. In particular if it is larger than that found in the 8-moment case or vice versa. From a theoretical point of view the question is rather involved. Indeed the additional Lagrangian multipliers, associated to new moments corresponding to weight functions represented by powers of energy with an exponent greater than one, are zero at equilibrium. Therefore the equilibrium states are located at the boundary of the realizability region. This implies that small perturbations can have both positive and negative sign causing a loose of integrability, limiting the validity of the nonlinear models. Preliminary numerical experiments confirm such a conjecture (see Figure 2).

*Acknowledgement.* The authors acknowledge the financial support by M.I.U.R. (PRIN 2007 *Equazioni cinetiche e idrodinamiche di sistemi collisionali e complessi*), P.R.A. University of Catania and University of Calabria (ex 60 %), CNR (grant n. 00.00128.ST74), the EU Marie Curie RTN project COMSON grant n. MRTN-CT-2005-019417.

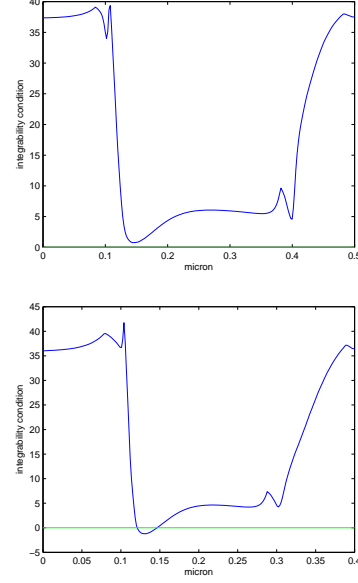


**Fig. 1.** Devices with channel length  $0.3\mu m$  and  $0.2\mu m$  respectively in the 8-moment case: integrability is guaranteed if the plotted function is greater than zero (see [2])

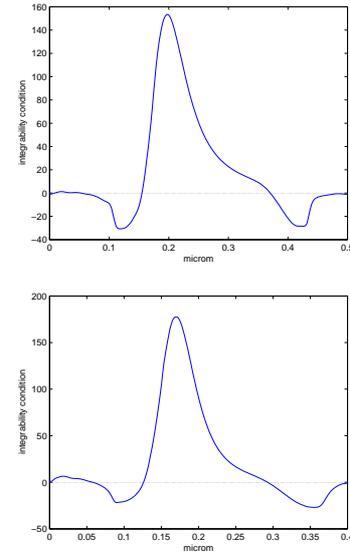


**Fig. 2.** Integrability in the devices with channel length  $0.3\mu m$  and  $0.2\mu m$  respectively in the 8-moment case

## References

1. A.M. Anile, G. Mascali and V. Romano, Recent developments in Hydrodynamical Modeling of semiconductors. In A. M. Anile, editor, *Mathematical Problems in Semiconductor Physics, Lecture Notes in Mathematics 1823*. Springer, Berlin, 2003.
2. S. La Rosa, G. Mascali, V. Romano. Exact Maximum Entropy Closure of the Hydrodynamical Model for Si Semiconductors: the 8-Moment Case preprint (2008).

# Hyperbolic PDAEs for semiconductor devices coupled with circuits

Giuseppe Ali<sup>1</sup>, Giovanni Mascali<sup>1</sup>, and Roland Pulch<sup>2</sup>

<sup>1</sup> Dipartimento di Matematica, Università della Calabria and INFN-Gruppo c. Cosenza, 87036 Cosenza, Italy  
giuseppe.ali@unical.it, g.mascali@unical.it

<sup>2</sup> Department of Mathematics and Sciences, Chair of Applied Mathematics and Numerical Analysis,  
Bergische Universität Wuppertal, Germany pulch@math.uni-wuppertal.de

**Summary.** In this paper, we address the problem of coupling a system of network equations corresponding to an electric circuit and the partial differential equations modelling a separate device.

## 1 Model of Electric Circuit

We consider an electric circuit, which, by adopting the formalism of Modified Nodal Analysis [1] can be described by a system of differential algebraic equations (DAEs) in the form

$$\begin{aligned} \mathbf{0} &= \mathbf{A}_C \frac{d}{dt} \mathbf{q}_C(\mathbf{A}_C^\top \mathbf{u}(t), t) + \mathbf{A}_R \mathbf{r}(\mathbf{A}_R^\top \mathbf{u}(t), t) \\ &\quad + \mathbf{A}_L \mathbf{j}_L(t) + \mathbf{A}_V \mathbf{j}_V(t) + \mathbf{A}_I \mathbf{i}(t) + \mathbf{A}_\lambda \boldsymbol{\lambda}(t), \\ \mathbf{0} &= \frac{d}{dt} \boldsymbol{\phi}_L(\mathbf{j}_L(t), t) - \mathbf{A}_L^\top \mathbf{u}(t), \\ \mathbf{0} &= \mathbf{A}_V^\top \mathbf{u}(t) - \mathbf{v}(t). \end{aligned} \quad (1)$$

The unknown functions are the state variables  $\mathbf{y} := (\mathbf{u}, \mathbf{j}_L, \mathbf{j}_V)^\top$ , where  $\mathbf{u}$  comprises the node voltages,  $\mathbf{j}_L$  the currents through inductances, and  $\mathbf{j}_V$  the currents through voltage sources. The currents  $\boldsymbol{\lambda}$  represent coupling variables, since they leave external devices and enter the electric network (or vice versa).

## 2 Refined Model for Devices

Complex elements like semiconductors in an electric circuit may require sophisticated modelling, see [2] for a review. We apply a 1-dimensional hydrodynamical model for semiconductor devices. For simplicity, we restrict to the case of purely negative doped regions in the semiconductor. Compactly the system of equations can be written in the form

$$\frac{\partial \mathbf{U}}{\partial t} + \frac{\partial \mathbf{F}(\mathbf{U})}{\partial x} = \mathbf{B}(\mathbf{U}, E), \quad (2)$$

where

$$\mathbf{U} = \begin{pmatrix} n \\ nV \\ nW \\ nS \end{pmatrix}, \quad \mathbf{F}(\mathbf{U}) = \begin{pmatrix} nV \\ n(\frac{1}{m^*} G_1 - 2\alpha G_2) \\ nS \\ nG_2 \end{pmatrix},$$

$$\mathbf{B}(\mathbf{U}, E) = \begin{pmatrix} 0 \\ d_{11}(W) nV + d_{12}(W) nS + q(2\alpha G_3 - \frac{1}{m^*}) nE \\ -n \frac{W-W^0}{\tau(W)} - qnVE \\ d_{21}(W) nV + d_{22}(W) nS - qnG_3 E \end{pmatrix}.$$

The respective variables and constants of the hydrodynamical model are given in Table 1.

The system (2) is coupled with the Poisson equation for the electric potential

$$-\epsilon \frac{\partial^2 \psi}{\partial x^2} = q(N_+(x) - n), \quad E = -\frac{\partial \psi}{\partial x}. \quad (3)$$

**Table 1.** Variables related to PDE system.

$n$	number density
$V$	average velocity
$W$	average energy
$S$	energy flux
$G_i^{ij}$	fluxes
$d_{ij}$	velocity and energy flux production coefficients
$W^0$	equilibrium energy
$\tau$	energy relaxation time
$\psi$	electric potential
$E$	electric field
$\epsilon$	dielectric constant
$q$	unit charge
$N_+$	donor concentration
$\alpha$	non-parabolicity factor
$m^*$	effective electron mass

The following initial values are considered

$$\begin{aligned} n(x, 0) &= N_+(x), & W(x, 0) &= W^0, \\ V(x, 0) &= S(x, 0) = 0. \end{aligned} \quad (4)$$

The corresponding boundary conditions read

$$\begin{aligned}
n(0, t) &= N_+(0), & n(\hat{L}, t) &= N_+(\hat{L}), \\
W(0, t) &= W(\hat{L}, t) = W^0, \\
\frac{\partial V}{\partial x}(0, t) &= \frac{\partial V}{\partial x}(\hat{L}, t) = \frac{\partial S}{\partial x}(0, t) = \frac{\partial S}{\partial x}(\hat{L}, t) = 0
\end{aligned}$$

with device length  $\hat{L}$ . The boundary conditions for the Poisson equation are determined by coupling the device to the system of DAEs, which models the connected electric circuit.

### 3 Coupling Conditions

We consider a device with just two connections to the surrounding circuit. Figure 1 illustrates the topological relations. The incidence matrix  $\mathbf{A}_\lambda$  specifies the position of the device within the electric network. In case of a single device, it holds

$$\mathbf{A}_\lambda \boldsymbol{\lambda} = \mathbf{A}_\lambda \begin{pmatrix} \lambda_l \\ \lambda_r \end{pmatrix} \equiv \mathbf{A}_D I, \quad (5)$$

with  $I := \lambda_l = -\lambda_r$ , and  $\mathbf{A}_D := \mathbf{A}_\lambda \begin{pmatrix} 1 \\ -1 \end{pmatrix}$ . In the case of just one device coupled to the electric circuit, the matrix  $\mathbf{A}_D$  reduces to a column vector.

The difference of the two boundary potentials, is given by

$$\psi(0, t) - \psi(\hat{L}, t) = \begin{pmatrix} 1 \\ -1 \end{pmatrix}^\top \mathbf{A}_\lambda^\top \mathbf{u}(t) = \mathbf{A}_D^\top \mathbf{u}(t). \quad (6)$$

We consider a diode of type  $n^+/n/n^+$  in the following and apply the corresponding hyperbolic model (2) in one space dimension. Then we can derive the expression

$$I(t) = \frac{\epsilon A}{\hat{L}} \mathbf{A}_D^\top \frac{d}{dt} \mathbf{u}(t) + J(t), \quad (7)$$

where  $J(t) := -\frac{qA}{L} \int_0^{\hat{L}} n(x, t) V(x, t) dx$ .

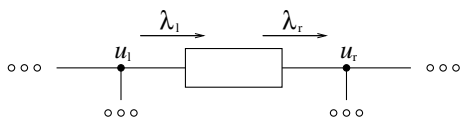


**Fig. 1.** Coupling of circuit and device by node voltages  $u_l, u_r$  and branch currents  $\lambda_l, \lambda_r$  ( $l$ : left,  $r$ : right).

### 4 Numerical results

The coupled system of PDAE's is numerically solved in the case of a  $n^+ - n - n^+$  diode coupled with an inductor, a capacitor and a resistor.

The results for the device voltage and current are represented in the following Figures

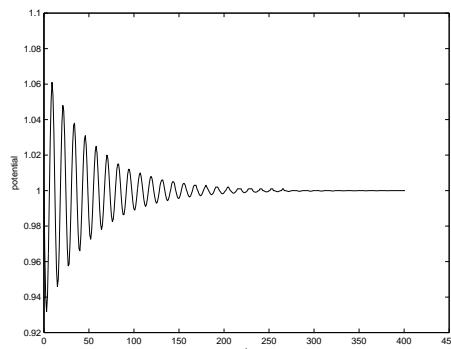


**Fig. 2.** Voltage (V) vs time (ps)

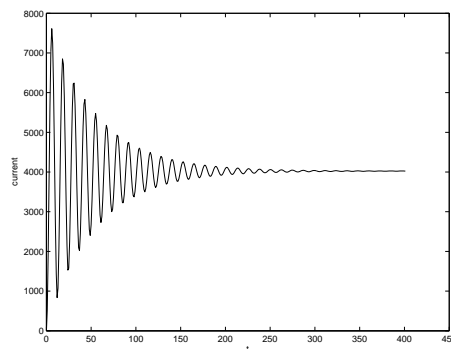


**Fig. 3.** Current (A) vs time (ps)

*Acknowledgement.* The authors acknowledge the financial support by P.R.A. University of Calabria (ex 60 %) and by the EU Marie Curie RTN project COMSON grant n. MRTN-CT-2005-019417.

### References

1. M. Günther, U. Feldmann, E.J.W. ter Maten, Modeling and discretization of circuit problems. In W.H.A. Schilders, E.J.W. ter Maten, editors, *Handbook of Numerical Analysis. Special Volume Numerical Analysis of Electromagnetism*. Elsevier North Holland, Amsterdam, 2005.
2. A.M. Anile, G. Mascali and V. Romano, Recent developments in Hydrodynamical Modeling of semiconductors. In A. M. Anile, editor, *Mathematical Problems in Semiconductor Physics, Lecture Notes in Mathematics 1823*. Springer, Berlin, 2003.

---

**Session**

**P 2**

---



# Consistent Initialization for Coupled Circuit-Device Simulation

Sascha Baumanns, Mónica Selva, and Caren Tischendorf

Mathematical Institute, University of Cologne, Weyertal 86-90, 50931 Köln

sbaumann@math.uni-koeln.de, mselva@math.uni-koeln.de, tischendorf@math.uni-koeln.de

**Summary.** A coupled circuit-device simulation leads to equation systems involving non-dynamic equations resulting from Kirchhoff's laws. Consequently, initial values can not be chosen arbitrarily – they have to be consistent. Here, we present an opportunity to calculate consistent initial values for the numerical integration based on a method of lines approach discretizing the circuit-device system in space first.

## 1 Model Equations for a Coupled Circuit-Device Simulation

Nowadays circuits are present in all parts of our live. From the practical point of view, the interest in circuit modeling is to replace as much laboratory testing as possible by numerical simulation in order to minimise costs.

### 1.1 The Circuit Equations

We focus here onto the modified nodal analysis (MNA) for modeling the network equations since it is used in most commercial circuit simulators. Furthermore, we restrict ourselves to circuits containing resistors, capacitors, inductors, independent voltage sources and independent current sources as well as semiconductors modeled by the device equations described in Section 1.2. This leads to a differential-algebraic equation (DAE) which is an equation of the form (see e.g. [2])

$$\begin{aligned} A_C \frac{d}{dt} q_C(A_C^\top e) + A_R g(A_R^\top e) + A_L j_L \\ + A_V j_V + A_S j_S + A_I i_s(t) &= 0 \quad (1) \\ \frac{d}{dt} \Phi(j_L) - A_L^\top e &= 0 \quad (2) \\ A_V^\top e - v_s(t) &= 0 \quad (3) \end{aligned}$$

Here, the unknowns are the node potentials  $e$ , the currents  $j_L$  through inductors, the currents  $j_V$  through voltage sources and the currents  $j_S$  through semiconductors.

### 1.2 The Device Equations

Companion models for semiconductor devices contain hundreds of parameters today and it is a

costly task to tune all parameters. On the other hand the companion models reflect the physical behavior only up to a certain level. The idea we want to follow here is to avoid companion models and model the semiconductors directly by a system of partial-differential equations (PDE). A standard approach here is to use the drift diffusion model

$$\begin{aligned} -\nabla(\varepsilon_S \nabla \psi) &= q(\mathbf{p} - \mathbf{n} + C) \text{ on } \Omega_S \quad (4) \\ -\nabla(\varepsilon_O \nabla \psi) &= 0 \text{ on } \Omega_O \quad (5) \end{aligned}$$

$$-\partial_t \mathbf{n} + \frac{1}{q} \nabla J_n(\mathbf{n}, \mathbf{p}, \psi) = R(\mathbf{n}, \mathbf{p}) \text{ on } \Omega_S \quad (6)$$

$$\partial_t \mathbf{p} + \frac{1}{q} \nabla J_p(\mathbf{n}, \mathbf{p}, \psi) = -R(\mathbf{n}, \mathbf{p}) \text{ on } \Omega_S \quad (7)$$

with

$$\begin{aligned} J_n(\mathbf{n}, \mathbf{p}, \psi) &= q\mu_n(U_T \nabla \mathbf{n} - \mathbf{n} \nabla \psi) \\ J_p(\mathbf{n}, \mathbf{p}, \psi) &= -q\mu_n(U_T \nabla \mathbf{p} - \mathbf{p} \nabla \psi) \end{aligned}$$

Here, the unknowns are the electrostatic potential  $\psi$ , the electron concentration  $\mathbf{n}$  and the hole concentration  $\mathbf{p}$ . The field  $\Omega_O$  describes the oxid area of the semiconductor. Correspondingly, the area of semiconducting material is denoted by  $\Omega_S$ .

The drift diffusion equations can be coupled with the MNA equations and we receive a so-called partial differential algebraic equation system (PDAE). The coupling conditions are given by the applied node potentials and the current through the semiconductor:

$$\begin{aligned} -j_{S_k} &= \int_{\Gamma_k} (J_n + J_p - \varepsilon_S \partial_t \nabla \psi) \nu dx, \Gamma_k \subseteq \Gamma_{DS} \quad (8) \\ -j_{S_k} &= \int_{\Gamma_k} (-\varepsilon_S \partial_t \nabla \psi) \nu dx, \Gamma_k \subseteq \Gamma_{DO} \quad (9) \end{aligned}$$

whereas  $\Gamma_{DO}$  consists of all contact boundaries of the oxyd and  $\Gamma_{DS}$  involves all contact boundaries of the semiconductor area (cf. [1]).

### 1.3 Space Discretized Circuit-Device System

After space discretisation of the drift diffusion equations (4)-(7) and the semiconductor current

equations (8)-(9) using a finite element method, the coupled system becomes a DAE of the form

$$\begin{aligned}
0 &= M_{AN,AN} A_S^\top \mathbf{e} + \mathbf{q}_S \\
&+ H_{AN} \mathcal{X}_{AN,DN} (\psi_{DN} + H_{DN}^\top A_S^\top \mathbf{e}) \\
&+ H_{AN} \mathcal{X}_{AN,FN} \mathcal{X}_{FN,FN}^{-1} [qC_\phi - \mathcal{X}_{FN,DN} \psi_{DN}] \\
&+ q H_{AN} \mathcal{X}_{AN,FN} \mathcal{X}_{FN,FN}^{-1} \\
&\cdot [\mathcal{Z}_{FN,FN_S} (\mathbf{P}_{FN_S} - \mathbf{N}_{FN_S}) \\
&\quad + \mathcal{Z}_{FN,DN_S} (p_{DN_S} - n_{DN_S})] \quad (10)
\end{aligned}$$

$$0 = \mathbf{j}_S + H_{AN} [J_{n\phi} + J_{p\phi}] + \frac{d}{dt} \mathbf{q}_S \quad (11)$$

$$\begin{aligned}
0 &= \mathcal{X}_{FN,FN} \boldsymbol{\Psi}_{FN} - qC_\phi \\
&+ q \mathcal{Z}_{FN,FN_S} (\mathbf{N}_{FN_S} - \mathbf{P}_{FN_S}) \\
&+ \mathcal{X}_{FN,DN} (\psi_{DN} + H_{DN}^\top A_S^\top \mathbf{e}) \\
&+ q \mathcal{Z}_{FN,DN_S} (n_{DN_S} - p_{DN_S}) \quad (12)
\end{aligned}$$

$$0 = \frac{d}{dt} \mathcal{Y}_{FN_S,FN_S} \mathbf{N}_{FN_S} + \frac{1}{q} J_{n\theta} + R_\theta \quad (13)$$

$$0 = \frac{d}{dt} \mathcal{Y}_{FN_S,FN_S} \mathbf{P}_{FN_S} - \frac{1}{q} J_{n\theta} + R_\theta \quad (14)$$

with  $\boldsymbol{\Psi}$ ,  $\mathbf{N}$  and  $\mathbf{P}$  are vectors representing the coefficients in the linear combinations of the FEM basis functions for  $\psi$ ,  $\mathbf{n}$  and  $\mathbf{p}$ , respectively. Furthermore, we used the indexes  $AN$ ,  $FN$ ,  $DN$ ,  $AN_S$ ,  $FN_S$ ,  $DN_S$  to indicate that the corresponding matrices vectors have to be evaluated at all nodes, all free nodes, all Dirichlet boundary nodes, the nodes in the semiconducting area, the free nodes in the semiconducting area, and the Dirichlet boundary nodes in the semiconducting area, respectively.

For the coupled circuit-device simulation we have to solve the DAE system resulting from (1)-(3) and (10)-(14) (cf. [4] for one-dimensional semiconductor models).

## 2 Consistent Initial Values

Some components of the solution are determined by constraints. For initial value problems, these constraints restrict the choice of initial values, since there is not a solution through every given initial value.

One of the difficult parts in solving DAEs numerically is to determine a consistent set of initial conditions in order to start the integration. A set of initial conditions are called consistent if there exists a solution of the DAE passig through the conditions. The problem of computing initial values can formulate as follow: Given some user defined initial values for the DAE not necessarily consistent. Modify them in such a way that there exists a solution passing through them.

To calculate consistent initial values for the DAE system (1)-(3) and (10)-(14) we exploit its

special structure and obtain the following result which is an extension of the results in [3] to the 2D and 3D case.

**Theorem 1.** *Let all capacitances, inductances and resistances in the network are passive. Then, the DAE system (1)-(3) and (10)-(14) has index 1 if and only if the circuit does not involve cutsets of current sources and inductances and loops of voltages sources, capacitances and semiconductor branches.*

*For a consistent initialization of this DAE system, initial values for the current through inductors  $\mathbf{j}_L$ , the capacitive branch voltages  $A_C^\top \mathbf{e}$ , the semiconductor charges  $\mathbf{q}_S$ , the concentration of electrons  $\mathbf{N}$  and the concentration of holes  $\mathbf{P}$  can be freely chosen. Every solution of the system*

$$\begin{aligned}
Q_C^\top A_{Rg} (A_R^\top \mathbf{e}) + Q_C^\top A_L \mathbf{j}_L + Q_C^\top A_V \mathbf{j}_V \\
+ Q_C^\top A_S \mathbf{j}_S + Q_C^\top A_I i_s(t) = 0,
\end{aligned}$$

(3), (10) and (12) with  $\mathbf{j}_L = j_{L0}$ ,  $A_C^\top \mathbf{e} = A_C^\top e_0$ ,  $\mathbf{q}_S = q_{S0}$ ,  $\mathbf{N} = N_0$  and  $\mathbf{P} = P_0$  provides a consistent initial value for the coupled system (1)-(3) and (10)-(14).

For index-2-DAEs or higher, so-called hidden constraints appear. Hence consistent values have to be chosen in such a way that not only the explicit equations of the DAE but additionally these hidden constraints have to be fulfilled as well. Thus a proper characterization of the hidden constraints becomes necessary. The study of the index 2 case is subjected to ongoing research.

## References

1. M. Bodestedt and C. Tischendorf. PDAE models of integrated circuits and index analysis. *Math. Comput. Model. Dyn. Syst.*, 13(1):1–17, 2007.
2. D. Estévez Schwarz and C. Tischendorf. Structural analysis of electric circuits and consequences for MNA. *Int. J. Circ. Theor. Appl.*, 28:131–162, 2000.
3. M. Selva. An index analysis from coupled circuit and device simulation. *Scientific Computing in Electrical Engineering, Proceedings of the SCEE-2004 Conference held in Capo d' Orlando, Italy, Springer Verlag, Berlin*, pages 121–128, 2006.
4. M. Selva and C. Tischendorf. Numerical analysis of DAEs from coupled circuit and semiconductor simulation. *Appl. Num. Math.*, 53(2-4):471–488, 2005.

# Heating of semiconductor devices in electric circuits

Markus Brunk<sup>1</sup> and Ansgar Jünger<sup>2</sup>

<sup>1</sup> Norwegian University of Science and Technology, Department of Mathematical Sciences, N-7491 Trondheim, Norway [markus.brunk@math.ntnu.no](mailto:markus.brunk@math.ntnu.no)

<sup>2</sup> Vienna University of Technology, Institute for Analysis and Scientific Computing, Wiedner Hauptstr. 8-10, 1040 Wien, Austria [juenger@anum.tuwien.ac.at](mailto:juenger@anum.tuwien.ac.at)

**Summary.** A coupled model of thermal network and semiconductor model equations is proposed. The device is modeled by the energy-transport equations and an heat flow equation for the temperature of the crystal lattice. An energy conserving source term for the heat-flow equation is presented. The thermal network is described by a system of simplified heat flow equations. Device and network are thermally coupled via the lattice temperature and hot charge carrier effects. Numerical results for a *pn* diode and a frequency multiplier are presented.

## 1 Introduction

In application, thermal modeling of electric circuits has been taken into account by accompanying thermal networks consisting of one-dimensional and lumped heat flow equations. Parasitic effects and high frequencies in the circuits, however, require a more detailed consideration of thermal effects in semiconductor devices.

We apply the energy-transport equations as (electric) semiconductor model to allow for local thermal effects in terms of the charge carrier temperature  $T_n$ . The (scaled) energy-transport equations consist of conservation laws for the electron density  $n$  and electron energy density  $w$ ,

$$n_t - \operatorname{div} J_n = -R(n, p),$$

$$w_t - \operatorname{div} J_w = -J_n \cdot \nabla V + W_n(n, T_n) - \frac{3}{2} T_n R(n, p),$$

with constitutive relations for the particle current density  $J_n$  and the energy current density  $J_{w_n}$ :

$$J_n = \mu_n \left( \nabla n - \frac{n}{T_n} \nabla V \right),$$

$$J_{w_n} = \frac{3}{2} \mu_n (\nabla(nT_n) - n \nabla V),$$

where  $R(n, p)$  denotes the generation-recombination term,  $p$  is the hole density, which is computed from analogue equations,  $W_n(n, T_n)$  is the relaxation-time term, and  $\mu_n$  the (scaled) electron mobility. The equations are coupled to the Poisson equation for the electric potential  $V$ :

$$\lambda^2 \Delta V = n - p - C(x),$$

where  $\lambda$  is the scaled Debye length and  $C(x)$  the doping concentration. The lattice temperature  $T_L$  is modeled by the (scaled) heat flow equation

$$\rho_L c_L \partial_t T_L - \operatorname{div}(\kappa_L \nabla T_L) = H,$$

with material density  $\rho_L$ , heat capacity  $c_L$ , heat conduction  $\kappa_L$  and an appropriate heat source  $H$ .

## 2 Heat source and thermal coupling

We present a heat source term that ensures energy-conservation for the coupled system of energy-transport and heat flow equation:

$$H = -W_n - W_p + R(E_g - T_L E'_g + \frac{3}{2}(T_n + T_p)) \\ + \alpha (J_n \cdot \nabla [E_c - T_L E'_c] + J_p \cdot \nabla [E_v - T_L E'_v]),$$

with scaling constant  $\alpha$ , the band edges  $E_c$  and  $E_v$ , and the energy gap  $E_g$ .  $T_p$  denotes the hole temperature,  $W_p$  the corresponding relaxation-time term for the holes and  $J_p$  denotes the hole current density. In order to take into account the thermal radiation to environment, for simulations the term  $S_L(T_L - T_{\text{env}})$  with the environmental temperature  $T_{\text{env}}$  and the transmission function  $S_L = S_L(x)$  has to be added to the source term.

Coupling of the device and thermal network equations is taken into account in terms of boundary conditions for  $T_L$  and the semiconductor heat flux, that enters the surrounding thermal network. A quasi stationary approach leads to the (scaled) semiconductor heat flux

$$J_{\text{th}}^S = \beta (-\kappa_L \nabla T_L - [E_c J_n + E_v J_p] - J_{w_n} + J_{w_p}),$$

where  $J_{w_p}$  denotes the energy flux density of the holes.  $\beta$  denotes a scaling constant, see [3]. Thermal interaction in terms of the lattice temperature as well as hot carrier effects is considered.

The device model is described by partial differential equations. The thermal network equations result in partial differential (algebraic) equations - depending on the topology of the network. For thermal-electric simulation of circuits these equations are coupled with the differential algebraic equations resulting from MNA, thus that a *coupled system of nonlinear partial differential-algebraic equations* has to be solved, see [1, 3].

### 3 Numerical results

As numerical examples we consider a  $100\text{ nm}$   $pn$  diode with a maximum doping of  $5 \cdot 10^{23}\text{ m}^{-3}$ . For simplicity we model the positive (minority) charge carriers by the simpler drift-diffusion model. Moreover, assuming it to be a non-degenerate homostructure device and neglecting the direct dependency of the energy gap on  $T_L$  a simplified heat source term is used. For the contribution of the drift-diffusion model to the heat source we use the widespread term  $-J_p V$ . For radiation we assume a value of  $S_L = 4 \cdot 10^{15}\text{ W}/(\text{m}^3\text{K})$ .

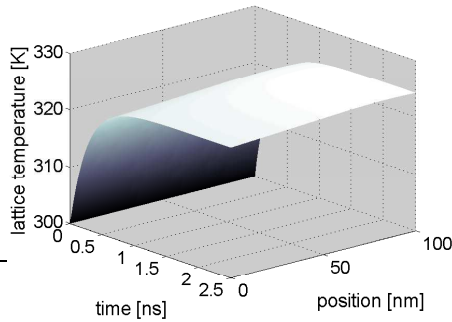


**Fig. 1.** Lattice temperature in a  $0.1\text{ }\mu\text{m}$   $pn$  diode biased with  $1.5\text{ V}$ .

Firstly, we bias the device with a bias of  $1.5\text{ V}$  starting in thermal equilibrium. In Figure 1 the lattice temperature is depicted and we see that it converges to the stationary state where the lattice heats up by  $25\text{ K}$ .

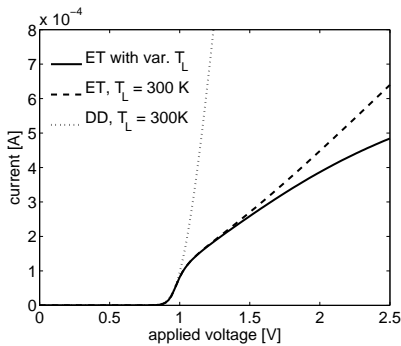


**Fig. 2.** Current-voltage curve of a  $0.1\text{ }\mu\text{m}$   $pn$  diode for different models.

In Figure 2 we see the stationary computed IV-characteristic of the considered device. We compare the drift-diffusion model with the energy-transport model with and without lattice heating. Obviously, the thermal effects influence the electric behavior of the considered device. Finally

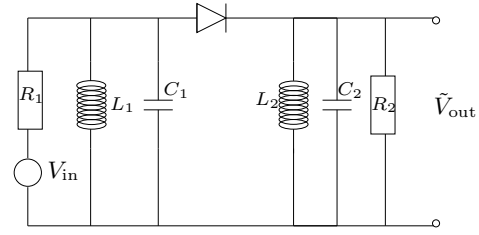


**Fig. 3.** Frequency multiplier.

we simulate the frequency multiplier depicted in Figure 3 containing the considered device, where the parameters are chosen such that the resonance frequency is given at  $3.2\text{ GHz}$ . The circuit is biased with a sinusoidal signal of  $v(t) = 3 \cdot \sin(3.2 \cdot 2\pi \cdot 10^9\text{ Hz}t)\text{ V}$ . The lattice temperature in the device is depicted in Figure 4 and a strong device heating can be observed.

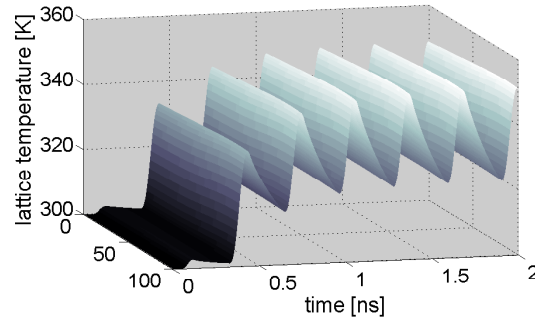


**Fig. 4.** Lattice temperature in a  $0.1\text{ }\mu\text{m}$   $pn$  diode in the frequency multiplier.

*Acknowledgement.* The authors acknowledge partial support from the German Federal Ministry of Education and Research (BMBF), grant 03JUNAVN, and from the FWF Wissenschaftskolleg “Differential equations”.

### References

1. M. Brunk and A. Jüngel. Numerical coupling of electric circuit equations and energy-transport models for semiconductors. *SIAM J. Sci. Comput.* 30 (2008), 873-894.
2. M. Brunk and A. Jüngel. Simulation of thermal effects in optoelectronic devices using coupled energy-transport and circuit models. To appear in *Math. Models Meth. Appl. Sci.*, 2008.
3. M. Brunk. Numerical coupling of thermal-electric network models and energy-transport equations including optoelectronic semiconductor devices. *PhD-thesis*. Johannes Gutenberg-university, Mainz, 2008.

# Surrogate Modeling of Low Noise Amplifiers Based on Transistor Level Simulations

Luciano De Tommasi<sup>1</sup>, Dirk Gorissen<sup>2</sup>, Jeroen Croon<sup>3</sup>, and Tom Dhaene<sup>2</sup>

<sup>1</sup> University of Antwerp, Department of Mathematics and Computer Science, Middelheimlaan 1, B-2020 Antwerp, Belgium and NXP Semiconductors, High Tech Campus 37, PostBox WY4-01, NL-5656AE Eindhoven, Netherlands [luciano.detommasi@ua.ac.be](mailto:luciano.detommasi@ua.ac.be), [luciano.de.tommasi@nxp.com](mailto:luciano.de.tommasi@nxp.com)

<sup>2</sup> Ghent University - IBBT, Depart. of Information Technology (INTEC), Gaston Crommenlaan 8 Bus 201, B-9050 Ghent, Belgium [dirk.gorissen@ugent.be](mailto:dirk.gorissen@ugent.be), [tom.dhaene@ugent.be](mailto:tom.dhaene@ugent.be)

<sup>3</sup> NXP-TSMC Research Center, High Tech Campus 37, PostBox WY4-01, NL-5656AE Eindhoven, Netherlands [jeroen.croon@nxp.com](mailto:jeroen.croon@nxp.com)

**Summary.** The paper deals with the identification of surrogate models of RF low noise amplifiers. The behavior of such circuit blocks can be evaluated via accurate transistor-level simulations. Since a transistor level simulation is quite a time-consuming process, the possibility of extensive trade-off investigations is often limited during the design process.

Surrogate modeling involves the construction of a global model based onto a certain number of transistor level simulations. It provides a good-enough approximate description of the circuit block over the design space, but being much faster to evaluate than an additional transistor level simulation.

## 1 Introduction

Accurate surrogate models for single RF and microwave devices have been already developed (e.g. using ANNs [1]). In this work, we do not model a single device like a MOSFET, but a complete (though simple) RF circuit block: a Low Noise Amplifier (LNA). Future work will include the analysis of other circuit blocks (e.g. mixers, VCOs, ...).

An LNA (see fig. 1) is the typical first stage of a receiver, having the main function of providing the gain needed to suppress the noise of subsequent stages, such as a mixer. In addition it has to give negligible distortion to the signal while adding as little noise as possible [2]. The behavior of an LNA can be fully described by means of the admittance and noise functions, which are evaluated via accurate transistor-level simulations. Such functions can be easily used to determine the performance figures (gain, input impedance, noise figure and power consumption) used by designers [3]. Each simulation typically requires one-two minutes, which is a too long time to allow a designer to explore how performance figures of LNA scale with key circuit-design parameters, such as the dimensions of transistors, passive components, signal properties and bias

conditions. Therefore, the transistor level model can be usefully replaced with an accurate surrogate model (based on transistor level simulations) which is much cheaper to evaluate.

Our previous investigations [4], [5] exploited a first order analytical model, which enabled to run a lot of different experiments with several different model types, being much cheaper to evaluate than a transistor level model. Such experiments have shown that rational functions, ANNs and Kriging models are the most promising model types for the admittance and noise functions of an LNA.

The goal of this work is the validation of the results obtained with the simple analytical model, when a more accurate transistor-level model is used. In particular, we aim to study the accuracy of surrogate models as a function of the number of design variables (inputs) and number of data samples in the design space.

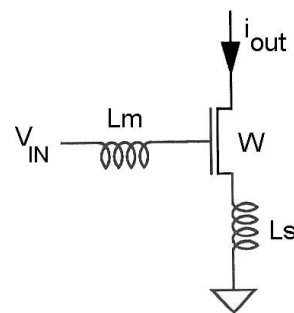


**Fig. 1.** A narrowband Low Noise Amplifier.

## 2 Experimental Setup

The surrogate modeling approach developed in this paper, is based on the SURrogate MOdeling (SUMO) Matlab Toolbox [4]. It is linked with the

Cadence SPECTRE simulator, which runs the transistor level simulations, so providing the samples of the LNA describing functions.

Models types considered in this work are Artificial Neural Networks (ANNs) and Rational Functions (RFs). The ANNs implementation included in the SUMO Toolbox is built on the Matlab Neural Network Toolbox. The network is trained with Bayesian regularization and its topology is determined by a Genetic Algorithm (GA). RFs have two different implementations to optimize the complexity, one based on a custom stochastic hill climber and another one based on a GA.

The modeling loop starts with an initial Latin hypercube design. Then, the adaptive sampling loop starts. In order to improve the accuracy, new samples are selected using one of the adaptive sampling algorithm available in the SUMO toolbox. Experience has showed that gradient sample selector [6] usually gives the best results. It performs a trade off between a density based sample selection and error-based sample selection: both the undersampled and non-linear regions are automatically identified and sampled more densely. In order to judge the quality of the models, k-fold crossvalidation is applied. The termination criteria can be chosen as follows: the modeling stops either when a predefined maximum number samples is reached or when the root relative square error is below a predefined threshold.

### 3 Results

The authors performed a preliminary analysis of the achievable accuracy as function of the number of samples and the number of design parameters, based on a first order analytical model of the LNA (fig. 2) [7].

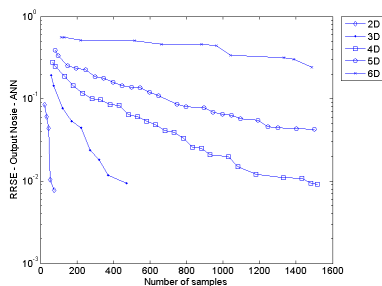


**Fig. 2.** Root relative square error as function of the number of samples and number of design parameters. Surrogate models were built from an approximate, analytical description of LNA.

Results shown in fig. 2 will be validated replacing the approximate analytical model with

the one provided by transistor level simulator.

Figure 3 shows a preliminary result based on transistor level simulations: the model of the output noise figure, built with ANNs and 113 samples. A very good agreement between the model and the samples (crosses) is achieved.

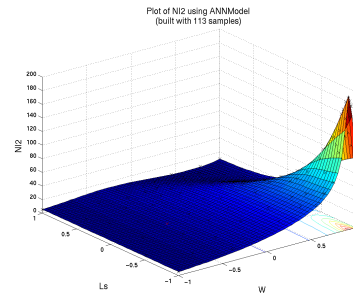


**Fig. 3.** Surrogate model of output noise figure as function of device width  $W$  and inductance  $L_s$  built using SUMO Toolbox and SPECTRE simulations.

*Acknowledgement.* This work was supported in part by the European Commission through the Marie Curie Actions of its Sixth Program under the contract number MTKI-CT-2006-042477.

### References

1. Q. J. Zhang and K. C. Gupta. *Neural Networks for RF and Microwave Design*. Artech House Inc., 2000.
2. Thomas H. Lee. *The Design of CMOS Radio-Frequency Integrated Circuits*. Cambridge University Press, 2004.
3. J.A. Croon, D.M.W. Leenaerts, D.B.M. Klaassen. Accurate Modeling of RF Circuit Blocks: Weakly-Nonlinear Narrowband LNAs. *Proceedings of the IEEE Custom Integrated Circuits Conference (CICC)*, 2007.
4. D. Gorissen, L. De Tommasi, J. Croon and T. Dhaene. Automatic Model Type Selection with Heterogeneous Evolution: An application to RF circuit block modeling. *Proceedings of the IEEE Congress on Evolutionary Computation (WCCI)*, 2008.
5. D. Gorissen, L. De Tommasi, W. Hendrickx, J. Croon and T. Dhaene. RF circuit block modeling via Kriging surrogates. *Proceedings of the 17th International Conference on Microwaves, Radar and Wireless Communications (MIKON)*, 2008.
6. Karel Crombecq. *A gradient based approach to adaptive metamodeling*. Technical Report, University of Antwerp, 2007.
7. D. Gorissen, L. De Tommasi, K. Crombecq, T. Dhaene. *Sequential Modeling of a Low Noise Amplifier with Neural Networks and Active Learning*. Technical Report, University of Antwerp, 2008.

# On Local Handling of Inner Equations in Compact Models

Uwe Feldmann, Masataka Miyake, Takahiro Kajiwara, and Mitiko Miura-Mattausch

USDL-AdSM, Hiroshima-University, 1-3-1 Kagamiyama, Higashi-Hiroshima, 739-8530 Japan  
 uwe.feldmann@online.de, {miyake-m053223, ancient-future, mmm}@hiroshima-u.ac.jp

**Summary.** The burden of solving inner equations in compact semiconductor models is often shifted to the host circuit simulator. Schur complement techniques may help to reduce the size of both the model stamp and memory needs, and – at least for large circuits – overall CPU time. Some practical aspects of applying these concepts in compact modeling are discussed.

## 1 Introduction

State-of-the art models of semiconductor devices in circuit simulation exhibit an increasing number of implicit model internal equations, either by introducing intrinsic circuit nodes, or by using auxiliary (nonlinear and/or differential) equations for more accurate description of device behavior. These equations are often exported to the host simulator. This is easy to implement, in general, but also may give rise to a huge model stamp and suffers from the overlinear complexity of the sparse solver in memory and CPU time, unless sophisticated ordering strategies or hierarchical solver concepts are employed. Furthermore, robustness and efficiency (parallel processing!) are to a large extent simulator dependent.

Our objective is to implement compact models with local solver concepts, such that the device internal equations are as far as possible hidden from the host simulator. The benefits are obvious: Small model stamps, reduced simulator dependence, and possibly higher efficiency due to higher degree of locality and parallelism. Of course, there are also risks: Higher expense per model evaluation, convergence problems, and much higher efforts for model development. The first risk should be overcompensated by better overall efficiency, at least for large circuits. Due to the second risk we pursue only hierarchical versions of a single level Newton method, with a special focus to make sure that convergence is (almost) the same as if the equations were exported to the host simulator. And finally, the third risk can be reduced by the concept to perform the local handling in some kind of intermediate layer between the model itself and the host simulator. The second and the third item distinguish this approach from previous attempts to apply local solver concepts for model evaluation [2].

The techniques employed here are not new at all, cf. [1,3]. However, to our knowledge they have not yet been used directly in compact model development. This contribution makes a first step into this direction. First, Schur complement techniques are shortly reviewed. Then some special aspects of their usage in SPICE like simulators will be discussed. A simple MOSFET model serves as an example. Finally, the current state and future work will be described.

## 2 Review of Schur Complement Techniques

We formulate the problem for the DC and (after time discretization) transient analysis: Solve the nonlinear coupled system

$$\mathbf{f}_i(\mathbf{x}_i, \mathbf{x}_m) = \mathbf{0} \quad (1)$$

$$\mathbf{f}_m(\mathbf{x}_i, \mathbf{x}_m) = \mathbf{0} \quad (2)$$

where index  $i$  denotes the model internal equations and variables, and  $m$  denotes the outer equations from Modified Nodal Analysis and network variables. (For the ease of notation a circuit with one single device is considered.) Application of a single level Newton method yields the linear system for the Newton corrections  $\Delta\mathbf{x}_i, \Delta\mathbf{x}_m$ :

$$\begin{pmatrix} \frac{\partial \mathbf{f}_i}{\partial \mathbf{x}_i} & \frac{\partial \mathbf{f}_i}{\partial \mathbf{x}_m} \\ \frac{\partial \mathbf{f}_m}{\partial \mathbf{x}_i} & \frac{\partial \mathbf{f}_m}{\partial \mathbf{x}_m} \end{pmatrix} \begin{pmatrix} \Delta\mathbf{x}_i \\ \Delta\mathbf{x}_m \end{pmatrix} = - \begin{pmatrix} \mathbf{f}_i \\ \mathbf{f}_m \end{pmatrix} \quad (3)$$

From the upper equation we get

$$\Delta\mathbf{x}_i = - \left( \frac{\partial \mathbf{f}_i}{\partial \mathbf{x}_i} \right)^{-1} \left( \mathbf{f}_i + \frac{\partial \mathbf{f}_i}{\partial \mathbf{x}_m} \Delta\mathbf{x}_m \right) \quad (4)$$

and plug into the lower equation yields:

$$\begin{aligned} & \left[ \frac{\partial \mathbf{f}_m}{\partial \mathbf{x}_m} - \frac{\partial \mathbf{f}_m}{\partial \mathbf{x}_i} \left( \frac{\partial \mathbf{f}_i}{\partial \mathbf{x}_i} \right)^{-1} \frac{\partial \mathbf{f}_i}{\partial \mathbf{x}_m} \right] \Delta\mathbf{x}_m \\ & = - \left[ \mathbf{f}_m - \frac{\partial \mathbf{f}_m}{\partial \mathbf{x}_i} \left( \frac{\partial \mathbf{f}_i}{\partial \mathbf{x}_i} \right)^{-1} \mathbf{f}_i \right] \end{aligned} \quad (5)$$

Equation (5) is the Schur equation which the host simulator has to solve. Once the latter has computed a solution  $\Delta\mathbf{x}_m$ , the Newton correction for the inner system can be calculated from (4).



# Transient Analysis of Nonlinear Circuits Based on Waves

Carlos Christoffersen

Department of Electrical Engineering, Lakehead University, 955 Oliver Road, Thunder Bay, Ontario P7B 5E1, Canada [c.christoffersen@ieee.org](mailto:c.christoffersen@ieee.org),

**Summary.** A new approach for transient analysis of nonlinear circuits is presented. The circuit equations are formulated as functions of waves in fictitious transmission lines. The waves are calculated following a procedure that resembles the actual signal propagation in a circuit and is fully parallelizable. A strongly nonlinear circuit is used as a case study.

## 1 Introduction

Circuit-level simulation of complex systems is a challenging task in terms of memory and CPU time. It is thus of great interest to find more efficient methods for circuit-level simulation. At the core of nonlinear circuit analysis is the solution of a system of nonlinear algebraic equations. Solving this system of equations using Newton method requires the decomposition of a large (normally sparse) matrix for each iteration. This matrix is particularly large in the case of harmonic balance (HB) or techniques based on multiple time dimensions [1].

This paper presents a transient analysis approach that requires only one matrix decomposition for a given time step size. This approach was inspired in the multiple reflections technique [2] and wave digital simulation of circuits [3,4]. Wave digital filters [5] were developed to replace analog filters with a digital structure. Several methods have been proposed for transient simulation using waves but they have limitations handling nonlinearities or do not scale well with the size of the circuit. Felderhoff [3] proposed a convergent relaxation method that can treat several nonlinear devices and is easily parallelizable. The method proposed in this paper is also parallelizable and can handle arbitrary static and dynamic nonlinearities.

## 2 Formulation

Assume that the total number of ports of all devices in a given circuit is equal to  $n$ . For each port, we associate a reference impedance  $Z_j$ . The voltage and current at Port  $j$  can be expressed as

$$v_j = v_j^+ + v_j^- \quad (1)$$

$$i_j = \frac{v_j^+ - v_j^-}{Z_j}, \quad (2)$$

where  $v_j^+$  and  $v_j^-$  are the incident and reflected waves at Port  $j$  as seen from the devices as shown in Fig. 1. The circuit topology defines the rela-

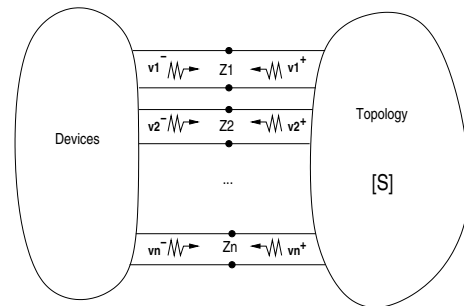


Fig. 1. Circuit partition

tionship between the vector of incident and reflected waves,  $\mathbf{v}^+$  and  $\mathbf{v}^-$ , respectively. Let  $\mathbf{Q}$  and  $\mathbf{B}$  be the full cut-set and loop-set matrices for a given tree in the circuit. The vectors of all port currents ( $\mathbf{i}$ ) and port voltages ( $\mathbf{v}$ ) satisfy

$$\mathbf{Q}\mathbf{i} = \mathbf{0} \quad (3)$$

$$\mathbf{B}\mathbf{v} = \mathbf{0}. \quad (4)$$

Combining (1) and (2) with (3) and (4) the following equation is obtained:

$$\begin{bmatrix} \mathbf{QG} \\ -\mathbf{B} \end{bmatrix} \mathbf{v}^+ = \begin{bmatrix} \mathbf{QG} \\ \mathbf{B} \end{bmatrix} \mathbf{v}^-,$$

where  $\mathbf{G}$  is a diagonal matrix that has the reciprocal of the reference impedances ( $Z_j$ ) in its diagonal. Matrices  $\mathbf{Q}$ ,  $\mathbf{G}$  and  $\mathbf{B}$  are sparse and thus  $\mathbf{v}^+$  can efficiently be obtained for large circuits.

The reference impedance at sources and linear devices can be chosen such that there are no reflections from the device back to the network [4]. Nonlinear devices will cause reflections. In this paper it is proposed to calculate these reflections using Newton's method. For example, suppose the current in a nonlinear device is given by

$$i_j = f(v_j),$$

with  $f()$  a nonlinear function. An error function is defined as follows:

$$F(v_j^+) = Z_j f(v_j^+ + v_j^-) - v_j^+ + v_j^- = 0.$$

This can easily be generalized for multi-port nonlinear devices, both static and dynamic. Moreover, the same idea can be applied to a complete subcircuit.

Using this formulation, only one large matrix decomposition is necessary for the complete simulation. This decomposition could eventually be eliminated if an automatic way to decompose the topology in adaptors is developed. The computation performed at each iteration is completely parallelizable: propagation of waves through the topology is essentially a matrix-vector product and the Newton method for each device is independent of the rest of the circuit. This iterative process resembles the actual propagation of signals in a physical circuit.

### 3 Case Study

The circuit shown in Fig. 2 was simulated to test the approach proposed in this paper. The circuit parameters are:  $C = 4 \mu\text{F}$ ,  $R_S = 50 \Omega$ ,  $R_L = 5 \text{ k}\Omega$ . The source is sinusoidal with a peak of 3 V and a frequency of 500 Hz. The diode parameters are  $I_S = 1 \text{ fA}$ ,  $N = 1$ ,  $C_j = 100 \text{ nF}$ ,  $M_j = 0.5$ ,  $V_j = 1 \text{ V}$  and  $F_C = 0.5$ . The reference impedances were chosen to avoid reflections where possible and a value of  $50 \Omega$  was used for the diode ports. A transient simulation with a du-

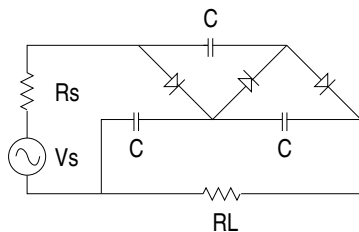


Fig. 2. Nonlinear circuit

ration of 8 ms and a time step equal to  $50 \mu\text{s}$  was performed. The simulation results are compared with a Spice simulation in Fig. 3.

The convergence of this method as described here is linear, but it can be made superlinear using Steffensen-like updates. An average of 30 iterations per sample point were necessary to achieve a tolerance of  $10^{-8}$ . The number of iterations was at least 11 and at most 42 for each sample point.

Several issues must still be addressed. The most important is a rigorous convergence analysis. Another issue is that the choice of reference

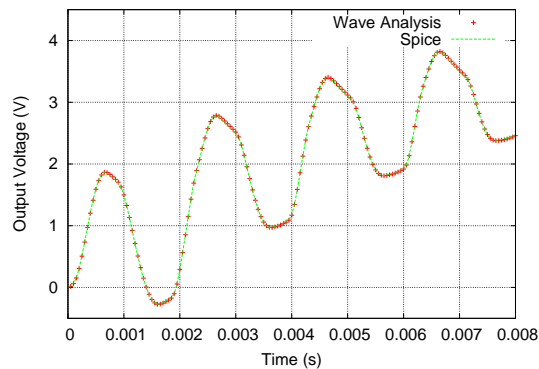


Fig. 3. Comparison of voltages at load resistor

impedance in each nonlinear port affects the convergence rate, but currently there is no method to predict the optimum value.

The Spice simulation is significantly faster in this example, but the proposed method was not optimized for speed. Many improvements are still possible to reduce the computational cost of each iteration. If a comparable performance can be achieved for small circuits, then due to its parallel nature the proposed method may become more efficient for very large circuits or when applied to analyses where several samples/harmonics are calculated at once such as in HB or techniques based on multiple time dimensions [1].

*Acknowledgement.* This work was funded by the Natural Sciences and Engineering Research Council of Canada (NSERC).

### References

1. J. Roychowdhury. Analyzing circuits with widely separated time scales using numerical PDE methods. *IEEE Trans. on Circuits and Systems— I: Fundamental Theory and Applications*, Vol. 48, No. 5, May 2001, pp. 578–594.
2. A. R. Kerr. A technique for determining the local oscillator waveforms in a microwave mixer. *IEEE Trans. on Microwave Theory and Techniques*, October 1974, pp. 828–831.
3. T. Felderhoff. Jacobi’s method for massive parallel wave digital filter algorithm. *Proc. of the IEEE Conference on Acoustics, Speech and Signal Processing*, vol. 3, May 1996, pp. 1621–1624.
4. A. Fiedler and H. Grotstollen. Simulation of power electronic circuits with principles used in wave digital filters. *IEEE Trans. on Industry Applications*, Vol. 33, No 1, Jan./Feb. 1997, pp. 49–57.
5. A. Fettweis. Wave Digital Filters: Theory and Practice. *IEEE Proceedings*, Vol 74, Feb. 1986, pp. 270–327.

# Time-Domain Preconditioner for Harmonic Balance Jacobians

Mikko Honkala<sup>1</sup> and Ville Karanko<sup>2</sup>

<sup>1</sup> Helsinki University of Technology, Faculty of Electronics, Communications and Automation, Department of Radio Science and Engineering, P.O.Box 3000, FI-02015 TKK, Finland [mikko.a.honkala@tkk.fi](mailto:mikko.a.honkala@tkk.fi)

<sup>2</sup> AWR-APLAC Corporation, P.O. Box 284, FI-02600 Espoo, Finland [ville.karanko@aplac.com](mailto:ville.karanko@aplac.com)

**Summary.** Preconditioning is crucial for the convergence of GMRES iteration in the harmonic balance analysis of RF and microwave circuits. This paper presents a variant of the time-domain preconditioner for harmonic balance Jacobians. The efficiency of the preconditioner is demonstrated with realistic simulation examples.

## 1 Introduction

The harmonic balance (HB) [1] method is a well-established analysis method for RF and microwave circuits. It is a frequency-domain technique for periodic and quasi-periodic steady-state analysis.

In HB analysis, the circuit equations are represented in terms of Fourier coefficients. This results in a system of nonlinear algebraic equations, which are usually solved using the inexact Newton method, i.e., the Newton–Raphson method with an iterative linear solver. The typical choice for the linear solver is GMRES.

The efficiency of a linear iterative solver depends heavily on the preconditioner used. Naturally, most preconditioners for HB equations are in the frequency domain, but for highly nonlinear circuits, especially for frequency dividers, time-domain preconditioners [2–4], which take nonlinear behavior better into account, become attractive.

This paper proposes a variant of the time-domain preconditioner.

## 2 Harmonic Balance

The nodal harmonic balance equations are

$$\mathbf{F}(\mathbf{u}) = \mathbf{I}(\mathbf{u}) + \mathbf{j}\Omega\mathbf{Q}(\mathbf{u}) + \mathbf{U}, \quad (1)$$

where  $\mathbf{u}$  is the nodal voltage vector,  $\mathbf{I}$  is the nonlinear nodal current vector,  $\Omega$  is the frequency domain differentiation matrix, and  $\mathbf{U}$  is the vector of excitation currents. The nonlinear equation (1) is typically solved using iterative methods like inexact Newton with a preconditioned linear solver GMRES.

The inexact-Newton iteration requires a Jacobian matrix

$$\mathbf{J} = \mathbf{j}\Omega\mathbf{C} + \mathbf{G}, \quad (2)$$

where  $\mathbf{C}$  and  $\mathbf{G}$  are the nodal capacitance and conductance matrices, respectively.

In time domain, the Jacobian (no oversampling) is

$$\tilde{\mathbf{J}} = \Gamma^{-1}\mathbf{J}\Gamma = \mathbf{D}\tilde{\mathbf{C}} + \tilde{\mathbf{G}}, \quad (3)$$

where

$$\tilde{\mathbf{G}} := \Gamma^{-1}\mathbf{G}\Gamma = \begin{bmatrix} \mathbf{g}_1 & 0 & 0 & \dots & 0 \\ 0 & \mathbf{g}_2 & 0 & \dots & 0 \\ 0 & 0 & \mathbf{g}_3 & \dots & 0 \\ & & & \ddots & \\ 0 & 0 & 0 & \dots & \mathbf{g}_n \end{bmatrix}, \quad (4)$$

and, similarly,

$$\tilde{\mathbf{C}} := \Gamma^{-1}\mathbf{C}\Gamma, \quad (5)$$

where  $\mathbf{g}_k, \mathbf{c}_k$  are block matrices and the difference operator  $\mathbf{D} = \Gamma^{-1}\mathbf{j}\Omega\Gamma$  is a matrix having general form

$$\mathbf{D} = \begin{bmatrix} 0 & \alpha_1\mathbf{I} & \alpha_2\mathbf{I} & \dots & \alpha_{-1}\mathbf{I} \\ \alpha_{-1}\mathbf{I} & 0 & \alpha_1\mathbf{I} & \dots & \alpha_{-2}\mathbf{I} \\ \alpha_{-2}\mathbf{I} & \alpha_{-1}\mathbf{I} & 0 & \dots & \alpha_{-3}\mathbf{I} \\ & & & \ddots & \\ \alpha_1\mathbf{I} & \alpha_2\mathbf{I} & \dots & \alpha_{-1}\mathbf{I} & 0 \end{bmatrix}. \quad (6)$$

The matrix  $\mathbf{I}$  is the  $(m \times m)$  identity matrix ( $m$  is the number of nodes in the circuit or in one block), and coefficients  $\alpha_k$  are the weights of time-domain difference operator.

Since, for strongly nonlinear circuits the resistive nonlinearities are dominant, it is tempting to approximate the equations by considering them in this form and further approximating the difference operator  $\mathbf{D}$  by some typical finite difference.

## 3 Time-domain preconditioners

Time-domain preconditioners for single-tone HB Jacobians have the form

$$\mathbf{K} = \mathbf{\Gamma}(\mathbf{DC} + \mathbf{G})\mathbf{\Gamma}^{-1}. \quad (7)$$

As stated above, the main problem when constructing a time-domain preconditioner is how to efficiently approximate the difference matrix. One of the simplest and the most frequently used, but not most efficient, way is to use backward-Euler (BE) differentiation. Then, the difference matrix is

$$\mathbf{D} = \begin{bmatrix} \frac{\mathbf{I}}{\Delta t_1} & 0 & 0 & \dots & \frac{-\mathbf{I}}{\Delta t_1} \\ \frac{-\mathbf{I}}{\Delta t_2} & \frac{\mathbf{I}}{\Delta t_2} & 0 & \dots & 0 \\ 0 & \frac{-\mathbf{I}}{\Delta t_3} & \frac{\mathbf{I}}{\Delta t_3} & \dots & 0 \\ & & \ddots & \ddots & \\ 0 & 0 & \dots & \frac{-\mathbf{I}}{\Delta t_n} & \frac{\mathbf{I}}{\Delta t_n} \end{bmatrix}. \quad (8)$$

Since there is a nonzero block in the upper-right corner, the matrix is not cheaply invertible and, therefore, this block is ignored. Then, the equation  $(\mathbf{DC} + \mathbf{G})\mathbf{x} = \mathbf{b}$  can be solved efficiently in a block-wise manner.

The disadvantage of ignoring the upper-right block can be diminished, e.g., by iteration as shown in Ref. [4]. It, however, increases the cost and there is no guarantee that the iteration converges.

The variant of the time-domain preconditioner proposed in this paper compensates the absence of the upper-right block by applying forward-Euler integration at the first time point. Then,  $\mathbf{D}$  is

$$\mathbf{D} = \begin{bmatrix} \frac{-\mathbf{I}}{\Delta t_1} & \frac{\mathbf{I}}{\Delta t_1} & 0 & \dots & 0 \\ \frac{-\mathbf{I}}{\Delta t_2} & \frac{\mathbf{I}}{\Delta t_2} & 0 & \dots & 0 \\ 0 & \frac{-\mathbf{I}}{\Delta t_3} & \frac{\mathbf{I}}{\Delta t_3} & \dots & 0 \\ & & \ddots & \ddots & \\ 0 & 0 & \dots & \frac{-\mathbf{I}}{\Delta t_n} & \frac{\mathbf{I}}{\Delta t_n} \end{bmatrix}. \quad (9)$$

## 4 Simulation results

The preconditioners were implemented in the in-house development version of the APLAC circuit simulator. The tests were run on several relevant industrial circuits with an oversampling factor of 2. The circuit details are presented in Table 1.

**Table 1.** Number of nodes, harmonics used, resistors, capacitors, inductances, BJTs, MOSFETs, and diodes of example circuits.

Circ.	nodes	harmonics	R	C	L	BJT	Mos.	D.
1	272	16	72	36	-	-	288	-
2	9	16	3	1	-	1	-	-
3	31	64	2	-	-	1	12	-
4	80	8	14	1	3	8	-	-

The simulation results with different preconditioners are presented in Table 2. FD, TD1, and

TD2 stands for the standard frequency-domain block Jacobi preconditioner, the BE preconditioner, and the time-domain preconditioner proposed, respectively. A dash indicates that the HB simulation, i.e., inexact Newton iteration, did not converge.

**Table 2.** Number of GMRES iterations  $N_{\text{GMRES}}$ , number of HB iterations  $N_{\text{HB}}$  and simulation times  $t$  with different preconditioners.

c.	Prec.	$N_{\text{GMRES}}$	$N_{\text{HB}}$	$t/s$
1	FD	4721	59	195
	TD1	637	20	46
	TD2	-	-	-
2	FD	2451	23	0.51
	TD1	297	23	0.14
	TD2	196	23	0.10
3	FD	1376	49	19.1
	TD1	177	29	7.3
	TD2	-	-	-
4	FD	1462	26	4.6
	TD1	1528	26	6.5
	TD2	695	20	3.1

## 5 Conclusion

A variant of a time-domain preconditioner that tries to diminish the lack of periodicity in the BE preconditioner was proposed. In some cases, it worked fine, but unfortunately, in some cases not.

## References

1. Kenneth S. Kundert, Jacob K. White, and Alberto Sangiovanni-Vincentelli. *Steady-State Methods for Simulating Analog and Microwave Circuits*. Kluwer Academic Publishers, Boston, 1990.
2. D. Long, R. Melville, K. Ashby, and B. Horton. Full-chip harmonic balance. In *Proceedings of the IEEE 1996 Custom Integrated Circuits Conference*, pages 379–382, May 1997.
3. O. Nastov. *Spectral methods for Circuit Analysis*. PhD thesis, MIT, EECS, 1999.
4. Fabrice Veersé. Efficient iterative time preconditioners for harmonic balance RF circuit simulation. In *Proceedings of the 2003 IEEE/ACM International Conference on Computer-Aided Design*, pages 251–254, Washington, DC, USA, 2003. IEEE Computer Society.

# Evaluation of Oscillator Phase Transfer Functions

M.M. Gourary<sup>1</sup>, S.G. Rusakov<sup>1</sup>, S.L. Ulyanov<sup>1</sup>, M.M. Zharov<sup>1</sup>, B.J. Mulvaney<sup>2</sup>, and K.K. Gullapalli<sup>2</sup>

<sup>1</sup> IPPM, Russian Academy of Sciences, Moscow, Russia [gourary@ippm.ru](mailto:gourary@ippm.ru)

<sup>2</sup> Freescale Semiconductor Inc., Austin, Texas, USA [brian.mulvaney@freescale.com](mailto:brian.mulvaney@freescale.com)

**Summary.** A general expression for the phase transfer functions of an oscillator for frequencies close to harmonics of oscillator fundamental is derived. The numerical testing and comparison with some known results are performed.

## 1 Introduction

In this paper we obtain the phase transfer functions of an oscillator through the analysis of asymptotic behavior of Linear Periodically Time-Varying (LPTV) solution of oscillator circuit. The analysis is performed in frames of Harmonic Balance (HB) technique. Below we present basic expressions of LPTV HB analysis.

The LPTV analysis is performed after steady-state solution of an oscillator is obtained. The solution vector  $X$  involves nodal harmonics of oscillator fundamental  $\omega_0$  representing coefficients of Fourier series of periodic waveforms  $x(t)$ . Vector  $X$  consists of components  $X_{kl}$ , where  $k, l$ , are harmonic and nodal indexes respectively.

The quasi-periodic small signal model of oscillator is similar to the cyclostationary HB system for forced circuits [1]

$$J(\Delta\omega) \cdot \Delta X = B \quad (1)$$

Here a component  $B_{kl}$  of rhs vector  $B$  represents harmonic signal with frequency  $k\omega_0 + \Delta\omega$  applied to the  $l$ th circuit node. The vector  $\Delta X$  defines the small signal solution, and  $J(\Delta\omega)$  is a conversion matrix for the given frequency offset  $\Delta\omega$

$$J(\Delta\omega) = G + j(\Omega + \Delta\omega \cdot E)C \quad (2)$$

Here  $G, C$  are block Toeplitz matrices of harmonics of nodal conductances and capacitances,  $\Omega$  is a block-diagonal matrix of harmonic frequencies  $\Omega = \text{diag}[\dots, -k\omega_0, \dots, 0, \dots, k\omega_0, \dots]$ . The matrix (2) at zero offset coincides with the HB Jacobian matrix at the steady-state solution  $J(0) = J_0 = G + j\Omega \cdot C$ . So (2) can be written as

$$J(\Delta\omega) = J_0 + j\Delta\omega \cdot C \quad (3)$$

The Jacobian matrix  $J_0$  is singular, and so there exists the eigenvector  $U$  corresponding to zero

eigenvalue and the eigenvector  $V$  of the transposed Jacobian matrix such that

$$J_0 \cdot U = 0, \quad J_0^T \cdot V = V^T \cdot J_0 = 0 \quad (4)$$

The eigenvector  $U$  is a frequency domain representation of time derivatives of the large signal oscillator solution  $dx/dt$ . The eigenvector  $V$  is a frequency domain representation of the perturbation projection vector (PPV) introduced in [2]. The traditional normalization of  $V$  is defined as follows

$$V^T C U = 1 \quad (5)$$

## 2 Evaluation of Transfer Function

To obtain the transfer function it is needed to consider only one component in rhs vector. So we assume that the vector  $B$  contains only one nonzero component corresponding to harmonic  $k$  and node  $l$

$$B = e^{(kl)} \quad (6)$$

where unit vector  $e^{(kl)}$  selects  $kl$  component of rhs.

To analyze the solution of (1, 6) at small offset we transform (1, 6) into the equivalent linear system with nonsingular matrix by the method proposed in [3]. First we form a new equation by left multiplying (1) by PPV. Taking into account (3, 4, 6) we obtain

$$j\Delta\omega V^T C \Delta X = V_{kl} \quad \text{or} \quad V^T C \Delta X = \frac{V_{kl}}{j\Delta\omega} \quad (7)$$

Then we replace the equation (1) corresponding with the only nonzero component of the excitation (6) by the obtained equation (7). To simplify notations we assume the equation to be replaced is the last one in (1). Thus we obtain the transformed linear system

$$\hat{J} \Delta X = \frac{V_{kl}}{j\Delta\omega} e^{(kl)}, \quad (8)$$

where  $\hat{J}(\Delta\omega) = \begin{bmatrix} \bar{J} \\ V^T C \end{bmatrix}$ . Here  $\bar{J}$  is matrix  $J$  without the last row.

Note that in general case the matrix  $\widehat{J}(\Delta\omega)$  is not singular with  $\Delta\omega = 0$ . So at small offset one can neglect the matrix dependence on the offset

$$\widehat{J}(\Delta\omega) = \widehat{J}_0 + O(\Delta\omega) \approx \widehat{J}_0 = \begin{bmatrix} \bar{J}_0 \\ V^T C \end{bmatrix} \quad (9)$$

So the solution of (8) can be represented as

$$\Delta X(\Delta\omega) = \frac{V_{kl}}{j\Delta\omega} \widehat{J}_0^{-1} \cdot e^{(kl)} \quad (10)$$

From the definition of  $U$  (4) and  $\widehat{J}_0$  (9) it can be concluded that the matrix-vector product  $\widehat{J}_0 \cdot U$  contains only one nonzero component corresponding with replaced row

$$\widehat{J}_0 \cdot U = V^T C U \cdot e^{(kl)} = e^{(kl)} \quad (11)$$

The last equality in (11) follows from (5). Thus  $\widehat{J}_0^{-1} \cdot e^{(kl)} = U$ , and (10) can be written as

$$\Delta X(\Delta\omega) = \frac{V_{kl}}{j\Delta\omega} U \quad (12)$$

The component  $\Delta X_{mn}(\Delta\omega)$  of the vector (12) defines the magnitude of the harmonic  $m\omega_0 + \Delta\omega$  at  $n$ th node. So the time domain waveform at node  $n$  is defined as the sum of all harmonics at the node

$$\begin{aligned} \Delta x_n(t) &= \sum_m \Delta X_{mn}(\Delta\omega) \exp j(m\omega_0 + \Delta\omega)t \\ &= \exp j\Delta\omega t \cdot \sum_m \Delta X_{mn}(\Delta\omega) \exp jm\omega_0 t \end{aligned} \quad (13)$$

After substituting (12) into (13) we obtain

$$\Delta x_n(t) = \left( \frac{V_{kl}}{j\Delta\omega} \exp j\Delta\omega t \right) \cdot \sum_m U_{mn} \exp jm\omega_0 t \quad (14)$$

It has been pointed out that  $U_{nm}$  are harmonics of large signal time derivatives. So the sum in (14) represents Fourier series of  $dx_n/dt$ . Thus

$$\Delta x_n(t) = \frac{dx_n}{dt} \cdot \frac{V_{kl}}{j\Delta\omega} \exp j\Delta\omega t \quad (15)$$

This expression gives the voltage waveform at  $n$ th node resulted from the unit excitation (6). To obtain the phase transfer factor we can consider the waveform due to the phase modulation of oscillator solution  $x(t)$ . Supposing the magnitude of the phase modulation  $\Phi$  to be small we can apply first order Taylor expansion

$$\begin{aligned} x_n \left( t + \frac{\Phi}{\omega_0} \exp j\Delta\omega t \right) &= x_n(t) \\ &+ \frac{dx_n}{dt} \cdot \frac{\Phi}{\omega_0} \exp j\Delta\omega t \\ \text{or } \Delta x_n(t) &= \frac{dx_n}{dt} \cdot \frac{\Phi}{\omega_0} \exp j\Delta\omega t \end{aligned} \quad (16)$$

From comparison of (15) with (16) the phase magnitude  $\Phi$  can be determined. Its value is equal to the transfer factor  $H_{kl}^\phi$  from the sideband frequency of  $k$ th harmonic of the excitation at  $l$ th node to the baseband frequency of the phase

$$H_{kl}^\phi(\Delta\omega) = \Phi = \frac{\omega_0}{j\Delta\omega} V_{kl} \quad (17)$$

The evaluation of the transfer function  $H^\phi(\Delta\omega)$  can be easily implemented in a circuit simulator. PPV harmonics  $V$  can be obtained by the algorithm [4].

### 3 Validation

At low input frequency ( $\omega \ll \omega_0$ ) the transfer factor is defined by (17) with  $k = 0$ . It corresponds with the traditional VCO representation as an ideal integrator in PLL macromodels [5]  $\phi = K_{\text{VCO}} \nu_{\text{inp}} / j\omega$ , where  $K_{\text{VCO}}$  is the DC sensitivity of oscillation frequency. The sensitivity analysis of the steady-state solution confirms that  $K_{\text{VCO}} = \partial\omega_0 / \partial\nu_{\text{inp}} = \omega_0 V_{0,\text{inp}}$ .

Phase noise analysis can be done using (17). When unmodulated white noise source is attached to  $l$ th node the phase PSD is evaluated by

$$S_\phi = S \sum_k \left| H_{kl}^\phi(\Delta\omega) \right|^2 = \left( S \omega_0^2 \sum_k |V_{kl}|^2 \right) / \Delta\omega^2 \quad (18)$$

where  $S$  is the input PSD. This expression corresponds with time domain expressions in [4]. Numerical experiments performed by SPICE simulations also confirm the correctness of (17).

### References

1. V. Rizzoli, F. Mastri, and D. Masotti. General noise analysis of nonlinear microwave circuits by the piecewise harmonic balance technique. *IEEE Trans. Microwave Theory Tech.*, 42:807–819, May 1994.
2. A. Demir, A. Mehrotra, and J. Roychowdhury. Phase Noise in Oscillators: A Unifying Theory and Numerical Methods for Characterization. *IEEE Trans. on Circuits and Systems - I*, 47:655–674, May 2000.
3. M.M. Gourary, S.G. Rusakov, S.L. Ulyanov, M.M. Zharov, B.J. Mulvaney, and K.K. Gullapalli. New Numerical Technique for Cyclostationary Noise Analysis of Oscillators. *Proc. of the 37th European Microwave Conference*, Munich, 2007, pages 1173–1176.
4. A. Demir, D. Long, and J. Roychowdhury. Computing Phase Noise Eigenfunctions Directly from Steady-State Jacobian Matrices. *Int. Conf. Computer-Aided Design*, 283–288, Nov. 2000.
5. Ken Kundert. Predicting the Phase Noise and Jitter of PLL-Based Frequency Synthesizers. [www.designers-guide.org/Analysis/PLLnoise+jitter.pdf](http://www.designers-guide.org/Analysis/PLLnoise+jitter.pdf)

# Quasiperiodic steady-state analysis of electronic circuits by a spline basis

Hans Georg Brachtendorf<sup>1</sup>, Angelika Bunse-Gerstner<sup>2</sup>, Barbara Lang<sup>2</sup>, and Siegmard Lampe<sup>2</sup>

<sup>1</sup> University of Applied Science of Upper Austria [brachtd@fh-hagenberg.at](mailto:brachtd@fh-hagenberg.at),

<sup>2</sup> University of Bremen, Germany [Bunse-Gerstner@math.uni-bremen.de](mailto:Bunse-Gerstner@math.uni-bremen.de)

**Summary.** Multitone Harmonic Balance (HB) is widely used for the simulation of the quasiperiodic steady-state of RF circuits. HB is based on a Fourier expansion of the waveforms. Unfortunately, trigonometric polynomials often exhibit poor convergence properties when the signals are not quasi-sinusoidal, which leads to a prohibitive run-time even for small circuits. Moreover, the approximation of sharp transients leads to the well-known Gibbs phenomenon, which cannot be reduced by an increase of the number of Fourier coefficients.

In this paper we present alternative approaches based on cubic or exponential splines for a (quasi-) periodic steady state analysis. Furthermore, it is shown below that the amount of coding afford is negligible if an implementation of HB exists.

## 1 Summary

Electronic circuits lead to a system of generally nonlinear differential-algebraic equations (DAEs) of first order of dimension  $N$

$$f(v(t), t) = i(v(t)) + \frac{d}{dt} q(v(t)) + b(t) = 0 \quad (1)$$

$v : \mathbb{R} \rightarrow \mathbb{R}^N$  is the vector of the unknown node voltages and branch currents.  $q : \mathbb{R}^N \rightarrow \mathbb{R}^N$  is the vector of charges and magnetic fluxes,  $i : \mathbb{R}^N \rightarrow \mathbb{R}^N$  the vector of sums of currents entering each node and branch voltages. Furthermore  $b(t) : \mathbb{R} \rightarrow \mathbb{R}^N$  is the vector of input sources.

Circuit designers are often interested in the steady-state of the circuit, driven by a multi-tone signal. For clarity, we restrict below to the 2-tone case

$$b(t) = \sum_{k_1=-\infty}^{\infty} \sum_{k_2=-\infty}^{\infty} B_s(k_1, k_2) \cdot e^{(jk_1\omega_1 t)} e^{(jk_2\omega_2 t)} \quad (2)$$

In [1–3] it has been shown that a reformulation of the underlying ordinary DAE (1) into an appropriate partial DAE system eases the numerical treatment of the multitone problem. This method has been widely accepted by different research groups, i.e. [4–7].

*Theorem:*

*Consider the system of ordinary differential-algebraic equations (1) with quasi-periodic stimulus (2) and the partial DAE system*

$$f(\hat{v}(t_1, t_2)) = i(\hat{v}(t_1, t_2)) + \frac{\partial}{\partial t_1} q(\hat{v}(t_1, t_2)) + \frac{\partial}{\partial t_2} q(\hat{v}(t_1, t_2)) + b(t_1, t_2) = 0 \quad (3)$$

where the quasiperiodic stimulus  $b(t_1, t_2)$  is defined by

$$b(t_1, t_2) := \sum_{k_1=-\infty}^{\infty} \sum_{k_2=-\infty}^{\infty} B(k_1, k_2) \cdot e^{(jk_1\omega_1 t_1)} e^{(jk_2\omega_2 t_2)}$$

with Fourier coefficients  $B(k_1, k_2)$ .

Then

$$v(t) = \sum_{k_1=-\infty}^{\infty} \sum_{k_2=-\infty}^{\infty} V(k_1, k_2) \cdot e^{(jk_1\omega_1 + jk_2\omega_2)t}$$

is a steady-state solution of the ordinary differential-algebraic equation (1), if and only if

$$\hat{v}(t_1, t_2) = \sum_{k_1=-\infty}^{\infty} \sum_{k_2=-\infty}^{\infty} \hat{V}(k_1, k_2) \cdot e^{(jk_1\omega_1 t_1)} e^{(jk_2\omega_2 t_2)} \quad (4)$$

is a steady-state solution of the partial differential-algebraic equation as well. The two solutions are related by  $v(t) = \hat{v}(t, t)$  for all  $t \in \mathbb{R}$  and the relation  $V(k_1, k_2) = \hat{V}(k_1, k_2)$  holds. ■

The theorem states, that a solution of the underlying ordinary DAE can be obtained along a characteristic of the partial DAE.

Consider the two-tone signal  $v(t)$  depicted in fig. 1. Due to Nyquist's theorem, the time-step for a numerical solution of the underlying partial DAE should be at least twice the highest frequency of the waveform. However, the simulation interval on the other hand should be reciprocal to the lowest frequency of interest. Hence, the runtime depends highly on the ratios of the frequencies involved. In practical applications, the envelope is in the kHz or MHz range and the carrier frequency is often several GHz or higher. Simple transient simulation is therefore prohibitive.

Alternatively, consider the corresponding multitone signal  $\hat{v}(t_1, t_2)$  shown in fig. 2 with periodic boundary conditions along the  $t_1, t_2$  axes. The original signal  $v(t)$  is regained along the special characteristic  $t_1 = t_2 = t$ , i.e.  $v(t) = \hat{v}(t, t)$ .

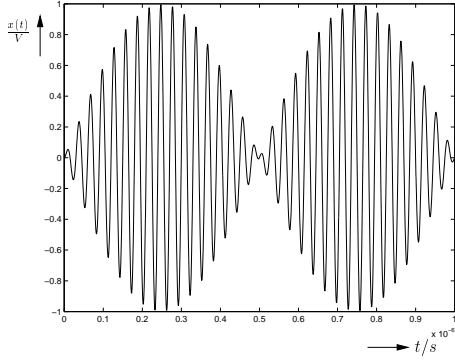


Fig. 1. Quasiperiodic signal example.

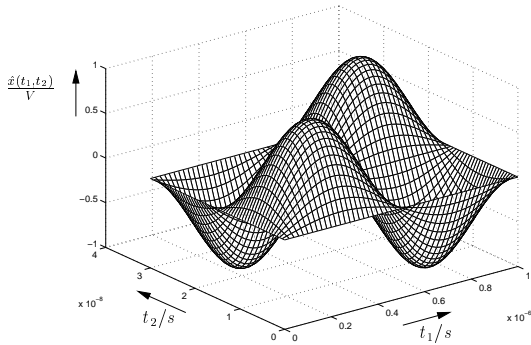


Fig. 2. Multitone signal example.

Please note the different scalings of the axes. The stiffness of the underlying ordinary DAE is casted into these different time-scales. This allows for a discretization with different grid-spacings and therefore a more appropriate discretization. The partial DAE formulation circumvents therefore the limitations of Nyquist's theorem.

Another way to consider the method is in the frequency domain as shown in fig. 3. The waveform  $v(t)$  has a broad but very sparse spectrum which is clustered along integer multiples of the carrier  $f_0$ . On the other hand, a reordering leads to the artificial two-dimensional spectrum illustrated in fig. 4, which is now a compact representation of the signal.

The spectrum of the waveform  $\hat{v}(t_1, t_2)$  is clustered and can therefore be compactly represented using a 2-dimensional Fourier transform.

The Fourier expansion used by the Harmonic Balance method (HB) of the unknown waveforms (4) is not appropriate for waveforms with sharp edges, because the approximation leads to the well-known Gibb's phenomenon. An approximation of the waveforms by a cubic or exponential spline basis is often better suited due to the finite support of the basis functions. We show that the coding of the spline approximation into an HB simulator is simple. Moreover, designers are mainly interested in Fourier coefficients and

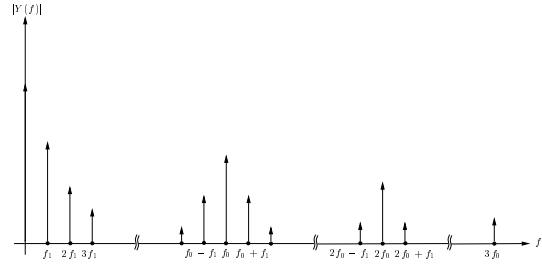


Fig. 3. Signal spectrum of  $v(t)$ .

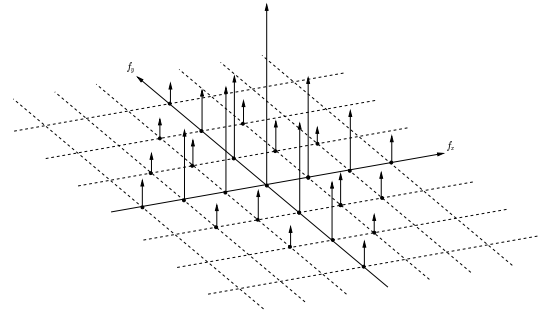


Fig. 4. Artificial spectrum of  $\hat{v}(t_1, t_2)$ .

not in the coefficients of the spline basis. We derive further a simple map from the spline to the Fourier basis.

## References

1. H. G. Brachtendorf. *Simulation des eingeschwungenen Verhaltens elektronischer Schaltungen*. Shaker, Aachen, 1994.
2. H. G. Brachtendorf. On the relation of certain classes of ordinary differential algebraic equations with partial differential algebraic equations. *Technical Report 1131G0-791114-19TM*, Bell-Laboratories, 1997.
3. H. G. Brachtendorf, G. Welsch, R. Laur, and A. Bunse-Gerstner. Numerical steady state analysis of electronic circuits driven by multi-tone signals. *Electronic Engineering*, **79**(2):103–112, April 1996.
4. R. Pulch and M. Günther. A method of characteristics for solving multirate partial differential equations in radio frequency application. *Preprint 07, IWRMM, Universität Karlsruhe*, 2000.
5. J. Roychowdhury. Efficient methods for simulating highly nonlinear multi-rate circuits. In *Proc. IEEE Design Automation Conf.*, pages 269–274, 1997.
6. J. Roychowdhury. Analyzing circuits with widely separated time scales using numerical pde methods. *IEEE Transactions on Circuits and Systems I - Fundamental Theory and Applications*, **48**:578–594, May 2001.
7. F. Constantinescu, M. Nitescu, F. Enache, 2D time domain analysis of nonlinear circuits using pseudo-envelope initialization., *Proceedings of the 2-nd International Conference on Circuits and Systems for Communication*, Moscow, 2004.

# Accurate Simulation of the Devil's Staircase of an Injection-Locked Frequency Divider

Tao Xu and Marissa Condon

Research Institute for Networks and Communications Engineering (RINCE), School of Electronic Engineering, Dublin City University, Dublin 9, Ireland [taoxu@eeng.dcu.ie](mailto:taoxu@eeng.dcu.ie), [condonm@eeng.dcu.ie](mailto:condonm@eeng.dcu.ie)

**Summary.** The Devil's Staircase of an Injection-Locked Frequency Divider (ILFD) is simulated in a novel and efficient manner in this contribution. In particular, the method of Multi-Phase Conditions-Based Envelope Following (MPCENV) is utilised. The locking range of the ILFD is then determined from the Devil's Staircase. The proposed method is applied to an LC oscillator based ILFD and the results are validated by comparison with experimental results.

## 1 Introduction

In general, Injection-Locked Frequency Dividers (ILFD) are used in the negative feedback of a frequency synthesizer as a prescaler to divide the frequency by a fixed number. In comparison with the traditional static [1] frequency dividers, the ILFDs consume less power but at the expense of a narrow locking range. Hence, the accurate determination of the locking range is important in the design of ILFDs. The Devil's Staircase [2] was introduced as an experimental method to measure the locking range. However, simulation would be a cheaper and preferable means of determining the locking range.

Since the ILFD is an oscillator with an injected signal, it can take thousands of cycles to lock the oscillator. Hence, traditional transient analysis takes far too long to be of use. However, the envelope-following methods provide an effective alternative. Here, we use the Multi-Phase Conditions-Based Envelope Following [3] (MPCENV) method to determine the locking range in an efficient manner.

## 2 Determination of the Locking Range

### 2.1 MPCENV Approach

The basis for envelope following methods is as follows:

The circuit solution is assumed to be composed of fast oscillations whose amplitude and

frequency varies much more slowly than the oscillations themselves. Let the period of the fast oscillation be  $T$ . In the case of oscillators, this will vary slowly. Let  $T_{\text{env}}$  be the envelope timestep over which the response of the system can be extrapolated.

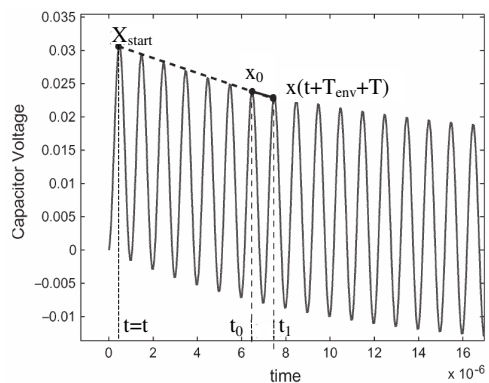


**Fig. 1.** Backward-Euler-based envelope-following method

As can be seen in Fig. 1, let  $x_0$  be the state at  $t_0 = t + T_{\text{env}}$ . Now  $x(t + T_{\text{env}} + T)$  is determined from  $x_0$  using an accurate simulation of one period  $T$ . Using the Implicit Euler Method for stability purposes, the envelope following process is described by

$$\frac{x(t + T_{\text{env}} + T) - x_0}{T} = \frac{x_0 - X_{\text{start}}}{T_{\text{env}}}. \quad (1)$$

Since  $T_{\text{env}}$  and  $T$  are also unknowns two further equations are required. They are shown as below:

$$x_{0l} = c \quad (2)$$

$$x(t + T_{\text{env}} + T)_l = c \quad (3)$$

where  $l$  denotes the  $l_{\text{th}}$  state variable and  $c$  is a constant. In our implementation,  $c$  is obtained by a short traditional transient simulation.

### 2.2 Devil's Staircase

The Devil's Staircase [2] is a plot of  $f_{\text{inj}}/f_0$  against  $f_{\text{inj}}$ . Figure 2 shows the experimental results for

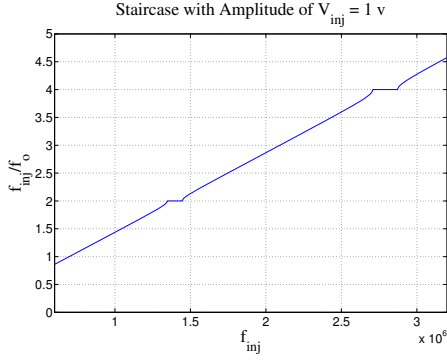


**Fig. 2.** The staircase obtained from experiment.

the ILFD. For simulation purposes, the injected frequency,  $f_{inj}$  is varied and  $f_0$  is determined from the MPCENV as:

$$f_0 = \frac{1}{T}. \quad (4)$$

### 3 Case Study and Numerical Results

The LC oscillator-based ILFD is selected as an example. The schematic is shown as below.

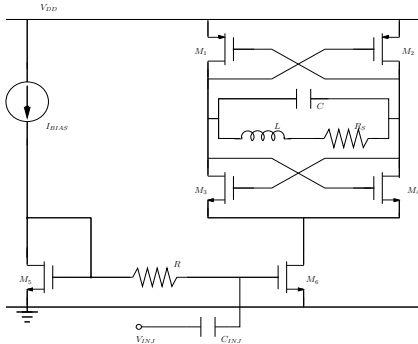


**Fig. 3.** Circuit schematic

The governing equations are:

$$C \frac{dV_C}{dt} = I_L - (A + daV_{inj})V_C + \frac{A + daV_{inj}}{V_{DD}^2} V_C^3, \quad (5)$$

$$L \frac{dI_L}{dt} = -I_L R - V_C, \quad (6)$$

where  $A$  and  $da$  are the coefficients obtained from the negative resistance [4].

The result obtained from the proposed method is shown in Fig. 4. Both the simulation and experimental results concur that the ILFD is locked when  $f_{inj}/f_0$  is an even number [4] i.e., 2 and 4 as shown in Fig. 2 and 4. Table 1 shows the locking ranges captured from the staircases. The error

between the simulation and experimental results is less than 5%.

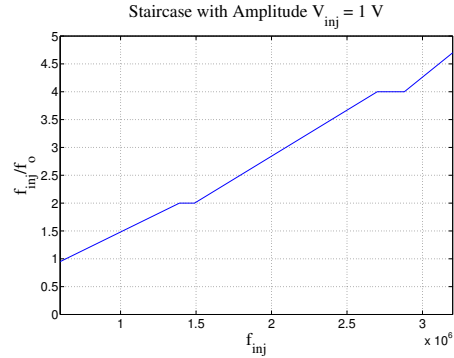


**Fig. 4.** The staircase obtained from simulation.

$V_{inj}$	$f_{inj}/f_0=2$		$f_{inj}/f_0=4$	
	S (MHz)	E (MHz)	S (MHz)	E (MHz)
1V	0.1	0.099	0.18	0.165
1.5V	0.14	0.146	0.235	0.241

**Table 1.** Locking range captured from staircases, where S and E represent **Simulation** and **Experiment**

### 4 Conclusions

A technique based on the Multi-Phase Conditions-Based Envelope Following (MPCENV) algorithm has been proposed for the determination of the locking range of ILFDs. The simulation technique is advantageous for design and analytical work as it is far less costly than experimental determination. Results for an LC-oscillator based ILFD confirm its efficacy.

### References

1. U. Singh, and M. Green, "Dynamics of high-frequency CMOS dividers", In *Proc. IEEE ISCAS*, vol.5, pp.421-424, May 2002.
2. D. O'Neill, D. Bourke and M. P. Kennedy, "The devil's staircase as a method of comparing injection-locked frequency divider topologies," In *Proc. ECCTD*, vol.3, pp.317-320, Sept. 2005.
3. T. Mei and J. Roychowdhury, "A time-domain oscillator envelope tracking algorithm employing dual phase conditions", *IEEE Trans. on Computer-Aided Design of Integrated Circuits and Systems*, Vol. 27, No. 1, January 2008.
4. T. Xu, Z. Ye, and M.P. Kennedy, "Mathematical Analysis of Injection-Locked Frequency Dividers", In *Proc. NOLTA*, pp.639-642, Sept. 2006.

# Nonlinear distortion in differential circuits with single-ended and balanced drive

Timo Rahkonen

University of Oulu, Finland [timo.rahkonen@ee.oulu.fi](mailto:timo.rahkonen@ee.oulu.fi)

**Summary.** Nowadays most of the high-resolution analog components have a fully balanced structure, i.e. they have differential input and output signals. This improves the tolerance against common mode interference and doubles the dynamic range, but also brings some new problems. The circuit now needs impedance match and stability analysis of both the differential and common mode operation, and also mode conversions from common mode to differential and vice versa may be of importance.

In circuit simulations the use of differential excitation is not a problem, but measuring instruments lag behind (at least if you do not buy new equipment): often the devices are characterised by driving the circuit from one port at a time with single-ended signals, and the differential or common mode behaviour is solved mathematically. Hence it is important to know when you can rely on single-ended measurements, and when these will give a different result compared to real balanced drive.

Circuit theory includes a lot of tricks used to study balanced circuits. For RF circuits, the formalism was presented by Bockelman and Eisenstadt [1]. They assumed that the balanced circuit (let us assume it is a fully differential amplifier, though the technique can handle any N-port with a mixture of single-ended and balanced signals) is measured by single-ended measurements as a linear 4-port, and presented the linear matrix transforms needed to calculate differential and common mode drives. This technique is called mixed-mode presentation, and it converts a 4-port s-parameter matrix to four 2-port matrices, one describing the truly differential operation, one common mode behaviour, and two remaining ones the mode conversions between these two. The latter are important for example when studying the rejection of even order distortion or other common mode interference.

Bockelman presented his formulation to s parameters, but the idea can naturally be extended to any linear parameters (see [2]), and normal design methods can be used - for example, one can pick the common-mode only presentation, and calculate the stability circles for the common mode matching impedances. The above needs only some matrix algebra, but due to simulator support it is usually avoided by simulating the device so that the device to be simulated is embedded between two ideal baluns (balanced-to-unbalanced transformers) and it is driven successively by common mode and differential signals. In more expensive simulations, however,

it would be helpful to have a sufficient signal processing functions that would enable the designer to drive the circuit with a single test signal containing both modes, and based on this simulation, track their mode changes inside the circuit.

The previous analysis assumes superposition to be valid and obviously does not operate in non-linear circuits. As the single-ended driving technique is largely used, however, it is valuable to know what exactly happens to the nonlinear distortion, when we drive the circuit with single-ended and balanced signals. For this analysis, we need a tool capable of plotting different distortion mechanisms separately.

Heiskanen et al. [3] have written a standard AC Volterra analysis software so that it stores all the different contributions of distortion in vector form - distortion from each nonlinear device and mixing mechanism can be plotted separately, and their phase relation is immediately visualised. The tool is written so that it calculates the nonlinear spectrum by a convolution of lower-order spectra, and this is performed so that mixing from different harmonic bands is calculated and stored separately. This makes it possible to track how much third-order distortion is actually generated by down or up-conversion from DC or 2nd harmonic bands. This feature is employed in the following analysis.

The purpose of this paper is the following: a fully balanced amplifier is driven both with a balanced and a single-ended test signal, and the differences in the generated distortion are recognised and explained. To illustrate it, the term-wise Volterra analysis software described in [3] is used.

The mechanism to be illustrated is the following. It is well known that a common-mode signal easily generates even-order distortion. This can be seen e.g. in 1, that models a bipolar differential pair, where  $I_0$  is the bias current and  $R_o$  is the output impedance of the current source. In balanced mode  $v_1 = -v_2$  and the bias current remains constant. However, with single-ended drive the common mode variation also modulates the bias current, causing additional even-order distortion, that is normally not seen in the  $\tanh(\cdot)$  response. The generated 2nd-order distortion will then be coupled back to the input via the DC feedback of the amplifier, and mix to the fundamental band, generating 3rd-order distortion. Hence, with single-ended drive a portion of the compression/expansion behaviour is caused by even-order distortion, that normally is very small in a device that is driven with balanced input signal.

$$i(t) = (I_0 + \frac{v_1 + v_2}{Ro}) \cdot \tanh(\frac{v_1 - v_2}{V_i}) \quad (1)$$

The contribution of this paper is to illustrate the above phenomenon using the Volterra analysis software [3]. It can plot all the 2nd and 3rd-order distortion components in a vector form, with magnitude and phase shown. This helps in understanding which phenomena are compressing, which expansive, and it also capable of illustrating the numerous cancelling effects inside a balanced circuit.

## References

1. D. Bockelman, W. Eisenstadt. Combined differential and common mode scattering parameters: theory and simulation. *IEEE Trans. on Microwave Theo. and Tech.*, , vol. 43, no 7, July 1995, pp. 1530-1539.
2. T. Rahkonen, J. Kortekangas. Mixed-mode parameter analysis of fully differential circuits. *IEEE Int'l Symposium on Circ. and Syst.*, Vancouver, Canada, May 23-26 2004, vol. 1, pp. 269-272.
3. A. Heiskanen, T. Rahkonen. 5th-order electro-thermal multi-tone Volterra simulator with component level output. *IEEE Int'l Symposium on Circ. and Syst.*, Bangkok, Thailand, May 25-28 2003, vol. 4, pp. 612-615.

# Speed-up techniques for time-domain system simulations

Timo Rahkonen

University of Oulu, Finland timo.rahkonen@ee.oulu.fi

**Summary.** Often, hardware description languages like Verilog-A or VHDL-AMS are used to build behavioral analog models and hence speed up the simulations of systems that contain a lot of DSP, long data sequences, and few analog parts. However, these models still rely on standard numerical transient analysis, that is slow in applications, that for some reason require much smaller time step than the sample duration.

This paper studies several situations, that are computationally expensive, and shows some ways to speed up the long transient simulations. Especially in the following applications, we need to simulate long sequences of data to catch some statistical properties of the signal, while very high oversampling is needed to model the non-ideal effects to be studied:

- Settling errors of the switched-capacitor (SC) integrators in A/D converters
- Small timing errors and slew rate errors (i.e., glitches) in the output of transmitter D/A converters
- Behaviour of modulated, linearly assisted switch-mode power supplies

The basic analysis techniques suited for the above applications have reported before, for example in [1], [2] and [3]. In this paper, the two of these techniques will be slightly expanded, verified more thoroughly, and applied for a more complex system.

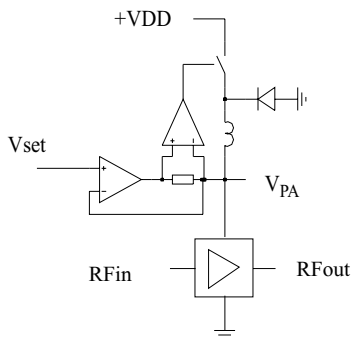


**Fig. 1.** Structure of an envelope tracking (ET) RF power amplifier.

Envelope tracking (see Fig. 1) is a popular technique to enhance the power efficiency of an RF transmitter. Here the supply voltage of the RF power amplifier is modulated by combination of a switch-mode

DC/DC downconverter, and an assisting linear amplifier. The input signal  $V_{SET}$  is sampled, but the linear settling within the sample period, high slew-rates of the signals controlling the switches, as well as the asynchronous control of the DC/DC converter force us to use a time step much smaller than the sampling period. This results in long simulation times. In [1] the simulation speed was enhanced by modeling the linear settling within one sample period by a linear state model of the switcher/amplifier combination

$$\begin{aligned} sX &= A \cdot X + B \cdot U \\ Y &= C \cdot X + D \cdot U. \end{aligned} \quad (1)$$

This traditional state model has the following general solution

$$x(t) = \phi(t) \cdot x(0) + \int_0^t \phi(t - \tau) B u(\tau) d\tau \quad (2)$$

where  $x(0)$  is the initial state vector and

$$\begin{aligned} \phi(t) &= \expm(At) \\ &= I + At + \frac{A^2 t^2}{2!} + \dots \end{aligned} \quad (3)$$

Assuming that the input signals  $U$  are stepwise constant (output of a D/A converter, for example), (2) can be simplified into form

$$x(t) = \phi(t) \cdot x(0) + A^{-1} \cdot (\phi(t) - I) \cdot B \cdot U. \quad (4)$$

This is readily solvable at any time point with normal matrix operations, without iteration or intermediate time points. Hence, this approach can be used to analyse the linear settling of filters, switches and other piecewise linear circuits without oversampling, but at the sample rate of the piece-wise constant input signal. One practical problem related to this approach is the formulation of the state matrix presentation.

Sometimes the response of the switched systems is not linear, and this is typically the case in SC amplifiers and integrators. Now the linear solution (4) can not be used. Several nonlinear behavioural models have been proposed, but they typically are simplified, for example excluding the effects of output related nonlinearities. However, the nonlinearity is deterministic, and can be pre-characterised for a given set of input signals. Such an approach is used in [3] to make a realistic but fast model of the first integrator in a sigma-delta ADC.

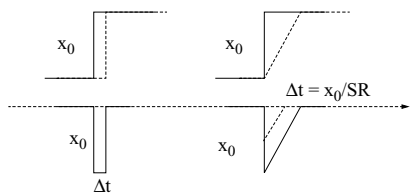


**Fig. 2.** Skew and slew rate errors in the output of a D/A converter

Yet another very expensive phenomenon to model is the small timing skew in a segmented D/A structure (illustrated in Fig. 2): here a portion of the output gets delayed by some picoseconds, resulting spurious spectral responses. Even more difficult to model is a finite slew rate in the output, because one needs a very high oversampling ratio to catch the shape of the slow-rate phenomenon. In [2] standard Fourier analysis was used to show that correct spectral response is actually achieved by using a lumped error model, where the area of the error is simply integrated and summed up to the correct value. Below are the lumped models of a timing skew with amplitude  $x_0$  and duration of  $\Delta t$ , and slew-rate error with amplitude  $x_0$  and duration of  $\Delta t$ .

$$\begin{aligned} e_{skew} &= x_0 \cdot \Delta t \\ e_{SR} &= \frac{x_0 \cdot \Delta t}{2} \end{aligned} \quad (5)$$

In this paper, the above analysis ideas will be studied a bit further by building up a simulation of following test cases:

- Comparison of lumped skew and slew rate error model and a precise linear settling result.
- System simulation of transmitter consisting of two time-interleaved D/A converters and a linear reconstruction filter.
- Finally, a technique for compressing a standard MNA matrix to a state matrix presentation is sought.

The first case is an extension of [2] where a simple numerical overampling was used as a reference for checking the validity of the lumped error models. Here, the lumped model will be compared against the solution given by the linear, time-varying state models. The test setup consists of a D/A converter with time skew errors, and a reconstruction filter, and the results of a lumped model and a linear solution calculated piecewise over all small time-skewed periods are compared.

The second case (see Fig. 3) is a previously presented D/A conversion system [4], that achieves linear phase image filtering by extending the hold duration of the samples: when the length of the hold time

equals the sample period, the notch of the sample-and-hold  $\text{sinc}/f$  frequency response is at the sample frequency. By extending the hold time (unfortunately, this requires the use of two parallel and time-interleaved D/A converters that can overlap their outputs) the notch can be brought down to filter the first image band. This operation has been verified in practice, but its simulation is quite lengthy, too, and here it serves as a test bench for really comparing the state model and lumped model presentation.

Last, ways to easily create the state model from netlist or a standard MNA matrix presentation are studied.

As a conclusion, this paper experiments methods to speed-up long time-domain system simulations by employing linear state modeling and lumped modeling of time skew errors. The experimented methods will be verified by Matlab simulations.

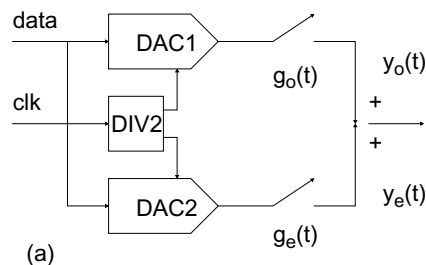


**Fig. 3.** Structure of a time-interleaved D/A converter pair.

## References

1. T. Rahkonen, O-P Jokitalo. Design of a linearly assisted switcher for a supply modulated RF transmitter. *Springer journal on Analog integrated circ. and signal proc.*, , vol. 54, no 2, February 2008, pp. 113-119.
2. T. Rahkonen, H. Repo. Efficient behavioral modelling of small timing errors in A/D and D/A converters. *Kluwer Academic journal on Analog Integrated Circuits and Signal Processing*, vol. 46, no. 1, January 2006, pp. 29-36.
3. M. Neitola, T. Rahkonen. Look-up based settling error modeling in Simulink. Submitted to *SCEE 2008 conference*.
4. T. Rahkonen, J. Aikkila. Linear phase reconstruction filtering using hold time longer than one sample period. *IEEE Trans. Circ. Syst. I*, vol. 51, no. 1, January 2004, pp.178-181.

# Lookup-Table Based Settling Error Modeling in SIMULINK

Marko Neitola and Timo Rahkonen

University of Oulu, Finland marko.neitola@ee.oulu.fi, timo.rahkonen@ee.oulu.fi

**Summary.** Behavioral modeling of circuit nonlinearities in a discrete-time simulator is essential especially in case of large mixed-signal systems. A delta-sigma (DS) converter is a good example of such system, because it is inherently a nonlinear and it needs long time-domain simulations to ensure the stability.

There are many publications, e.g [1–3], on how to model not only the settling error but most dominant non-idealities in a single SIMULINK behavioral model. This work concentrated only on the settling error part and provided a very simple, amplifier topology independent methodology. The behavioral model is based on characterization simulations using a comprehensive set of initial input and output transients. The resulting settling error table will be integrated into a SIMULINK-model using a lookup-table (LUT) block. The error model can be either one- or two-dimensional according to the capacitor network.

In the characterization of an amplifier, the settling error data can be originated from any simulator, and the amplifier detail level can be just as comprehensive as needed. In this work, we will show an example which used transient simulation data from a nonlinear state-space MATLAB-model of a two-pole amplifier. This amplifier is used in a switched-capacitor (SC) integrator.

Once the amplifier model is constructed, a designer may re-characterize and simulate the integrator quickly within a parameter sweep. Moreover, this approach avoids constructing complex output related analytical equations which are typically modeled as group of conditional function blocks in SIMULINK.

The behavioral SIMULINK-simulations of DS A/D-converter were made by sweeping the parameters that affect the slew-rate and phase margin of a SC-integrator. This type of behavioral simulation enables the designer to establish performance boundaries that makes less conservative parameter dimensioning possible.

The lookup-table approach is not tied to any specific SC-circuit model. In this work, we use a popular SC-integrator model of a parasitic insensitive SC-integrator as a case study. The initial voltage at the input of the amplifier is recognized by studying passive charge transfer in the capacitive network around the amplifier. All capacitors are initially charged to some voltage. When the capacitors are reconnected, the total charge is passively re-distributed, resulting in initial voltages  $v_{i0}$  and  $v_{o0}$  at the input and output of the operational amplifier. It is quite straightforward to construct charge-sharing equations for both phases of an SC-integrator.

Two switching capacitance networks of course results on two settling transients. Therefore, the settling error modeling is based on the error table acquired from two separate characterizations. This table is either one- or two-dimensional depending on the capacitor network topology. In our case study, the sampling phase  $\phi_1$  requires a two-dimensional error model as the charge transfer phase  $\phi_2$  only requires a one-dimensional settling error model. This means that in phase  $\phi_1$ , all integrator input signals and one output signals contribute to the initial input and output voltages.

The amplifier settling error is an error table obtained from settling simulations. These simulations can be performed by a simulation platform of users choice. This can be Spice, Verilog-A, VHDL-AMS, MATLAB, etc. The amplifier connected to a capacitance network is first excited with full range of input signals. Then, the simulated settling errors for both integrator phases and for each initial condition pairs are tabulated. Here we used MATLAB to create a realistic nonlinear state-space model of the amplifier. The settling error-table is obtained by simulating the state-space model defined by a group of differential equations and some nonlinear behavior.

In a single characterization shown in Fig. 1, we have a set of amplifier output voltage settling simulations for a hundred different initial input and output voltages. The settling errors are then compared to ideal results and the settling error is stored. In our case study, the settling error  $\epsilon_1$  from phase  $\phi_1$ , is dependent on  $v_{i0}$  and  $v_{o0}$ . For  $\phi_2$ , the error  $\epsilon_2$  is only dependent on  $v_{o0}$ .

The error tables are now used in SIMULINKs one- and two-dimensional lookup tables called "Lookup Table" and "Lookup Table (2-D)" [4]. In the sampling phase (phase  $\phi_1$ ) the LUT is two-dimensional and produces settling error  $\epsilon_1(n)$ . In the charge transfer phase, the LUT is one-dimensional and produces settling error  $\epsilon_2(n)$ .

The objective for the behavioral model was to observe delta-sigma A/D-converters performance as a function of slew-rate and closed-loop phase margin of an integrator. The model of a second order DS A/D-converter is presented in Fig. 2. It is a one-bit DS converter with oversampling ratio of 32. Sampling frequency is 10MHz and the integrator open-loop bandwidth is 65MHz. The LUT-block first calculates the initial voltages according to input and output signals using the charge sharing equations. After this, the lookup-tables are used to determine the settling errors  $\epsilon_1(n)$  and  $\epsilon_2(n)$ . In our case study, the error  $\epsilon_2(n)$  is summed to the output of the integrator and

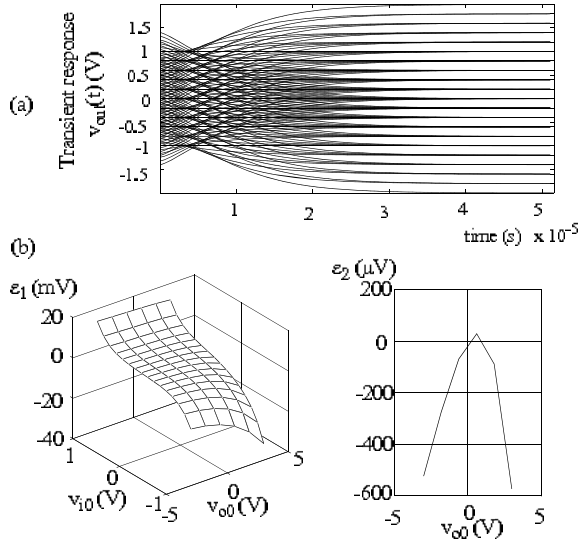


Fig. 1. a) Settling curves and b) the settling errors.

the sampling phase error  $\epsilon_1(n)$  is a two-dimensional error-model summed to the integrator input. The latter was found dominant settling error model throughout the parameter sweep.

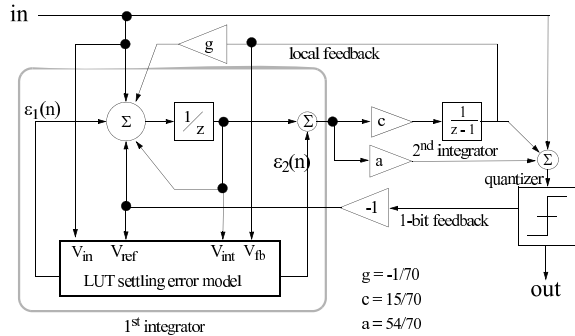


Fig. 2. SIMULINK-model of a second order DS A/D converter.

A full sweep contained 1024 characterizations and simulations. For each iteration, SNDR and SFDR performances were calculated. The object was to find performance boundaries as a function of slew-rate and phase margin. The result shown in Fig. 3 shows the 6 dB deterioration boundary of SFDR and 3 dB boundary of SNDR.

Initially, the DS converter had one-bit quantizer, and the boundary is shown in black graph in Fig. 3 a and b. The gray graph is the boundary for a three-bit DS-converter. The three-bit converter had the same converter topology with seven quantizer levels and coefficients optimized for three-bit quantizer. Concentrating only on the performance boundaries, the difference between these two converters can be seen in two areas:

1. With small slew-rates the three-bit converters SNDR and SFDR performance deteriorates less easily. This is explained by the fact that the three-bit feedback signal has significantly smaller

step-size, making the amplifier less susceptible to slew-rate.

2. In case of low phase margin and large slew-rate, the SNDR boundary of one-bit system is at lower phase margins simply due to some 25 dB lower maximum SNDR performance.

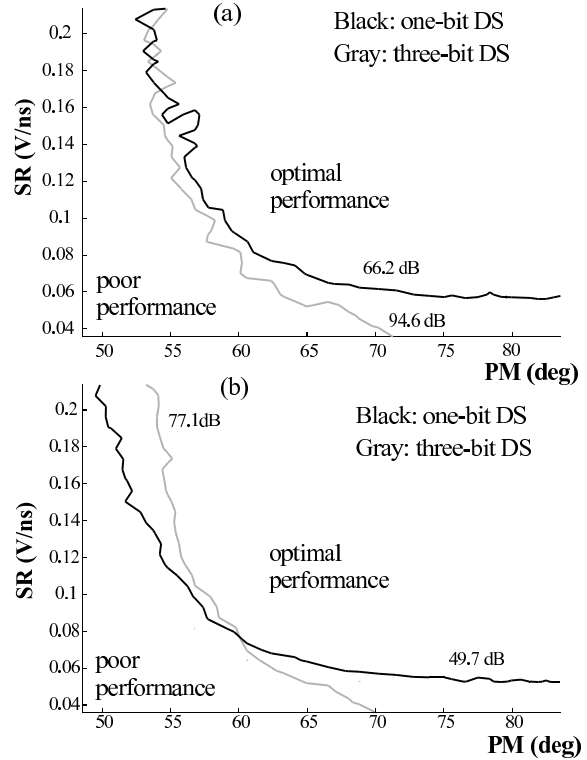


Fig. 3. Performance boundaries: a) 6 dB SFDR and b) 3 dB SNDR performance deterioration.

## References

1. W. M Koe and J. Zhang. Understanding the Effect of Circuit Non-idealities on Sigma-Delta Modulator. *Proceedings of the 2002 IEEE International Workshop on Behavioral Modeling and Simulation*, 94–101, 2002.
2. A. Fornasari, P. Malcovati, F. Maloberti. Improved Modeling of Sigma-delta Modulator Non-idealities in Simulink. *IEEE International Symposium on Circuits and Systems*, Vol.6:5982–5985, 2005.
3. H. Zare-Hoseini, I. Kale and O. Shoaei. Modeling of Switched-Capacitor Delta-Sigma Modulators in Simulink. *IEEE tr. Instrumentation and measurement*, Vol.54:1646–1654, 2005.
4. The Mathworks inc. *Simulink Release Notes, version R14 and higher*.

# BRAM - Backward Reduced Adjoint Method

Z. Ilievski<sup>1</sup>, W.H.A. Schilders<sup>1,2</sup>, and E.J.W. ter Maten<sup>1,2</sup>

<sup>1</sup> CASA - Technische Universiteit Eindhoven, 5600 MB Eindhoven z.ilievski@tue.nl

<sup>2</sup> NXP Semiconductors, Eindhoven

**Summary.** This paper describes the current available methods for the transient sensitivity analysis of electronic circuits and demonstrates how, by their adaptation through the inclusion of model order reduction techniques, the computational time needed to obtain satisfactory sensitivity values can be vastly reduced. The discussion is limited to linear problems.

## 1 Circuit Analysis

### 1.1 Circuit Equations

Equation (1) shows the Differential-Algebraic Equation that describes the behaviour of a standard electrical circuit that, on solving, will give the values of all the circuit states,

$$\frac{d}{dt} [\mathbf{q}(\mathbf{x}(t, \mathbf{p}), \mathbf{p})] + \mathbf{j}(\mathbf{x}(t, \mathbf{p}), \mathbf{p}) = \mathbf{s}(t, \mathbf{p}) \quad (1)$$

Here  $\mathbf{x}(t, \mathbf{p}) \in \mathbf{R}^N$  is the state vector which represents the node voltages and the currents through the voltage defined elements. The vector function  $\mathbf{j} \in \mathbf{R}^N$  describes the current behaviour and  $\mathbf{q} \in \mathbf{R}^N$  the charge and flux behaviour, all source values can be found in  $\mathbf{s}(t, \mathbf{p}) \in \mathbf{R}^N$

The vector  $\mathbf{p} \in \mathbf{R}^P$  represents the parameters of a component, such as the width and length of a resistor, on which a state  $\mathbf{x}(t, \mathbf{p})$  could depend upon.

Equation (1) can be rewritten as system (2), in which  $\mathbf{C} = \partial \mathbf{q} / \partial \mathbf{x}$  and  $\mathbf{G} = \partial \mathbf{j} / \partial \mathbf{x}$ ,

$$\mathbf{C} \dot{\mathbf{x}}(t, \mathbf{p}) + \mathbf{G} \mathbf{x}(t, \mathbf{p}) = \mathbf{s}(t, \mathbf{p}) \quad (2)$$

For the linear case that we are considering the coefficient matrices  $\mathbf{C}$  &  $\mathbf{G}$  are constant in time, they themselves are also dependent on the parameters  $\mathbf{p} \in \mathbf{R}^P$ . For electrical circuits,  $\mathbf{C}$  is a singular matrix.

### 1.2 Circuit Observation Functions

In addition to observing each individual circuit state the observation of the total performance of a circuit or a subcircuit can be done. For example, in an amplifier you may want to observe its total

gain; or perhaps take a closer look at the energy used by one of its resistors.

Equation (3) shows the form of the energy observation function. Relevant node or state values are already available for selection from the analysis in section 1.1,

$$\mathbf{G}_{\mathbf{F}}(\mathbf{x}(\mathbf{p}), \mathbf{p}) = \int_0^T \mathbf{F}(\mathbf{x}(t, \mathbf{p}), \mathbf{p}) \cdot dt \quad (3)$$

## 2 Sensitivity Types

### 2.1 State Sensitivity

Each state in (1) may have a dependence on one of the parameters in  $\mathbf{p}$ , this means it is sensitive to any parameter changes. Equation (4) shows an expression for these state sensitivities,

$$\hat{\mathbf{x}}(t, \mathbf{p}) \equiv \frac{\partial \mathbf{x}(t, \mathbf{p})}{\partial \mathbf{p}} \in R^{N \times P} \quad (4)$$

### 2.2 Observation Function Sensitivity

The function sensitivities are found in a similar way, they are the differentials of the observation function with respect to the parameters  $\mathbf{p}$ , (5) shows this sensitivity and also reveals the presence of the state sensitivity  $\hat{\mathbf{x}}$ ,

$$\frac{d\mathbf{G}_{\mathbf{F}}}{d\mathbf{p}} = \int_0^T \left( \frac{\partial \mathbf{F}}{\partial \mathbf{x}} \cdot \hat{\mathbf{x}} + \frac{\partial \mathbf{F}}{\partial \mathbf{p}} \right) \cdot dt \quad (5)$$

## 3 Sensitivity Analysis

Generally it is the calculation of the sensitivity of the observation function that is most useful, if possible with the avoidance of the calculation of the state sensitivities. In the following, in addition to  $N$  and  $P$ ,  $F$  is the number of observation functions.

### 3.1 Direct Forward Method

In this approach, after an initial forward state solution by a Newton-Raphson procedure involving the coefficient matrix  $\mathbf{Y} = \frac{1}{\Delta t} \mathbf{C} + \mathbf{G}$ , each state sensitivity value is explicitly calculated by recursion [1, 2]. To complete the calculation of the observation function sensitivities these state sensitivities are substituted into the integrand in (5), the total computational cost [3, SCEE, 2006] of one time integrand step is  $\mathcal{O}(\min(F, P)N^2 + FPN)$  operations.

### 3.2 Adjoint Transient Sensitivity Method

In [3] we give a full description of an approach based on (backward) adjoint integration [4], we were able to re-express the observation function integrand in terms of a function  $\lambda^*(t) \in \mathbf{R}^{F \times N}$ .

After an initial transient analysis, and suitably chosen boundary conditions a second equation (6), the Backward Adjoint Equation, yields unique values of  $\lambda(t)$ ,

$$\mathbf{C}^* \frac{d\lambda}{dt} - \mathbf{G}^* \lambda = -\left(\frac{\partial \mathbf{F}}{\partial \mathbf{x}}\right)^*. \quad (6)$$

The integrand of (5) has been reduced to an impressive  $\mathcal{O}(PN + FP)$ . When solving (6), each time integration requires  $W + \mathcal{O}(FN^2)$  operations.

The remaining burden is the  $W = \mathcal{O}(N^\alpha)$  ( $1 \leq \alpha \leq 3$ ) work needed for the LU-decompositions when integrating backward in time.

### 3.3 Backward Reduced Adjoint Method

We have noticed that (6) has the same form as the original circuit system (2), which suggests that both the forward and backward steps of section 3.2 could share important basic characteristics. We have carried out a more thorough analysis since our initial findings in [3], and these will be described in this presentation.

#### Proper Orthogonal Decomposition

The Proper Orthogonal Decomposition (POD) is a method that is popular for forming a description and obtaining the basis  $\mathbf{U}$  of a system by collecting its output behaviour  $X \in \mathbf{R}^{n,m}$ ,

$$\mathbf{X} = \mathbf{U}\mathbf{\Sigma}\mathbf{V}^T \quad (7)$$

$$\frac{1}{N} \mathbf{X}\mathbf{X}^T = \frac{1}{N} \mathbf{U}\mathbf{\Sigma}\mathbf{V}^T \mathbf{V}\mathbf{\Sigma}\mathbf{U}^T = \frac{1}{N} \mathbf{U}\mathbf{\Sigma}^2 \mathbf{U}^T \quad (8)$$

### Backward Reduction Step

The important step here is that we are able to reuse the effort in the forward analysis to construct projection matrices that can give a reduced  $W = \mathcal{O}(N_k^\alpha)$  (mentioned in section 3.2) where  $k$  is the number of dominant eigenvalues required for a satisfactory approximation.

This immediately gives rise to an attractive BRAM method, we will give a more vigorous explanation of the BRAM method in our paper.

### Other Considerations

We will pay extra attention to the following points.

- We have noticed that if we replace a component with an ever increasing equivalent series of components and then interpolate the states an eigenvalue stretch phenomenon is observed.
- The use of the projection matrix  $\mathbf{P}$ , itself dependant (and sensitive) on circuit parameters, reveals an extra term in the state sensitivity expression when projecting back in to the original space, as shown in (9). Here  $\tilde{\mathbf{x}}$  is the approximated state.

$$\frac{\partial \mathbf{x}}{\partial \mathbf{p}}(t, \mathbf{p}) \approx \frac{\partial \mathbf{P}(\mathbf{p})}{\partial \mathbf{p}} \cdot \tilde{\mathbf{x}}(t, \mathbf{p}) + \mathbf{P}(\mathbf{p}) \cdot \frac{\partial \tilde{\mathbf{x}}}{\partial \mathbf{p}}(t, \mathbf{p}) \quad (9)$$

*Acknowledgement.* The authors acknowledge the support by TU Eindhoven, NXP and by the EU Marie Curie RTN project COMSON grant n. MRTN-CT-2005-019417.

### References

1. L. Daldoss, P. Gubian, M. Quarantelli: *Multi-parameter time-domain sensitivity computation*, IEEE Trans. on Circuits and Systems - I: Fund. Theory and Applics, Vol. 48-11, pp. 1296–1307, 2001.
2. Y. Favennec, M. Girault, D. Petit: *The adjoint method coupled with the modal identification method for nonlinear model reduction*, Inverse Probl. in Science and Engng., Vol. 14, No. 3, 153–170, 2006.
3. Z. Ilievski, H. Xu, A. Verhoeven, E.J.W ter Maten, W.H.A. Schilders, R.M.M. Mattheij, *Adjoint transient sensitivity analysis in circuit simulation* SCEE2006, Scientific Computing in Electrical Engineering, Springer ISBN 978-3-540-71979-3, p183 -189,
4. Y. Cao, S. Li, L. Petzold, R. Serban: *Adjoint sensitivity for differential-algebraic equations: the adjoint DAE system and its numerical solution*, SIAM J. Sci. Comput., Vol. 24-3, pp. 1076–1089, 2002.

# Applications of Eigenvalue Inclusion Theorems in Model Order Reduction

E. Fatih Yetkin<sup>1</sup> and Hasan Dağ<sup>2</sup>

<sup>1</sup> İstanbul Technical University, Informatics Institute İstanbul, Turkey fatih@be.itu.edu.tr,

<sup>2</sup> Kadir Has University, İstanbul, Turkey hasan.dag@khas.edu.tr

**Summary.** We suggest a simple and efficient method based on the Gerschgorin eigenvalue inclusion theorem to compute a Reduced Order Model (ROM) to lower greatly the order of a state space system. This method is especially efficient in multi time scaled systems but it also works in other cases under some assumptions.

## 1 Introduction

The computational cost of the simulation of today's technological equipment can be very high. Hence the model order reduction methods have very wide application areas especially in sub-micron electronic device and microelectronic mechanical system (MEMS) modeling and simulation [1]. In general, a single input single output (SISO) system can be defined with the state equations in the standard form as below.

$$\begin{aligned}\dot{\mathbf{x}} &= \mathbf{A}\mathbf{x} + \mathbf{b}u \\ y &= \mathbf{c}^T\mathbf{x} + du\end{aligned}\quad (1)$$

where  $\mathbf{A} \in \mathcal{R}^{n \times n}$ ,  $\mathbf{b}, \mathbf{c} \in \mathcal{R}^n$  and  $d$  is a scalar. Here, the dimension of the state space  $n$  is very large and the model order reduction techniques are employed to build an  $m^{\text{th}}$  order system where  $m \ll n$ . The reduced system can be given as below,

$$\begin{aligned}\dot{\hat{\mathbf{x}}} &= \hat{\mathbf{A}}\hat{\mathbf{x}} + \hat{\mathbf{b}}u \\ y &= \hat{\mathbf{c}}^T\hat{\mathbf{x}} + du\end{aligned}\quad (2)$$

where  $\hat{\mathbf{A}} \in \mathcal{R}^{m \times m}$ ,  $\hat{\mathbf{b}}, \hat{\mathbf{c}} \in \mathcal{R}^m$  and  $d$  is a scalar [2]. Using the dominant eigenmodes is one of the best ways to build a reduced state space but it is not computationally feasible due to huge cost to compute all eigenmodes of the system at hand. Therefore, computing only the dominant poles of a transfer matrix can also be an effective way for computing the reduced system matrices [3]. In this study we suggest a new method based on the eigenvalue inclusion theorems such as that of Gerschgorin's. Gerschgorin discs are very useful and there are computationally efficient methods to determine the area of possible eigenvalue locations of a given matrix.

First a possible eigenvalue location and the number of eigenvalues are determined using one of these theorems. Then, the random complex numbers laid in Gerschgorin discs can be used instead of the original eigenvalues of  $A$ . These random eigenvalue estimates can be used to build a projection matrix to reduce the order of the system at hand with a reasonable frequency domain error. The approximate eigenvectors of the matrix  $A$  form the transformation matrix.

Gerschgorin discs are also used in conjunction with Singular Perturbation Approximation for reducing a system order [4]. This method requires that the system matrix  $A$  lend itself to partitioning so that it can be partitioned into two subsystems called fast and slow subsystems. They can be separated by their proximity to the origin of eigenvalues. To identify and separate these subsystems Gerschgorin theorem can be applied.

## 2 Method and Algorithm

Singular perturbation analysis based methods give very rapid and accurate results for small and multi-time scaled systems. But if system size gets larger, computational cost of the matrix inverses becomes infeasible. Therefore, more efficient strategies have to be developed. A given system's characteristic is determined by its eigenvalue. If we are interested in a reduced order model of a system at hand it is natural to select a group of dominant eigenvalues and construct the reduced model using those eigenvalues. On the other hand, computing a set of dominant eigenvalues of a matrix itself is a computationally expensive work. Thus, we choose to find approximation to the dominant eigenvalues. In order to have a good approximation to the eigenvalues of interest we use the Gerschgorin disks since all eigenvalues lie within the union of those disks. After selecting a group of approximate eigenvalues randomly within the union of the disks the transform matrices have to be computed to round all system triple into a reduced order.

If an approximate eigenvalue set is estimated with the Gerschgorin or Brauer theorem then the

approximate eigenvectors associated with these approximate eigenvalues can also be estimated. With this estimated set of eigenvectors we can build a transformation matrix to convert whole system to a reduced order system.

The last part of the work is estimating the eigenvectors corresponding to approximate eigenvalues. These eigenvectors have to be orthonormalized after estimation. The orthonormalized eigenvectors form a transformation matrix that is used to reduce the system order.

$$\begin{aligned} A_r &= V^T A V \\ \mathbf{b}_r &= V^T \mathbf{b} \\ \mathbf{c}_r^T &= \mathbf{c}^T V \end{aligned} \quad (3)$$

### 3 Numerical Examples

A fifth order random system is selected to make a comparison between suggested method and singular perturbation approximation. Using the Gerschgorin theorem, one can say that there are 3 separate eigenvalues very close to the origin. Then  $(A, \mathbf{b}, \mathbf{c})$  triple have to be reorganized due to eigenvalues and the associated rows. Then non-intersecting sets of Gerschgorin circles has to be employed to divide matrices in blocks. In this case we have three non-intersecting sets but we only consider to smallest set. Therefore the other two sets can be written as one set. We can separate system triple  $(A, \mathbf{b}, \mathbf{c})$  into blocks to apply singular perturbation approximation.

The original and the reduced systems frequency responses are given in Fig. 1 and 2.

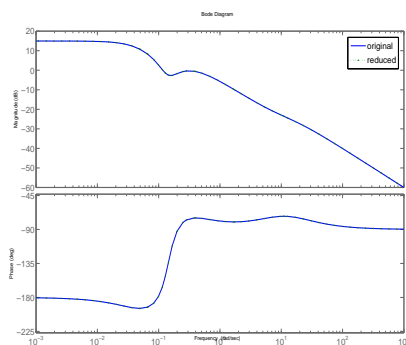


**Fig. 1.** Frequency plots of the original and reduced systems with singular perturbation approximation.

### 4 Conclusions and Future Work

In this study, dominant poles of the linear state space system are estimated using the Gerschgorin

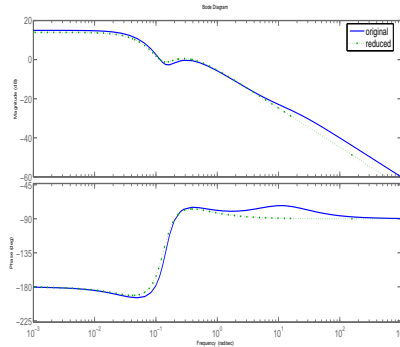


**Fig. 2.** Bode diagrams of reduced and full system with suggested new method.

theorem. This estimation is then used for producing the associated approximate eigenvectors. Then orthonormalized set of these approximate eigenvectors are used as a projection matrix to reduce the system order. The method gives very accurate results especially for multi-time systems -meaning that when the eigenvalues of matrix  $\mathbf{A}$  grouped in separate Gerschgorin discs. In these type of systems singular perturbation approximations also can be very successful. However, if whole eigenvalues of system lied in same location of the complex plane and Gerschgorin discs are nested, singular perturbation approximation does not work. The suggested method works well for both cases, but for the second case one has to run the algorithm several times for a satisfactory result. Therefore, more sophisticated eigenvalue inclusion theorems have to be employed for the second case. Future work is focused on using Brauer theorem and Gleyse method in algorithm to produce more accurate results.

### References

1. Meijs, N.P. , Smedes, T., Accurate Interconnect Modeling: Towards Multi-million Transistor Chips As Microwave Circuits. *Int. Conf. On CAD, Proc. of ICCAD'96* p. 244-251, 1996.
2. Tan, S. X. D, He, L., Advanced Model Order Reduction Techniques in VLSI Design, Cambridge University Press, Cambridge, 2007.
3. Rommes, J.: Methods for Eigenvalue Problems with Applications in Model Order Reduction, Ph.D. Thesis, Univ. of Utrecht, 2007.
4. Ansary, A., De Abreu-Garca, J.A.: A Simple Algorithm for Time Scale Separation, *Proceedings of the 15th International Conference on Industrial Electronics, Control, and Instrumentation (IECON'89)*, Vol. 2, p. 445, Philadelphia, PA, November 6-10, 1989.

# Hierarchical Model-Order Reduction Flow

Mikko Honkala<sup>1</sup>, Pekka Miettinen<sup>1</sup>, Janne Roos<sup>1</sup>, and Carsten Neff<sup>2</sup>

<sup>1</sup> Helsinki University of Technology, Department of Radio Science and Engineering, P.O.Box 3000, FI-02015 TKK, Finland {mikko,pekka,janne}@ct.tkk.fi

<sup>2</sup> NEC Laboratories Europe, IT Research Division, NEC Europe Ltd., Rathausallee 10, D-53757 St. Augustin, Germany neff@ccr1-nece.de

**Summary.** In this abstract, a Hierarchical Model-Order Reduction (HMOR) flow is proposed, where the linear parts of a circuit are hierarchically divided into independently reducible subcircuits. The impact of the hierarchical structure and circuit partitioning to three MOR methods are discussed, and some simulation results are presented.

## 1 Introduction

In this abstract the Hierarchical Model-Order Reduction (HMOR) of very large linear blocks of nonlinear circuits is considered. The HMOR hierarchically divides the circuit into subcircuits that can be independently reduced and then put together. The benefits of the HMOR are:

1. Very large circuits can be simulated in limited computer resources.
2. Circuit partitioning makes possible to apply parallel processing in a natural way.
3. The computational cost can be minimized by analyzing the repetitive structures only once.
4. The most suitable MOR method can be chosen for each subcircuit independently.

In the literature, HMOR is considered previously, e.g., in Ref. [1].

## 2 Hierarchical MOR flow

Here, a hierarchical netlist-in-netlist-out MOR flow is presented. The flow utilizes hMETIS [2] partitioning algorithms for circuit partitioning and uses the MOR methods in a hierarchical manner. The MOR methods considered are PRIMA [3], (modified) Liao–Dai [4], and TICER [5].

The HMOR flow proposed is presented briefly in the following.

1. *Netlist parsing:* extract the graph presentations of all the RLC circuits from the ‘messy’ (hierarchical) nonlinear SPICE netlist.
2. *Circuit partitioning:*
  - a) separate disconnected parts.

- b) divide each RLC graph (using hMETIS) into appropriate subcircuit graphs and map the graphs back into circuit netlists.
3. *Matrix construction:* build, for each subcircuit,  $\mathbf{G}$ ,  $\mathbf{C}$ , and  $\mathbf{B}$ , the conductance, capacitance, and selector matrix of the MNA formulation, respectively.
  4. *Model-order reduction:* use an appropriate MOR method for each subcircuit: PRIMA for RLC blocks, and Liao–Dai or TICER for RC blocks.
  5. *Macromodel realization:* synthesize each reduced subcircuit using resistors, capacitors, and, if needed, Voltage-Controlled Current Sources (VCCSes).
  6. *Netlist reconstruction:* include each macromodel in the proper position in the final netlist to achieve the original hierarchical structure.

## 3 Hierarchy and circuit partitioning

Consider a netlist consisting of linear and nonlinear components defined in hierarchical subcircuits (see Fig. 1). The netlist has, in addition to the main-level circuit (treated as a subcircuit equal to other subcircuits in the following), three different types of subcircuits. Each subcircuit may have nonlinear components (MOSFETs, diodes, etc.) and/or linear RLC components.

The subcircuit may have several disconnected RLC parts, and the same subcircuit can be placed several times in different levels of hierarchy.

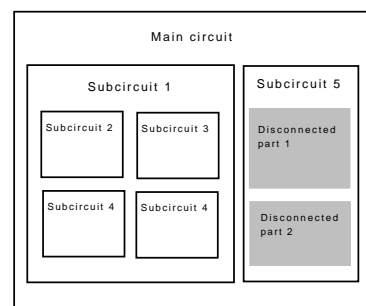


**Fig. 1.** The hierarchical structure of a circuit.

If the netlist is processed hierarchically, each subcircuit needs to be analysed only once, compared to a typical approach, where the whole netlist is first flattened with all the hierarchical structures written out for each reference. For example, Subcircuit 4 in Fig. 1 needs to be analyzed only once.

The subcircuit may contain disconnected RLC parts (e.g., see Subcircuit 5 in Fig. 1). If they are not separated into different subcircuits, numerical problems may arise. Even if no problems would occur, the disconnection is, in any case, a natural location for further partitioning.

Some MOR methods are based on partitioning, like Liao–Dai that employs low-order macromodels. For methods for which the partitioning is not an essential part of the algorithm (e.g., PRIMA) it is not clear whether further partitioning improves the performance. However, the partitioning is useful for large subcircuits in order to be able to reduce them at all with limited computer resources.

The goal of the circuit partitioning regarding MOR is to obtain such subcircuits that have a large number of internal nodes compared to external port nodes. Partitionings fulfilling this criterion are best suitable for MOR, since the behaviour of internal nodes are not interest and they may be reduced.

## 4 MOR methods

The three methods in the HMOR flow are chosen for their different approaches to MOR.

The well-known RLC MOR method PRIMA [3] employs congruence transformations to project a large system of equations onto a smaller subspace, so that passivity is preserved during reduction.

The Liao–Dai method [4] divides the circuit into smaller subcircuits, computes the first two moments of  $y$ -parameters of each subcircuit, and realizes the  $y$ -parameters by matching moments of RC macromodels.

TICER [5] is a nodal-elimination-based RC MOR method.

## 5 Simulation example

The HMOR flow has been implemented using C and MATLAB.

The Liao–Dai algorithm is tested with a large RC netlist. The results with several partitions are presented in Table 1, where  $N_p$ ,  $n$ , R, C,  $E_{tr}$ ,  $T_{tr}$ , and  $t_{tr}$  are the average partition size, number of

nodes, number of resistances, number of capacitances, error of transient analysis, CPU time of transient analysis, and normalized CPU time of transient analysis, respectively.

**Table 1.** Liao–Dai results for RC circuit with several partitions.

$N_p$	$n$	R	C	$E_{tr}/\%$	$T_{tr}/s$	$t_{tr}$
orig.	1537	10432	197	-	4.04	1.00
106	556	8515	573	0.009	5.77	1.43
53	237	3261	255	0.009	1.35	0.33
26	81	543	95	0.008	0.37	0.09
13	34	137	54	0.008	0.27	0.07
7	27	109	47	0.008	0.26	0.06
2	17	62	35	0.008	0.24	0.06
1	15	44	29	0.010	0.24	0.06

As can be seen from Table 1, the partitioning plays the key role in controlling the size and accuracy of the reduced circuit.

## 6 Conclusions

The hierarchical MOR flow was presented. It was shown how to reduce very large circuits using hierarchical circuit division. Without division the circuit may be so large that it is impossible to manage the computational cost.

*In the planned full paper, the MOR methods will be presented in detail and their suitability on HMOR will be discussed. More simulation results will be presented.*

## References

1. Y.-M. Lee, Y. Cao, T.-H. Chen, J. M. Wang, and C. C.-P. Chen. HiPRIME: Hierarchical and Passivity Preserved Interconnect Macromodeling Engine for RLCK Power Delivery. *IEEE Transactions on Computer-Aided design of Integrated Circuits and Systems*, 24:797–806, 2005.
2. G. Karypis and V. Kumar. *hMETIS, A Hypergraph Partitioning Package Version 1.5.3*.
3. A. Odabasioglu, M. Celik, and L. T. Pileggi. PRIMA: passive reduced-order interconnect macromodeling algorithm. *IEEE Transactions on Computer-Aided design of Integrated Circuits and Systems*, 17:645–654, 1998.
4. H. Liao and W. W.-M. Dai. Partitioning and reduction of RC interconnect networks based on scattering parameter macromodels. In *Digest of Technical Papers of IEEE/ACM International Conference on Computer Aided Design*, pages 704–709, 1995.
5. B. N. Sheehan. Realizable Reduction of RC Networks. in *IEEE Transactions on Computer-Aided Design of Integrated Circuits and Systems*, 26:1393–1407, 2007.

# Partitioning-based RL-in–RL-out MOR Method

Pekka Miettinen, Mikko Honkala, and Janne Roos

Helsinki University of Technology, Faculty of Electronics, Communications and Automation, Department of Radio Science and Engineering, P.O.Box 3000, FI-02015 TKK, Finland {pekka,mikko,janne}@ct.tkk.fi

**Summary.** This abstract proposes a netlist-in–netlist-out-type Model-Order Reduction (MOR) method suitable for the reduction of very large RL circuit blocks. The method relies on partitioning the circuit into subcircuits that can be approximated efficiently with low-order macromodels. The efficiency of the method is demonstrated with realistic simulations.

## 1 Introduction

Although the study of linear MOR with interconnect circuits has been centered mainly on RC and RLC circuits, some pure RL MOR algorithms have also been presented, e.g., in Refs. [1] and [2]. The demand for RL MOR arises in certain situations, such as when modeling a conductor’s skin effect with lumped elements or when operating at high frequencies, where the capacitances play a minor part.

Furthermore, one important motivation for the RL MOR presented in this abstract is the possibility to use it (linked with circuit partitioning) on a single RL block appearing inside a much larger RLC circuit. In this case, the RL MOR method is used as one of the many specialized methods in a complete MOR tool.

The basic idea behind the proposed RL MOR method is to partition the circuit into smaller subcircuits, which may then be approximated with relatively simple low-order macromodels, and finally, combined back together. The concept of low-order macromodels via partitioning was first presented in Ref. [3] for RC circuits. This was further studied and refined in Ref. [4] with support for RLC circuits by using also PRIMA [5] for the partitioned subcircuits. However, simulations with the original PRIMA algorithm resulted often with numerical stability issues.

In this abstract, a stable RL MOR method for the special case of RL circuits is proposed, inspired by the original RC MOR method in Ref. [3]. The proposed RL-in–RL-out MOR method may be conceptually divided into three steps: circuit partitioning (Sect. 2), calculation of  $y$ -parameter moments (Sect. 3), and macromodel synthesis (Sect. 4).

## 2 Circuit partitioning

Since the RL MOR method is based on approximating interconnects between port nodes with low-order macromodels, it is necessary to perform a partition on the large RL(C) circuit prior to macromodel synthesis. The quality of the subcircuits is essential; if the subcircuits are too complex, the low-order macromodel used later is not accurate enough to model the partition, while if the subcircuit is too simple, the magnitude of the reduction is small and the MOR is of little use.

METIS is an algorithm package for partitioning large irregular graphs, partitioning large meshes, and computing fill-reducing orderings of sparse matrices. The use of METIS and hMETIS algorithms especially in circuit partitioning was studied in Ref. [4], where it was noted that they both produced excellent partitionings of equal size. In this abstract, we consider the hMETIS algorithm as a partitioning method in the complete MOR flow [4].

## 3 Calculation of $y$ -parameter moments

Once the RL(C) circuit is partitioned into RL subcircuits, the  $y$ -parameters are needed to obtain the corresponding macromodel. The Laplace-domain circuit equations for an RL circuit can be expressed as

$$\begin{cases} (\mathbf{G} + \frac{1}{s}\mathbf{\Gamma})\mathbf{x}(s) = \mathbf{B}\mathbf{u}(s) \\ \mathbf{i}(s) = \mathbf{L}^T\mathbf{x}(s), \end{cases} \quad (1)$$

where  $\mathbf{x}$  denotes the nodal voltages and port currents,  $\mathbf{u}$  denotes the port voltages, and  $\mathbf{i}$  denotes the port currents. Here,  $\mathbf{B} = \mathbf{L}$  is a selector matrix consisting of ones, minus ones, and zeroes,

$$\mathbf{G} = \begin{bmatrix} \mathbf{G}_{11} & \mathbf{M}_u \\ -\mathbf{M}_u^T & 0 \end{bmatrix} \quad \mathbf{\Gamma} = \begin{bmatrix} \mathbf{\Gamma}_{11} & 0 \\ 0 & 0 \end{bmatrix}. \quad (2)$$

Matrices  $\mathbf{G}_{11}$  and  $\mathbf{\Gamma}_{11}$  contain the conductance and inductance element stamps, and  $\mathbf{M}_u$  consist of the stamps for the port-voltage sources. Solving now for the port currents and defining

$\mathbf{A} \equiv -\mathbf{G}^{-1}\mathbf{\Gamma}$  and  $\mathbf{R} \equiv -\mathbf{G}^{-1}\mathbf{B}$  results in the following  $y$ -parameter matrix:

$$\mathbf{Y}(s) = \mathbf{L}^T \left( \mathbf{I} - \frac{1}{s} \mathbf{A} \right)^{-1} \mathbf{R}, \quad (3)$$

Finally, the term  $(\mathbf{I} - \frac{1}{s} \mathbf{A})^{-1}$  can be expanded into a Neumann series to obtain

$$\mathbf{Y}(s) = \mathbf{M}_0 + \mathbf{M}_1 \frac{1}{s} + \mathbf{M}_2 \frac{1}{s^2} + \dots \quad (4)$$

The block moments of  $\mathbf{Y}$  can be calculated using the relation  $\mathbf{M}_i = \mathbf{L}^T \mathbf{A}^i \mathbf{R}$ . Note that the dimension ( $N$ -by- $N$ ) of the block moments  $\mathbf{M}_i$  is the same as the number ( $N$ ) of ports in the (sub)circuit.

## 4 Macromodel synthesis

For an  $N$ -port, the admittance between the  $i$ th port and ground is given by the sum of the  $i$ th row (or column) of its  $\mathbf{Y}$ -matrix,  $\mathbf{Y}(s)$ . The admittance connecting port- $i$  and port- $j$  is  $-y_{ij}$ . Thus, the circuit synthesis problem amounts to synthesizing admittances between pairs of ports and between a port and ground with lumped  $R$  and  $L$  elements. Once  $\mathbf{M}_0$  and  $\mathbf{M}_1$  have been calculated, each element of  $\mathbf{Y}(s)$  can be approximated as

$$y_{ij} \approx m_0^{ij} + m_1^{ij} s. \quad (5)$$

Using a direct synthetization, the first two moments are realized with parallel  $R$  and  $L$  elements. For off-diagonal elements  $y_{ij} (i \neq j)$ ,

$$R_{ij} = -\frac{1}{m_0^{ij}} \quad \text{and} \quad L_{ij} = -\frac{1}{m_1^{ij}}. \quad (6)$$

For diagonal elements  $y_{ii}$ ,

$$R_{ii} = \frac{1}{m_0^{i0}} \quad \text{and} \quad L_{ii} = \frac{1}{m_1^{i0}}. \quad (7)$$

## 5 Simulation results

The RL MOR algorithm was verified and simulated with several interconnect RL circuits, of which two representative cases are shown in Table 1. Here,  $n$ ,  $R$ ,  $L$ ,  $cp$ ,  $E_{tr}$  and  $T_{tr}$  mean the number of nodes, resistances, inductances, element reduction ratio, relative transient analysis error, and transient analysis CPU time, respectively. From the table it can be seen that the algorithm achieves excellent reduction of CPU time with only a minimal error. Figure 1 shows the comparison of transient simulations with the original and reduced circuit c2. *In the planned full paper, the RL MOR method is presented in more detail, and more types of different RL circuits are simulated, along with a comparison to other MOR methods.*

**Table 1.** Simulation results

circuit	$n$	$R$	$L$	$cp/\%$	$E_{tr}/\%$	$T_{tr}/s$
orig. c1	2000	2000	2000	-	-	3.25
reduc. c1	63	34	41	97.6	0.198	0.10
orig. c2	10000	10000	10000	-	-	123
reduc.c2	154	99	102	99.0	0.354	0.16

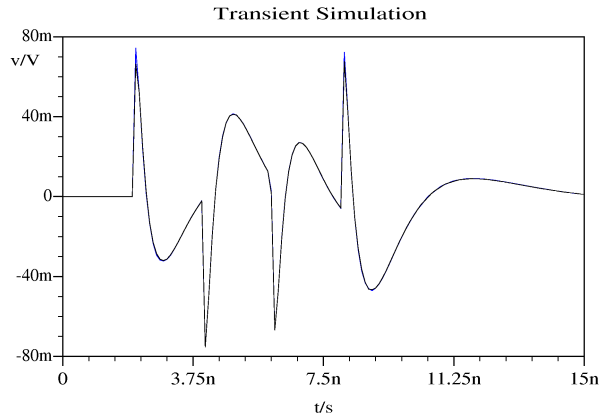


**Fig. 1.** Transient simulation of original and reduced circuit c2 (the curves are nearly indistinguishable).

## 6 Conclusions

In this abstract, a new RL MOR method capable of efficient reduction of very large RL circuits was proposed. Using partitioning to generate smaller subcircuits, a method of calculating the block moments of the  $y$ -parameters was described and a macromodel realization for the first two moments derived. Finally, simulation results showing excellent reduction were presented.

## References

1. S. Mei and Y.I. Ismail. Modeling Skin Effect with Reduced Decoupled R-L Circuits. *Proceedings of the 2003 International Symposium on Circuits and Systems*, 4:588–591, 2003.
2. Q. Yu and E.S. Kuh. Accurate Reduced RL Model for Frequency Dependant Transmission Lines. *The 9th International Conference on Electronics, Circuits and Systems*, 2:761–764, 2002.
3. H. Liao and W.W.-M. Dai. Partitioning and Reduction of RC Interconnect Networks Based on Scattering Parameter Macromodels. *Digest of Technical Papers of IEEE/ACM International Conference on Computer Aided Design*, 704–709, 1995.
4. P. Miettinen. Hierarchical Model-Order Reduction Tool for RLC Circuits. Master's thesis, Helsinki University of Technology, 2007.
5. A. Odabasioglu, M. Celik, and L.T. Pileggi. PRIMA: Passive Reduced-Order Interconnect Macromodeling Algorithm. *IEEE Transactions on Computer-Aided design of Integrated Circuits and Systems*, 17:645–654, 1998.

# Nonlinear model order reduction based on trajectory piecewise linear approach: comparing different linear cores

Kasra Mohaghegh<sup>1,3</sup> and Michael Striebel<sup>2,3</sup>

<sup>1</sup> Bergische Universität Wuppertal mohaghegh@math.uni-wuppertal.de

<sup>2</sup> TU Chemnitz michael.striebel@mathematik.tu-chemnitz.de

<sup>3</sup> NXP Semiconductors, Eindhoven

**Summary.** Refined models for MOS-devices and increasing complexity of circuit designs create the need for Model Order Reduction (MOR) techniques that are capable of treating nonlinear problems. In time-domain simulation the Trajectory PieceWise Linear (TPWL) approach is promising as it is designed to use MOR methodologies for linear problems as the core of the reduction process. We compare different linear approaches with respect to their performance when used as kernels for TPWL.

## 1 Introduction

The tendency to analyze and design systems of ever increasing complexity is becoming more and more a dominating factor in progress of chip design. Along with this tendency, the complexity of the mathematical models increases both in structure and dimension. Complex models are more difficult to analyze, and due to this it is also more difficult to develop control algorithms. Therefore Model Order Reduction is of utmost importance. For linear systems, quite a number of approaches are well-established and have proved to be very useful. However, accurate models for MOS-devices introduce highly nonlinear equations. And, as the packing density in circuit design is growing, very large nonlinear systems arise. Hence, there is a growing request for reduced order modeling of nonlinear problems. In transient analysis the Trajectory PieceWise Linear approach [5] is a promising technique as it makes use of linear MOR methods. A brief introduction to TPWL is given below.

Analysing the TPWL approach, we are interested in how different linear MOR techniques perform when used as a linear kernel, how robust the reduced model are and how they behave when combined to more complex systems.

## 2 MOR for linear problems

A continuous time-invariant (lumped) multi-input multi-output linear dynamical system is of the form:

$$\begin{cases} C \frac{dx(t)}{dt} = -Gx(t) + Bu(t) \\ y(t) = Lx(t) + Du(t), \quad x(0) = x_0, \end{cases} \quad (1)$$

where  $x(t) \in \mathbb{R}^n$  is the inner state;  $u(t) \in \mathbb{R}^m$  is the input,  $y(t) \in \mathbb{R}^p$  is the output. The dimension  $n$  of the state vector is called the order of the system.  $C$ ,  $G$ ,  $B$ ,  $L$  and  $D$  are the state space matrices. The dimension  $n$  of the system is of the order of elements contained in the circuit. As VLSI systems exhibit a large density of elements,  $n \gg \max(m, p)$  is usually very large.

Basically, MOR techniques aim to derive a system:

$$\begin{cases} \tilde{C} \frac{d\tilde{x}(t)}{dt} = -\tilde{G}\tilde{x}(t) + \tilde{B}u(t), \quad \tilde{x}(t) \in \mathbb{R}^q \\ y(t) = \tilde{L}\tilde{x}(t) + \tilde{D}u(t), \quad \tilde{x}(0) = \tilde{x}_0 \end{cases} \quad (2)$$

of order  $q$  with  $q \ll n$  that can then replace the original high-order system (1) in a sense, that the input-output behaviour, described by the transfer function in the frequency domain, of both systems is similar.

The reduction can be carried out by means of different techniques. Aiming at a combination with TPWL we concentrate on projection based approaches, namely SPRIM [2], PRIMA [3], and PMTBR [4]. The first two rely on Krylov subspace methods, which provide numerically robust algorithms for generating approximations to the transfer function of the full system (1) that match a certain number of its moments. Owing to their robustness and low computational cost, Krylov subspace algorithms proved suitable for reduction of large-scale systems, and gained considerable popularity, especially in electrical engineering.

PRIMA combines the moment matching approach with projection to arrive at a reduced system of type (2). Its main features is that it produces provably passive order reduced models.

SPRIM which can preserve reciprocity or the block structure of the circuit matrices, inherent to RLC circuits is also studied. SPRIM generates provably passive and reciprocal macromodels of multiport RLC circuits. The SPRIM models match twice as many moments as the corresponding PRIMA models obtained with same amount

of computational work, also SPRIM is less restrictive to  $C$  &  $G$  in system (1), see [1].

PMTBR is a projection MOR technique that exploits the direct relation between the multi-point rational projection framework and the Truncated Balanced Realization (TBR). This approach can take advantage of some a priori knowledge of the system properties, and it is based in a statistical interpretation of the system Gramians.

*Example 1.* [6] We consider the RLC ladder network shown in Fig. 1. The MNA modeling leads to odd  $n$ . We take  $n = 401$  and arrange  $R_1 = \frac{1}{2}$ ,  $R_2 = \frac{1}{5}$  and all inductors and capacitors have unit value.

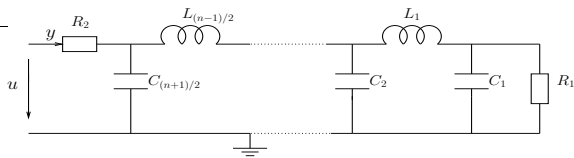


Fig. 1. RLC Circuit of order  $n$ .

The original transfer function is reduced by three linear techniques (PRIMA, SPRIM and PMTBR) from order 401 to order 37. Figure 2 presents the most dominant error parts for these methods.

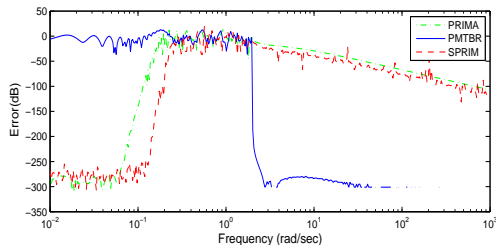


Fig. 2. Corresponding error plot.

### 3 MOR for nonlinear systems – TPWL

An electrical circuit that contains nonlinear elements, like MOS-transistors, can be described by a nonlinear differential-algebraic equation (DAE) of the form

$$\frac{d}{dt}[q(x(t))] + j(x(t)) + Bu(t) = 0 \quad (3)$$

with  $q, j : \mathbb{R}^n \rightarrow \mathbb{R}^n$ ,  $u : \mathbb{R} \rightarrow \mathbb{R}^m$ ,  $B \in \mathbb{R}^{n \times m}$ . Again, one is interested in replacing (3) by a system of much smaller dimension. At present, however, only linear MOR techniques are well-enough developed.

TPWL [5, 7], the trajectory piecewise linear approach, allows MOR techniques developed for the linear problem (1) to be applied to nonlinear system (3). This is done by linearizing (3) several times along a trajectory, reducing the linear local ersatz systems and recomposing these models again. The latter step is done by means of a weighted sum, i.e. a linear combination of all the submodels available. To represent the nonlinear characteristics by a series of linear models, typical input signals  $u(t)$  are applied, giving typical trajectories which are then used in the described procedure. Hence, TPWL leads to an order-reduced model that is trained to replace the full nonlinear systems for a certain class of input signals.

We compare the behaviour of TPWL, when PRIMA, SPRIM and PMTBR are used as reduction kernel. Furthermore, we study the sensitivity of the reduced models w.r.t. different inputs. We apply the TPWL to a chain of nonlinear inverters. Observations made lead to considerations on improvements of the weighting, i.e. the process of recombining the local reduced linear models.

*Acknowledgement.* The work presented is supported by the Marie Curie RTN and ToK projects COMSON and O-MOORE-NICE!, respectively.

### References

1. R.W.Freund. Structure-Preserving Model Order Reduction of RCL Circuit Equations. In: *Model Order Reduction: Theory, Research Aspects and Applications*, H.A. van der Vorst, W.H.A.Schilders & J.Rommes (eds.): Springer-Verlag 2008, to appear.
2. R.W.Freund. SPRIM: structure preserving reduced-order interconnect macromodeling. *Proc. ICCAD*, pp. 80-87, 2004.
3. A.Odabasioglu, M.Celik, L.Paganini. PRIMA: Passive reduced-order interconnect macromodeling algorithm. *IEEE TCAD of Integ. Circuits and Systems*, vol. 17(8), pp. 645-654, 1998.
4. J.Phillips, L.M.Silveira. Poor's man TBR: a simple model reduction scheme. *Proc. DATE*, vol. 2, pp. 938-943, 2004.
5. M.J.Rewieński. A Trajectory Piecewise-Linear Approach to Model Order Reduction of Nonlinear Dynamical Systems. Ph.D. thesis, MIT, USA, 2003.
6. D.C.Sorensen. Passivity Preserving Model Reduction via Interpolation of Spectral Zeros: *System and Control Letters*, vol. 54(4), pp. 347-360, 2005.
7. T.Voß, R.Pulch, J.ter Maten, A.El Guennouni. Trajectory piecewise linear approach for nonlinear differential-algebraic equations in circuit simulation. In: G.Ciuprina, D.Ioan (eds.): *Proc. SCEE. Mathematics in Industry*, vol. 11, Springer, pp. 167-174, 2007.

# On Model Order Reduction for Perturbed Nonlinear Neural Networks with Feedback

Marissa Condon<sup>1</sup> and Georgi G. Grahovski<sup>1,2</sup>

<sup>1</sup> School of Electronic Engineering, Dublin City University, Glasnevin, Dublin 9, Ireland  
Marissa.Condon@dcu.ie, grah@eeng.dcu.ie

<sup>2</sup> Institute for Nuclear Research and Nuclear Energy, Bulgarian Academy of Sciences,  
72 Tzarigradsko chaussee, 1784 Sofia, Bulgaria grah@inrne.bas.bg

**Summary.** The paper addresses the dynamical properties of large-scale perturbed nonlinear systems of the Hopfield type with feedback. In particular, it focuses on the hyperstability of the equilibria of the system. It proceeds to examine the effect of the empirical balanced truncation model reduction technique on the hyperstability properties. The results are illustrated using a numerical test case.

## 1. Introduction/Motivation

Neural networks have attracted the attention of the scientific community for several decades [2, 7] and of these, one of the most important nonlinear neural networks is the Hopfield model [5, 6] which was introduced by J. J. Hopfield in the 1980s. It has been extensively studied (see, e.g., [8] and the references therein) and has found many important applications in diverse areas such as pattern recognition, associative memory and combinatorial optimisation.

The study of the stability of the equilibrium points is an important area which has been the focus of study over the past number of years. One of the reasons for its importance is that if an equilibrium of a Hopfield neural network is globally asymptotically stable, then the domain of attraction of this point is the entire state space [8].

A special subclass of the Hopfield neural networks are Hopfield networks models with feedback. In this case, an additional functional dependence is imposed between the inputs and the corresponding outputs. This is related to the passivity property of the considered system [9].

In most of the applications involving neural networks, the model equations form a large-scale system (see e.g. [8] and the references therein). For example, there are approximately  $10^{12}$  neurons in the human brain [2]. As a rule, this leads to costly and inefficient computations. Therefore, model reduction is of paramount importance. The reduced model must mirror the properties of the original system if it is to be of practical utility.

In the present article, the effect of model reduction on the hyper/stability properties of the

nonlinear Hopfield model with feedback is studied.

## 2. Perturbed Hopfield model with feedback

Consider the following system of non-linear ODE's (known as Hopfield models [5, 6]) in the form:

$$\dot{x}_i = -b_i x_i + \sum_{j=1}^N A_{ij} G_j(x_j) + U_i(t), \quad (1)$$

where  $i = 1, \dots, n$ ,  $b_i$ 's are constants,  $A_{ij}$  form a constant matrix and the external inputs  $U_i(t)$  are functions of the time variable  $t$ . The functions  $G_j$  are, in general, nonlinear with respect to the state variables  $x_j$ ,  $j = 1, \dots, N$  (here  $N$  is the number of the neurons in the network). The second term in (1) gives the interconnection between the neurons.

The corresponding perturbed version of the Hopfield model (1) takes the form

$$\dot{x}_i = -\tilde{b}_i x_i + \sum_{j=1}^N \tilde{A}_{ij} \tilde{G}_j(x_j) + U_i(t), \quad (2)$$

where  $\tilde{b}_i = b_i + \Delta b_i$ ,  $\tilde{A}_{ij} = A_{ij} + \Delta A_{ij}$  (note, that  $\Delta A_{ij}$  does not need to be a symmetric) and  $\tilde{G}_j(u_j) = G_j(u_j) + \Delta G_j(u_j)$ ,  $1 \leq i \leq n$ . Here  $\Delta b_i$ ,  $\Delta A_{ij}$  and  $\Delta G_j(u_j)$  are considered as (small) perturbations of the system (1).

Model order reduction (Empirical Balance truncation) is applied to the model equations (1), and the paper studies the qualitative behaviour of the solutions of the reduced perturbed model. Special attention is paid to the Popov hyper-stability properties.

The feedback in the Hopfield model (1) is introduced by defining a function  $F$  relating the inputs  $U_i(t)$  with the corresponding outputs  $y_i(t)$ :  $U_i = F(y_i)$  (see section 3 below).

### 3. Model Reduction

The Hopfield model corresponds to a nonlinear system of the generic form:

$$\begin{aligned}\dot{\mathbf{x}}(t) &= \mathbf{f}(t, \mathbf{x}(t)) + \mathbf{B}(t)\mathbf{u}(t) \\ \mathbf{y}(t) &= \mathbf{h}(t, \mathbf{x}(t))\end{aligned}\quad (3)$$

where  $\mathbf{f} : \mathbb{R}^n \rightarrow \mathbb{R}^n$  and  $\mathbf{h} : \mathbb{R}^n \rightarrow \mathbb{R}^q$  are nonlinear functions, the vector  $\mathbf{u}(t) \in \mathbb{R}^n$  is the input to the system (3), while the vector  $\mathbf{y}(t) \in \mathbb{R}^q$  is regarded as an output. For the model equations (1), we identify

$$\mathbf{f}(t, \mathbf{x}(t)) = -b_i x_i + \sum_{j=1}^n A_{ij} G_j(x_j)$$

and the feedback is given by a nonlinear function  $F(\mathbf{y})$  relating the output  $\mathbf{y}(t)$  of the system (3) and its input  $\mathbf{u}(t)$ :  $\mathbf{u}(t) = -F(\mathbf{y})$ . The block-scheme of such a model is depicted on fig. 1.

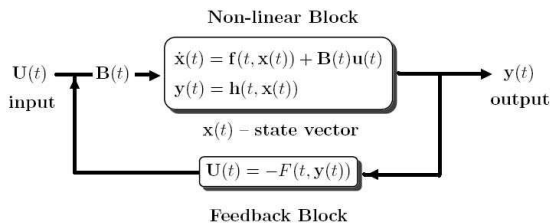


**Fig. 1.** A block-scheme of a nonlinear systems (3) with feedback

The reduced model (via empirical balanced truncation) that corresponds to (3) has the form:

$$\begin{aligned}\dot{\mathbf{z}}(t) &= \mathbf{IITf}(t, T^{-1}\mathbf{I}\mathbf{I}^*\mathbf{z}(t)) + \mathbf{IITB}(t)\mathbf{u}(t) \\ \mathbf{y}(t) &= \mathbf{h}(t, T^{-1}\mathbf{I}\mathbf{I}^*\mathbf{z}(t))\end{aligned}\quad (4)$$

where  $T$  is the transformation matrix which casts into a diagonal form both the empirical *controllability* and *observability* gramians, associated with the nonlinear system (3), and  $\mathbf{I}$  is a Galerkin projection [3].

### 4. Hyperstability of Neural Networks with Feedback

The hyperstability property of dynamical systems is a generalisation of Lyapunov stability. It gives the most general conditions to be imposed on the system in (3) in order to ensure that the solutions are bounded.

For a completely controllable and completely observable linear time-varying system, the series of conditions that guarantee hyperstability are: the Kalman-Yakubovich equation and the Popov integral inequality [9].

For general nonlinear systems in the form of (3) (as opposed to the linear time-varying system), this paper will provide nonlinear analogues of the Kalman-Yakubovich equation and the Popov inequality through the corresponding nonlinear controllability and nonlinear observability gramians [3].

### 5. Model Reduction and Hyperstability of Neural Networks

Since most of the nonlinear neural networks with feedback that are of interest are large-scale systems, it is important to determine whether model order reduction for such systems will affect its hyperstability. In this paper, it is shown that empirical balanced truncation preserves hyperstability.

*Finally, these results are illustrated by a numerical example.*

*Acknowledgement.* The authors wish to acknowledge the financial support of Science Foundation Ireland for this research.

### References

1. A. C. Antoulas, *Approximation of Large-Scale Dynamical Systems* (Advances in Design and Control Series), SIAM, Philadelphia (2003).
2. Borisjuk A., Friedman A., Ermentrout B. and Terman D., *Tutorials in Mathematical Biosciences I: Mathematical Neuroscience*, Lecture Notes in Mathematics **1860**, Springer-Verlag, Berlin, 2005.
3. Condon M. and Ivanov, R. Nonlinear systems-algebraic gramians and model reduction. *J. Nonl. Sci.* **14** (2004), 405–414.
4. M. Condon, G. G. Grahnovski, Stability and Model Order Reductions of Nonlinear Systems with Applications to Neural Networks I: Hopfield Type Models, *Preprint 2008*.
5. J. J. Hopfield *Neural Networks and Physical Systems with Emergent Collective Computational Abilities*, Proc. Nat. Acad. Sci. USA **79** (1982), 2554–2558; *Neurons with graded response have collective computational properties like those of two-state neurons*, Proc. Nat. Acad. Sci. USA **81** (1984), 3088–3092.
6. J. J. Hopfield and D. W. Tank, Computing with neural circuits: A model, *Science*, vol. 233, pp. 625–633, 1986.
7. Leah Edelstein-Keshet, *Mathematical Models in Biology*, Classics in Applied Mathematics **46**, SIAM, Philadelphia, 2005.
8. A. N. Michel, D. Liu, *Qualitative Analysis and Synthesis of Recurrent Neural Networks*, Marcel Dekker Inc., New York, 2004.
9. V. M. Popov, *Hyperstability of Control Systems*, Die Grundlehren der Mathematischen Wissenschaften **245**, Springer-Verlag, Berlin, 1973.

---

**Session**

**CE 2**

---



# High-order discontinuous Galerkin methods for computational electromagnetics and uncertainty quantification

J.S. Hesthaven<sup>1</sup>, T. Warburton<sup>2</sup>, C. Chauviere<sup>3</sup>, and L. Wilcox<sup>4</sup>

<sup>1</sup> Division of Applied Mathematics, Brown University, Providence, RI 02912, USA  
Jan.Hesthaven@Brown.edu

<sup>2</sup> Department of Computational and Applied Mathematics, Rice University, Houston, TX 77005, USA  
timwar@rice.edu

<sup>3</sup> Laboratoire de Mathématiques, Université Blaise Pascal, 63177 Aubière, France  
cedric.chauviere@math.univ-bpclermont.fr

<sup>4</sup> Institute for Computational Engineering and Sciences (ICES), University of Texas at Austin, Austin, TX 78712, USA lucasw@ices.utexas.edu

**Summary.** We discuss time-domain discontinuous Galerkin methods for the high-order accurate and geometrically flexible modeling of electromagnetic problems, touching also on extensions to frequency domain formulations. Using such techniques, we further explore efficient probabilistic ways of dealing with uncertainty and uncertainty quantification in electromagnetics applications. Whereas the discussion often draws on scattering applications, the techniques are applicable to general problems in CEM.

## 1 Introduction

As successful at the classic finite-difference time-domain method has been for solving EM problems, its limitations are emerging as a bottleneck in emerging applications. This is particularly the case for problems characterized by being electrically large scale, for problems where interactions with complex geometries and/or materials are of importance or for problems with a high dynamic range in which case high accuracy is required.

To address these shortcomings, several alternatives have emerged during the last decade, most notably finite-element time-domain methods and hybrid finite-element, finite-difference methods. While these offer geometric flexibility and even high-order accuracy, they also result in implicit computational methods for time-dependent methods. Yet another alternative is finite-volume methods which has the geometric flexibility and explicit nature but suffers from difficulties when high-order accuracy is requested.

## 2 DG Methods for EM Problems

By combining the benefits of finite-element and finite-volume methods, one recovers what has become known as discontinuous Galerkin methods

(DG) [6] which has gained increasing interest during the last decade as a suitable general modeling tool for EM problems, primarily in the time-domain [3, 4] but also for frequency domain problems [5].

We consider the time-domain Maxwell's equations as a conservation law

$$\mathbf{Q} \frac{\partial \mathbf{q}}{\partial t} + \nabla \cdot \mathbf{F}(\mathbf{q}) = 0, \quad (1)$$

where  $\mathbf{q}$  is the state vector given by  $\mathbf{q} = (\mathbf{E}, \mathbf{H})^T$  and the components of the tensor  $\mathbf{F}$  are

$$\mathbf{F}_i(\mathbf{q}) = \begin{pmatrix} -\mathbf{e}_i \times \mathbf{H} \\ \mathbf{e}_i \times \mathbf{E} \end{pmatrix}, \quad (2)$$

where  $\mathbf{e}_i$  denotes the Cartesian unit vectors and we have the material matrix  $\mathbf{Q}$ . We assume that the computational domain,  $\Omega$ , is tessellated by triangles in two spatial dimensions and tetrahedrons in three spatial dimensions. Given an element  $D$  of the tessellation, the represent the local solution  $\mathbf{q}_N$  restricted to  $D$  is given as

$$\mathbf{q}_N(\mathbf{x}, t) = \sum_{i=1}^N \tilde{\mathbf{q}}_i(t) L_i(\mathbf{x}), \quad (3)$$

where  $\tilde{\mathbf{q}}_i$  reflects nodal values, defined on the element. The function  $L_i(\mathbf{x})$  signifies an  $i$ th order Lagrange polynomial. The discrete solution,  $\mathbf{q}_N$ , of Maxwell's equations is required to satisfy

$$\begin{aligned} & \int_D \left( \mathbf{Q} \frac{\partial \mathbf{q}_N}{\partial t} + \nabla \cdot \mathbf{F}(\mathbf{q}_N) - \mathbf{S}_N \right) L_i(\mathbf{x}) d\mathbf{x} \\ & = \oint_{\partial D} \hat{\mathbf{n}} \cdot [\mathbf{F}(\mathbf{q}_N) - \mathbf{F}^*] L_i(\mathbf{x}) d\mathbf{x}. \end{aligned} \quad (4)$$

In (4),  $\mathbf{F}^*$  denotes a numerical flux, whose expression can be found in [4], and  $\hat{\mathbf{n}}$  is an outward pointing unit vector defined at the boundary  $\partial D$  of the element  $D$ . Note that this is an entirely

local formulation, and relaxing the continuity of the elements decouples the elements, resulting in a block-diagonal global mass matrix which can be trivially inverted in preprocessing. The local nature of the scheme allows for the use of an explicit Runge-Kutta method for the time discretization.

As an application example, computed using this approach, we show in Fig. 1 the scattered field on a missile-like structure with a 1GHz incident field.

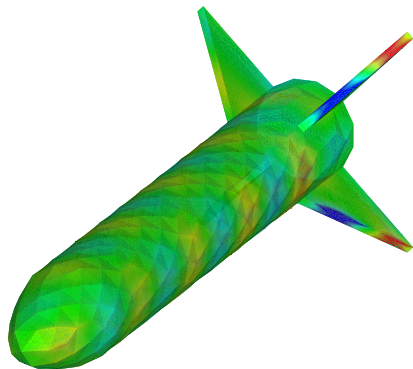


**Fig. 1.** 1Gz scattered field on missile computed using a DG time-domain method.

### 3 Accounting for Uncertainty in EM using DG

While computational methods have become increasingly accurate, their reliance on exact data (e.g. the geometry of the objects, the material parameters, the sources terms, etc.) is becoming a bottleneck in the modeling of complex problems. A standard way to deal with this lack of knowledge or uncertainty, is to assume that some of the parameters are random and compute macroscopic quantities (e.g. means and variances) through Monte-Carlo sampling with the advantage of its simplicity. However, the rate of convergence of Monte-Carlo is quite slow since it is proportional to  $\sqrt{M}$ , where  $M$  is the number of samples. Therefore, designing more efficient numerical methods for the solution of stochastic partial differential equations with random inputs or random coefficients is meeting growing interest.

As an illustration of the versatility of the DG approach, we shall discuss how ideas of probabilistic modeling through Wiener Chaos expansions can be combined to enable the accurate and efficient modeling of large scale EM problems with uncertainty [1, 2]. In Fig. 2 we illustrate this by

showing the bistatic radar cross section (RCS) for a  $ka = \pi$  PEC sphere with a uniformly distributed 10% uncertain radius, clearly showing the sensitivity of the radar signature. These results are obtained at a fraction of the cost associated with a brute-force Monte Carlo approach.

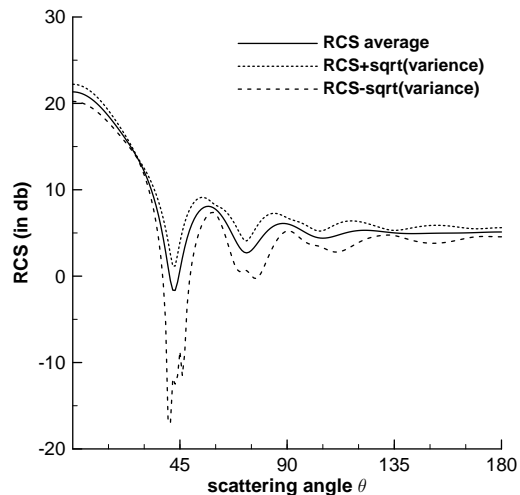


**Fig. 2.** Radar cross section and sensitivity for  $ka = \pi$  sphere of uncertain radius.

*Acknowledgement.* Partial support for this work by the National Science Foundation, the Airforce Office of Scientific Research, and the US Airforce Test & Evaluation Program is acknowledged.

### References

1. C. Chauviere, J.S. Hesthaven, and L. Lurati. Computational Modeling of Uncertainty in Time-Domain Electromagnetics. *SIAM J. Sci. Comp.* 28:751–775, 2006.
2. C. Chauviere, J.S. Hesthaven, and L. Wilcox. Efficient Computation of RCS from Scatterers of Uncertain Shapes. *IEEE Trans. Antennas Propagat.* 55:1437–1448, 2007.
3. J. S. Hesthaven. High-Order Accurate Methods in Time-Domain Computational Electromagnetics. A Review. *Advances in Imaging and Electron Physics* 127:59–123, 2003.
4. J. S. Hesthaven and T. Warburton. High-Order Nodal Methods on Unstructured Grids. I. Time-Domain Solution of Maxwell’s Equations. *J. Comput. Phys.*, 181:186–221, 2002.
5. J.S. Hesthaven and T. Warburton. High Order Nodal Discontinuous Galerkin Methods for the Maxwell Eigenvalue Problem. *Royal Soc. London Ser A* 362:493-524, 2004.
6. J.S. Hesthaven and T. Warburton, *Nodal Discontinuous Galerkin Methods: Algorithms, Analysis, and Applications*. Springer Texts in Applied Mathematics 54, Springer Verlag, New York, 2008.

# Using Nudg++ to Solve Poisson’s Equation on Unstructured Grids

Christian R. Bahls, Gisela Pöplau, and Ursula van Rienen

Universität Rostock, A.-Einstein-Str. 2, D-18051 Rostock [christian.bahls@uni-rostock.de](mailto:christian.bahls@uni-rostock.de),  
[gisela.poeplau@uni-rostock.de](mailto:gisela.poeplau@uni-rostock.de), [ursula.van-rienen@uni-rostock.de](mailto:ursula.van-rienen@uni-rostock.de)

**Summary.** In this paper we explore the viability of using nodal discontinuous Galerkin methods as implemented in the software library Nudg++ [4] to compute the space charge field of an electron or positron bunch. We benchmark this method by comparing results from this scheme with solutions obtained from other sources.

## 1 Introduction

Being known from the early 70’s [6] discontinuous Galerkin finite element methods (DG-FEM) have only recently become popular as a method for the numerical solution of partial differential equations arising in computational fluid dynamics or computational electromagnetism.

Though being primarily developed with hyperbolic partial differential equations in mind, with some small modifications DG-FEM can also be used to solve elliptic PDEs.

The objective of this paper is to apply DG-FEM to the calculation of space charge fields of particle bunches. The efficient computation of these fields is one of the primary focuses of beam dynamics simulations as needed for the design of future accelerator facilities like the XFEL [1] or the ILC [2].

## 2 Using DG-FEM for the Solution of Elliptic PDEs

Our aim is the estimation of the solution  $u(x)$  of Poisson’s equation in the domain  $\Omega \subseteq \mathbb{R}^3$ :

$$-\Delta u(x) = f(x), \quad \forall x \in \Omega. \quad (1)$$

We use Dirichlet boundary conditions on  $\partial\Omega_D$  and Neumann boundary conditions on  $\partial\Omega_N$ :

$$u(x) = g_D(x), \quad \forall x \in \partial\Omega_D, \quad (2)$$

$$\frac{\partial u(x)}{\partial \mathbf{n}(x)} = g_N(x), \quad \forall x \in \partial\Omega_N. \quad (3)$$

In the context of space charge calculations  $u(x)$  denotes the potential and  $f(x)$  the source term  $f(x) = \rho(x)/\varepsilon_0$  with the charge density  $\rho(x)$  and the vacuum permittivity  $\varepsilon_0$ .

## Applying DG-FEM to Poisson’s Equation

When looking at the operator resulting from the discretisation of Poisson’s equation (1) using DG-FEM with a central flux we find that it has a non-trivial kernel. This problem can be mitigated by using an altered flux that penalizes discontinuities at element boundaries as described in [3].

To numerically approximate the solution of Poisson’s equation (1) we use the special class of nodal discontinuous Galerkin methods provided by the C++ library Nudg++ [4].

## 3 Numerical Investigations

We assess the viability of this approach to compute the space charge field of charged particles by computing the electric field of different test configurations. Further we compare these solutions with results derived from analytic considerations and from computations with other methods [5].

*Acknowledgement.* This work is supported by the DFG under contract number RI 814/18-1 and partly by DESY, Hamburg.

## References

1. DESY, Hamburg, Germany. *Das europäische Röntgenlaserprojekt XFEL*, 2005.
2. GDE (Global Design Effort), [www.linearcollider.org](http://www.linearcollider.org). *What is the ILC?*
3. J.S. Hesthaven and T. Warburton. *Nodal Discontinuous Galerkin Methods: Algorithms, Analysis, and Applications*, volume 54 of *Texts in Applied Mathematics*. Springer Verlag, New York, 2008.
4. N. Nunn and T. Warburton. *Nudg++: a Nodal Unstructured Discontinuous Galerkin framework*. [www.nudg.org](http://www.nudg.org).
5. G. Pöplau and U. van Rienen. A self-adaptive multigrid technique for 3D space charge calculations. *IEEE Transactions on Magnetics*, 44(4):to appear, 2008.
6. W.H. Reed and T.R. Hill. Triangular mesh methods for the neutron transport equation. Tech. report LA-UR-73-479, Los Alamos Scientific Laboratory, 1973.



# From the Boundary Element DDM to Trefftz Finite Element Methods on Arbitrary Polyhedral Meshes

Dylan Copeland<sup>1</sup>, Ulrich Langer<sup>1,2</sup>, and David Pusch<sup>2</sup>

<sup>1</sup> Institute of Computational Mathematics, Johannes Kepler University Linz, Altenbergerstr. 69, A-4040 Linz, Austria [dylan.copeland@jku.at](mailto:dylan.copeland@jku.at), [ulanger@numa.uni-linz.ac.at](mailto:ulanger@numa.uni-linz.ac.at)

<sup>2</sup> RICAM, Austrian Academy of Sciences, Altenbergerstr. 69, A-4040 Linz, Austria [david.pusch@oeaw.at](mailto:david.pusch@oeaw.at)

**Summary.** We derive and analyze new boundary element (BE) based finite element discretizations of potential-type, Helmholtz and Maxwell equations on arbitrary polygonal and polyhedral meshes. The starting point of this discretization technique is the symmetric BE Domain Decomposition Method (DDM), where the subdomains are the finite elements. This can be interpreted as a local Trefftz method that uses PDE-harmonic basis functions. This discretization technique leads to large-scale sparse linear systems of algebraic equations which can efficiently be solved by Algebraic Multigrid preconditioned conjugate gradient methods in the case of the potential equation and by Krylov subspace iterative methods in general.

## 1 Introduction

We introduce new finite element methods based on the symmetric boundary element domain decomposition method presented in [3], which can be applied with general polygonal or polyhedral meshes. Each element of the mesh may be any polygon or polyhedron, as we treat the elements as subdomains. There are many important practical applications where one wants to discretize PDEs on such kinds of meshes without further decomposition of the polyhedra. Boundary integral operators are utilized to obtain a method which solves for traces of the solution on the element surfaces, from which the solution may be obtained via a representation formula. Simple, low-order boundary element spaces are used to approximate traces on the element surfaces, yielding a finite element method with PDE-harmonic basis functions.

Since boundary integral operators are used only locally, piecewise constant coefficients are admissible, and the coupling of boundary element functions is local. Consequently, sparse linear systems are obtained, which can be solved by Krylov iterative methods. In the case of the potential equation, the resulting system is symmetric and positive definite, and algebraic multigrid is a very effective preconditioner in the conjugate gradient solver.

## 2 The Potential Equation

Let  $\Omega \subset \mathbb{R}^d$  be a bounded domain with a polygonal ( $d = 2$ ) or polyhedral ( $d = 3$ ) Lipschitz boundary  $\Gamma = \partial\Omega$ . As a model problem, we consider the potential equation

$$-\operatorname{div}(a(x)\nabla u(x)) = f(x) \quad \text{for } x \in \Omega \quad (1)$$

with the Dirichlet boundary condition  $u = g$  on  $\Gamma$ . We assume that the coefficient  $a$  is piecewise constant,  $f \in L_2(\Omega)$ , and  $g \in H^{1/2}(\Gamma)$ . Further, we suppose that there is a non-overlapping decomposition of our domain  $\Omega$  into  $e_h$  shape-regular polygonal elements  $\Omega_i$  such that  $\overline{\Omega} = \bigcup_{i=1}^{e_h} \overline{\Omega}_i$ ,  $\Omega_i \cap \Omega_j = \emptyset$  for  $i \neq j$ ,  $\Gamma_i = \partial\Omega_i$ ,  $\overline{\Gamma}_{ij} = \overline{\Gamma}_i \cap \overline{\Gamma}_j$  and  $a(x) = a_i > 0$  for  $x \in \Omega_i$ ,  $i = 1, \dots, e_h$ . Under the assumptions made above, there obviously exists a unique weak solution  $u \in H^1(\Omega)$  of the BVP (1).

Using the local Dirichlet-to-Neumann map

$$a_i \partial u / \partial \nu_i = a_i S_i u|_{\Gamma_i} - N_i f \quad \text{on } \Gamma_i, \quad (2)$$

we observe that the variational formulation of (1) is equivalent to the associated variational formulation on the skeleton  $\Gamma_S = \bigcup_{i=1}^{e_h} \Gamma_i$  (see, e.g., [4]): find  $u \in H^{1/2}(\Gamma_S)$  with  $u = g$  on  $\Gamma$  such that

$$\sum_{i=1}^{e_h} \int_{\Gamma_i} a_i (S_i u_i) v_i ds_x = \sum_{i=1}^{e_h} \int_{\Gamma_i} (N_i f) v_i ds_x \quad (3)$$

for all  $v \in H_0^{1/2}(\Gamma_S)$ , where  $u_i$  and  $v_i$  denote the traces of  $u$  and  $v$  on  $\Gamma_i$ , respectively. The Steklov–Poincaré operator  $S_i$  and the Newton potential operator  $N_i$  have different representations (see again [4]). Here we are using the symmetric representation

$$S_i = D_i + (0.5I + K_i') V_i^{-1} (0.5I + K_i) \quad (4)$$

of the local Steklov–Poincaré operator  $S_i$  via the local single layer potential integral operator  $V_i$ , the local double layer potential operator  $K_i$ , its adjoint  $K_i'$ , and the local hypersingular boundary integral operator  $D_i$ , see, e.g., [5] for the definition

and properties of these boundary integral operators. The operator  $N_i = V_i^{-1}\tilde{N}_{i,0}$  is defined by the Newton potential operator

$$(\tilde{N}_{i,0}f)(x) = \int_{\Omega_i} U^*(x-y)f(y)dy, \quad x \in \Gamma_i, \quad (5)$$

where  $U^*(x) = 1/(4\pi|x|)$  denotes the fundamental solution of the Laplace operator  $-\Delta$  for  $d = 3$ .

For simplicity we use continuous piecewise linear boundary element functions for approximating the potential  $u$  on the skeleton  $\Gamma_S$  and piecewise constant boundary element functions for approximating the normal derivatives  $t_i = \partial u/\partial\nu_i$  on the boundary  $\Gamma_i$  of the polygonal element  $\Omega_i$ . This yields the element stiffness matrices  $\mathbf{S}_{i,h} = a_i\mathbf{D}_{i,h} + a_i(0.5\mathbf{I}_{i,h}^\top + \mathbf{K}_{i,h}^\top)(\mathbf{V}_{i,h})^{-1}(0.5\mathbf{I}_{i,h} + \mathbf{K}_{i,h})$  and the element vectors  $\mathbf{f}_{i,h} = \mathbf{I}_{i,h}^\top(\mathbf{V}_{i,h})^{-1}\mathbf{f}_{i,h}^N$ , where the matrices  $\mathbf{V}_{i,h}$ ,  $\mathbf{K}_{i,h}$ ,  $\mathbf{D}_{i,h}$  and  $\mathbf{I}_{i,h}$  arise from the BE Galerkin approximation to the local boundary integral operators  $V_i$ ,  $K_i$ ,  $D_i$ , and to the identity operator  $I_i$  living on  $\Gamma_i$ , respectively.  $\mathbf{I}_{i,h}$  is nothing but the mass matrix. The vector  $\mathbf{f}_{i,h}^N$  is defined by the Newton potential identity

$$(\mathbf{f}_{i,h}^N, \mathbf{t}_{i,h}) = \int_{\Gamma_i} \int_{\Omega_i} U^*(x-y)f(y)dy t_{h,i}(x)ds_x \quad (6)$$

for all vectors  $\mathbf{t}_{i,h}$  corresponding to the piecewise constant functions  $t_{h,i}$  on  $\Gamma_i$ . Now, we obtain the BE-based FE system

$$\mathbf{S}_h \mathbf{u}_h = \mathbf{f}_h \quad (7)$$

by assembling the stiffness matrix  $\mathbf{S}_h$  and the load vector  $\mathbf{f}_h$  from the element stiffness matrices  $\mathbf{S}_{i,h}$  and the element load vectors  $\mathbf{f}_{i,h}$ , respectively, and by incorporating the Dirichlet boundary condition as usual.

The solution of (7) provides an approximation to the Dirichlet trace of the solution to (1) on the boundary  $\partial\Omega_i$  of all elements  $\Omega_i$ ,  $i = 1, \dots, e_h$ . Applying the Dirichlet-to-Neumann map locally (i.e. element-wise), we may obtain an approximate solution  $\tilde{u}_h$  to  $u$  in each element  $\Omega_i$  via the representation formula (see, e.g., [4] or [5]).

Following [3] we immediately obtain the discretization error estimate  $O(h^{3/2})$  in the mesh-dependent norm  $\|v\|_h^2 := \sum_{i=1}^{e_h} \|v|_{\Gamma_i}\|_{H^{1/2}(\Gamma_i)}^2$  for a sufficiently (piecewise) smooth solution  $u$ , where  $u_h$  is the continuous piecewise linear function on the skeleton  $\Gamma_{S,h}$  corresponding to the Dirichlet nodal values and to the nodal values from the solution vector  $\mathbf{u}_h$  of (7). This yields the usual  $O(h)$  estimate of the discretization error  $u - \tilde{u}_h$  in the  $H^1(\Omega)$ -norm.

We refer the reader to [2] for more detailed description and for the results of our numerical experiments.

### 3 Generalization to the Helmholtz and Maxwell Equations

Consider the interior Dirichlet boundary value problem for the Helmholtz equation

$$-\Delta u(x) - \kappa^2 u(x) = f \quad \text{for } x \in \Omega, \quad (8)$$

with  $u = g$  on  $\Gamma$ . We assume that the wavenumber  $\kappa > 0$  is constant, or piecewise constant and not an interior eigenvalue, and  $g \in H^{1/2}(\Gamma)$ .

The BE-based FE method for the Helmholtz equation is formally identical to the method presented in the previous section for the potential equation (with  $a = 1$ ). One only needs to use different operators  $D_i$ ,  $K_i$ , and  $V_i$  based on the fundamental solution  $U^*(x) = e^{i\kappa|x|}/(4\pi|x|)$  for the Helmholtz operator, see, e.g., [5].

We also study a similar method for the time-harmonic Maxwell equation

$$\mathbf{curl} \mathbf{curl} \mathbf{u} - \kappa^2 \mathbf{u} = \mathbf{0} \quad \text{in } \Omega, \quad (9)$$

with the Dirichlet boundary condition  $\gamma_t \mathbf{u} := \mathbf{u} \times \mathbf{n} = \mathbf{g}$  on  $\Gamma$ , where  $\mathbf{n}$  is the outward unit normal vector. The BE-based FE method for (9) involves quite technical trace spaces and boundary integral operators. For details and results, see [1].

*Acknowledgement.* The authors gratefully acknowledge the financial support of the FWF research project P19255.

### References

1. D. Copeland. Boundary-element-based finite element methods for Helmholtz and Maxwell equations on general polyhedral meshes. Technical Report 2008-11, RICAM, Linz, 2008.
2. D. Copeland, U. Langer, and D. Pusch. From the boundary element ddm to local trefftz finite element methods on arbitrary polyhedral meshes. Technical Report 2008-10, RICAM, Linz, 2008.
3. G.C. Hsiao and W.L. Wendland. Domain decomposition in boundary element methods. In *Proceedings of the Fourth International Symposium on Domain Decomposition Methods for Partial Differential Equations* (ed. by R. Glowinski and Y.A. Kuznetsov and G. Meurant and J. Périaux and O. B. Widlund), Moscow, May 21-25, 1990, pages 41–49, Philadelphia, 1991. SIAM.
4. U. Langer and O. Steinbach. Coupled finite and boundary element domain decomposition methods. In *Boundary Element Analysis: Mathematical Aspects and Application*, ed. by M. Schanz and O. Steinbach, *Lecture Notes in Applied and Computational Mechanics, Volume 29*, pages 29–59, Berlin, 2007. Springer.
5. O. Steinbach. *Numerical Approximation Methods for Elliptic Boundary Value Problems. Finite and Boundary Elements*. Springer, New York, 2008.

# Reduced Basis Method for Electromagnetic Field Computations

Jan Pomplun and Frank Schmidt

Zuse Institute Berlin, Takustrasse 7, D-14195 Berlin, Germany pomplun@zib.de, frank.schmidt@zib.de

**Summary.** We explain the reduced basis (RB) method applied to electromagnetic field computations with the finite element method. Rigorous numerical simulations for practical applications often become very time consuming. The RB method allows to split up the solution process off an e.g. geometrically parameterized problem into an expensive offline and a fast online part. For an actual simulation only the fast online part is evoked. We apply the RB method to the simulation of a parameterized phase shift mask.

## 1 Introduction

The finite element method (FEM) has been successfully applied to a large number of nano-optical problem classes [2, 5]. The computation time of a single FEM simulation however can become very long especially for 3D problems. Design, optimization and inverse problems usually involve a large number of such simulations having an underlying layout with a few varying geometrical parameters. The RB method can be applied to this setup [4]. In the offline step the underlying model is solved rigorously several times for different values of the geometrical parameters. These solutions built the reduced basis. The full parameterized problem is projected onto the RB which results in a significant reduction of the problem size. In the online step the reduced problem is solved.

## 2 Reduced Basis Method

For electromagnetic field computations Maxwell's equations have to be solved:

$$\nabla \times \mu^{-1} \nabla \times \mathbf{E} - \omega^2 \epsilon_p \mathbf{E} = 0. \quad (1)$$

Since we consider geometrically parameterized problems the material distribution described by the permittivity  $\epsilon_p$  is parameter dependent which is denoted by the subscript  $p$ . Discretizing (1) with the finite element method leads to a linear system of equations [3] with parameter dependent coefficients and solution:

$$A_p u_p = f. \quad (2)$$

In practice the number of unknowns (dimension of  $u_p$ ) can be up to several millions. Now suppose that  $u_p$  stays on a low dimensional sub manifold of the complete solution space if we vary the parameters  $p$ . Then it is reasonable to solve (2) only on this subspace, i.e. the full system is projected onto a reduced basis  $U$ . Usually the reduced basis is built by a number of so called snapshot solutions, which are rigorous solutions of (2) for different parameter values  $p_i$ :  $U = [u_{p_1}, u_{p_2}, \dots, u_{p_N}]$ . The reduced basis is computed in the offline step. The projected system reads:

$$[U^H A_p U] \lambda_p = U^H f \quad (3)$$

which is a system of dimension  $N$  ( $\propto 100$ ) much smaller than the original problem. After solving (3) in the online step the reduced basis solution is obtained by  $\hat{u}_p = U \lambda_p$ .

### 2.1 Affine Parameter Dependence

The expensive steps performing a reduced basis computation for an actual parameter set  $\hat{p}$  is according to (3) the assembling of  $A_{\hat{p}}$  and the projection step onto the RB  $U$ . These steps can also be performed offline if the matrix  $A_p$  has an affine parameter dependence defined by:

$$A_p = \sum_{i=1}^M g_i(p) A^{(i)} \quad (4)$$

$$\Rightarrow [U^H A_p U] = \sum_{i=1}^M g_i(p) [U^H A^{(i)} U].$$

The matrices  $[U^H A^{(i)} U]$  can be assembled and projected offline. For finite elements on a rectangular grid such an affine parameter dependence is given [6]. For unstructured triangular grids however the matrix entries of  $A_p$  are rational expressions in the parameters with different roots in the denominator leading to a non-affine parameter dependence. This non-affine dependence is due to the term  $g_p = \frac{1}{\det J_p} J_p^T J_p$  assembling the local finite element matrices.  $J_p$  is the Jacobian of the transformation of a reference triangle onto a parameter dependent physical triangle of the computational domain [3].

## 2.2 Empirical Interpolation

Empirical interpolation [1] is a method to decompose a matrix with non-affine parameter dependence into a form according to (4):

$$A_p \approx \sum_{j=1}^L \alpha_j(p) \tilde{A}^j. \quad (5)$$

The basic idea is to assemble a few snapshot matrices  $\tilde{A}^j$  for certain parameters  $p_j$  and to determine the coefficients  $\alpha_j(\hat{p})$  by a fit of the non-affine function  $g_{\hat{p}}$  with functions  $g_{p_j}$ :

$$\|g_{\hat{p}} - \alpha_j(\hat{p})g_{p_j}\| \stackrel{!}{=} \min.$$

Increasing the number of interpolation matrices, i.e.  $L$  should allow a more accurate approximation of  $A_p$  (5) and therewith a more accurate reduced basis solution.

## 3 Example

As an example we compute transmission of light through a phase shift mask [6]. The parameterized geometry is shown in Fig. 1. To quantify the

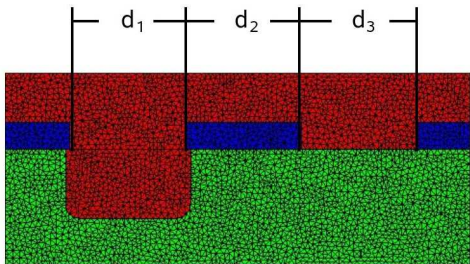


**Fig. 1.** Parameterized phase shift mask for reduced basis computations.

quality of the reduced basis solution for a certain parameter set  $\hat{p} = \{d_1, d_2, d_3\}$  we compare it to the exact finite element solution for this parameter set. Figure 2 shows the convergence of the reduced basis solution for increasing dimension of the reduced basis and different number of parameter sets  $L$  for empirical interpolation. The error is computed in the  $L_2$  norm. For comparison the reduced basis solution without empirical interpolation is shown. We observe that the reduced basis solution converges exponentially towards the exact finite element solution. For fixed  $L$  the convergence is as fast as without empirical interpolation but stops at a specific level. However taking a more accurate empirical interpolation dimension  $L$  this level can be lowered.

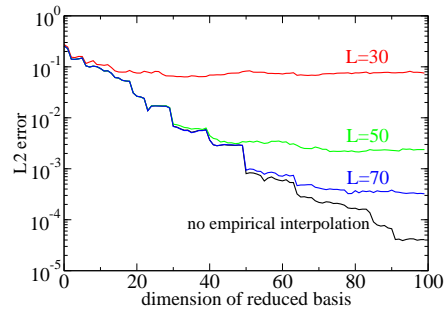


**Fig. 2.** Convergence of reduced basis solution for increasing dimension of reduced basis and different dimension of empirical interpolation ansatz  $L$ .

## 4 Conclusions

We have shown that the reduced basis method is very well suited for electromagnetic field computations with a parameterized geometry. Exponential convergence was observed for transmission of light through a phase shift mask. For finite elements on an unstructured grid a non-affine parameter dependence of the system matrix is obtained. However with empirical interpolation the assembling of the reduced basis system can be performed offline.

*Acknowledgement.* We acknowledge fruitful and stimulating discussions with Zhenhai Zhu from Cadence Design Systems, Inc.

## References

1. M. Barrault, N.C. Nguyen, Y. Maday, and A.T. Patera. An "empirical interpolation" method: Application to efficient reduced-basis discretization of partial differential equations. *C. R. Acad. Sci. Paris*, I(339):667–672, 2004.
2. S. Burger, R. Köhler, L. Zschiedrich, W. Gao, F. Schmidt, R. März, and C. Nölscher. Benchmark of FEM, Waveguide and FDTD Algorithms for Rigorous Mask Simulation. In J. T. Weed and P. M. Martin, editors, *Photomask Technology*, volume 5992, pages 378–389. Proc. SPIE, 2005.
3. Peter Monk. *Finite Element Methods for Maxwell's Equations*. Oxford University Press, 2003.
4. A.T. Patera and G. Rozza. *Reduced Basis Approximation and A Posteriori Error Estimation for Parametrized Partial Differential Equations*. MIT Pappalardo Graduate Monographs in Mechanical Engineering, 1. edition, 2006.
5. J. Pomplun, S. Burger, F. Schmidt, F. Scholze, C. Laubis, and U. Dersch. Metrology of EUV masks by EUV scatterometry and finite element analysis. In *Photomask and NGL Mask Technology XV*, volume 7028, page 24. Proc. SPIE, 2008.
6. Z. Zhu and F. Schmidt. An efficient and robust mask model for lithography simulation. volume 6925, page 126. Proc. SPIE, 2008.

# Surface Integrated Field Equations Method for solving 3D Electromagnetic problems

Zhifeng Sheng<sup>1</sup> and Patrick Dewilde<sup>2</sup>

<sup>1</sup> Circuits and Systems, EEMCS, TUDelft, The Netherlands [z.sheng@ewi.tudelft.nl](mailto:z.sheng@ewi.tudelft.nl),

<sup>2</sup> Circuits and Systems, EEMCS, TUDelft, The Netherlands [p.dewilde@ewi.tudelft.nl](mailto:p.dewilde@ewi.tudelft.nl)

**Summary.** This paper describes how the Surface Integrated Field Equations method (SIFE) can be implemented to solve 3D Electromagnetic (EM) problems on substrates in which high contrast materials occur. It gives an account of the promising results that are obtained with it when compared to traditional approaches. Advantages of the method are the highly improved flexibility and accuracy for a given discretization level, at the cost of higher computational complexity.

**Key words:** Integrated Field Equations, time domain, high contrasts, computational method

## 1 Method Outline

In our previous work, we have used the Surface Integrated Equations method for solving 2D electromagnetic problems [2], in which domains are present that exhibit highly contrasting material properties (electric and/or magnetic) with each other. In this paper, we develop the method further to solve 3D electromagnetic problems.

In strongly heterogeneous media such as modern chips, the constitutive parameters can jump by large amounts upon crossing the material interfaces. On a global scale, the EM field components are not differentiable and Maxwell's equations in differential form cannot be used, one has to resort to the original integral form of the EM field relations as the basis for the computational method.

Let  $\mathcal{D}$  be the domain of interest with boundary  $\partial\mathcal{D}$ ,  $\mathcal{S}$  be any (sufficiently smooth and small) surface ( $\mathcal{S} \in \mathcal{D}$ ) with boundary  $\partial\mathcal{S}$  in  $\mathcal{D}$ ,  $\mathcal{T}$  be a time interval with boundary points  $\partial\mathcal{T}$ . For any  $\mathcal{S}$  and  $\mathcal{T}$ , Maxwell's equations in surface integrated form are (using Einstein's summation convention for repeated indices, which is consistently used throughout this paper):

$$\int_{t \in \mathcal{T}} dt \oint_{\mathbf{x} \in \partial\mathcal{S}} H_k(\mathbf{x}, t) dl_k = \int_{\mathbf{x} \in \mathcal{S}} D_q(\mathbf{x}, t) ds_q \Big|_{t \in \partial\mathcal{T}},$$

$$\int_{t \in \mathcal{T}} dt \oint_{\mathbf{x} \in \partial\mathcal{S}} E_k(\mathbf{x}, t) dl_k = - \int_{\mathbf{x} \in \mathcal{S}} B_q(\mathbf{x}, t) ds_q \Big|_{t \in \partial\mathcal{T}},$$

where  $dl_k = \tau_k dl$ ,  $ds_q = \nu_q ds$ ,  $\nu_q$  is the unit vector normal to the bounded surface area  $\mathcal{S}$ . This

vector is oriented toward the side of advance of a right-hand screw as it is turned around  $\partial\mathcal{S}$  in the direction of the unit vector  $\tau_k$ .

The constitutive relations are:

$$D_k(\mathbf{x}, t) = \int_{t'=0}^{\infty} \eta_{k,r}(\mathbf{x}, t') E_r(\mathbf{x}, t-t') dt' + P_k^{\text{ext}}(\mathbf{x}, t),$$

$$B_j(\mathbf{x}, t) = \int_{t'=0}^{\infty} \zeta_{j,p}(\mathbf{x}, t') H_p(\mathbf{x}, t-t') dt' + M_j^{\text{ext}}(\mathbf{x}, t).$$

where  $P_k^{\text{ext}}$  is the (field-independent) external electric polarization (C/m<sup>2</sup>);  $M_j^{\text{ext}}$  is the (field-independent) external magnetization (T); Assuming instantaneously reacting isotropic media, the constitutive relations take the form:

$$\eta_{k,r}(\mathbf{x}, t) = \epsilon(\mathbf{x})\delta(t) + \sigma(\mathbf{x})\delta_{k,r}H(t)$$

$$\zeta_{k,r}(\mathbf{x}, t) = \mu(\mathbf{x})\delta(t) + \kappa(\mathbf{x})\delta_{k,r}H(t)$$

where  $\kappa$  is the linear magnetic hysteresis (H/m.s),  $\delta(t)$  the Dirac delta distribution in time  $t$ ,  $H(t)$  the Heaviside unit step function and  $\delta_{k,r}$  the symmetrical unit tensor of rank 2 (Kronecker tensor).

To satisfy the partial continuity conditions on material interfaces, we construct a so called 'consistent linear discretization schema' that meets the continuity requirements across interfaces exactly, using a 3D tetrahedra mesh combined with a consistent linear interpolation [1] of electric and magnetic field strengths.

Furthermore, we use in this paper simple boundary conditions to truncate the computational domain (our goal being to show the validity of the method, we are developing a package with general boundary conditions).

## 2 Discretization schema

The electric and magnetic field strengths are interpolated with linear nodal expansion functions in homogeneous subdomains, where the EM field is totally continuous. At material interfaces, however, the field strengths are interpolated with edge based linear expansion functions. We refer to [2] for details on this novel kind of approximation that allows for partial discontinuities at

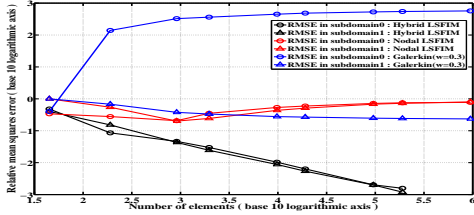


Fig. 1. Relative mean squares error (RMSE) in H computed with SIFE method and Galerkin's method.

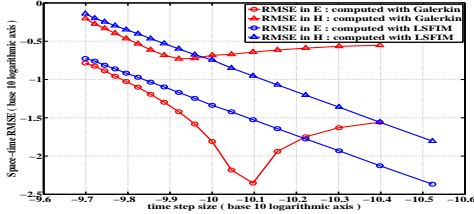


Fig. 2. Mean square error Vs time step size comparison of the methods tested

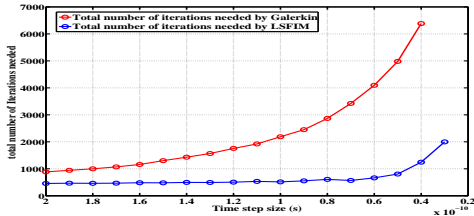


Fig. 3. Total number of iterations Vs time step size

interfaces, in particular the discontinuity of normal components. We use, in addition, a regular time stepping schema with time step chosen in accordance with the space discretization, and the trapezium rule to approximate the time integrals.

After properly assembling the local matrices we obtain an overdetermined system of equations that we solve numerically using the Bicg-stab method. We have studied the source of over-determination, which can be reduced to numerical transformations of local quantities and can hence be controlled adequately (this issue is beyond the scope of the present paper - here we suffice with computing a least squares solution directly using a pre-conditioner). The pre-conditioner that we use incorporates incomplete Cholesky factorization on the system matrix, which may introduce a lot of fill-ins in the incomplete Cholesky factor. Reordering of the system matrix significantly reduces the fill-ins. For time domain problems, the solution of the previous time instant is used for the initial guess of the current time instant.

### 3 Numerical experiments

We present a number of numerical experiments for the 3D case that show the superior performance of the method. In particular:

- We verify the accuracy and convergence of spacial discretization schema through 3D magnetostatic problems with extreme high contrast in permeability, for which an analytic solution is known. As indicated in Fig. 1, the SIFE method based on hybrid linear finite element delivers accurate solutions while the conventional Galerkin method does not.
- We verify the accuracy and stability of the method in the time domain by comparing our method with the conventional Galerkin method on computing 3D EM fields in inhomogeneous media in the time domain for which analytic solution are available. As indicated in Fig. 2 and Fig. 3, the time domain convergence rate of the SIFE method is higher than Galerkin's method without increasing computational cost.
- We are working on a software package that shall demonstrate the practical usage of our method in VLSI circuit simulation by simulating EM wave propagation through the substrate and the interconnect in the time domain.

### 4 Conclusions

The SIFE method holds considerable promise to solve three dimensional time domain electromagnetic problems, in which high contrasts between different types of materials exist and irregular structures are present. It handles irregular structures and partial discontinuities in a systematically correct and elegant fashion. Its accuracy and stability has now been demonstrated and verified with numerical experiments. With these basic properties being established, we are now working on improvements of the computational properties of the method in terms of numerical complexity and versatility.

### References

1. Gerrit Mur. The finite-element modeling of three-dimensional electromagnetic fields using edge and nodal elements. *IEEE transactions on antennas and propagation*, 41(7), July 1993.
2. Zhifeng Sheng, Rob Remis, and Patrick Dewilde. A least-squares implementation of the field integrated method to solve time domain electromagnetic problems. *Computational Electromagnetics in Time-Domain, 2007. CEM-TD 2007. Workshop on*, pages 1-4, 15-17 Oct. 2007.

# A Novel Staggered Finite Volume Time Domain Method

Thomas Lau, Erion Gjonaj, and Thomas Weiland

Institut für Theorie Elektromagnetischer Felder,  
Technische Universität Darmstadt, Darmstadt, Germany 64289  
lau@temf.tu-darmstadt.de, gjonaj@temf.tu-darmstadt.de, weiland@temf.tu-darmstadt.de

**Summary.** This work presents a novel finite volume time domain method on Cartesian grids. In comparison to the finite difference time-domain scheme of Yee the method offers a better accuracy while still maintaining a compact stencil. Additionally, mimetic discrete vectoranalytical operators for the method are constructed.

## 1 Introduction

In the majority of finite volume time-domain (FVTD) methods the electric degrees of freedom (DOF) and the magnetic DOF are co-located on the same spatial position [2]. Unfortunately, compared to the classical finite difference time-domain (FDTD) scheme of Yee [4] this co-location reduces the accuracy of the FVTD method. Hence, one approach to increase the accuracy of the FVTD method, motivated by the Yee scheme, is to stagger the DOFs. However, the staggering can be performed in three different ways: First, staggering the electric and magnetic fields, only. Second, staggering the vectorial components of the DOFs, only. Third, combining both approaches and staggering the electric and magnetic DOFs and each of their vectorial components. The last approach corresponds to the staggering applied in the Yee scheme.

In this work the authors restrict their investigation to the second strategy, and only consider the specific staggering, shown in figure 1.

## 2 Construction of the FVTD method

Starting point for constructing the FVTD method, neglecting electric currents for the sake of brevity, is the volume integral formulation of Maxwell's equations [1] over a domain  $\Omega$ :

$$\forall V \subseteq \Omega, \frac{d}{dt} \int_V \mu \mathbf{H} dV = - \int_{\partial V} d\mathbf{A} \times \mathbf{E}, \quad (1)$$

$$\forall V \subseteq \Omega, \frac{d}{dt} \int_V \epsilon \mathbf{E} dV = \int_{\partial V} d\mathbf{A} \times \mathbf{H} \quad (2)$$

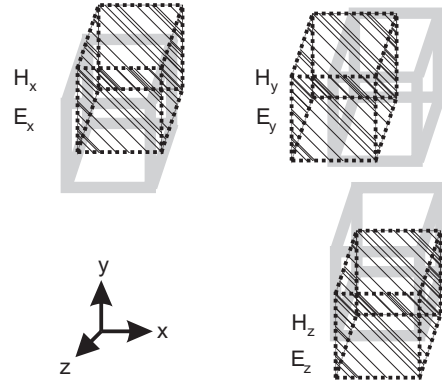


**Fig. 1.** Staggering of the field DOFs. The DOFs are defined, according to the vectorial component they represent, on three different dual volumes (shaded) with respect to the primary grid cell (gray).

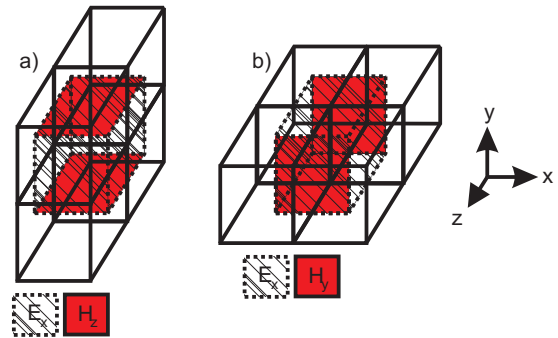


**Fig. 2.** The time evolution of the integral of  $E_x$  over its control volumes (shaded cell) solely depends on the fluxes through the  $y$  and  $z$  faces, respectively. Figure a) shows the flux through the  $y$  face (red) which is uniquely defined by the values of  $H_z$  on its control volumes (solid cells). Figure b) shows the flux through the  $z$  face (red) of the same cell which is uniquely defined by the values of  $H_y$  on its control volumes (solid cells).

with the electric field,  $\mathbf{E}$ , and the magnetic field,  $\mathbf{H}$ . Different materials in  $\Omega$  are characterized by their permeability,  $\mu$ , and permittivity,  $\epsilon$ , respectively. The domain  $\Omega$  is discretized by restricting the arbitrary volumes  $V$  in equation (1) and (2) to a finite set of specific control volumes  $\{V_x\}$ ,  $\{V_y\}$  and  $\{V_z\}$  for each vectorial component respectively. For a primary Cartesian grid,  $\{x_i, y_j, z_k\}$  with  $i = 1 \dots I$ ,  $j = 1 \dots J$ ,  $k = 1 \dots K$ , the vol-

umes are defined by

$$[V_x]_{ijk} = [x_i, x_{i+1}] [y_j, y_{j+1}] [\tilde{z}_k, \tilde{z}_{k+1}], \quad (3)$$

$$[V_y]_{ijk} = [\tilde{x}_i, \tilde{x}_{i+1}] [y_j, y_{j+1}] [z_k, z_{k+1}], \quad (4)$$

$$[V_z]_{ijk} = [x_i, x_{i+1}] [\tilde{y}_j, \tilde{y}_{j+1}] [z_k, z_{k+1}], \quad (5)$$

$$\tilde{x}_i = \frac{(x_i + x_{i-1})}{2}, \dots \quad (6)$$

The field DOF are defined by the volume averages of the electric and magnetic field components  $\mathbf{e}_\alpha$  and  $\mathbf{h}_\alpha$ . From equation (2) the update equation for  $E_x$  is calculated as

$$\frac{d}{dt} \int_{V_x} E_x dV = \int_{\partial V_x} dA_y H_z - \int_{\partial V_x} dA_z H_y. \quad (7)$$

Assuming that the field components are *constant* inside their control volumes, respectively, it is possible to calculate the fluxes directly. This is illustrated in figure 2 for the component  $E_x$ . In the same manner the equations for the other components of the electric and magnetic fields are derived. Assigning constant, *effective* material parameters  $\epsilon$  and  $\mu$  to each control volume a semi discrete approximation of the equations (1) and (2) is obtained.

### 3 Properties of the FVTD method

It is possible to define, in analogy to the FIT method [3], discrete vector analytical operators div, grad, rot which mimics the algebraic properties of their continuous counterparts.

The dispersion relation of the FVTD method on a Cartesian grid with grid spacing  $\Delta$  and time step  $\Delta t$  is

$$\sin\left(\frac{\Delta t \omega}{2}\right) = \sigma^2 (K_{\text{Yee}} - \delta K),$$

$$K_{\text{Yee}} = \left( \sin^2\left(\frac{\beta_x}{2}\right) + \sin^2\left(\frac{\beta_y}{2}\right) + \sin^2\left(\frac{\beta_z}{2}\right) \right),$$

$$\delta K = \frac{1}{2} \sum_{\gamma \neq \delta} \sin^2\left(\frac{\beta_\gamma}{2}\right) \sin^2\left(\frac{\beta_\delta}{2}\right),$$

$$\sigma = c\Delta t / \Delta (\text{Courant number}),$$

with  $\gamma, \delta \in \{x, y, z\}$ . A more detailed analysis reveals that the dispersion properties of the FVTD are in average superior to that of the Yee scheme. This is illustrated in figure 3 which shows the relative error in the phase velocity for five grid points per wavelength at the stability limit of both methods, respectively. The maximal stable time step of the FVTD method is roughly 1.7 times higher than that of the Yee scheme on a homogeneous mesh. Both schemes offer a magic time step at their stability limit. For the Yee scheme waves along the space diagonals and for the FVTD method waves along the axes are propagated exactly.

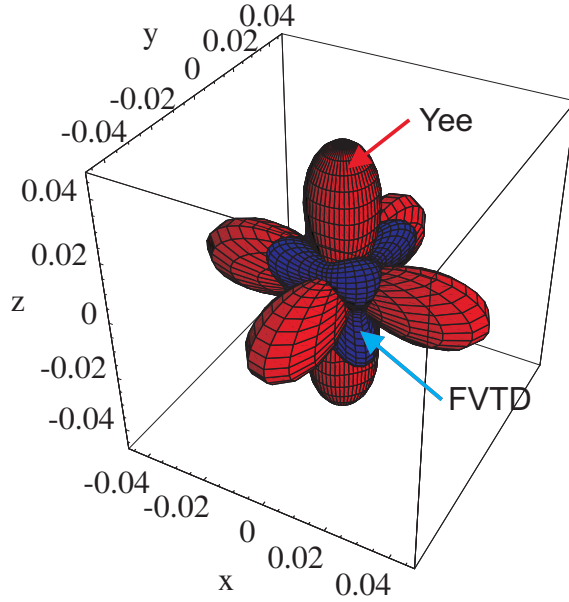


**Fig. 3.** Relative error in the phase velocity of the Yee scheme and the FVTD method for five grid points per wavelength at their stability limit, respectively.

### References

1. E. J. Rothwell and M. J. Cloud. *Electromagnetics*. CRC Press, Boca Raton, 2001.
2. V. Shankar, W. F. Hall, and A. H. Mohammadian. A time-domain differential solver for electromagnetic scattering problems. *Proc. of IEEE*, 77:709–721, 1989.
3. T. Weiland. A discretisation method for the solution of maxwell’s equations for six-component fields. *Elektrotechnik und bertragungstechnik (AE)*, 31:116–120, 1977.
4. K. S. Yee. Numerical solution of initial value boundary problems involving maxwell’s equations in isotropic media. *IEEE Trans. Antennas Propag.*, 14:302–307, 1966.

---

**Session**

**CS 2**

---



# Wavelets in circuit simulation

Emira Dautbegovic

Qimonda, Am Campeon 1-12, 85579 Neubiberg, Germany [emira.dautbegovic@qimonda.com](mailto:emira.dautbegovic@qimonda.com)

**Summary.** Wavelet theory is a relatively recent area of scientific research, with a very successful application in a broad range of problems such as image and signal processing, mathematical modeling, electromagnetic scattering and many more. The key wavelet property contributing to this success is the capability of a simultaneous time and frequency representation of a signal. The potential exploitation of this property for a next-generation, wavelet-based simulation of analog circuits is discussed in this paper.

## 1 Circuit simulation

Analog circuit simulation is the standard industry approach to verify an integrated circuit (IC) operation at the transistor level before committing a designed circuit to the expensive manufacturing process. A starting point for an analog circuit simulator (e.g. SPICE and its derivatives) is usually a text file (netlist) that describes the circuit elements (resistors, capacitors, transistors, etc.) and their connections. This input is then parsed and translated to a data format reflecting the underlying mathematical model of the system. This is done by applying the basic physical laws (such as energy and charge conservation laws) onto network topology and taking into account characteristic equations for the network elements. The most used “translation” approach is the modified nodal analysis (MNA). This automatic modeling approach aims to preserve the topological structure of the network instead of describing a system with a minimal set of unknowns. The resulting mathematical model is in form of an initial-value problem of differential-algebraic equations (DAEs). For example, network equations in charge/flux oriented MNA formulation have a following semi-implicit nonlinear form:

$$\mathbf{A} \frac{d\mathbf{q}(\mathbf{x})}{dt} + \mathbf{f}(\mathbf{x}) = \mathbf{s}(t). \quad (1)$$

The incidence matrix  $\mathbf{A}$  has entries  $\{0, 1, -1\}$  and is in general singular.  $\mathbf{x}$  is the vector of node potentials and specific branch voltages and  $\mathbf{q}$  is the vector of charges and fluxes.  $\mathbf{f}$  comprises static contributions, while  $\mathbf{s}$  contains the contributions of independent sources.  $t$  is the time.

The underlying DAE system (1) is then solved using Newton’s method, implicit integration meth-

ods and sparse matrix techniques. In general, (1) is a stiff system (i.e. contains characteristic constants of several orders of magnitude) and suffers from poor smoothness properties of modern transistor model equations. Furthermore, if more general models for network elements are utilized, or refined models are used to include second order and parasitic effects, an ill-conditioned problem may arise and very special care must be taken to avoid divergence during the numerical solution of such a system.

Modern industrial circuit simulators are facing two serious challenges today: the simulation of very large circuits with millions of transistors (e.g. memory chips) on the one hand, and simulation of RF circuits comprising multitone oscillatory circuits with widely-separated tones and high amount of digital content, on the other hand.

The sheer size of the simulation of large circuits containing millions of transistors yields simulations that are impractical (they can last weeks, even longer than a month) or infeasible due to extreme memory and computational requirements.

On the other hand, when simulating RF circuits or circuits that contain RF portions standard analog circuit simulators are both inefficient, due to the presence of multitone signals with widely separated tones, and inadequate since linearization around DC operating point done by a standard circuit simulator causes loss of information on non-linear effects. Therefore, a specialized RF simulator based on either the frequency-domain Harmonic Balance or the time-domain Shooting algorithm [1] is employed for the simulation of RF circuits. Both methods make an a-priori assumption that the signals present in a circuit are (quasi) periodic and have a narrow-band spectrum (i.e. contain only a small number of frequencies). With the first assumption, an RF simulator gains efficiency of simulations but loses generality (i.e. ability to simulate non-RF circuits). Furthermore, the second assumption is being considerably violated lately, since modern RF designs feature an ever-increasing number of frequencies present in their spectrum (due to a sharp increase in digital content), as well as include intrinsically broadband circuit parts (e.g. high-ratio dividers).

Currently, the RF front-end is usually designed by employing a frequency domain RF simulator, while the rest of the circuit is designed in the time domain employing the standard circuit simulation techniques. Due to this separation during the design process, these RF/non-RF circuits are usually not realized on the same die in order to keep spurious couplings between them as small as possible, since they cannot be easily characterized in a common simulation environment. However, with the trend towards ever-decreasing chip size, integration of RF and non-RF part on a same die is eminent and new simulation tools that can support these designs are urgently needed.

## 2 Wavelets in circuits simulation

Wavelet-based algorithms are already in productive use in a broad range of scientific computation applications, such as image and signal processing (signal and image compression, nonlinear filtering, etc.), numerical analysis (solving operator equations, boundary value problems, large matrix equations, etc.), the compression of the FBI fingerprints data, to name just few. Factors contributing to this success are the intrinsic property of the localized support of a wavelet basis, the numerically efficient Multi-Resolution Analysis (MRA) framework and the adaptive approximation approach, which leads to a uniform error distribution over approximation interval.

The name *wavelet* or *ondelette* was coined in the early 1980's by French researchers [2] meaning the small wave. Smallness refers to the fact that a wavelet is a locally supported function (i. e. of limited duration) and wave refers to the condition that it has to be an oscillatory function (i. e. has an average zero value).

In circuit simulation wavelets may be used as basis functions to represent electrical signals. The wavelet basis is formed via translations and dilatations from a single wavelet function  $\Psi(x)$ , called *mother wavelet*, and noted as:

$$\Psi_{s,\tau}(x) = \frac{1}{\sqrt{s}} \Psi\left(\frac{x-\tau}{s}\right), \quad (2)$$

where  $(s, \tau) \in \mathbb{R}^+ \times \mathbb{R}$ . All wavelets from a specific basis are shifted (parameter  $\tau$ ) and dilated/compressed (by factor  $s$ ) versions of this mother wavelet. The translation parameter  $\tau$  is responsible for the localization in time of a corresponding wavelet. The scaling parameter  $s$ , or the scale, is related to the frequency in that it is the frequency inverse. Therefore, the high scale corresponds to low frequencies or a global view of the signal and low scales correspond to high frequencies or a detailed view of the signal. Finally,

the factor  $1/\sqrt{s}$  is used for energy normalization across different scales. From the definition it is clear that a wavelet basis intrinsically supports a *simultaneous* time-frequency representation of signal.

The ongoing investigation into use of wavelets [3–7] has shown that their intrinsic properties make wavelets the natural candidate for a successful successor of time-marching (transient analysis) and/or frequency domain (Harmonic Balance analyses) paradigms used in circuit simulation today. However, although valuable as a proof-of-concept, current wavelet approaches to circuit simulation are essentially academic in scope, with algorithms tested only on small and simple sample circuits.

In conclusion, a substantial effort is necessary to drive further advances in wavelet-based simulation techniques to the point when wavelet analysis is mature enough to be driven into productive use within industrial simulators. However the expected benefit that a wavelet-based simulation engine could bring both in quantitative terms (reduction in computation time and memory requirements) as well as qualitative terms (analyzing signals with resolutions adapted to a problem at hand) is well worth allocating effort in a bid to develop the next-generation circuit simulators, capable of answering industrial challenges of tomorrow.

## References

1. K. Kundert. Simulation methods for RF integrated circuits. *Proc. IEEE/ACM Int. Conf. Computer-Aided Design*, pages 752–765, 1997.
2. A. Grossmann and J. Morlet. Decomposition of hardy functions into square integrable wavelets of constant shape. *SIAM Journal of Mathematical Analysis*, 15:723–736, 1984.
3. D. Zhou and W. Cai. A fast wavelet collocation method for high-speed circuit simulation. *IEEE Trans. Circuit and Systems*, 46:920–930, 1999.
4. N. Soveiko, E. Gad, and M. Nakhla. A wavelet-based approach for steady-state analysis of nonlinear circuits with widely separated time scales. *IEEE Microwave and Wireless Components Letters*, 17:451–453, 2007.
5. C.E. Christoffersen and M.B. Steer. State-variable-based transient circuit simulation using wavelets. *IEEE Microwave and Wireless Components Letters*, 11:161–163, 2001.
6. E. Dautbegovic, M. Condon, and C. Brennan. An efficient nonlinear circuit simulation technique. *IEEE Trans. Microwave Theory and Techniques*, 53:548–555, 2005.
7. A. Bartel, S. Knorr, and R. Pulch. Wavelet-based adaptive grids for multirate partial differential-algebraic equations. *submitted to Appl. Numer. Math.*, 2007.

# Hybrid Analysis of Nonlinear Time-Varying Circuits Providing DAEs with at Most Index 1

Satoru Iwata<sup>1</sup>, Mizuyo Takamatsu<sup>2</sup>, and Caren Tischendorf<sup>3</sup>

<sup>1</sup> Research Institute for Mathematical Sciences, Kyoto University, Kyoto 606-8502, Japan  
iwata@kurims.kyoto-u.ac.jp

<sup>2</sup> Department of Mathematical Informatics, Graduate School of Information Science and Technology,  
University of Tokyo, Tokyo 113-8656, Japan mizuyo\_takamatsu@mist.i.u-tokyo.ac.jp

<sup>3</sup> Mathematical Institute, University of Cologne, Weyertal 86-90, 50931 Köln, Germany  
tischendorf@math.uni-koeln.de

**Summary.** Commercial packages for a transient circuit simulation are often based on the modified nodal analysis which allows an automatic setup of model equations and needs a nearly minimal number of variables. However, it may lead to DAEs with higher index. Here, we present a hybrid analysis for nonlinear time varying circuits leading to DAEs with at most index 1. This hybrid analysis is based on the network topology only. Consequently, an automatic setup of the hybrid equations from netlists is possible.

## 1 Introduction

When modelling electrical circuits for a transient simulation, one has to regard Kirchhoff's laws for the network and the constitutive laws for the different types of network elements. They are originally based on the branch voltages  $\mathbf{u}$  and the branch currents  $\mathbf{i}$  existing in the network. They form the basis for all modelling approaches as for instance the popular modified nodal analysis.

Concerning the huge number of variables involved (all branch voltages and branch currents) one is interested in a reduced system reflecting the complete circuit behaviour that can be generated automatically. Whereas the modified nodal analysis focusses on a description depending mainly on nodal potentials, our hybrid analysis approach here bases on certain branch voltages and branch currents obtained from a construction of normal trees, i.e. from trees containing all independent voltage sources, no independent current source, a maximal number of capacitive branches and a minimal number of inductive branches.

Such normal trees have already been used in [1] for state approaches for linear RLC networks. The results have been extended in [4] for linear circuits containing ideal transformers, nullors, independent and controlled sources, resistors, inductors, and capacitors, and, under a topological restriction, gyrators. Furthermore, it formed the basis for developing a hybrid approach for RLC

networks providing a DAE system with minimal index [3].

Here, we follow the hybrid approach in [3] but use projection techniques (cf. [2]) in order to prove the index results for general nonlinear time-varying circuit systems.

## 2 Hybrid Analysis

Here, we consider nonlinear time-varying circuits composed of resistors, inductors, capacitors, voltage and current sources. For simplicity, we restrict to independent sources only. The case of dependent sources is under current research but seems no to form a limit of the approach when certain topological criteria are satisfied.

Let  $\Gamma = (W, E)$  be the network graph with vertex set  $W$  and edge set  $E$ . An edge in  $\Gamma$  corresponds to a branch that contains one element in the circuit. We denote the set of edges corresponding to independent voltage sources and independent current sources by  $E_v$  and  $E_j$ , respectively. We split  $\bar{E}_{vj} := E \setminus (E_v \cup E_j)$  into  $E_y$  and  $E_z$ , i.e.,  $E_y \cup E_z = \bar{E}_{vj}$  and  $E_y \cap E_z = \emptyset$ . A partition  $(E_y, E_z)$  is called an *admissible partition*, if  $E_y$  includes all the capacitances, and  $E_z$  includes all the inductances.

We call a spanning tree  $T$  of  $\Gamma$  a *reference tree* if  $T$  contains all edges in  $E_v$ , no edges in  $E_j$ , and as many edges in  $E_y$  as possible. Note that a reference tree  $T$  may contain some edges in  $E_z$ . The cotree of  $T$  is denoted by  $\bar{T} = E \setminus T$ . A reference tree is called *normal* if it contains as many edges corresponding to capacitors and as few edges corresponding to inductors as possible.

We denote the vector of currents through all branches of the circuit by  $\mathbf{i}$ , and the vector of voltages across all branches by  $\mathbf{u}$ . Let  $V$ ,  $J$ ,  $C$ , and  $L$  denote the sets of independent voltage sources, independent current sources, capacitors, and inductors, respectively. Moreover,  $G$  and  $R$  denote the

sets of conductors and resistors in  $E_y$  and  $E_z$ , respectively. Given an admissible partition  $(E_y, E_z)$  and a normal reference tree  $T$ , we split  $\mathbf{i}$  and  $\mathbf{u}$  into

$$\mathbf{i} = (\mathbf{i}_V, \mathbf{i}_C^\tau, \mathbf{i}_G^\tau, \mathbf{i}_C^\lambda, \mathbf{i}_G^\lambda, \mathbf{i}_R^\tau, \mathbf{i}_L^\tau, \mathbf{i}_R^\lambda, \mathbf{i}_L^\lambda, \mathbf{i}_J)$$

and

$$\mathbf{u} = (\mathbf{u}_V, \mathbf{u}_C^\tau, \mathbf{u}_G^\tau, \mathbf{u}_C^\lambda, \mathbf{u}_G^\lambda, \mathbf{u}_R^\tau, \mathbf{u}_L^\tau, \mathbf{u}_R^\lambda, \mathbf{u}_L^\lambda, \mathbf{u}_J)$$

where the subscripts correspond to elements and the superscripts  $\tau$  and  $\lambda$  designate the tree  $T$  and the cotree  $\bar{T}$ .

The physical characteristics of elements determine *constitutive equations*. Conductors included in  $E_y$  are modelled by constitutive equations of the form

$$\mathbf{i}_G^\tau = \mathbf{g}^\tau(\mathbf{u}_G^\tau, \mathbf{u}_G^\lambda) \quad \text{and} \quad \mathbf{i}_G^\lambda = \mathbf{g}^\lambda(\mathbf{u}_G^\tau, \mathbf{u}_G^\lambda). \quad (1)$$

Resistors included in  $E_z$  are modelled by

$$\mathbf{u}_R^\tau = \mathbf{r}^\tau(\mathbf{i}_R^\tau, \mathbf{i}_R^\lambda) \quad \text{and} \quad \mathbf{u}_R^\lambda = \mathbf{r}^\lambda(\mathbf{i}_R^\tau, \mathbf{i}_R^\lambda). \quad (2)$$

All capacitors are given by

$$\mathbf{i}_C^\tau = \frac{d}{dt} \mathbf{q}^\tau(\mathbf{u}_C^\tau, \mathbf{u}_C^\lambda) \quad \text{and} \quad \mathbf{i}_C^\lambda = \frac{d}{dt} \mathbf{q}^\lambda(\mathbf{u}_C^\tau, \mathbf{u}_C^\lambda). \quad (3)$$

All inductors are given by

$$\mathbf{u}_L^\tau = \frac{d}{dt} \phi^\tau(\mathbf{i}_L^\tau, \mathbf{i}_L^\lambda) \quad \text{and} \quad \mathbf{u}_L^\lambda = \frac{d}{dt} \phi^\lambda(\mathbf{i}_L^\tau, \mathbf{i}_L^\lambda). \quad (4)$$

Independent voltage and current sources simply read as

$$\mathbf{u}_V = \mathbf{v}_s(t) \quad \text{and} \quad \mathbf{i}_J = \mathbf{j}_s(t). \quad (5)$$

Kirchhoff's current law may be written as

$$Q\mathbf{i} = 0$$

where  $Q$  denotes the *fundamental cutset matrix*:

$$\begin{pmatrix} \mathbf{i}_V & \mathbf{i}_C^\tau & \mathbf{i}_G^\tau & \mathbf{i}_C^\lambda & \mathbf{i}_G^\lambda & \mathbf{i}_R^\tau & \mathbf{i}_L^\tau & \mathbf{i}_R^\lambda & \mathbf{i}_L^\lambda & \mathbf{i}_J \\ \left( \begin{array}{cccccccccc} I & 0 & 0 & A_{VC} & A_{VG} & 0 & 0 & A_{VR} & A_{VL} & A_{VJ} \\ 0 & I & 0 & A_{CC} & A_{CG} & 0 & 0 & A_{CR} & A_{CL} & A_{CJ} \\ 0 & 0 & I & 0 & A_{GG} & 0 & 0 & A_{GR} & A_{GL} & A_{GJ} \\ 0 & 0 & 0 & 0 & 0 & I & 0 & A_{RR} & A_{RL} & A_{RJ} \\ 0 & 0 & 0 & 0 & 0 & 0 & I & 0 & A_{LL} & A_{LJ} \end{array} \right), \end{pmatrix}$$

Kirchhoff's voltage law provides

$$B\mathbf{u} = 0$$

with  $B$  being the *fundamental loop matrix*

$$\begin{pmatrix} \mathbf{u}_V & \mathbf{u}_C^\tau & \mathbf{u}_G^\tau & \mathbf{u}_C^\lambda & \mathbf{u}_G^\lambda & \mathbf{u}_R^\tau & \mathbf{u}_L^\tau & \mathbf{u}_R^\lambda & \mathbf{u}_L^\lambda & \mathbf{u}_J \\ \left( \begin{array}{cccccccccc} -A_{VC}^\tau & -A_{CC}^\tau & 0 & I & 0 & 0 & 0 & 0 & 0 & 0 \\ -A_{VG}^\tau & -A_{CG}^\tau & -A_{GG}^\tau & 0 & I & 0 & 0 & 0 & 0 & 0 \\ -A_{VR}^\tau & -A_{CR}^\tau & -A_{GR}^\tau & 0 & 0 & -A_{RR}^\tau & 0 & I & 0 & 0 \\ -A_{VL}^\tau & -A_{CL}^\tau & -A_{GL}^\tau & 0 & 0 & -A_{RL}^\tau & -A_{LL}^\tau & 0 & I & 0 \\ -A_{VJ}^\tau & -A_{CJ}^\tau & -A_{GJ}^\tau & 0 & 0 & -A_{RJ}^\tau & -A_{LJ}^\tau & 0 & 0 & I \end{array} \right). \end{pmatrix}$$

### 3 Hybrid Equations

Performing the hybrid analysis presented in [3], we obtain the hybrid equation system

$$\begin{aligned} -A_{CR}^\tau \mathbf{u}_C^\tau - A_{GR}^\tau \mathbf{u}_G^\tau - A_{RR}^\tau \mathbf{r}^\tau + \mathbf{r}^\lambda &= A_{VR}^\tau \mathbf{v}_s(t) \\ -A_{CL}^\tau \mathbf{u}_C^\tau - A_{GL}^\tau \mathbf{u}_G^\tau - A_{RL}^\tau \mathbf{r}^\tau \\ -A_{LL}^\tau \dot{\phi}^\tau + \dot{\phi}^\lambda &= A_{VL}^\tau \mathbf{v}_s(t) \\ A_{CG} \mathbf{g}^\lambda + A_{CR} \mathbf{i}_R^\lambda + A_{CL} \mathbf{i}_L^\lambda \\ + \dot{\mathbf{q}}^\tau + A_{CC} \dot{\mathbf{q}}^\lambda &= -A_{CJ} \mathbf{j}_s(t) \\ \mathbf{g}^\tau + A_{GG} \mathbf{g}^\lambda + A_{GR} \mathbf{i}_R^\lambda + A_{GL} \mathbf{i}_L^\lambda &= -A_{GJ} \mathbf{j}_s(t) \end{aligned}$$

with

$$\begin{aligned} \mathbf{q}^\tau &= \mathbf{q}^\tau(\mathbf{u}_C^\tau, A_{VC}^\tau \mathbf{v}_s(t) + A_{CC}^\tau \mathbf{u}_C^\tau), \\ \mathbf{q}^\lambda &= \mathbf{q}^\lambda(\mathbf{u}_C^\tau, A_{VC}^\tau \mathbf{v}_s(t) + A_{CC}^\tau \mathbf{u}_C^\tau), \\ \mathbf{g}^\tau &= \mathbf{g}^\tau(\mathbf{u}_G^\tau, A_{VG}^\tau \mathbf{v}_s(t) + A_{CG}^\tau \mathbf{u}_G^\tau + A_{GG}^\tau \mathbf{u}_G^\tau), \\ \mathbf{g}^\lambda &= \mathbf{g}^\lambda(\mathbf{u}_G^\tau, A_{VG}^\tau \mathbf{v}_s(t) + A_{CG}^\tau \mathbf{u}_G^\tau + A_{GG}^\tau \mathbf{u}_G^\tau), \\ \mathbf{r}^\tau &= \mathbf{r}^\tau(-A_{RR} \mathbf{i}_R^\lambda - A_{RL} \mathbf{i}_L^\lambda - A_{RJ} \mathbf{j}_s(t), \mathbf{i}_R^\lambda), \\ \mathbf{r}^\lambda &= \mathbf{r}^\lambda(-A_{RR} \mathbf{i}_R^\lambda - A_{RL} \mathbf{i}_L^\lambda - A_{RJ} \mathbf{j}_s(t), \mathbf{i}_R^\lambda), \\ \phi^\tau &= \phi^\tau(-A_{LL} \mathbf{i}_L^\lambda - A_{LJ} \mathbf{j}_s(t), \mathbf{i}_L^\lambda), \\ \phi^\lambda &= \phi^\lambda(-A_{LL} \mathbf{i}_L^\lambda - A_{LJ} \mathbf{j}_s(t), \mathbf{i}_L^\lambda). \end{aligned}$$

This hybrid equation system depends on the branch voltages  $\mathbf{u}_C^\tau$  of capacitances of the tree, the branch voltages  $\mathbf{u}_G^\tau$  of conductances of the tree, the branch currents  $\mathbf{i}_R^\lambda$  of the resistances of the cotree and the branch currents  $\mathbf{i}_L^\lambda$  of the inductances of the cotree only.

**Theorem 1.** *The hybrid equation system has at most index 1.*

The proof bases on the tractability index concept using a projector based analysis.

Higher index variables as known from the modified nodal analysis do not appear in the hybrid system. If one is interested in e.g. a current through a loop of voltages and capacitances, one can calculate it easily after the numerical integration of the hybrid system. This way, the usually larger error in the higher index variables does not influence the integration process.

### References

1. P. R. Bryant. The order of complexity of electrical networks. *Pro. IEE (GB), Part C*, 106:174–188, 1959.
2. D. Estévez Schwarz and C. Tischendorf. Structural analysis of electric circuits and consequences for MNA. *Int. J. Circ. Theor. Appl.*, 28:131–162, 2000.
3. S. Iwata and M. Takamatsu. Index minimization of differential-algebraic equations in hybrid analysis for circuit simulation. *Math. Programming*, to appear.
4. G. ReiBig. Extension of the normal tree method. *Int. J. Circ. Theor. Appl.*, 27:241–265, 1999.

# Convergence Issues of Ring Oscillator Simulation by Harmonic Balance Technique

M.M. Gourary<sup>1</sup>, S.G. Rusakov<sup>1</sup>, S.L. Ulyanov<sup>1</sup>, M.M. Zharov<sup>1</sup>, and B.J. Mulvaney<sup>2</sup>

<sup>1</sup> IPPM, Russian Academy of Sciences, Moscow, Russia [gourary@ippm.ru](mailto:gourary@ippm.ru)

<sup>2</sup> Freescale Semiconductor Inc., Austin, Texas, USA [brian.mulvaney@freescale.com](mailto:brian.mulvaney@freescale.com)

**Summary.** Poor convergence properties of harmonic balance algorithm for ring oscillators are explained by the existence of multiple solutions of the algebraic system corresponding with each physical oscillation. The approach to improve the convergence is proposed.

## 1 Introduction

Difficulties in Harmonic Balance (HB) simulation of ring oscillators (RO) with large number of stages were reported in [1]. We performed an investigation of the problem on the base of HB simulations of CMOS RO with the continuation algorithm with frequency adjusting [2,3]. The investigation results are presented in this paper.

The continuation algorithm with frequency adjusting is the homotopy algorithm specially designed to prevent the convergence of Newton iterations to DC point. It is based on the incorporating of an artificial voltage source (probe) into the circuit. The probe magnitude corresponding to the oscillation voltage is obtained by varying the magnitude from zero (DC solution) until probe current is null. The probe frequency is varying in such a way that the phase of probe current is zero. The initial value of the frequency  $\omega_0$  is defined by AC oscillation conditions at unstable DC point

$$\Im(Z(\omega_0)) = 0 \quad \Re(Z(\omega_0)) < 0 \quad (1)$$

where  $Z(\omega)$  is the input impedance.

The convergence difficulties in the simulation of CMOS RO are illustrated with the following examples. The continuation curves (probe current vs probe voltage) have simple form for 3- and 5-stage oscillators (see Fig. 1).

But for 7-stage RO the simulation exposes a complex continuation process (Fig. 2) and fails after some thousand steps. A similar effect is observed in RO with larger number of stages.

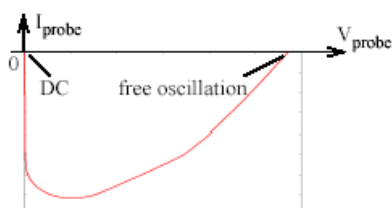


Fig. 1. Continuation curve. 5-stage RO

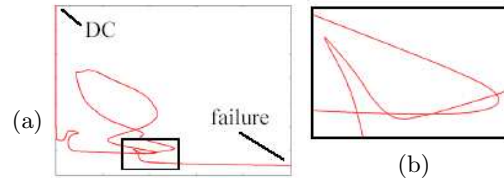


Fig. 2. Continuation curve. (a) 7-stage RO (b) fragment

The analysis of (1) for 7-stage RO shows that there exists an additional frequency value satisfying conditions (1). The simulation with this initial frequency is successfully performed providing the simple continuation curve. However, simulation results essentially differ from the transient simulation; the frequency (2.33 GHz) is almost four times higher than in transient simulation (570.4 MHz) and the sinusoidal output waveform evidently differs from the pulsed one obtained by transient simulation. Thus the simulation determines another RO solution. Note that no additional solutions for 3 and 5 stage oscillators exist.

One can suppose the existence of two solutions to be the source of poor convergence due to the appearance of additional attractive points for continuation trajectories. However this cannot explain the successful convergence to the second solution in spite of the existence of the first solution. More detailed analysis of the problem is considered below.

## 2 Explanation

The existence of additional (unstable) solutions in RO is well-known [4]. It can be understood by considering  $n$ -stage RO containing ideal inverters with equal delay time  $\tau$ . In this case the keeping of self-oscillations requires the output signal of the chain to be delayed from the input signal by integer number of periods:  $n\tau = T/2 + mT$ . Thus the frequency of  $m$ th solution is unambiguously defined by the frequency of the first solution

$$f_m^{(n)} = (2m - 1)f_1^{(n)} \quad m = 1, 2, 3, \dots \quad (2)$$

In real RO the number of possible periodic oscillations cannot be infinite because at high frequency the inverter amplifying property decrease,

and generation conditions (1) cannot be met. The poor HB convergence cannot be explained by additional solutions only. The explanation can be obtained if one will take into account the effect of multiple numerical representations of the periodic solution. The effect can be described as follows.

Each T-periodic function can be also considered as the function with period  $kT$  and frequency  $f/k$ , where  $k$  is an integer. HB method for oscillators reduces the steady-state problem to the solving of nonlinear algebraic system with respect to the vector containing unknown oscillation frequency and harmonics of circuit variables:

$$X = [f, A_1, A_2, \dots, A_i, \dots] \quad (3)$$

Here  $A_i$  is the vector of  $i$ th harmonics of circuit variables. But if the vector (3) defines the periodic state of the oscillator then this state can be also defined by vectors

$$\begin{aligned} X' &= \left[ \frac{f}{2}, 0, A_1, 0, A_2, \dots, 0, A_i, \dots \right] \\ X'' &= \left[ \frac{f}{3}, 0, 0, A_1, 0, 0, A_2, \dots, 0, 0, A_i, \dots \right] \end{aligned} \quad (4)$$

We shall refer vectors (4) as the images of the basic solution vector (3).

Thus for each steady-state behavior of the oscillator there exists infinite set of images representing parasitic solutions of HB system. It is natural to assume that the effect of the image depends on the deviation of its frequency from the frequency of the solution to be found. In the case of the single steady state solution its own images have no effect on the convergence because their frequencies are essentially less than the basic frequency. But if there exists a number of solutions then their images can complicate the continuation process when the frequency of the sought-for solution is close to the frequency of any image of other solution.

Presented considerations explain the pointed above behavior of the continuation process for 7-stage RO. The second solution is easily simulated because its frequency 2.33 GHz is much higher than the frequencies of images of the first solution. But the continuation process for the first solution with frequency 570 MHz is deteriorated due to the 4th image of the second solution with frequency  $2.33 \text{ GHz}/4 = 582.5 \text{ MHz}$ .

Note that in ideal RO the frequency of any additional solution is a multiple of the basic frequency (2). Taking into account that real RO approaches the ideal one on the increase of the number of stages we can explain poor HB convergence of RO with large number of stages.

The presented explanation was also confirmed by simulations of another types of RO. Particularly the method proposed in [1] for the simulation of RO with identical stages was analyzed.

The results of numerical experiments are in good agreement with the proposed theory.

### 3 Convergence Improvement

From the presented analysis we conclude that to improve the convergence we need to decrease the effect of foreign images on the desired solution.

One can pointed out that under truncated set of harmonics an image is not an exact solution of HB system, and we expect that this effect will decay with the reducing of the number of considering harmonics. The most decay (or full elimination) of the effect can be awaited when the number of harmonics is less than image index, because first  $l - 1$  harmonics of  $l$ th image are zeroes.

This assumption was supported by the simulations with small number of harmonics. The experiments showed that HB simulation with only one harmonic provides the evaluated oscillation frequency to be close to its true value. No convergence difficulties were observed in experiments, and continuation trajectories have simple form similar with Fig. 1. Obtained results allowed to propose the following modification of continuation method for RO.

1. The continuation algorithm is performed for the state vector containing only one harmonic.
2. The obtained truncated solution is considered as the initial guess of Newton iterations.
3. Newton iterations for HB autonomous system are performed with required number of harmonics.

The implementation of the algorithm into HB simulator allowed to evaluate RO with considered CMOS inverter up to 15 stages. Besides computational efforts were essentially reduced.

### References

1. X. Duan and K. Mayaram. An Efficient and Robust Method for Ring-Oscillator Simulation Using the Harmonic-Balance Method. *IEEE Trans. Computer-Aided Design*, 24(8):1225–1233, 2005.
2. M. Gourary, S. Ulyanov, M. Zharov, S. Rusakov, K. K. Gullapalli, and B. J. Mulvaney. Simulation of high-Q oscillators. *IEEE/ACM International Conference on Computer-Aided Design*, pp. 162–169, Nov. 1998.
3. M. Gourary, S. Ulyanov, M. Zharov, S. Rusakov, K. K. Gullapalli, and B. J. Mulvaney. A robust and efficient oscillator analysis technique using harmonic balance. *Computer Methods in Applied Mechanics and Engineering*, 181:451–466, Jan. 2000.
4. P. Selting, Q. Zheng. Numerical stability analysis of oscillating integrated circuits. *ELSEVIER J. of Computational and Applied Mathematics*, 82:367–378, 1997.

# Stochastic Models for Analysing Parameter Sensitivities

Roland Pulch

Lehrstuhl für Angewandte Mathematik und Numerische Mathematik, Bergische Universität Wuppertal, Gaußstr. 20, D-42119 Wuppertal [pulch@math.uni-wuppertal.de](mailto:pulch@math.uni-wuppertal.de)

**Summary.** Mathematical modelling of electric circuits yields systems of differential algebraic equations. Often some technical parameters exhibit uncertainties. We arrange a stochastic model by considering these parameters as random variables. The resulting stochastic processes provide global information on the parameter sensitivity. We apply the generalised polynomial chaos to construct efficient numerical methods for solving the model. According numerical simulations are presented.

## 1 Stochastic Modelling

We consider an initial value problem of a system of differential algebraic equations (DAEs)

$$A(\mathbf{p})\dot{\mathbf{x}}(t) = \mathbf{f}(t, \mathbf{x}(t), \mathbf{p}), \quad \mathbf{x}(t_0) = \mathbf{x}_0 \quad (1)$$

with unknown solution  $\mathbf{x} : [t_0, t_1] \rightarrow \mathbb{R}^k$  and a matrix  $A(\mathbf{p}) \in \mathbb{R}^{k \times k}$ . In the DAE (1), the parameters  $\mathbf{p} \in \mathbb{R}^l$  are included and thus the solution becomes parameter dependent:  $\mathbf{x}(t) = \mathbf{x}(t; \mathbf{p})$ . Partial derivatives with respect to  $\mathbf{p}$  yield local information on the sensitivity of the solution.

Assuming some uncertainties, we replace the parameters by random variables  $\mathbf{p} = \mathbf{p}(\omega)$  on a probability space  $(\Omega, \mathcal{A}, P)$ . Thereby, a relatively large range of the variables can be chosen to achieve global information on the dependence. Consequently, the solution of the system (1) becomes a stochastic process  $\mathbf{X} : [t_0, t_1] \times \Omega \rightarrow \mathbb{R}^k$ . The according stochastic system reads

$$A(\mathbf{p}(\omega))\dot{\mathbf{X}}(t, \omega) = \mathbf{f}(t, \mathbf{X}(t, \omega), \mathbf{p}(\omega)), \quad \mathbf{X}(t_0, \omega) = \mathbf{x}_0. \quad (2)$$

Crucial data like expected values and variances of the process have to be determined efficiently by numerical methods.

This stochastic approach can be used for an arbitrary DAE system. We focus on DAEs resulting from mathematical models of electric circuits. In particular, oscillators are considered, where analysing the stability of periodic solutions represents an important task.

## 2 Application of Polynomial Chaos

The data of the stochastic model from Sect. 1 can be computed by Monte-Carlo simulation or its more sophisticated variants. However, a huge number of simulations based on (2) often has to be performed to achieve sufficiently accurate results. Alternatively, the approach of the generalised polynomial chaos yields efficient numerical methods for stationary problems, see [2].

We apply the generalised polynomial chaos to the transient problem (2). Assuming finite second moments with respect to a specific Sobolev norm, the stochastic process exhibits the representation

$$\mathbf{X}(t, \omega) = \sum_{i=0}^{\infty} \mathbf{v}_i(t) \Phi_i(\mathbf{p}(\omega)) \quad (3)$$

with coefficient functions  $\mathbf{v}_i : [t_0, t_1] \rightarrow \mathbb{R}^k$  and orthogonal basis polynomials  $\Phi_i : \mathbb{R}^l \rightarrow \mathbb{R}$ . The orthogonality is based on the inner product following from the expected value denoted by  $\langle \cdot \rangle$ , i.e.,  $\langle \Phi_i \Phi_j \rangle = \langle \Phi_i^2 \rangle \delta_{ij}$ .

To construct a numerical technique, the series (3) is truncated and inserted in the stochastic system (2), which causes a residual. Using the Galerkin approach, we obtain a larger system of DAEs

$$\sum_{i=0}^m \langle \Phi_l(\mathbf{p}) \Phi_i(\mathbf{p}) A(\mathbf{p}) \dot{\mathbf{v}}_i(t) \rangle = \left\langle \Phi_l(\mathbf{p}) \mathbf{f} \left( t, \sum_{i=0}^m \mathbf{v}_i(t) \Phi_i(\mathbf{p}), \mathbf{p} \right) \right\rangle \quad (4)$$

for  $l = 0, 1, \dots, m$ , where the unknowns are the time-dependent functions  $\mathbf{v}_i$ . In this system, the expected values are evaluated component-wise. We solve the system (4) with according initial values by standard integrators. Boundary value problems can be investigated in case of oscillators, which imply periodic solutions.

Given a numerical solution of (4), the expected value and the variance of the process are approximated directly via

$$\begin{aligned} \langle \mathbf{X}(t, \cdot) \rangle &\doteq \mathbf{v}_0(t), \\ \text{Var}(\mathbf{X}(t, \cdot)) &\doteq \sum_{i=1}^m \mathbf{v}_i(t)^2 \langle \Phi_i(\mathbf{p})^2 \rangle, \end{aligned} \quad (5)$$

where the operations are done component-wise again. Thus we have to solve the extended system (4) only once.

For integrating the system (4), evaluations of the expected values in the right-hand side are required at each used time point. Applying multidimensional quadrature formulas demands a large computational effort. In this case, the approach of stochastic collocation becomes superior to the above strategy, see [3]. Nevertheless, the nonlinear function  $\mathbf{f}$  may exhibit multiplicative structures, which allow for an efficient method based on the polynomial chaos.

The approach of the polynomial chaos can be applied in many applications, see [1]. Random oscillators modelled by ordinary differential equations are considered in [4]. The use of the polynomial chaos seems to be a relatively open task in case of DAEs. For example, the index of the extended system (4) with respect to the index of the original system (1) has to be analysed.

### 3 Numerical Simulation

As test example, we apply the circuit of a Schmitt trigger given in Fig. 1. This circuit transforms a sinusoidal input signal to a digital output signal. Mathematical modelling yields a nonlinear system (1) of dimension  $k = 5$ . We substitute the capacitance included in the matrix  $A$  by a uniformly distributed random variable in  $[10^{-9}\text{F}, 10^{-7}\text{F}]$ . Since a relatively large range is specified, a local sensitivity analysis is not sufficient here.

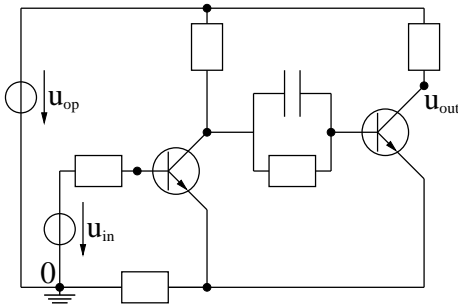


Fig. 1. Schmitt trigger circuit.

We use the stochastic model from Sect. 1 and the approach of the polynomial chaos from Sect. 2 with the expansion (3) based on Legendre polynomials up to degree  $m = 3$ . Trapezoidal rule solves an initial value problem of the system (4). We determine data applying (5). Figure 2 illustrates the resulting expected value of the output voltage and three samples for different capacitances. The corresponding standard deviation is shown in Fig. 3.

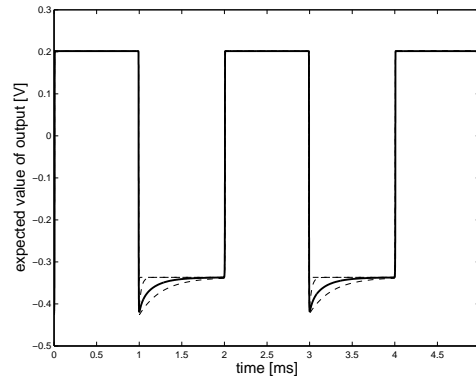


Fig. 2. Expected value (solid line) and three samples (dashed lines) of output voltage.

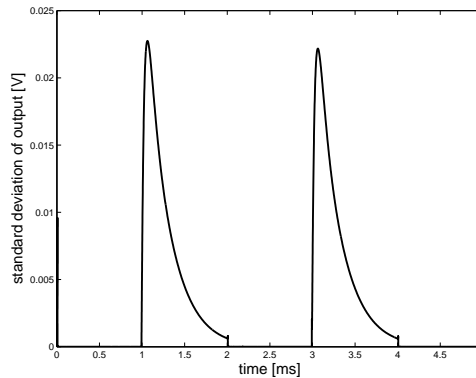


Fig. 3. Standard deviation of output voltage.

We recognise that the variation of the capacitance does not influence the upper values of the digital output signal but the lower values. The standard deviation or variance, respectively, indicate directly the subintervals, where the solution is sensitive with respect to the parameter, and the corresponding magnitudes.

### References

1. F. Augustin, A. Gilg, M. Paffrath, P. Rentrop and U. Wever. Polynomial chaos for the approximation of uncertainties: chances and limits. To appear in: *Euro. Jnl. of Applied Mathematics*.
2. R.G. Ghanem and P.D. Spanos. *Stochastic Finite Elements*. (Rev. Ed.) Dover Publications Inc., Mineola, New York, 2003.
3. A. Loeven, J. Witteveen and H. Bijl. Probabilistic collocation: An efficient non-intrusive approach for arbitrarily distributed parametric uncertainties. In M.B. Bragg, editor, *Proceedings of 45th Aerospace Sciences Meeting and Exhibit*, 1–14, 2007.
4. D. Lucor, C.H. Su and G.E. Karniadakis. *Generalized polynomial chaos and random oscillators*. *Int. J. Numer. Meth. Engng.*, 60:571–596, 2004.

# Simultaneous Step-size and Path Control for Efficient Transient Noise Analysis

Werner Römisch<sup>1</sup> and Thorsten Sickenberger<sup>2</sup>

<sup>1</sup> Institute of Mathematics, Humboldt-Universität zu Berlin, Unter den Linden, D-10099 Berlin, Germany  
romisch@math.hu-berlin.de

<sup>2</sup> Department of Mathematics, Universität zu Köln, Weyertal 86-90, D-50931 Cologne, Germany  
sickenberger@math.uni-koeln.de

**Summary.** Transient noise analysis requires an efficient numerical time integration by mean-square convergent numerical methods. We develop a strategy for controlling the step-size and the number of solution paths simultaneously in one approximation. The strategy is based on the sampling error of the mean-square approximation of the local discretisation error and yields an approximate solution which consists of a tree of solution paths that is extended, reduced or kept fixed adaptively. An algorithm to generate these trees is described.

## 1 Transient noise analysis in circuit simulation

Transient noise analysis means time domain simulation of noisy electronic circuits. The current technological progress in microelectronics is driven by the desire to decrease feature sizes, increase frequencies and the need for low supply voltages. Integrated circuits become much more complex, parasitic effects become predominant and the signal-to-noise ratio decreases. To address the signal-to-noise ratio the modelling and the simulation can be improved by taking the inner electrical noise into account.

We deal with the thermal noise of resistors as well as the shot noise of semiconductors. We consider mathematical models where the noise is taken into account by means of sources of Gaussian white noise that are added to the deterministic network equations. This leads to systems of stochastic differential algebraic equations (SDAEs) of the form

$$A \frac{d}{dt} q(x(t)) + f(x(t), t) + \sum_{r=1}^m g_r(x(t), t) \xi_r(t) = 0,$$

where  $g_r(x, t)$  denotes the vector of noise intensities for the  $r$ -th noise source, and  $\xi$  is an  $m$ -dimensional vector of independent Gaussian white noise sources.

A crucial property of the arising SDAEs is the large number of small noise sources that are included. Fortunately, even in current chip designs,

the noise level is still smaller in magnitude compared to the wanted signal, which can be used for the construction of efficient numerical schemes.

The focus here is on numerical methods to simulate solution paths, i.e., strong approximations of the solution of the arising large system of index-1 SDAEs, since only such paths can reveal the phase noise. The calculation of hundreds or even a thousand solution paths are necessary for getting sufficient numerical confidence about the phase or the opening of eye-diagrams.

For this task we present adaptive linear multi-step Maruyama schemes, together with a new step-size and path selection control.

## 2 Adaptive numerical methods

We consider stochastic analogues of the variable coefficient two-step backward differentiation formula (BDF<sub>2</sub>) and the trapezoidal rule, where only the increments of the driving Wiener process are used to discretize the diffusion part. Both the BDF<sub>2</sub>-Maruyama method and the stochastic trapezoidal rule of Maruyama type have only an asymptotic order of strong convergence of 1/2.

However, the noise intensities contain small parameters and the error behaviour is much better. In fact, the errors are dominated by the deterministic terms as long as the step-size is large enough. Also the smallness of the noise allows special estimates of the local error terms, which can be used to control the step-size. We aim at an efficient estimate of the mean-square of local errors by means of a number of simultaneously computed solution paths. This leads to an adaptive step-size sequence that is identical for all paths.

Depending on the available information we will monitor different quantities to satisfy accuracy requirements, such that the designer of a circuit can choose whether he would like to control the accuracy of the charges and fluxes or of the nodal potentials and branch current throughout the numerical integration.

### 3 A solution path tree algorithm

In the analysis so far, the number of simultaneously computed sample paths has not been specified. It influences the sampling error in the approximation of the  $L_2$ -norm in the error estimate. Our aim in tuning the number of paths is to balance the local error and the sampling error.

The best number of paths  $M_\ell$  depends on the time-point  $t_\ell$  and is realized by approximate solutions generated on a tree of paths that is extended, reduced or kept fixed adaptively. Figure 1 gives an impression, how a solution path tree looks like. At each time-step the optimal expansion

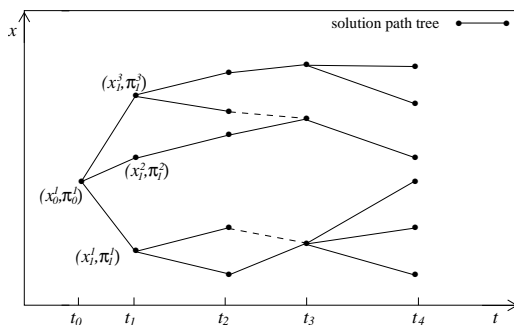


**Fig. 1.** A solution path tree: Variable time-points  $t_\ell$ , solution states  $x_\ell^i$  and path weights  $\pi_\ell^i$ .

sion or reduction problem is formulated by means of combinatorial optimization models. The path selection is modelled as a mass transportation problem in terms of the  $L_2$ -Wasserstein metric. This solution path tree algorithm has been implemented in practice. The results presented in the next section show its performance.

### 4 Numerical results

We consider a model of an inverter circuit with a MOSFET transistor, under the influence of thermal noise (see Fig. 2). The thermal noise of the resistor and of the MOSFET is modelled by additional white noise current sources that are shunt in parallel to the original, noise-free elements. To highlight the effect of the noise, we scaled the diffusion coefficient by a factor of 1000.

We have applied the solution path tree algorithm to this example. The upper graph in

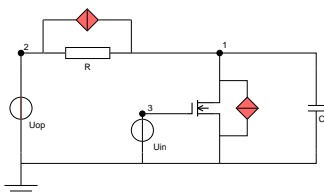


**Fig. 2.** Thermal noise sources in a MOSFET inverter circuit

Fig. 3 shows the computed solution path tree together with the applied step-sizes. The lower graph shows the simulation error (solid line), its error bound (dashed line) and the used number of paths (marked by  $\times$ ), vs. time. The results in-

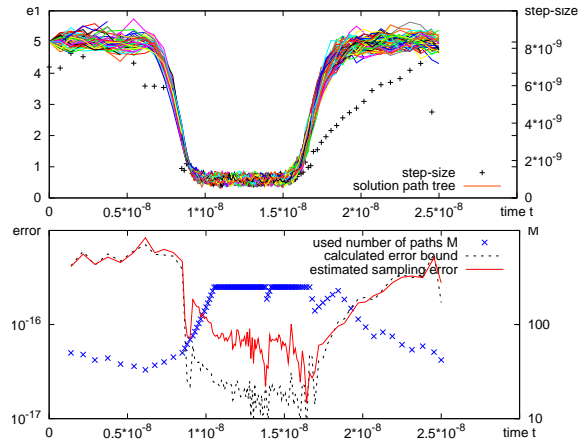


**Fig. 3.** Simulation results for the noisy inverter circuit: Solution path tree and step-sizes (top), sampling error, its error bound and the number of paths (bottom).

dicates that there exists a region where we have to use very much paths. This is exactly the area in which the MOSFET is active and the input signal is inverted. Outside this region the algorithm proposes approximately 70 simultaneously computed solution paths.

*Acknowledgement.* We wish to thank Dr. Renate Winkler (Uni Wuppertal) and Dr. Georg Denk (Qimonda) for the excellent cooperation. Support of BMBF through project 03RONAVN and of the EU through the project ICESTARS is gratefully acknowledged.

### References

1. G. Denk, W. Römisch, Th. Sickenberger, and R. Winkler. Efficient Transient Noise Analysis in Circuit Simulation. In W. Jäger, H.-J. Krebs, editors, *Mathematics - Key Technology for the Future*. Springer, Berlin, 2008.
2. Th. Sickenberger. Efficient transient noise analysis in circuit simulation. Phd thesis, Humboldt-Universität zu Berlin, Berlin, 2008.
3. Th. Sickenberger and E. Weinmüller and R. Winkler. Local error estimates for moderately smooth problems: Part II - SDEs and SDAEs with small noise. Preprint 07-07, Inst. für Mathematik, HU Berlin, 2007. Submitted for publication.
4. Th. Sickenberger and R. Winkler. Adaptive Methods for Transient Noise Analysis. In G. Ciuprina and D. Ioan, editors, *Scientific Computing in Electrical Engineering SCEE 2006*, p. 403–410. Springer, Berlin, 2007.

---

**Session**

**CS 3**

---



# Parametric Reduced Order Models for Passive Integrated Components Coupled with their EM Environment

Daniel Ioan

Politehnica University of Bucharest, Spl. Independentei 313, 060042, Romania [1mn@1mn.pub.ro](mailto:1mn@1mn.pub.ro)

**Summary.** The paper focuses on the implementation and use of a new type of boundary conditions - *Electric and Magnetic Hooks* - in the Finite Integration Technique applied for the simulation of passive devices in full-wave electromagnetic field regime. This type of boundary conditions offers a new and effective possibility to carry out domain decomposition for the modelling of very large scale problems, such as complex on-chip passive devices.

## 1 Introduction

While next-generation integrated circuits designs will always be challenged by an increased number of trouble spots, surely the most important one in this case is related to the nature of the electromagnetic coupling among the down-scaled individual devices to be integrated on one chip. New coupling mechanisms, including EM field coupling, are becoming too strong to be neglected [1].

To address these problems, a European research project entitled: *Comprehensive High Accuracy Modelling of Electromagnetic - Chameleon-RF* ([www.chameleon-rf.org](http://www.chameleon-rf.org)) was started within FP6. The general objective of the Chameleon-RF project is that of developing methodology and prototype tools that take a layout description of typical RF functional blocks that will operate at RF frequencies up to  $60GHz$  and transform them into sufficiently accurate, reliable electrical simulation models taking EM coupling and variability into account.

## 2 Boundary conditions and hooks definition

One of the main theoretical problems encountered in the modelling of RF components is the difficulty to define a unique terminal voltage, independent of the integration path. The solution found in our approach is to adopt appropriate boundary conditions (EMCE) for the field problem associated to the analysed components, in order to allow the consistency with the electrical circuit which contains this component. The correct definition of the component terminals (used for intentional interconnections) and connectors ("hooks" which represent parasitic couplings) was an important challenge of our research [2].

## 3 Domain Partitioning

The geometric complexity of nowadays designs can be handled only by Domain Decomposition (DD). Interface Relaxation (IR) is a frequently encountered iterative form of DD solvers [3]. It assumes a splitting of the domain into a set of non-overlapping sub-domains and considers the associated PDE problems defined on each one of them. The novelty of this paper is that it analyses the convergence properties of new interface approximations, based on electric and magnetic hooks, which were proposed the first time in [4] to describe the parasitic EM interaction between components in RF-ICs.

The hooks technique has practical importance when their number is reduced to  $1 \dots 10$ . With such values, the sub-domains having different shapes can be modeled independently in parallel. Afterwards the reduced size models (represented as matrices - frequency dependent circuit functions, state equations or reduced order Spice circuits) are interconnected, aiming to obtain a model for the global system. Unlike DD, which is basically an iterative process, in the proposed approach of Domain Partitioning (DP), due to the reduced numbers of hooks, the interface iterations can be removed and the resulted technique is a "direct", not an iterative one, as DD is.

## 4 Numerical approach

This concept of EMCE (Electro-Magnetic Circuit Element) was implemented on a prototype software tool developed in the frame of the FP6/Chameleon-RF project. The numerical method used for the discretization of the EM field equation is the Finite Integration Technique (FIT), whose one of the first promoters was T. Weiland [5]. FIT uses two orthogonal staggered grids, the *electric grid*, and the *magnetic grid* on which electrical and magnetic quantities are defined, respectively (Fig.1). An electric terminal is defined on the electric grid, so it is placed exactly on the domain boundary, whereas a magnetic terminal is defined on the magnetic grid, so it is placed a bit under the geometrical boundary.

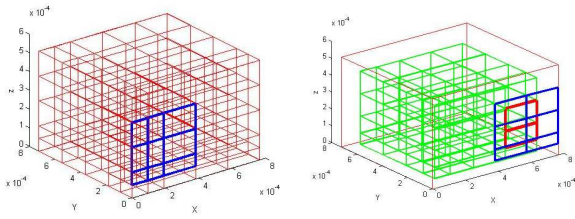


**Fig. 1.** Electric terminal on the electric grid (left); Magnetic terminal on magnetic grid (right).

FIT is applied for the EMCE formulation, in order to obtain the following discrete time-domain model

$$\mathbf{C} \frac{d\mathbf{x}}{dt} + \mathbf{G}\mathbf{x} = \mathbf{B}\mathbf{u}, \quad \mathbf{y} = \mathbf{L}\mathbf{x}, \quad (1)$$

where  $\mathbf{x}$  is the state space vector,  $\mathbf{u}$  is the vector of input quantities and  $\mathbf{y}$  is the vector of output quantities. The input/output quantities are solely related to the terminals. Each terminal introduces one input and one output quantity. For instance, if an electric terminal is voltage excited, its voltage is a component of the input vector and the current flowing through it (entering in the domain) is an output quantity. Similarly, if a magnetic terminal is excited in magnetic voltage, this one will be an input quantity and the magnetic flux entering in the domain through this terminal will be an output quantity. Thus, the number of inputs is always equal to the number of outputs.

## 5 Validation and numerical results

The method described above was validated on a series of test structures: CHRf benchmarks [6]. In the case of a coupled spiral coils the reference result was obtained by simulating the coupled coils as a whole device. Two separate EMCE models were extracted, each corresponding to a single coil, but with hooks on the cutting interface.

Figure 2 shows the results obtained from the simulation of the coupled coils without DD and with DD decomposition in three cases: with all possible electric and magnetic hooks (case in which each electric and magnetic node on the common surface represents a distinct terminal - the surface is in this case transparent for the EM field), only with electric hooks, and only with magnetic hooks. The full simulation perfectly overlaps the simulation with DD and with node-by-node interconnection between the models thus validating the theory of hooks and its implementation in the framework of the FIT numerical methods. The use of magnetic hooks is very important to catch the output behaviour on the whole frequency range, whereas the electric hook become more important at higher frequencies, due to the

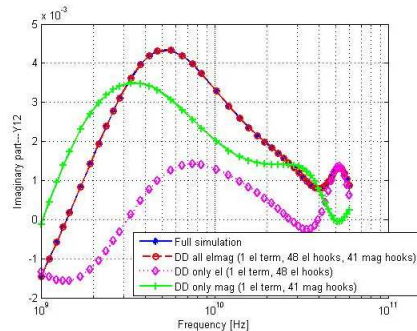


**Fig. 2.** Imaginary part of the admittance obtained from full simulation, and simulation using DD.

capacitive effects that cannot be neglected any more.

## 6 Conclusions

The paper illustrated how a new type of boundary conditions (hooks) can be implemented in FIT and used in EM coupling simulations to obtain independent models of sub-problems. The parasitic and intentional coupling between either time domain or frequency domain models was modeled.

If only node-hooks are used, the interface conditions are imposed node by node, and the coupled numerical model is equivalent to the numerical model obtained with FIT applied for the whole domain, providing that the grid used is the union of grids used for each sub-problem. Alternative solutions include iterative procedures as in DD or a convenient reduction of the number of hooks and thus number of terminals of sub-models. In the latter case, the magnetic terminals are surface-hooks, each hook including more than one node of the discretization grid.

## References

1. T. Yao, M.Q. Gordon, K.K.W.Tang, K.H.K. Yau, M-T Yang, P.Schvan, S.P. Voinigescu Algorithmic Design of CMOS LNAs and Pas for 60 GHz Radio *IEEE Journal on Solid State Circuits* vol.42, no.5, pp.1044-1048, 2007.
2. D. Ioan, G. Ciuprina, L.M. Silveira Effective Domain Partitioning with Electric and Magnetic Hooks *Proceedings of the CEFC 2008*.
3. Domain decomposition web-page. [www.ddm.org](http://www.ddm.org).
4. D. Ioan, W. Schilders, G. Ciuprina, N. Meijs, W. Schoenmaker Models for integrated components coupled with their EM environment *COMPEL Journal* vol. 27, no.4, pp.820-828, 2008.
5. T. Weiland A discretization method for the solution of Maxwell's equations for 6 component fields *AEU, Electronics and Communication* vol. 31, pp. 116-120, 1977.
6. Chameleon-RF website, [www.chameleon-rf.org](http://www.chameleon-rf.org).

# Stability of the Super Node Algorithm for EMC Modelling of ICs

M.V. Ugryumova and W.H.A. Schilders

Eindhoven University of Technology, CASA, Den Dolech 2, 5612 AZ Eindhoven m.v.ugryumova@tue.nl

**Summary.** The super node algorithm performs model order reduction based on physical principals. Although the algorithm provides us with compact models, its stability has not thoroughly been studied yet. The loss of stability is a serious problem because simulations of the reduced network may encounter artificial behavior which render the simulations useless. We prove that the algorithm delivers unstable models and we will present a way to overcome this problem.

## 1 Introduction

FASTERIX is a layout simulation tool for EMC (electromagnetic compatibility) modelling. It transforms PCB properties into an equivalent RLC circuit model which is then reduced into a compact one with approximately the same behavior. As a reduction technique it uses the so called 'super node algorithm'.

The approach of compact equivalent circuits makes FASTERIX an excellent and fast program for the frequency analysis of the electromagnetic behavior for PCB's. The reader is referred to [1], [3], for more information about the methods in FASTERIX. Although the super node algorithm provides us with compact models, the problem of carrying out simulations in the time domain still exists. One can think of using another reduction techniques instead of the super node algorithm, which can preserve stability and passivity. The advantage of the super node algorithm is that it is inspired by physical insight into the models, and produces reduced RLC circuits depending on the maximum predefined frequency. This fact makes the algorithm an attractive technique for EMC modelling.

We briefly review the algorithm, and give a sketch of the proof that it delivers unstable reduced models. Corresponding example is considered.

## 2 Derivation of the model used in FASTERIX

FASTERIX translates electromagnetic properties of a PCB into a circuit model which is described by the system of Kirchhoff's equations

$$(\mathbf{R} + s\mathbf{L})I - \mathbf{P}V = 0 \quad (1)$$

$$\mathbf{P}^T I + s\mathbf{C}V = J \quad (2)$$

where  $\mathbf{R} \in \mathfrak{R}^{\varepsilon \times \varepsilon}$  is the resistance matrix,  $\mathbf{L} \in \mathfrak{R}^{\varepsilon \times \varepsilon}$  is the inductance matrix,  $\mathbf{P} \in \mathfrak{R}^{\varepsilon \times \eta}$  is an incidence matrix,  $\mathbf{C} \in \mathfrak{R}^{\eta \times \eta}$  is the capacitance matrix,  $I \in C^\varepsilon$  is the vector of currents flowing in the branches,  $V \in C^\eta$  is a vector of voltages at the nodes. Vector  $J \in C^\varepsilon$  collects the terminal currents flowing into the interconnection system. Value  $s$  is a complex number with negative imaginary part:  $s = -j\omega$ . Matrices  $\mathbf{R}$ ,  $\mathbf{L}$ ,  $\mathbf{C}$  are symmetric and positive definite.

In order to obtain an equivalent network model, the set of all nodes in the circuit described by (1)-(2) is subdivided into two subsets  $N$  and  $N'$  where  $N$  denotes the subset of nodes which are retained in the reduced circuit, and  $N'$  is for all other nodes. Due to this, vectors  $V$ ,  $J$  and matrices  $\mathbf{P}$ ,  $\mathbf{C}$  are partitioned into blocks, see [1], [4] (chapter 8).

If we consider the voltage at the nodes (from the subset  $N$ ) as an input  $v^{(p)}$ , and currents flowing into the system through the nodes as an output  $i^{(p)}$ , we come to the following system:

$$\left( \underbrace{\begin{pmatrix} \mathbf{R} & -\mathbf{P}_{N'} \\ \mathbf{P}_{N'}^T & \mathbf{0} \end{pmatrix}}_{\mathbf{G}} + s \underbrace{\begin{pmatrix} \mathbf{L} & \mathbf{0} \\ \mathbf{0} & \mathbf{C}_{N'N'} \end{pmatrix}}_{\mathbf{C}} \right) x = \begin{pmatrix} \mathbf{P}_N \\ -s\mathbf{C}_{N'N} \end{pmatrix} v^{(p)}, \quad (3)$$

$$i^{(p)}(s) = (\mathbf{P}_N^T \ s\mathbf{C}_{N'N}^T) x + s\mathbf{C}_{NN}v^{(p)}, \quad (4)$$

where  $x = (I, V_{N'})^T$ . It should be noted that in (3) the matrix  $\mathbf{G}$  is positive real, and matrix  $\mathbf{C}$  is positive semi-definite. It is enough to prove that the unreduced system is stable.

The currents  $i^{(p)}$  obtained each time under a unity voltage  $v^{(p)}$  at a particular input terminal, the others being grounded, constitute the columns of the desired admittance matrix  $\mathbf{Y}$ . The following holds

$$\mathbf{Y}\mathbf{v} = \mathbf{i}. \quad (5)$$

Matrix  $\mathbf{Y}$  describes the reduced circuit at a particular frequency  $\omega$ .

### 3 Super Node Algorithm

The super node algorithm constructs an approximation of  $\mathbf{Y}$ , which describes the reduced circuit at any frequency  $0 < \omega < \Omega$  as

$$\mathbf{Y} \sim (s)^{-2}\mathbf{Y}_R + (s)^{-1}\mathbf{Y}_L + \mathbf{Y}_G + (s)\mathbf{Y}_C. \quad (6)$$

Each pair of nodes in the reduced circuit contains a branch, Fig. 1. Resistance  $R$ , inductance  $L$ , capacitance  $C$ , and resistance of conductance  $G$  can be found from the admittance matrices  $\mathbf{Y}_R$ ,  $\mathbf{Y}_L$ ,  $\mathbf{Y}_G$  and  $\mathbf{Y}_C$  in (6). Thus the reduced circuit described by (6) can be used in a circuit analysis program.

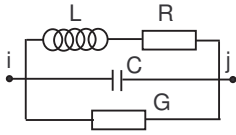


Fig. 1. High frequency branch between two nodes

#### Stability

For carrying out reliable simulations in the time domain, first it should be checked that the system is stable [2].

An illustration of possible stability violation is given below. Figure 2 shows an example of simulations in the time domain for lowpass filter model generated by FASTERIX. This model is supposed to be valid up to 10 GHz. The reason why the

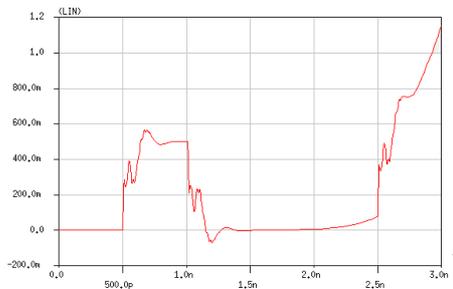


Fig. 2. Simulation in the time domain

transient analysis fails is explained by the non-stability of the reduced model.

To show that the algorithm does not preserve stability, we suggest to follow all reduction steps and check stability at the each step. At the first step, the system (3)-(4) is subdivided into two systems by introducing the following expansions of  $I$  and  $V_{N'}$  in powers of  $(ik_0h)$

$$V_{N'} = V_0 + V_1(ik_0h), \quad (7)$$

$$I = I_0 + I_1(ik_0h), \quad (8)$$

where  $k_0$  is the free space wave number. Pairs  $(I_0, V_0)$  and  $(I_1, V_1)$  are obtained from two sets of equations which are found from (3)-(4) by gathering appropriate terms with orders  $(ik_0h)^0$  and  $(ik_0h)^1$ . It can be checked that the two new systems are again stable.

At the second step, the state space vectors of the systems from the previous step are expanded through frequency independent quantities, see [1], [4] (chapter 8), for details. In fact, (6) is a sum of outputs of the two systems under the expansions. Thus, it is important to investigate whether the state space vectors of the systems have unstable poles. The following representation of the state space vector of the 1-st system has been obtained

$$x_1 = (\mathbf{A}_1(s\mathbf{M}_1 + \mathbf{M}_2)^{-1} + \mathbf{A}_2(s\mathbf{M}_3 + \mathbf{I})^{-1}) \mathbf{A}_3 \times \\ \times (\mathbf{G}_1 + s\mathbf{C}_1)^{-1} \mathbf{B}_{i1} V_N^{(p)}. \quad (9)$$

Taking into account the properties of the matrices:  $\mathbf{C}_1$  and  $\mathbf{M}_3$  are positive semi-definite,  $\mathbf{I}$  and  $\mathbf{G}_1$  are positive real and  $\mathbf{M}_1$  is indefinite, in general, we conclude that (9) does not correspond to analytic function for all  $s$  with  $Re(s) > 0$ . Similar result can be obtained for the state space vector of the second system. Thus, this fact proves non-stability of the reduced model described by (6). We will present changes in the algorithm, in order to guarantee its stability.

#### References

1. R.Du Cloux, G.P.J.F.M Maas, and Wachters A.J.H. Quasi-static boundary element method for electromagnetic simulations of pcbs. *Philips J. Res.*, 48:117-144, 1994.
2. E.A. Guillemin. *Synthesis of Passive Networks*. Wiley, New York, 1957.
3. R.F. Milsom. Rf simulation of passive ics using fasterix. Report rp3506, Philips Electronics, 1996.
4. W.H.A. Schilders and E.J.W ter Maten. *Special volume : numerical methods in electromagnetics*. Elsevier, Amsterdam, 2005.

# GABOR: Global-Approximation-Based Order Reduction

Janne Roos, Mikko Honkala, and Pekka Miettinen

Helsinki University of Technology, Faculty of Electronics, Communications and Automation, Department of Radio Science and Engineering, P.O.Box 3000, FI-02015 TKK, Finland {`janne,mikko,pekka`}@`ct.tkk.fi`

**Summary.** This abstract proposes a new approach for the Model-Order Reduction (MOR) of RLC-circuit blocks. Instead of Taylor-series-like local fitting using implicit moment matching, a global approximation of the matrix-valued  $s$ -domain transfer function is generated. Then, the Krylov-like subspace spanned by the ‘moments’ of this approximation is used to set up the projection matrices needed for MOR. The proposed MOR approach preserves passivity, reciprocity, and the properties of the global approximation.

## 1 Introduction

Typical Krylov subspace Model-Order Reduction (MOR) methods [1–3] are based on implicit moment matching. This approach results in a Taylor-series-like approximation, which is exact at the expansion point (e.g., at the origin of the complex plane), but which loses accuracy when moving far away (e.g., towards high frequencies). Therefore, one avenue to reduce (or, at least, to spread more equally) the approximation error could be to base the MOR on a global approximation.

This abstract proposes a new MOR approach for RLC-circuit blocks: Global-Approximation-Based Order Reduction (GABOR). GABOR preserves passivity and reciprocity, and matches the ‘moments’ of the global approximation.

## 2 Preliminaries

PRIMA [1] operates with Y-parameters; SPRIM [2] and ENOR [3], in turn, are formulated using Z-parameters. Due to lack of space, but without loss of generality, let us limit the discussion to treatment of Z-parameters, only.

Let us consider an RC-only circuit with  $n$  nodes and  $N$  port nodes, excited by  $N$  current sources for obtaining the Z-parameter matrix. Now, a PRIMA-like formulation results in

$$\begin{aligned} \mathbf{Z}(s) &= \mathbf{L}^T(\mathbf{G} + s\mathbf{C})^{-1}\mathbf{B} \\ &= \mathbf{L}^T(\mathbf{I} + s\mathbf{G}^{-1}\mathbf{C})^{-1}\mathbf{G}^{-1}\mathbf{B} \\ &\triangleq \mathbf{L}^T(\mathbf{I} - s\mathbf{A})^{-1}\mathbf{R} \\ &= \mathbf{L}^T\mathbf{R} + \mathbf{L}^T\mathbf{A}\mathbf{R}s + \mathbf{L}^T\mathbf{A}^2\mathbf{R}s^2 + \dots \\ &\triangleq \mathbf{M}_0 + \mathbf{M}_1s + \mathbf{M}_2s^2 + \dots \end{aligned} \quad (1)$$

where  $\mathbf{G}$  and  $\mathbf{C}$  are  $n$ -by- $n$  conductance and capacitance matrices, respectively,  $\mathbf{L} = \mathbf{B}$  is an  $n$ -by- $N$  selector matrix, and  $\mathbf{M}_i = \mathbf{L}^T\mathbf{A}^i\mathbf{R}$  are the moments. In particular,  $\mathbf{Z}(0) = \mathbf{M}_0 = \mathbf{L}^T\mathbf{G}^{-1}\mathbf{B}$ .

For an RL-only circuit, with inductances treated as in Ref. [3], we get the dual version of (1):

$$\begin{aligned} \mathbf{Z}(s) &= \mathbf{L}^T(\mathbf{G} + \frac{1}{s}\mathbf{\Gamma})^{-1}\mathbf{B} \\ &= \mathbf{L}^T(\mathbf{I} + \frac{1}{s}\mathbf{G}^{-1}\mathbf{\Gamma})^{-1}\mathbf{G}^{-1}\mathbf{B} \\ &\triangleq \mathbf{L}^T(\mathbf{I} - \frac{1}{s}\hat{\mathbf{A}})^{-1}\mathbf{R} \\ &= \mathbf{L}^T\mathbf{R} + \mathbf{L}^T\hat{\mathbf{A}}\mathbf{R}\frac{1}{s} + \mathbf{L}^T\hat{\mathbf{A}}^2\mathbf{R}\frac{1}{s^2} + \dots \\ &\triangleq \mathbf{M}_0 + \mathbf{M}_{-1}\frac{1}{s} + \mathbf{M}_{-2}\frac{1}{s^2} + \dots \end{aligned} \quad (2)$$

Now, we have  $\mathbf{Z}(\infty) = \mathbf{M}_0 = \mathbf{L}^T\mathbf{G}^{-1}\mathbf{B}$ .

## 3 Derivation of GABOR

Applying nodal formulation (that is, *not* MNA) to an RLC circuit, we obtain [3]

$$\begin{aligned} \mathbf{Z}(s) &= \mathbf{L}^T(s\mathbf{C} + \mathbf{G} + \frac{1}{s}\mathbf{\Gamma})^{-1}\mathbf{B} \\ &= \mathbf{L}^T(s\mathbf{G}^{-1}\mathbf{C} + \mathbf{I} + \frac{1}{s}\mathbf{G}^{-1}\mathbf{\Gamma})^{-1}\mathbf{G}^{-1}\mathbf{B} \\ &\triangleq \mathbf{L}^T(s\mathbf{D} + \mathbf{I} + \frac{1}{s}\mathbf{E})^{-1}\mathbf{R} \end{aligned} \quad (3)$$

When truncated to a finite number of moments, (1) and (2) are, still, accurate near  $s = 0$  and  $s = \infty$ , respectively. The idea behind GABOR is to (try to) combine the best properties of (1) and (2) for an RLC circuit. In particular, the term  $(\dots)^{-1}$  in (3) is approximated by ‘a combination of the moment series in (1) and (2)’:

$$\begin{aligned} \mathbf{Z}(s) &= \mathbf{L}^T(s\mathbf{D} + \mathbf{I} + \frac{1}{s}\mathbf{E})^{-1}\mathbf{R} = \\ &\dots + \mathbf{M}_{-2}\frac{1}{s^2} + \mathbf{M}_{-1}\frac{1}{s} + \mathbf{M}_0 + \mathbf{M}_1s + \mathbf{M}_2s^2 + \dots \end{aligned} \quad (4)$$

Let

$$\mathbf{M}_i = \mathbf{L}^T\mathbf{N}_i, \quad i = \dots, -2, -1, 0, 1, 2, \dots \quad (5)$$

Combining (4) and (5) and some algebra gives

$$\begin{aligned} (s\mathbf{D} + \mathbf{I} + \frac{1}{s}\mathbf{E}) \\ (\dots + \mathbf{N}_{-1}\frac{1}{s} + \mathbf{N}_0 + \mathbf{N}_1s + \dots) = \mathbf{R} \end{aligned} \quad (6)$$

Equating the negative/zero/positive powers of  $s$  results in the following matrix equation (truncated to  $\pm 3$  terms for convenience):



# Passivity-preserving balanced truncation model reduction of circuit equations

Tatjana Stykel and Timo Reis

Institut für Mathematik, MA 4-5, TU Berlin, Straße des 17. Juni 136, D-10623 Berlin, Germany  
 stykel@math.tu-berlin.de, reis@math.tu-berlin.de

**Summary.** We consider passivity-preserving model reduction of circuit equations using the bounded real balanced truncation method applied to the Moebius-transformed system. This method is based on balancing the solutions of the projected Lur'e and Lyapunov matrix equations. We also discuss their numerical solution exploiting the underlying structure of circuit equations.

## 1 Introduction

A modified nodal analysis (MNA) for linear RLC circuits yields a linear system of differential-algebraic equations (DAEs)

$$\begin{aligned} E\dot{x}(t) &= Ax(t) + Bu(t), \\ y(t) &= Cx(t), \end{aligned} \quad (1)$$

where

$$\begin{aligned} E &= \begin{bmatrix} A_c C A_c^T & 0 & 0 \\ 0 & \mathcal{L} & 0 \\ 0 & 0 & 0 \end{bmatrix}, \quad B = - \begin{bmatrix} A_{\mathcal{I}} & 0 \\ 0 & 0 \\ 0 & I \end{bmatrix} = C^T, \\ A &= \begin{bmatrix} -A_{\mathcal{R}} \mathcal{R}^{-1} A_{\mathcal{R}}^T & -A_{\mathcal{L}} & -A_{\mathcal{V}} \\ A_{\mathcal{L}}^T & 0 & 0 \\ A_{\mathcal{V}}^T & 0 & 0 \end{bmatrix}. \end{aligned} \quad (2)$$

Here  $A_c$ ,  $A_{\mathcal{L}}$ ,  $A_{\mathcal{R}}$ ,  $A_{\mathcal{V}}$  and  $A_{\mathcal{I}}$  are the incidence matrices describing the circuit topology, and  $\mathcal{R}$ ,  $\mathcal{L}$  and  $C$  are the symmetric, positive definite resistance, inductance and capacitance matrices, respectively. Linear RLC circuits are often used to model interconnects, transmission lines and pin packages in VLSI networks. The number  $n$  of state variables is called the *order* of the MNA system (1). It is related to the number of circuit elements and usually very large. This makes the analysis and numerical simulation of circuit equations unacceptably time consuming. Therefore, model order reduction is of great importance.

A general idea of model reduction is to approximate the large-scale system (1) by a reduced-order model

$$\begin{aligned} \tilde{E} \dot{\tilde{x}}(t) &= \tilde{A} \tilde{x}(t) + \tilde{B} u(t), \\ \tilde{y}(t) &= \tilde{C} \tilde{x}(t), \end{aligned} \quad (3)$$

where  $\tilde{E}$ ,  $\tilde{A} \in \mathbb{R}^{\ell, \ell}$ ,  $\tilde{B} \in \mathbb{R}^{\ell, m}$ ,  $\tilde{C} \in \mathbb{R}^{m, \ell}$  and  $\ell \ll n$ . It is required that the approximate system (3) captures the input-output behavior of (1) to a required accuracy and preserves passivity. This property is important in circuit simulation. Generally speaking, passivity means that system does not produce energy. System (1) is *passive* if and only if its transfer function  $\mathbf{G}(s) = C(sE - A)^{-1}B$  is *positive real*, i.e.,  $\mathbf{G}$  is analytic in the open right half-plane  $\mathbb{C}_+$  and  $\mathbf{G}(s) + \mathbf{G}^T(\bar{s})$  is positive semidefinite for all  $s \in \mathbb{C}_+$ , see [1].

## 2 Passivity-preserving balanced truncation

Balanced truncation model reduction is based on the transformation of the dynamical system into a balanced form whose controllability and observability Gramians are both equal to a diagonal matrix. Then a reduced-order model is determined by the truncation of the states corresponding to small diagonal elements of the balanced Gramians. Depending on system properties, different types of balancing may be introduced.

A passive reduced-order system can be computed using the *bounded real balanced truncation method* applied to a Moebius-transformed system

$$\begin{aligned} \mathcal{G}(s) &= (I - \mathbf{G}(s))(I + \mathbf{G}(s))^{-1} \\ &= -2C(sE - A + BC)^{-1}B + I. \end{aligned}$$

Note that  $\mathbf{G}(s)$  is positive real if and only if  $\mathcal{G}(s)$  is bounded real, i.e.,  $\mathcal{G}$  is analytic in  $\mathbb{C}_+$  and the matrix  $I - \mathbf{G}(s)\mathbf{G}^T(\bar{s})$  is positive semidefinite for all  $s \in \mathbb{C}_+$ , see [1]. In the bounded real balanced truncation method for  $\mathcal{G}$ , the *bounded real Gramians* are defined as minimal solutions  $X$  and  $Y$  of the *projected Lur'e equations*

$$\begin{aligned} EX\hat{A}^T + \hat{A}XE^T + 2P_l BB^T P_l^T &= -2K_c K_c^T, \\ EXC^T - P_l B M_0^T &= -K_c J_c^T, \\ J_c J_c^T &= I - M_0 M_0^T, \quad X = P_r X P_r^T, \end{aligned}$$

and

$$\begin{aligned}
E^T Y \hat{A} + \hat{A}^T Y E + 2P_r^T C^T C P_r &= -2K_o^T K_o, \\
-E^T Y B + P_r^T C^T M_0 &= -2K_o^T J_o, \\
J_o^T J_o &= I - M_0^T M_0, \quad Y = P_l^T Y P_l,
\end{aligned} \tag{4}$$

where  $\hat{A} = A - BC$ ,  $P_r$  and  $P_l$  are the spectral projectors onto the right and left deflating subspaces of the pencil  $\lambda E - \hat{A}$  corresponding to the finite eigenvalues and  $M_0 = \lim_{s \rightarrow \infty} \mathcal{G}(s)$ . Further, we define the *improper controllability* and *observability Gramians*  $X_{imp}$  and  $Y_{imp}$  of  $\mathcal{G}$  as unique symmetric, positive semidefinite solutions of the *projected discrete-time Lyapunov equations*

$$\begin{aligned}
\hat{A} X_{imp} \hat{A}^T - E X_{imp} E^T &= 2Q_l B B^T Q_l^T, \\
X_{imp} &= Q_r X_{imp} Q_r^T,
\end{aligned}$$

and

$$\begin{aligned}
\hat{A}^T Y_{imp} \hat{A} - E^T Y_{imp} E &= 2Q_r^T C^T C Q_r, \\
Y_{imp} &= Q_l^T Y_{imp} Q_l,
\end{aligned} \tag{5}$$

where  $Q_l = I - P_l$  and  $Q_r = I - P_r$ , see [4]. The reduced-order model (3) can then be computed by projecting

$$\tilde{E} = W^T E T, \quad \tilde{A} = W^T A T, \quad \tilde{B} = W^T B, \quad \tilde{C} = C T,$$

where the projection matrices  $W, T \in \mathbb{R}^{n, \ell}$  determine the left and right subspaces corresponding to the dominant bounded real characteristic values and non-zero improper Hankel singular values of  $\mathcal{G}$  defined as the square roots of the positive eigenvalues of  $X E^T Y E$  and  $X_{imp} \hat{A}^T Y_{imp} \hat{A}$ , respectively. One can show that the reduced-order system is passive. Furthermore, if

$$\|I + \mathbf{G}\|_{\mathbb{H}_\infty} (\pi_{\ell_f+1} + \dots + \pi_{n_f}) < 1,$$

where  $\pi_j$  are the truncated characteristic values of  $\mathcal{G}$ , then we have the following error bound

$$\|\tilde{\mathbf{G}} - \mathbf{G}\|_{\mathbb{H}_\infty} \leq \|\mathbf{G} + I\|_{\mathbb{H}_\infty}^2 (\pi_{\ell_f+1} + \dots + \pi_{n_f}).$$

Since the MNA matrices in (2) satisfy

$$E^T = S E S, \quad A^T = S A S, \quad B^T = S_1 C S,$$

where  $S = \text{diag}(I, -I, -I)$  and  $S_1 = \text{diag}(I, -I)$  are partitioned in accordance with  $A$  and  $C$ , respectively, we find that

$$P_l = S P_r^T S, \quad X = S Y S^T, \quad X_{imp} = S Y_{imp} S^T.$$

Thus, for circuit equations, it is enough to solve only one Lur'e equation and also one Lyapunov equation. The solutions of the dual equations are given for free.

If  $D_o = I - M_0^T M_0$  is nonsingular, the projected Lur'e equation (4) can be rewritten as the projected algebraic Riccati equation

$$\begin{aligned}
E^T Y A_o + A_o^T Y E + 2E^T Y B D_o^{-1} B^T Y E \\
+ 2P_r^T C^T D_c^{-1} C P_r = 0, \quad Y = P_l^T Y P_l,
\end{aligned}$$

where  $A_o = A - BC - 2P_l B D_o^{-1} M_0^T C P_r$  and  $D_c = I - M_0 M_0^T$ . This equation can be solved using Newton's method [2]. In each step of this method, the projected continuous-time Lyapunov equation of the form

$$E^T Z F + F^T Z E + P_r^T Q^T Q P_r = 0, \quad Z = P_l^T Z P_l$$

has to be solved for  $Z$ . For this propose, we can use the generalized alternating direction implicit method [5]. The projected discrete-time Lyapunov equation (5) can be solved using the generalized Smith method [5].

Note that the solution of the large projected Riccati equation has often a low numerical rank. Such a solution can be well approximated by a matrix of low rank. Moreover, this low-rank approximation can be constructed in factored form  $Y \approx \hat{L} \hat{L}^T$  with  $\hat{L} \in \mathbb{R}^{n, k}$  that significantly reduces the memory requirements when  $k \ll n$ .

A major difficulty in the numerical solution of the projected Lyapunov and Riccati equations with large matrix coefficients is that the spectral projectors  $P_l$  and  $P_r$  are required. Fortunately, the matrix coefficients (2) in the MNA circuit equations have some special block structure. We can exploit this structure to construct the required projectors in explicit form using a matrix chain approach from [3]. Furthermore, we give an explicit formula for the matrix  $M_0$  and present necessary and sufficient conditions for invertibility of  $D_o = I - M_0^T M_0$  in terms of the circuit topology.

*Acknowledgement.* This work is supported by the DFG Research Center MATHEON in Berlin and the BMBF, Grant 03STPAE3.

## References

1. B. Anderson and S. Vongpanitlerd. *Network Analysis and Synthesis*. Prentice Hall, Englewood Cliffs, NJ, 1973.
2. P. Benner, R. Byers, E. Quintana-Ortí, and G. Quintana-Ortí. Solving algebraic Riccati equations on parallel computers using Newton's method with exact line search. *Parallel Comput.*, 26:1345–1368, 2000.
3. R. März. Canonical projectors for linear differential algebraic equations. *Comput. Math. Appl.*, 31:121–135, 1996.
4. T. Stykel. Gramian-based model reduction for descriptor systems. *Math. Control Signals Systems*, 16:297–319, 2004.
5. T. Stykel. Low-rank iterative methods for projected generalized Lyapunov equations. *Electr. Trans. Numer. Anal.*, to appear.

# A new approach to passivity preserving model reduction

Roxana Ionutiu<sup>1</sup>, Joost Rommes<sup>2</sup>, and Athanasios C. Antoulas<sup>1</sup>

<sup>1</sup> William Marsh Rice University, Department of Electrical and Computer Engineering, MS-380, PO Box 1892, Houston, TX, 77251-1892, USA [roxana.ionutiu@rice.edu](mailto:roxana.ionutiu@rice.edu), [aca@rice.edu](mailto:aca@rice.edu)

<sup>2</sup> NXP Semiconductors, Corporate I&T/DTF, High Tech Campus 37, 5656 AE Eindhoven, The Netherlands [joost.rommes@nxp.com](mailto:joost.rommes@nxp.com)

**Summary.** A new model reduction method for circuit simulation is presented, which preserves passivity by interpolating dominant spectral zeros. These are computed as poles of an associated Hamiltonian system, using an iterative solver: the subspace accelerated dominant pole algorithm (SADPA). Based on a dominance criterion, SADPA finds relevant spectral zeros and the associated invariant subspaces, which are used to construct the passivity preserving projection. Our method reduces all passive circuits, including those not suitable for reduction with PRIMA.

## 1 Introduction

Model reduction for circuit simulation has been extensively studied (see [3] for a selection of recent results). In transmission lines, interconnections are modeled as systems with millions of internal variables, that are impossible to simulate in full dimension. A system of smaller dimension is needed to approximate the behavior of the original and replace it during simulation. RLC circuits describing the interconnect are *passive* systems, with *positive real* transfer functions [1], thus the reduced models should also be passive.

The framework involves approximation of an original dynamical system described by a set of differential algebraic equations in the form (1),

$$\mathbf{E}\dot{\mathbf{x}}(t) = \mathbf{A}\mathbf{x}(t) + \mathbf{B}\mathbf{u}(t), \quad \mathbf{y}(t) = \mathbf{C}\mathbf{x}(t) + \mathbf{D}\mathbf{u}(t), \quad (1)$$

where the entries of  $\mathbf{x}(t)$  are the system's internal variables,  $\mathbf{u}(t)$  is the system input and  $\mathbf{y}(t)$  is the system output, with dimensions  $\mathbf{x}(t) \in \mathbb{R}^n$ ,  $\mathbf{u}(t) \in \mathbb{R}^m$ ,  $\mathbf{y}(t) \in \mathbb{R}^p$ . Correspondingly,  $\mathbf{E} \in \mathbb{R}^{n \times n}$ ,  $\mathbf{A} \in \mathbb{R}^{n \times n}$ ,  $(\mathbf{A}, \mathbf{E})$  is a regular pencil,  $\mathbf{B} \in \mathbb{R}^{n \times m}$ ,  $\mathbf{C} \in \mathbb{R}^{p \times n}$ ,  $\mathbf{D} \in \mathbb{R}^{p \times m}$ . The *dimension* of  $\Sigma$  is  $n$ , usually very large. In circuit simulation, internal variables are chosen as the node voltages and loop currents:  $\mathbf{x}(t) = [\mathbf{v}(t), \mathbf{i}(t)]^T$ , and the system original  $\Sigma(\mathbf{E}, \mathbf{A}, \mathbf{B}, \mathbf{C}, \mathbf{D})$  is stable and passive. We aim for a reduced order model  $\hat{\Sigma}(\hat{\mathbf{E}}, \hat{\mathbf{A}}, \hat{\mathbf{B}}, \hat{\mathbf{C}}, \mathbf{D})$ , which similarly to (1), satisfies:  $\hat{\mathbf{E}}\dot{\hat{\mathbf{x}}}(t) = \hat{\mathbf{A}}\hat{\mathbf{x}}(t) + \hat{\mathbf{B}}\mathbf{u}(t)$ ,  $\hat{\mathbf{y}}(t) = \hat{\mathbf{C}}\hat{\mathbf{x}}(t) + \mathbf{D}\mathbf{u}(t)$ , where  $\hat{\mathbf{x}} \in \mathbb{R}^k$ ,  $\hat{\mathbf{E}} \in \mathbb{R}^{k \times k}$ ,  $\hat{\mathbf{A}} \in \mathbb{R}^{k \times k}$ ,  $\hat{\mathbf{B}} \in \mathbb{R}^{k \times m}$ ,  $\hat{\mathbf{C}} \in \mathbb{R}^{p \times k}$ ,  $\mathbf{D} \in \mathbb{R}^{p \times m}$ .  $\hat{\Sigma}$  is obtained by projecting the internal variables of the original system  $\mathbf{x}$  onto a subspace  $\text{ColSpan } \mathbf{V} \subset \mathbb{R}^{n \times k}$ , along

*Null*  $\mathbf{W}^* \subset \mathbb{R}^{k \times n}$ . The goal is to construct  $\mathbf{V}$  and  $\mathbf{W}$ , such that  $\hat{\Sigma}$  is stable and passive. Additionally,  $\mathbf{V}$  and  $\mathbf{W}$  should be computed efficiently. The reduced matrices are obtained as follows:

$$\hat{\mathbf{E}} = \mathbf{W}^* \mathbf{E} \mathbf{V}, \quad \hat{\mathbf{A}} = \mathbf{W}^* \mathbf{A} \mathbf{V}, \quad \hat{\mathbf{B}} = \mathbf{W}^* \mathbf{B}, \quad \hat{\mathbf{C}} = \mathbf{C} \mathbf{V}. \quad (2)$$

## 2 The method

We present the *dominant spectral zero interpolation method (dominant SZM)*, a passivity preserving model reduction method that extends beyond the scope of existing methods such as PRIMA [5]. Imposing no constraints on the system matrices, dominant SZM can reduce passive systems with an underlying possibly indefinite  $\mathbf{E}$  matrix, transmission line models with controlled sources, or circuits containing susceptance elements. The ingredient for passivity preservation are the spectral zeros of  $\Sigma(\mathbf{E}, \mathbf{A}, \mathbf{B}, \mathbf{C}, \mathbf{D})$ , defined as follows:

**Definition 1.** For system  $\Sigma$  with transfer function:  $\mathbf{H}(s) := \mathbf{C}(s\mathbf{E} - \mathbf{A})^{-1}\mathbf{B} + \mathbf{D}$ , the spectral zeros are all  $s \in \mathbb{C}$  such that  $\mathbf{H}(s) + \mathbf{H}^*(-s) = 0$ , where  $\mathbf{H}^*(-s) = \mathbf{B}^*(-s\mathbf{E}^* - \mathbf{A}^*)^{-1}\mathbf{C}^* + \mathbf{D}^*$ .

According to [2, 8], the spectral zero method uses a rational Krylov approach to construct the  $\mathbf{V}$  and  $\mathbf{W}$  which interpolate spectral zeros of  $\Sigma$ . Spectral zeros are solved efficiently from an associated Hamiltonian eigenvalue problem. In [2, 8], the selection of spectral zeros was still an open problem. We propose a solution as follows: we extend the concept of *dominance* from poles [7] to spectral zeros, and adapt the iterative solver SADPA for the computation of *dominant spectral zeros*. The corresponding invariant subspaces are obtained as a by-product of SADPA, and are used to construct the passivity preserving projecting matrices  $\mathbf{V}$  and  $\mathbf{W}$ . The procedure for passive reduction with dominant SZM follows [4]:

- 1) Given  $\Sigma(\mathbf{E}, \mathbf{A}, \mathbf{B}, \mathbf{C}, \mathbf{D})$ , construct the associated Hamiltonian system  $\Sigma_s$  described by (3), whose poles are the spectral zeros of  $\Sigma$ .

$$\mathbf{A}_s = \begin{pmatrix} \mathbf{A} & \mathbf{0} & \mathbf{B} \\ \mathbf{0} & -\mathbf{A}^* & -\mathbf{C}^* \\ \mathbf{C} & \mathbf{B}^* & \mathbf{D} + \mathbf{D}^* \end{pmatrix}, \quad \mathbf{E}_s = \begin{pmatrix} \mathbf{E} & \mathbf{0} & \mathbf{0} \\ \mathbf{0} & \mathbf{E}^* & \mathbf{0} \\ \mathbf{0} & \mathbf{0} & \mathbf{0} \end{pmatrix}, \quad \mathbf{B}_s = \begin{pmatrix} \mathbf{B} \\ -\mathbf{C}^* \\ \mathbf{0} \end{pmatrix} \mathbf{D}_s$$

$$\mathbf{C}_s = -\mathbf{D}_s (\mathbf{C} \quad \mathbf{B}^* \quad \mathbf{0}), \quad \mathbf{D}_s = (\mathbf{D} + \mathbf{D}^*)^{-1} \quad (3)$$

- 2) Solve the Hamiltonian eigenvalue problem  $(\mathbf{A}, \mathbf{R}, \mathbf{L}) = \text{eig}(\mathbf{A}_s, \mathbf{E}_s)$ , i.e.  $\mathbf{A}_s \mathbf{R} = \mathbf{E}_s \mathbf{R} \mathbf{A}$ ,  $\mathbf{L}^* \mathbf{A}_s = \mathbf{A} \mathbf{L}^* \mathbf{E}_s$ . Eigenvalues  $\mathbf{A} = \text{diag}(s_1, \dots, s_n, -s_1^*, \dots, -s_n^*)$  are the spectral zeros of  $\mathbf{\Sigma}$ , and  $\mathbf{R} = [\mathbf{r}_1, \dots, \mathbf{r}_{2n}]$ ,  $\mathbf{L} = [\mathbf{l}_1, \dots, \mathbf{l}_{2n}]$ .
- 3) Compute residues  $R_j$  associated with the stable<sup>1</sup> spectral zeros  $s_j$ ,  $j = 1 \dots n$  as follows:  $R_j = \gamma_j \beta_j$ ,  $\gamma_j = \mathbf{C}_h \mathbf{r}_j (\mathbf{I}_j^* \mathbf{E}_h \mathbf{r}_j)^{-1}$ ,  $\beta_j = \mathbf{I}_j^* \mathbf{B}_h$ .
- 4) Sort spectral zeros descendingly according to dominance criterion  $\frac{|R_j|}{|\text{Re}(s_j)|}$  [7, Chapter 3], and reorder right eigenvectors  $\mathbf{R}$  accordingly.
- 5) Retain the right eigenspace  $\hat{\mathbf{R}} = [\mathbf{r}_1, \dots, \mathbf{r}_k] \in \mathbb{C}^{2n \times k}$ , corresponding to the stable  $k$  most dominant spectral zeros.
- 5) Construct passivity projection matrices  $\mathbf{V}$  and  $\mathbf{W}$  from the rows of  $\hat{\mathbf{R}}$ :  $\mathbf{V} = \hat{\mathbf{R}}_{[1:n, 1:k]}$ ,  $\mathbf{W} = \hat{\mathbf{R}}_{[n+1:2n, 1:k]}$ , and reduce  $\mathbf{\Sigma}$  according to (2).

As explained in [2, 4, 8], by projecting with (2),  $\hat{\mathbf{\Sigma}}$  interpolates the  $k$  most dominant spectral zeros of  $\mathbf{\Sigma}$ , guaranteeing passivity and stability. For large-scale applications, a full solution to the eigenvalue problem in step 2), followed by the dominant sort 3)-4) is computationally unfeasible. Instead, the iterative solver SADPA [7, Chapter 3] is applied with appropriate adaptations for spectral zero computation [4], and the  $k$  most dominant spectral zeros and associated  $2n \times k$  right eigenspace  $\hat{\mathbf{R}}$  are obtained automatically.

### 3 Preliminary results

We reduce an RLC transmission line model with voltage controlled current sources [4]. The system has an associated singular and indefinite matrix  $\mathbf{E}$ , thus  $\mathbf{\Sigma}$  has poles at infinity. PRBT [6] does not apply to  $\mathbf{E}$  singular, and a deflation of infinite poles is required to make  $\mathbf{E}$  invertible. For large systems this can be computationally unfeasible, or must exploit a specific structure of  $\mathbf{E}$  and  $\mathbf{A}$ . PRIMA [5] on the other hand requires a definite  $\mathbf{E}$  and an  $\mathbf{A}$  matrix with special block symmetries. To apply PRIMA, stamps in  $\mathbf{E}$  and  $\mathbf{A}$  corresponding to the loop current variables should be negated, so that  $\mathbf{E}$  becomes definite. This requires knowledge of how the simulator generates states internally and makes reduction non-automatic and cumbersome in practice. Dominant SZM is more general, avoiding both the deflation step required by PRBT and the sign change in PRIMA.

Fig. 1 shows the reduced models from dominant SZM, modal approximation [7] and PRIMA. Already for  $k = 2$ , dominant SZM gives a passive reduced model which is indistinguishable from the original, while the other methods are less accurate. Table 1 summarizes approximation errors

<sup>1</sup>  $s \in \mathbb{C}$  is stable if  $\text{Re}(s) < 0$ .

and CPU times. SADPA computed two dominant spectral zeros, enabling efficient reduction with dominant SZM, when reduction with PRBT is computationally unfeasible. Passivity is preserved automatically even when  $\mathbf{E}$  is indefinite.

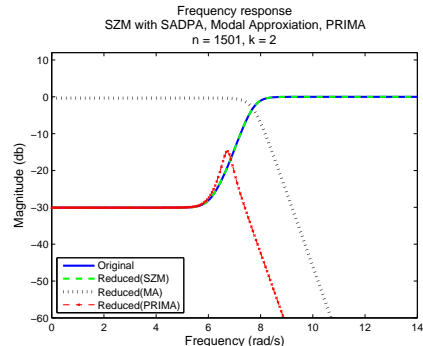


**Fig. 1.** Original and reduced models with dominant SZM, modal approximation and PRIMA.

**Table 1.** Transmission line reduction  $n = 1501$   $k = 2$

SADPA based	Error	Time(s)	Iterations
Dominant SZM	$1.89 \cdot 10^{-4}$	0.8	14
MA	1.24	0.98	35
Other methods	Error	Time(s)	Constraints
PRIMA	$9.98 \cdot 10^{-1}$	0.01	$\mathbf{E}$ definite otherwise unstable
PRBT	-	-	$\mathbf{E}$ singular deflation unfeasible

### References

1. A. C. Antoulas. *Approximation of Large-Scale Dynamical Systems*. SIAM, Philadelphia, PA, 2005.
2. A. C. Antoulas. A new result on passivity preserving model reduction. *Systems and Control Letters*, 54:361–374, 2005.
3. G. Ciuprina and D. Ioan, editors. *Scientific Computing in Electrical Engineering SCEE 2006*, volume 11 of *Mathematics in Industry*. Springer, Berlin, Germany, 2007.
4. R. Ionutiu, J. Rommes, and A.C. Antoulas. Passivity preserving model reduction using dominant spectral zero interpolation. Submitted for publication in *IEEE Trans. Comput.-Aided Design Integr. Circuits Syst.*, 2007.
5. A. Odabasioglu, M. Celik, and L.T. Pillegi. Prima. passive reduced-order interconnect macromodelling algorithm. 17:645–654, 1998.
6. J.R. Phillips, L. Daniel, and L.M. Silveira. Guaranteed passive balancing transformations for model order reduction. 22(8):1027–1041, 2003.
7. Joost Rommes. *Methods for eigenvalue problems with applications in model order reduction*. PhD thesis, Utrecht University, The Netherlands, 2007.
8. D.C. Sorensen. Passivity preserving model reduction via interpolation of spectral zeros. *Systems and Control Letters*, 54:347–360, 2005.

---

**Session**

**P 3**

---



# Analysis of a PDE Thermal Element Model for Electrothermal Circuit Simulation

Giuseppe Ali<sup>1</sup>, Andreas Bartel<sup>2</sup>, Massimiliano Culpo<sup>2</sup>, and Carlo de Falco<sup>3</sup>

<sup>1</sup> Università della Calabria [g.ali@mat.unical.it](mailto:g.ali@mat.unical.it)

<sup>2</sup> Bergische Universität Wuppertal [bartel@math.uni-wuppertal.de](mailto:bartel@math.uni-wuppertal.de), [culpo@math.uni-wuppertal.de](mailto:culpo@math.uni-wuppertal.de),

<sup>3</sup> Dublin City University [carlo.defalco@dcu.ie](mailto:carlo.defalco@dcu.ie)

**Summary.** In this work we address the well-posedness of the steady-state and transient problems stemming from the coupling of a network of lumped electric elements and a PDE model of heat diffusion in the Chip substrate.

## 1 Introduction

Due to downscaling, power densities become more important [5] and therefore thermal models to resolve the geometric layout, which fit seamlessly into the circuit design are necessary. A method for automatically deriving a thermal network model from the layout of an IC and substrate material properties was introduced in [1] and the numerical validation is in progress [2].

The novelty of this method compared to other existing approaches [3, 4] is that it does not work by fitting the parameters of a given network topology, but rather it consists of a parabolic PDE which can be connected to a network of lumped (electrical) device models to perform coupled system-level electrothermal simulation with a standard spice-like circuit simulator. The coupling is performed by controlling the average temperature of some substrate regions via a set of (controlled) voltage sources and the total power dissipated in some other regions via a set of (controlled) current sources. As an initial step towards the analysis of the coupled electro-thermal system, in this work we consider the equations obtained when the thermal element is controlled by a set of independent sources with finite internal resistance or conductance.

## 2 Statement of the problem

Let the domain  $\Omega \subset \mathbb{R}^d$ , with  $d = 1, 2, 3$ , model the IC substrate and  $\Omega_k$  be the *active region* of the  $k$ -th circuit element. We assume that  $\Omega$  be Lipschitz and that the family  $\{\Omega_k, k = 1, \dots, n\}$  satisfies the requirements:

1.  $\overset{\circ}{\Omega}_k \neq \emptyset, \bar{\Omega}_k \subset \Omega \quad \forall k = 1, \dots, n$
2.  $\bar{\Omega}_k \cap \bar{\Omega}_j = \emptyset \quad \forall j, k \in \{1, \dots, n\}, k \neq j.$

We denote by  $u(\mathbf{x}, t)$  the temperature at an instant  $t$  at each point  $\mathbf{x}$  in  $\Omega$ , we let  $q_k(t)/|\Omega_k|$  be the average temperature in the region  $\Omega_k$  at time  $t$  and  $p_k(t)$  the instantaneous Joule power per unit length, area or volume (in case  $d = 1, 2$  or  $3$ , respectively) dissipated by element  $k$ . The heat diffusion in the substrate is governed by the heat equation

$$\frac{\partial u}{\partial t} - \Delta u + \alpha u = f(\mathbf{p}), \quad \text{in } \Omega \times (0, T) \quad (1)$$

denoting by  $f(\mathbf{p})$  the function

$$f(\mathbf{x}, \mathbf{p}) = \sum_{k=1}^n p_k \mathbf{1}_{\Omega_k}(\mathbf{x}),$$

where the vector function  $\mathbf{p}$  is defined as

$$\mathbf{p}(t) = (p_1(t), \dots, p_n(t)),$$

and the symbol  $\mathbf{1}_{\Omega_k}$  represents the indicator function of the set  $\Omega_k$ . Equation (1) is supplemented with initial-boundary conditions

$$u(\mathbf{x}, 0) = u_0(\mathbf{x}), \quad \text{in } \Omega, \quad (2)$$

$$u + \beta \frac{\partial u}{\partial n} = g(t), \quad \text{on } \partial\Omega \times (0, T), \quad (3)$$

where  $g$  is the ambient temperature. Furthermore, the  $k$ -th average device temperature  $q_k$  is connected to  $u$  by the relation

$$\int_{\Omega_k} u(\mathbf{x}, t) d\Omega = q_k(t). \quad (4)$$

Finally, to close the system, we need to state constitutive relations for the vector of average temperatures

$$\mathbf{q}(t) = (q_1(t), \dots, q_n(t)),$$

and for the vector of instantaneous powers  $\mathbf{p}$  in terms of the electrical variables in the circuit. As anticipated in the introduction, in the present work we make the simplifying assumption that the thermal network be controlled via independent sources. Under such an assumption the constitutive relations can be cast into the form

$$a_k p_k + b_k q_k = c_k(t), \quad k = 1, \dots, n \quad (5)$$

where the  $c_k$  are given functions and  $a_k$  and  $b_k$  denote constant coefficients. Notice that  $a_k = 0$  for a given  $k$  indicates that the  $k$ -th region is attached to a voltage source fixing the value of its average temperature, while  $b_k = 0$  indicates that the Joule power dissipated in the  $k$ -th region has been assigned by attaching it to a current source. Summarizing, the problem we intend to investigate reads:

Given initial datum  $u_0(\mathbf{x})$  and ambient temperature  $g(t)$ , find  $u(\mathbf{x}, t)$ ,  $\mathbf{p}(t)$  and  $\mathbf{q}(t)$  such that equations (1)–(5) are satisfied, where  $\alpha$ ,  $\beta$ ,  $a_k$ ,  $b_k$  are known quantities and  $\alpha$ ,  $\beta \geq 0$ .

The above problem is related to the following kernel problem:

Given  $\mathbf{q}$  and  $g$ , find  $u(\mathbf{x})$  and  $\mathbf{p}$  such that:

$$\begin{cases} -\Delta u + \alpha u = f(\mathbf{p}), & \text{in } \Omega, \\ u + \beta \frac{\partial u}{\partial n} = g, & \text{on } \partial\Omega, \\ \int_{\Omega_k} u \, d\Omega = q_k & k = 1, \dots, n. \end{cases} \quad (6)$$

We sketch below our approach to prove the well-posedness of the kernel problem (6), such proof will be used, in the complete version of this work, as the basis for the analysis of the time-dependent problem (1)–(5).

*Sketch of the solution*

Since the differential operator in (6) is linear, we can represent the general solution, for any  $\mathbf{p}$ , as

$$u = u_* + \sum_{k=1}^n p_k u_k, \quad (7)$$

with  $u_*(\mathbf{x})$  solution of the problem

$$\begin{cases} -\Delta u_* + \alpha u_* = 0, & \text{in } \Omega, \\ u_* + \beta \frac{\partial u_*}{\partial n} = g, & \text{on } \partial\Omega, \end{cases} \quad (8)$$

and  $u_k(\mathbf{x})$ ,  $k = 1, \dots, n$ , solution of the problem

$$\begin{cases} -\Delta u_k + \alpha u_k = \mathbf{1}_{\Omega_k}, & \text{in } \Omega, \\ u_k + \beta \frac{\partial u_k}{\partial n} = 0, & \text{on } \partial\Omega, \end{cases} \quad (9)$$

Both problems (8) and (9) are uniquely solvable. Then we can write the conditions for  $q_k$  in (6)<sub>3</sub> as a linear algebraic system with variables  $p_k$ :

$$\sum_{k=1}^n \left\{ \int_{\Omega_j} u_k \, d\Omega \right\} p_k = q_j - \int_{\Omega_j} u_* \, d\Omega, \quad (10)$$

with  $j = 1, \dots, n$ . This system is uniquely solved if and only if

$$\text{the matrix } \left( \int_{\Omega_j} u_k \, d\Omega \right) \text{ is nonsingular.} \quad (11)$$

By multiplying equation (9)<sub>1</sub> by  $u_j$  and integrating on  $\Omega$ , we find ( $\beta > 0$ )

$$\begin{aligned} \int_{\Omega} (\nabla u_k \cdot \nabla u_j + \alpha u_k u_j) \, d\Omega \\ + \int_{\partial\Omega} \frac{1}{\beta} u_k u_j \, d\Omega = \int_{\Omega_k} u_j \, d\Omega, \end{aligned} \quad (12)$$

and we can write

$$\left( \int_{\Omega_k} u_j \, d\Omega \right) = \left( \langle u_j, u_k \rangle \right), \quad (13)$$

where  $\langle \cdot, \cdot \rangle$  is the scalar product defined by the left-hand side of (12). By the Cauchy-Schwartz inequality,

$$\det \left( \langle u_j, u_k \rangle \right) \geq 0, \quad (14)$$

and the equality holds if and only if the functions are linearly dependent. This occurrence is excluded by condition 2 on the subdomains  $\Omega_k$ .

### 3 Acknowledgments

The third author was supported by the European Commission in the framework of the CoMSON RTN project. The fourth author was supported by the Mathematics Applications Consortium for Science and Industry in Ireland (MACSI) under the Science Foundation Ireland (SFI) mathematics initiative.

### References

1. Massimiliano Culpò and Carlo de Falco. dynamical iteration schemes for coupled simulation. 2008.
2. Massimiliano Culpò, Carlo de Falco, Georg Denk, and Steffen Voigtmann. Automatic thermal network extraction and multiscale electro-thermal simulation. Work in progress 2008.
3. T. Grasser and S. Selberherr. Fully coupled electrothermal mixed-mode device simulation of sige hbt circuits. *Electron Devices, IEEE Transactions on*, 48(7):1421–1427, Jul 2001.
4. P.M. Igić, P.A. Mawby, M.S. Towers, and S. Batcup. Dynamic electro-thermal physically based compact models of the power devices for device and circuit simulations. *Semiconductor Thermal Measurement and Management, 2001. Seventeenth Annual IEEE Symposium*, pages 35–42, 2001.
5. International roadmap committee. International technology roadmap for semiconductors 2007. Technical report, ITRS, 2007.

# Efficient simulation of large-scale dynamical systems using tensor decompositions

F. van Belzen and S. Weiland

Eindhoven University of Technology, Department of Electrical Engineering, P.O. Box 513, 5600 MB Eindhoven, The Netherlands [f.v.belzen@tue.nl](mailto:f.v.belzen@tue.nl), [s.weiland@tue.nl](mailto:s.weiland@tue.nl)

**Summary.** Tensors are the natural mathematical objects to describe physical quantities that evolve over multiple independent variables. This abstract considers the computation of empirical projection spaces by decomposing the tensor that can be associated with the measurement data. We show how these projection spaces can be used to derive reduced order models. The procedure is applied to a two-dimensional heat diffusion problem.

## 1 Introduction

Most model reduction techniques such as balanced truncation, Krylov methods, and Proper Orthogonal Decompositions (POD) [5] are projection based methods. In this abstract, we examine the POD method to reduce the complexity of systems with both space and time as independent variables. The POD method leads to simplified models by applying a Galerkin projection on both the signals and the equation residuals of a dynamical model. The POD method is particularly popular in computational fluid dynamics applications where it simplifies spatial-temporal systems by inferring projection spaces from collections of spatially distributed data. These projection spaces are computed via singular value decompositions of matrices that have the total mesh size of the spatial geometry as its dimension. For spatial geometries that are two, three or larger dimensional, these computations become particularly cumbersome in combination with fine gridded mesh-sizes. Moreover, this computation generally neglects structures such as symmetries or Cartesian structures that may be present in the spatial geometry.

In this abstract we propose a method to compute data-dependent projection spaces that leaves Cartesian structures in multidimensional arrays of measured data intact. For this, we propose an extension of the concept of SVD to tensors.

## 2 Model reduction by projections

Consider an arbitrary linear  $N$ -dimensional system described by the Partial Differential Equa-

tion (PDE)

$$R\left(\frac{\partial}{\partial x_1}, \dots, \frac{\partial}{\partial x_N}\right)w = 0 \quad (1)$$

in which  $w : \mathbb{X} \subset \mathbb{R}^N \rightarrow \mathbb{R}$  is the (unknown) solution in  $N$  independent variables. Here,  $R \in \mathbb{R}^{\times 1}[\xi_1, \dots, \xi_N]$  is a real matrix valued polynomial in  $N$  indeterminates. Weak solutions of (1) are generally defined with respect to a Hilbert space  $\mathcal{H}$  of functions on a subset  $\mathbb{X}'$  of  $\mathbb{X}$  according to

$$\left\langle R\left(\frac{\partial}{\partial x_1}, \dots, \frac{\partial}{\partial x_N}\right)w, \varphi \right\rangle = 0 \quad \forall \varphi \in \mathcal{H}. \quad (2)$$

Given a basis  $\{\varphi_n\}$  of  $\mathcal{H}$  and a finite dimensional subspace  $\mathcal{H}_r = \text{span}\{\varphi_1, \dots, \varphi_r\}$  of  $\mathcal{H}$ , a reduced order model is defined by the collection of solutions  $w_r \in \mathcal{H}_r$  that satisfy (2) with  $\mathcal{H}$  replaced by  $\mathcal{H}_r$ . This is usually called a *Galerkin projection* of the original model [4].

## 3 Tensor decompositions

Suppose that the domain  $\mathbb{X}$  of (1) has an Euclidean structure  $\mathbb{X} = \mathbb{X}_1 \times \dots \times \mathbb{X}_N$ . In this section we propose a construction of the projection space  $\mathcal{H}_r$  that is inferred from a measured or simulated solution  $w$  of (1). More specifically, suppose that, for  $n = 1, \dots, N$ , the domain  $\mathbb{X}_n$  is gridded into a finite set of  $L_n$  elements and let  $X_n := \mathbb{R}^{L_n}$ . Suppose that  $w$  is a *Finite Element* (FE) solution of (1). Then  $w$  defines a multidimensional array  $W \in \mathbb{R}^{L_1 \times \dots \times L_N}$  with  $w_{\ell_1 \dots \ell_N}$  being the  $(\ell_1, \dots, \ell_N)$ th entry.

At a more abstract level  $W$  defines a tensor. An *order- $N$  tensor*  $T$  is a multilinear functional  $T : X_1 \times \dots \times X_N \rightarrow \mathbb{R}$  operating on  $N$  vector spaces  $X_1, \dots, X_N$ . Elements of  $T$ ,  $t_{\ell_1 \dots \ell_N}$ , can be defined with respect to bases for  $X_1, \dots, X_N$  according to  $t_{\ell_1 \dots \ell_N} = T(e_1^{\ell_1}, \dots, e_N^{\ell_N})$ , where  $\{e_n^{\ell_n}, \ell_n = 1, \dots, L_n\}$  is a basis for  $X_n$ ,  $n = 1, \dots, N$ .

A FE solution  $w$ , or its associated multidimensional array  $W$ , therefore defines the tensor

$$\mathcal{W} = \sum_{\ell_1=1}^{L_1} \dots \sum_{\ell_N=1}^{L_N} w_{\ell_1 \dots \ell_N} e_1^{\ell_1} \otimes \dots \otimes e_N^{\ell_N} \quad (3)$$

where  $e_1 \otimes \dots \otimes e_N$  is shorthand for the *rank-1 tensor*  $E(x_1, \dots, x_N) := \prod_{n=1}^N e_n^\top x_n$ .

The tensor (3) associated with the FE solution defines suitable projection spaces as follows. We propose the construction of orthonormal bases  $\{m_n^{\ell_n}, \ell_n = 1, \dots, L_n\}$  of  $X_n$  such that a coordinate change of  $\mathcal{W}$  with respect to these bases achieves that the truncated tensor

$$\mathcal{W}_T := \sum_{\ell_1=1}^{R_1} \dots \sum_{\ell_N=1}^{R_N} \hat{w}_{\ell_1, \dots, \ell_N} m_1^{\ell_1} \otimes \dots \otimes m_N^{\ell_N} \quad (4)$$

with  $R_n \leq L_n$ ,  $n = 1, \dots, N$ , will minimize the error  $\|\mathcal{W} - \mathcal{W}_T\|$ , in a suitable tensor norm, [2,3]. For order-2 tensors (matrices) this is achieved by the SVD. For higher-order tensors, it is not straightforward how to construct proper sets of orthonormal bases with this property. Different methods exist, including the Higher-Order Singular Value Decomposition [1] and the Tensor SVD [3].

Note that projection spaces are not only defined by the orthonormal bases. The truncation levels,  $R_n \leq L_n$  should also be chosen appropriately. This choice involves making a trade-off between complexity and accuracy.

## 4 2D heat diffusion example

Consider the following model of a heat transfer process on a rectangular plate of size  $L_x \times L_y$ :

$$0 = -\rho c_p \frac{\partial w}{\partial t} + \kappa_x \frac{\partial^2 w}{\partial x^2} + \kappa_y \frac{\partial^2 w}{\partial y^2}. \quad (5)$$

Here,  $w(x, y, t)$  denotes temperature on position  $(x, y)$  and time  $t$  and the rectangular spatial geometry defines the Cartesian product  $\mathbb{X} \times \mathbb{Y} := [0, L_x] \times [0, L_y]$ . Let  $\mathcal{H}_r = \mathcal{X}_{R_1} \times \mathcal{Y}_{R_2}$  with  $\mathcal{X}_{R_1} \subseteq \mathcal{X} = \mathcal{L}_2(\mathbb{X})$  and  $\mathcal{Y}_{R_2} \subseteq \mathcal{Y} = \mathcal{L}_2(\mathbb{Y})$  be finite dimensional subspaces spanned by  $R_1$  and  $R_2$  orthonormal bases functions  $\{\varphi_{\ell_1}\}$  and  $\{\psi_{\ell_2}\}$ , respectively. Solutions of the reduced model are then given by  $w_r(x, y, t) = \sum_{ij} a_{ij}(t) \varphi_i(x) \psi_j(y)$  with  $a_{ij}(t) = [A(t)]_{ij}$  a solution of the matrix differential equation

$$0 = -\rho c_p \dot{A} + \kappa_x F A + \kappa_y A P. \quad (6)$$

Here,  $F$  and  $P$  are defined as:

$$F = \begin{bmatrix} \langle \varphi_1, \ddot{\varphi}_1 \rangle & \dots & \langle \varphi_1, \ddot{\varphi}_{R_1} \rangle \\ \vdots & & \vdots \\ \langle \varphi_{R_1}, \ddot{\varphi}_1 \rangle & \dots & \langle \varphi_{R_1}, \ddot{\varphi}_{R_1} \rangle \end{bmatrix} \quad P = \begin{bmatrix} \langle \psi_1, \ddot{\psi}_1 \rangle & \dots & \langle \psi_1, \ddot{\psi}_{R_2} \rangle \\ \vdots & & \vdots \\ \langle \psi_{R_2}, \ddot{\psi}_1 \rangle & \dots & \langle \psi_{R_2}, \ddot{\psi}_{R_2} \rangle \end{bmatrix}$$

A FE solution of (5) is computed with grid sizes  $(L_1, L_2, L_3) = (50, 100, 500)$ , see Fig. 1. Orthonormal bases were computed using the Tensor SVD [3]. Basis functions are displayed in Fig. 2.

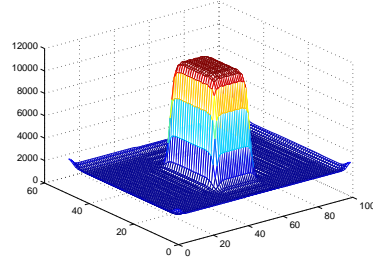


Fig. 1. Time slice of the FE solution of (5).

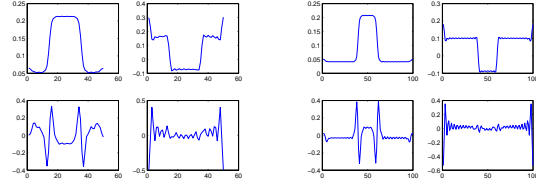


Fig. 2. First basis functions for  $\mathcal{X}$  (left) and  $\mathcal{Y}$  (right), computed using tensorial SVD.

## 5 Conclusion

In this abstract we considered model reduction for multidimensional systems using the POD method. For the computation of empirical projection spaces we proposed a method using tensor decompositions. The techniques proposed were applied to a two-dimensional heat diffusion problem. In the future, we plan to test the method on more complex examples and aim to compare different tensorial decompositions to assess accuracy, computational effort and reliability.

*Acknowledgement.* This work is supported by the Dutch Technologiestichting STW under project number EMR.7851.

## References

1. L. de Lathauwer et al. A Multilinear Singular Value Decomposition. *SIAM J. Matrix Anal. Appl.*, Vol. 21 (4), 2000.
2. T.G. Kolda. Orthogonal tensor decompositions. *SIAM J. Matrix Anal. Appl.*, Vol. 23 (1), 2001.
3. F. van Belzen, S. Weiland and J. de Graaf. Singular value decompositions and low rank approximations of multi-linear functionals. *Proc. 46th IEEE Conf. on Decision and Control*, 2007.
4. S. Volkwein and S. Weiland. An Algorithm for Galerkin Projections in both Time and Spatial coordinates. *Proc. 17th MTNS*, 2006.
5. M. Kirby. Geometric Data Analysis. *John Wiley*, 2001

# Magnetic Force Calculation applied to Magnetic Force Microscopy

Thomas Preisner, Michael Greiff, Josefine Freitag, and Wolfgang Mathis

Leibniz Universitaet Hannover, Appelstrasse 9A, 30167 Hannover, Germany [preisner@tet.uni-hannover.de](mailto:preisner@tet.uni-hannover.de), [greiff@tet.uni-hannover.de](mailto:greiff@tet.uni-hannover.de), [freitag@tet.uni-hannover.de](mailto:freitag@tet.uni-hannover.de), [mathis@tet.uni-hannover.de](mailto:mathis@tet.uni-hannover.de)

**Summary.** In IC failure analysis the detection of currents is often used to indicate the presence of a defective device. One method used for this analysis is the Magnetic Force Microscopy (MFM). The manufactured tips used for MFM measurements frequently show fabrication errors. Hence, in this work a theoretical model of the MFM was developed to verify and improve the results of laboratory MFM measurements. Furthermore, the influence of the thickness of the magnetic tip coating as well as different kinds of asymmetrical geometries are numerically investigated.

## 1 Introduction

Due to technical advances in the development of integrated circuits a reduction of the dimensions of electronic devices and structures is feasible. Consequently, the IC failure analysis, which makes use of occurring currents as a possible evidence for defective devices, becomes more complex. The magnetic field caused by these currents can be detected by using special methods such as the Magnetic Force Microscopy (MFM). In [1] it is demonstrated that the MFM technique is applicable for the detection of currents down to  $1\mu A$ . Furthermore, a comparison between laboratory measurements and a theoretical consideration in which the magnetic coated tip is approximated by several magnetic moments is shown. The resulting values of both approaches in [1] are on a picometer scale but the amplitudes differ from each other. As solely reason for these differences only the orthogonally assumed tip magnetization in the theoretical consideration is denoted; but some further effects must be considered. In an ideal case the tip is atomically sharp and features the geometry of a symmetric cone. In fact, a couple of atoms are located at the tip apex and even double tips might emerge depending on the manner of preparation. In addition a further reason for the differences is the technical unattainable geometric symmetry of the tip. Hence, in this study an improved model with more degrees of freedom was developed by using the finite element method (FEM). The main objectives are the verification

of the laboratory MFM measurement results and the investigation of the influences and effects due to variations of the tip geometry. For that purpose different force calculation methods like the Virtual Work Principle and the Maxwell Stress Tensor are implemented and compared with each other. It is a fact, both methods are often used to obtain the total force of an object under investigation, but the force distribution strongly differ from each other [4,5]. For this reason the Virtual Work Principle is implemented in our study in such a manner as it show in [4,5] to obtain local forces with physical meaning.

## 2 Micromagnetic Model

In order to develop an applicable theoretical model of the MFM it is necessary to describe the causes for the magnetic fields. Therefore two different sources must be considered, the current density  $\mathbf{J}$  and the material magnetization  $\mathbf{M}$ . The fundamental expression for such problems is the well known curl-curl equation

$$\nabla \times \frac{1}{\mu} (\nabla \times \mathbf{A}) = \nabla \times \frac{\mu_0}{\mu} \mathbf{M} + \mathbf{J}, \quad (1)$$

whereas  $\mathbf{A}$  is the magnetic vector potential,  $\mu$  is the material permeability and  $\mu_0$  is the permeability of free space. For the purpose of ensuring the uniqueness of the magnetic vector potential and making the solution of the coupled system numerically stable [2] the Coulomb gauge is added. Applying the method of weighted residuals and using Gauss law and a vector identity, the weak formulation can be obtained. As an example for a three dimensional model used in this work we consider a current carrying micro-conductor which is scanned by a cantilever holding the magnetic coated tip underneath. This arrangement is pictured in Fig. 1. In this approach we assume a conically shaped tip with an angle of  $30^\circ$ . This tip consists of a cobalt-chromium compound, which is orthogonally magnetized with respect to the sample surface. Analogous to [3] we set the value for the magnetization in negative

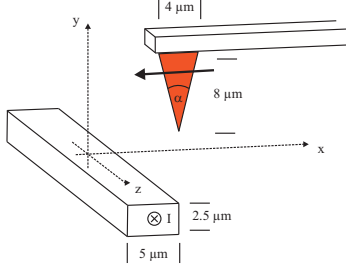


**Fig. 1.** Configuration of the 3D-model.

$y$ -direction to  $\mathbf{M} = 749 \frac{kA}{m}$ . Furthermore, we assume a hard ferromagnetic material, so that the permanent permeability of the conical magnetic coating is approximately  $\mu_r \approx 1$ . The thickness of this magnetic coating amounts to  $60nm$ . The micro-conductor features a width of  $5\mu m$ , a thickness of  $2.5\mu m$  and carries a current of  $1mA$ .

### 3 Results

The occurring forces during the scanning process between tip and the micro-conductor are calculated in a span of  $55\mu m$ . Therefore different formulations are applied and compared. The first one is the Virtual Work Principle, the second one the surface integration over Maxwells Stress Tensor. Furthermore, the Virtual Work Principle is implemented in such a manner as it is show in [4, 5] in order to obtain the force distribution on the magnetic coating of the tip. Therefore we solve (2) at the elements  $e$  corresponding to a node  $k$  in a direction  $i$

$$F_{ik} = - \sum_{e_k} \left[ \int_{\Omega_{e_k}} \frac{(\mathbf{B} - \mathbf{B}_r)^T}{\mu_0} \mathbf{J}^{-1} \frac{\delta \mathbf{J}}{\delta s_i} \mathbf{B} |\mathbf{J}| d\Omega_{e_k} - \int_{\Omega_{e_k}} \frac{(\mathbf{B} - \mathbf{B}_r)^T (\mathbf{B} - \mathbf{B}_r)}{2\mu_0} \frac{\delta |\mathbf{J}|}{\delta s_i} d\Omega_{e_k} \right] \quad (2)$$

where  $\mathbf{B}$  is the magnetic flux density,  $\mathbf{B}_r$  is the remanence flux density and  $\mathbf{J}$  is the Jacobian matrix. Finally we withdraw the intrinsic forces [4,5]. Concerning the total magnetic force, all three methods are in excellent agreement with each other. All the values are located in a  $pN$ -range. The active force with respect to the tip axis and a simulated MFM image is shown in Fig. 2.

In [1] the magnetically coated tip is approximated by using several magnetic moments and is compared to laboratory measurement values. The presented numerical results are perfectly concordant with these considerations. In Fig. 3 the force distribution of the magnetic coating at the point  $3.5\mu m$  to the right of the current carrying micro-conductor is shown.

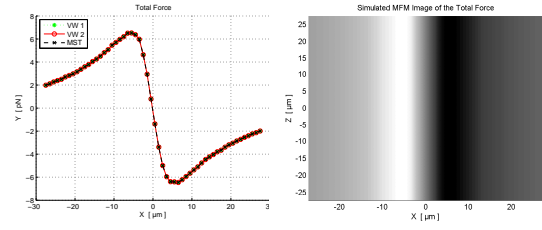


**Fig. 2.** Total force acting on the cantilever (left) and a simulated MFM image (right).

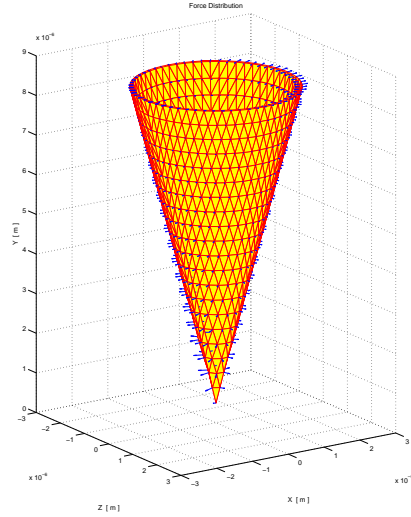


**Fig. 3.** Force distribution of the magnetic coated tip.

In this abstract only forces and simulations of a totally symmetric tip are shown. In the full paper the influences of tip asymmetry and different thicknesses of the magnetically coated film will be presented.

### References

1. A. Pu, A. Rahman, D.J. Thomson and G.E. Bridges. Magnetic force microscopy measurements of current on integrated circuits. *IEEE CCECE 2002*, 1:439–444, 1997.
2. K. Preis, I. Bardi, O. Biro, C. Magele, W. Renhart, K.R. Richter and G. Vrisk. Numerical analysis of 3D magnetostatic fields. *IEEE Trans. Magn.*, 27:3798–3803, 1991.
3. A. Carl, J. Lohau, S. Kirsch and E.F. Wassermann. Magnetization reversal and coercivity of magnetic force microscopy tips. *J. Appl. Phys.*, 89:6098–6104, 2001.
4. L.H. de Medeiros, G. Reyne, G. Meunier and J.P. Yonnet. Distribution of electromagnetic force in permanent magnets. *IEEE Trans. Magn.*, 34:3012–3015, 1998.
5. L.H. de Medeiros, G. Reyne and G. Meunier. About the distribution of forces in permanent magnets. *IEEE Trans. Magn.*, 36:3345–3348, 1999.

# EM Scattering Calculations using Potentials

Magnus Herberthson<sup>1,2</sup>

<sup>1</sup> Department of Sensor Informatics, Swedish Defence Research Agency, Box 1165, SE - 581 11 Linköping, Sweden [magnus.herberthson@foi.se](mailto:magnus.herberthson@foi.se)

<sup>2</sup> Department of Mathematics, Linköpings Universitet, 581 83 Linköping, Sweden [maher@mai.liu.se](mailto:maher@mai.liu.se)

**Summary.** EM scattering from PEC surfaces are mostly calculated through the induced surface current  $\mathbf{J}$ . In this paper, we consider PEC surfaces homeomorphic to the sphere, apply Hodge decomposition theorem to a slightly rewritten surface current, and show how this enables us to replace the unknown current with two scalar functions which serve as potentials for the current.

Implications of this decomposition are pointed out, and numerical results are demonstrated.

## 1 Introduction

There are numerous ways to address the problem of calculating the radar cross section of PEC surfaces [1, 2]. One method is to solve the electric field integral equation, (EFIE), where a standard reference is [3]. In frequency domain, taking the incoming field  $\mathbf{E}_i$  to be a plane wave we have  $\mathbf{E}_i = \mathbf{E}_0 e^{-i\mathbf{k}\cdot\mathbf{r}}$ . By choosing an adapted ON basis, the EFIE becomes [1, 3, 4],

$$\forall \mathbf{r} \in S : E_0 e^{-i\mathbf{k}z} \hat{\mathbf{x}} \hat{=} ikc\mu_0 \left( \mathbf{I} + \frac{1}{k^2} \nabla \nabla \cdot \right) \int_S g(\mathbf{r}, \mathbf{r}') \mathbf{J}(\mathbf{r}') dS' \quad (1)$$

where  $\mathbf{J}$  is the surface current on  $S$ ,  $g$  is the Greens function  $g(\mathbf{r}, \mathbf{r}') = \frac{e^{ik|\mathbf{r}-\mathbf{r}'|}}{4\pi|\mathbf{r}-\mathbf{r}'|}$ , and where  $\hat{=}$  means tangential equality (on  $S$ ).  $\mathbf{k}$ ,  $k$ ,  $\mu_0$ ,  $c$ , and  $\nabla$  have their usual meanings.

Since the electric field is a covariant vector field (i.e. a one-form) rather than a contravariant vector field the equality in (1) is, for each  $\mathbf{r} \in S$ , evaluated in  $T_p^*S$ , the cotangent space at  $p$ . It is therefore natural to use the theory of forms, and in particular Hodge decomposition theorem when addressing (1). For simplicity, we will assume that the surface  $S$  is closed and homeomorphic to a sphere.

## 2 Reformulation of EFIE

One first notes that the LHS of (1) is not an exact one-form. However, by multiplying both sides with  $e^{ikz}$ , the LHS is just the tangential part of  $\hat{\mathbf{x}}$ , i.e., the one-form  $dx$ , which is exact, i.e., a

gradient of a scalar function. For this reason, we introduce the following functions

$$h(\mathbf{r}, \mathbf{r}') = g(\mathbf{r}, \mathbf{r}') e^{ik(z-z')}, \mathbf{K}(\mathbf{r}') = e^{ikz'} \mathbf{J}(\mathbf{r}') \quad (2)$$

After multiplication with  $e^{ikz}$ , (1) becomes

$$e_0 \nabla x - \nabla \left[ \int_S h \hat{\mathbf{z}} \cdot \mathbf{K} dS' + \frac{i}{k} \int_S \mathbf{K} \cdot \nabla h dS' \right] \hat{=} ik \int_S h \mathbf{K} dS' - \hat{\mathbf{z}} \left[ ik \int_S h \hat{\mathbf{z}} \cdot \mathbf{K} dS' - \int_S \mathbf{K} \cdot \nabla h dS' \right] \quad (3)$$

This formulation is still in vector calculus notation, and theoretical advantage is that the LHS of (3) is now an exact one-form. Note, however, that the fictive current  $\mathbf{K}$  is a 'down sampled' version of  $\mathbf{J}$ , i.e., the oscillatory part  $e^{-ikz}$  is factored out. In practice, this may therefore allow for a much sparser sampling of the 'current'  $\mathbf{K}$ , and therefore reduced numerics. Also, note that complicated objects may require dense sampling over areas of resonance.

To proceed we now use the Hodge decomposition [5] applied to  $\mathbf{K}$ . The Hodge decomposition theorem asserts that, when  $S$  is compact, any one-form  $\mathbf{K}$  can be written uniquely as  $\mathbf{K} = d\Phi + \beta + \delta\psi$  where  $\Phi$  is a scalar,  $\beta$  is a harmonic one-form and  $\psi$  is a two-form. Moreover,  $d$  is the exterior derivative, the coderivative  $\delta$  is  $\delta = -*d*$ , where  $*$  is the Hodge star. However,  $\beta \in \text{Harm}^1(S)$  is zero since there are no nontrivial harmonic one-forms on  $S$ . Thus, with  $\Psi = *\psi$ , so that  $\Psi$  is a scalar function, we have that

$$\mathbf{K} = d\Phi + \delta*\Psi \cong \nabla_S \Phi + \hat{\mathbf{n}} \times \nabla_S \Psi$$

on  $S$ , which means that  $\mathbf{K}$  is expressed through the two scalar potentials  $\Phi$  and  $\Psi$ . Here,  $\hat{\mathbf{n}}$  is a unit normal to  $S$  and  $\nabla_S$  stands for the intrinsic gradient operator on  $S$ . Equation (3) now reads

$$\nabla \left[ e_0 x - \int_S (\langle d'z', \mathbf{K} \rangle + \frac{i}{k} \Delta'_S \Phi) h dS' \right] \hat{=} ik \int_S (k\mathbf{K} - \hat{\mathbf{z}} [k \langle d'z', \mathbf{K} \rangle + i \Delta'_S \Phi]) h dS' \quad (4)$$

where  $\Delta_S$  is the intrinsic laplace operator on  $S$ .

Depending on approach, equation (4) can be addressed in several ways. In the next section, we will consider a few of these.

### 3 Computational benefits

The factorization  $\mathbf{K}(\mathbf{r}') = e^{ikz'}\mathbf{J}(\mathbf{r}')$  may lead to sparser sampling. Since the external applied field is  $-E_0\hat{\mathbf{x}}e^{-ikz}$  we can expect that the induced current  $\mathbf{J}$  largely contains the oscillatory part  $e^{-ikz}$ . Therefore, in non-resonant areas, the 'current'  $\mathbf{K}$  resembles an envelope, which can be sampled much sparser than  $\mathbf{J}$ . For high frequencies, this can reduce the numerical problem substantially.

Another way of using (4) is to note that the left hand side is an exact one-form on  $S$ . Namely, by a discretization of  $\mathbf{K} = d\Phi + \delta*\Psi$  which gives  $\Phi$  and  $\Psi$   $n$  degrees of freedom each, we must in principle produce and solve a  $2n \times 2n$  system of equations

$$\begin{pmatrix} X & X \\ X & X \end{pmatrix} \begin{pmatrix} [\Phi]_{n \times 1} \\ [\Psi]_{n \times 1} \end{pmatrix} = \begin{pmatrix} v_1 \\ v_2 \end{pmatrix} \quad (5)$$

where  $[\Phi]_{n \times 1}$ ,  $[\Psi]_{n \times 1}$  are  $n \times 1$  vectors representing the fields  $\Psi$  and  $\Phi$ , where  $v_1, v_2$  also are  $n \times 1$  vectors and where  $X$  stands for various matrices of order  $n \times n$ . Instead of solving (5), it is obviously much cheaper to solve a system which takes the form

$$\begin{pmatrix} X & X \\ X & X \end{pmatrix} \begin{pmatrix} [\Phi]_{n \times 1} \\ [\Psi]_{n \times 1} \end{pmatrix} = \begin{pmatrix} v_1 \\ 0 \end{pmatrix} \quad (6)$$

since one can first solve the lower block row of (6) and then substitute in the upper block row. In principle, one  $2n \times 2n$  inversion is replaced with two  $n \times n$  inversions. One can go from (5) to (6) in several ways. Since the LHS of (4) is exact, one can take the exterior derivative and coderivative of (5) to get (6). One can also get (6) by testing (4) against suitable test functions directly.

### 4 Numerical results

Although this approach has been reported earlier, the full implementation using the scalar potentials  $\Phi$  and  $\Psi$  has not been demonstrated so far. Considering the space available, we will only exemplify the above approach in the most familiar case, i.e., the sphere. Illuminating a sphere of radius 1 m with a plane wave with  $\lambda = 1$  m, propagating along the  $z$  axis and with the electric field parallel to the  $x$  axis, the resulting potentials and currents are illustrated in Fig. 1-3. In Fig. 1, the scalar potential  $\Phi$  is shown as an intensity map over the surface.  $|\Phi|$  is given by the brightness, and the phase information is encoded in the colour. The gradient  $\nabla\Phi$  is shown with real (blue) and imaginary (red) parts. In Fig. 2,  $\Psi$  and the co-gradient  $\hat{\mathbf{n}} \times \nabla\Psi$  are displayed. In Fig. 3, the

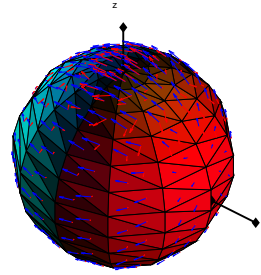


Fig. 1. The potential  $\Phi$  and its current.

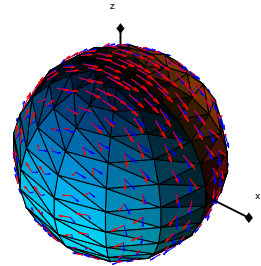


Fig. 2. The potential  $\Psi$  and its (co-)current.

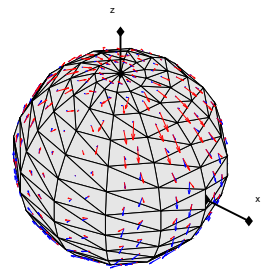


Fig. 3. The current  $\mathbf{K}$ .

total current  $\mathbf{K}$ , from which the physical current  $\mathbf{J}(\mathbf{r}) = e^{-ikz}\mathbf{K}(\mathbf{r})$  is obtained, is drawn.

A more detailed analysis will follow, but preliminary, the outcome of the calculations are in good agreement with expected results.

### References

1. Harrington, R. F., *Field Computation by Moment Methods*, IEEE Press, 1993.
2. Chew, W. C. et al, editors, *Fast and efficient algorithms in computational electromagnetics*, Artech House, 2001.
3. Rao, S. M., Wilton, D.R., Glisson, A.W., "Electromagnetic Scattering by Surfaces of Arbitrary Shape", *IEEE Trans. Antennas Propag.*, vol. **AP-30**, pp. 409-418, May 1982
4. Kristensson, G., "Spridningsteori med antenntillämpningar", *Studentlitteratur, Lund*, 1999
5. Göckeler, M., Schücker, T., "Differential geometry, gauge theories, and gravity", *Cambridge University Press*, 1987

# Simulation of large interconnect structures using a ILU-type preconditioner

D. Harutyunyan<sup>1,3</sup>, W. Schoenmaker<sup>2</sup>, and W.H.A. Schilders<sup>1,3</sup>

<sup>1</sup> Technische Universiteit Eindhoven, Den Dolech 2, 5612 AZ Eindhoven, The Netherlands  
{d.harutyunyan,w.h.a.schilders}@tue.nl,

<sup>2</sup> Magwel NV, Martelarenplein 13, B-3000 Leuven, Belgium wim.schoenmaker@magwel.com

<sup>3</sup> NXP Semiconductors, High Tech Campus 37, 5656 AE Eindhoven, The Netherlands  
{davit.harutyunyan,wil.schilders}@nxp.nl

**Summary.** For a fast simulation of on-chip interconnect structures we consider preconditioned iterative solution methods of large complex valued linear systems. The matrices are ill-conditioned and efficient preconditioners are indispensable to solve the linear systems accurately. We analyze the dual threshold ILUT preconditioner with BICGSTAB iterative solver and show that this preconditioner provides a very accurate solution for real life complicated problems in an efficient way.

## 1 Introduction

With the increasing complexity of on-chip interconnect structures more robust and fast simulation methods are necessary to understand the behavior of electromagnetic fields in such complex structures. Field simulation approaches provide more insight and preserve important physical characteristics of electromagnetic fields at a discrete level. The behavior of the electromagnetic fields is governed by the Maxwell equations. For many applications the potential formulation of the Maxwell equations is used which has several advantages. In particular, for on-chip interconnect structures the potential formulation allows separate modeling of fields on dielectric, semiconductor and metallic regions.

After discretization of time harmonic Maxwell equations we obtain a complex valued linear system of equations

$$Ax = b. \quad (1)$$

Rapid changes in material properties can affect the numerical properties of the matrix  $A$  and may result into slow convergence for iterative solvers. To overcome these problems good preconditioners are required to solve the linear system of equations accurately.

For ill-conditioned matrices the standard ILU factorization requires a small drop tolerance to

achieve good accuracy. However, with a small drop tolerance, the fill-in of the L and U matrices is not predictable and for large difficult problems it becomes almost impossible to construct the ILU factorization due to memory limitations.

To overcome the memory problems we use the ILUT( $p, \tau$ ) preconditioner [2], where  $p$  is a parameter which controls the number of fill-ins in the L and U matrices, and  $\tau$  is the drop tolerance. This preconditioner nowadays is widely used and has proved to be a very efficient and robust method for many complicated problems.

## 2 Potential formulation of the Maxwell equations

The potential formulation of the Maxwell equations in the frequency domain can be written as [1]:

$$\nabla \times \frac{1}{\mu} \nabla \times \mathbf{A} - k(-j\omega \mathbf{A} - \nabla V) = \mathbf{J}_{\text{diff}}, \quad (2a)$$

$$\nabla \cdot (\varepsilon(\nabla V + j\omega \mathbf{A})) = -\rho, \text{ in insulators} \quad (2b)$$

and semiconductors,

$$\nabla \cdot (k(\nabla V + j\omega \mathbf{A})) = 0 \text{ in metals}, \quad (2c)$$

where  $k = (\sigma + j\omega\varepsilon)$ . This formulation allows us to deal with different materials separately.

For the unique solution of (2) a gauge condition is necessary [3]. The following gauge condition is considered:

$$\frac{1}{\mu_0} \nabla (\nabla \cdot \mathbf{A}) + j\omega\varepsilon\xi \nabla V = 0 \quad (3)$$

where  $0 \leq \xi \leq 1$ . Equation (3) resembles to the Coulomb gauge for  $\xi = 0$  and to the Lorentz gauge for  $\xi = 1$ .

We note that the vector potential  $\mathbf{A}$  is a 1-form and the potential  $V$  is a 0-form. For the discretization of the vector potentials we apply the 'finite-surface method' [4], whose origin is found in the

Stokes' theorem. This discretization method preserves important physical characteristics of the electromagnetic fields at the discrete level and we obtain physically relevant solutions.

### 3 Numerical experiments

For a solution of large ill-conditioned linear systems (1) we apply the dual threshold incomplete ILUT preconditioner. The computational time required for the ILUT factorization can be significantly reduced by proper reordering of the matrix elements. We compare two common reordering methods: the symmetric reverse Cuthill-McKee reordering (SYMRCM) and the approximate minimum degree (AMD) reordering.

We present the numerical experiments on the interconnect structure given in Fig. 1. The structure dimension in micrometers is  $4.4 \times 5.5 \times 4.24$  and it consist of 3 metallic layers. The contacts between semiconductor and the first metallic layer is Tungsten and all the other metals and vias are copper.

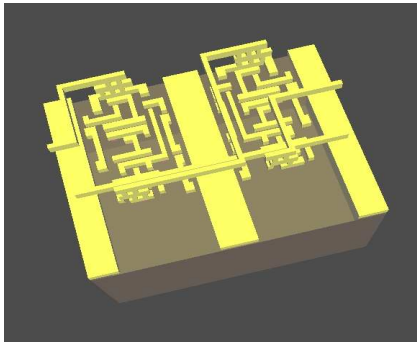


Fig. 1. Interconnect structure.

The frequency of interest is 500MHz and we generate a mesh which results into a system with 141513 unknowns. The convergence diagram of the relative residual of the BICGSTAB method is given in Fig. 2. In Fig. 3 eigenvalue distribution of the 25 smallest eigenvalues using the Jacobi-Davidson method are shown. It is clear that the preconditioner shifts the smallest eigenvalues far from the origin.

*Acknowledgement.* The first author was financed by the European Commission through the Marie Curie Actions of its Sixth Program under the project O-MOORE-NICE, contract number MTKI-CT-2006 - 042477.

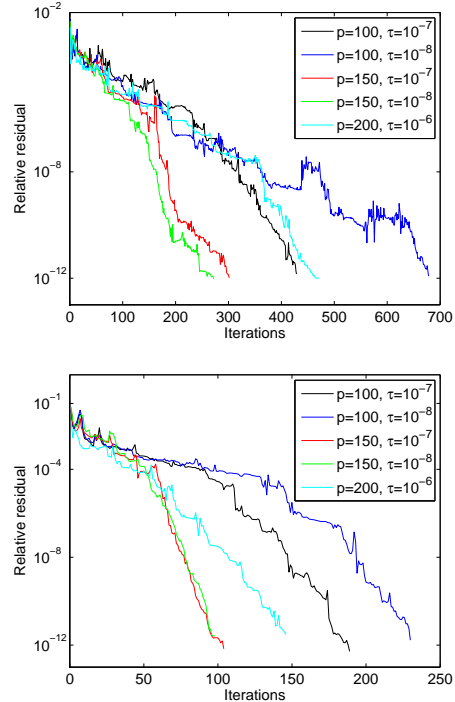


Fig. 2. Convergence diagram of relative residual. Top: SYMRCM reordering, Bottom: AMD reordering.

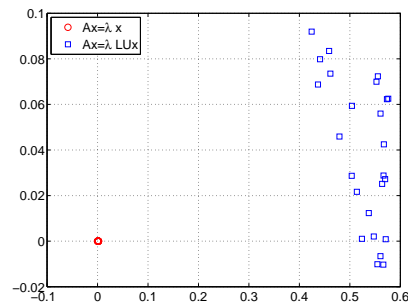


Fig. 3. The smallest 25 eigenvalues distribution of the original matrix and the preconditioned matrix.

### References

1. P. Meuris, W. Schoenmaker, and W. Magnus, *Strategy for electromagnetic interconnect modeling*, IEEE TCAD for IC **20** (2001), 753–762.
2. Yousef Saad, *ILUT: a dual threshold incomplete LU factorization*, Numer. Linear Algebra Appl. **1** (1994), no. 4, 387–402.
3. W. Schoenmaker and P. Meuris, *Geometry and computational electrodynamics-II selection of gauge condition*, Personal communication.
4. W. Schoenmaker, P. Meuris, W. Schilders, K.-J. van der Kolk, and N. van der Meijs, *Maxwell equations on unstructured grids using finite-integration methods*, Proceedings of the 12th SISPAD 2007, Vienna.

# Fast Linear Solver for Vector Fitting Method

M.M. Gourary<sup>1</sup>, S.G. Rusakov<sup>1</sup>, S.L. Ulyanov<sup>1</sup>, M.M. Zharov<sup>1</sup>, B.J.M. Mulvaney<sup>2</sup>, and B. Gu<sup>2</sup>

<sup>1</sup> IPPM, Russian Academy of Sciences, Moscow, Russia [gourary@ippm.ru](mailto:gourary@ippm.ru)

<sup>2</sup> Freescale Semiconductor Inc., Austin, Texas, USA [brian.mulvaney@freescale.com](mailto:brian.mulvaney@freescale.com)

**Summary.** A new algorithm to solve the least squares problem in Vector Fitting (VF) method is proposed. The algorithm is based on QR-decomposition that exploits the specific structure of the VF matrix. Numerical experiments confirmed the essential reduction of computational efforts. Besides a new solver provides better accuracy and requires much less memory than the standard Matlab sparse solver.

## 1 Introduction

The Vector Fitting (VF) method [1] approximates experimental data of vector transfer functions (TF) by rational functions defined by partial fractions

$$f_n(s) = \sum_m \frac{r_{mn}}{s p_m} + d_n + s h_n \quad (1)$$

VF is the iteration method. It iterates values of poles by solving the least squares (LS) problem with respect to the residues  $r_{mn}$ ,  $d_n$ ,  $h_n$ ,  $\tilde{r}_m$

$$\left( \sum_m \frac{\tilde{r}_m}{s_k - p_m} + 1 \right) \cdot f_n(s_k) = \sum_m \frac{r_{mn}}{s_k - p_m} + d_n + s_k h_n \quad (2)$$

Here  $m = 1 \dots N_p$  is pole index,  $n = 1 \dots N_{TF}$  is the index of TF component of the vector,  $s_k$  are frequencies of measured or simulated data ( $f_n(s_k)$ ),  $k = 1 \dots N_f$ .

In the paper we consider the most frequent case when for each frequency  $s_k$  samples  $f_n(s_k)$  are obtained for all TF ( $n$ ). In this case the size of (2) is  $N_s \times (N_p + N_{TF}(N_p + 2))$  where  $N_s$  is the total number of samples.

After solving (2) new values of poles are obtained as zeroes of  $\sigma$ -function

$$\sigma(s) = \sum_m \frac{\tilde{r}_m}{s_k - p_m} + 1 \quad (3)$$

But the application of VF to large size problems meet difficulties due to essential growth of computational efforts in solving (2) under the usage of the standard Matlab sparse solver. In this paper we present special-purpose algorithm to reduce the efforts. Reducing is achieved by taking into account specific structure of the linear system (2).

## 2 Algorithm Description

The system (2) can be represented as follows

$$Ax = b, \text{ where } x = [x_F \ x_S]^T, \quad (4)$$

$x_F$  is the vector of values  $r_{mn}$ ,  $d_n$ ,  $h_n$  and  $x_S$  is the vector of residues of  $\sigma(\tilde{r}_m)$ .

The system (4) is the overdetermined linear system, and its solution corresponds to the least squares (LS) problem  $\|Ax - b\|_2 \rightarrow \min$ . The Matlab solver obtains the solution by QR decomposition  $A = Q \cdot R$  with subsequent solving the upper triangle system  $Rx = Q^T \cdot b$ .

The effectiveness of the solver can be essentially improved due to the structure of  $A$  in (4)

$$A = [A_F \ A_S] \quad (5)$$

where  $N_s \times N_f(N_p + 2)$  matrix  $A_F$  has the block-diagonal form with  $N_{TF}$  identical blocks

$$A_F = \text{diag}(a, a, \dots, a) \quad (6)$$

The size of  $a$  is  $N_f \times (N_p + 2)$ . Due to such form the QR decomposition  $A_F = Q_F \cdot R_F$  can be easily performed by QR decomposition of each block  $a = q \cdot r$  taking into account that

$$R_F = \text{diag}(r, r, \dots, r) \quad (7)$$

$$Q_F = \text{diag}(q, q, \dots, q). \quad (8)$$

For convenience of the description we assume that the matrix  $A_S$  in (5) and rhs vector  $b$  also have block form (each block contains  $N_f$  rows)

$$A_S = [A_S^{(1)} \ A_S^{(2)} \ \dots \ A_S^{(N_{TF})}]^T, \quad (9)$$

$$b = [b^{(1)} \ b^{(2)} \ \dots \ b^{(N_{TF})}]^T$$

The following algorithm solves the problem (4).  
Algorithm with simple orthogonalization

1. QR decomposition of block  $a$

$$a = q \cdot r$$

2. Orthogonalize matrix with respect to  $Q_F$

$$H = Q_F^T \cdot A_S(H^{(k)} = q^T \cdot A_S^{(k)})$$

The result of orthogonalization is the matrix  $B_S$

$$B_S = A_S - Q_F \cdot H(B_S^{(k)} = A_S^{(k)} - q \cdot H^{(k)})$$

3. QR decomposition of  $B_S$

$$B_S = Q_S \cdot R_S$$

4. Solve upper triangle linear system

$$R_S \cdot x_S = b_S \text{ where } b_S = Q_S^T \cdot b$$

To perform VF iteration (3) it is sufficient to determine only subvector  $x_S$ , so after step 4 the algorithm can be stopped.

The experiments showed poor numerical properties of the algorithm due to insufficient accuracy of orthogonalization in step 2. In accurate arithmetic the orthogonalization must provide zero matrix  $Q_F^T \cdot Q_S = 0$ . But actually the values of entries of the matrix noticeably differ from zero, especially at higher orders. The reorthogonalization allows to essentially decrease values of matrix entries. In experiments with  $N_p = 20$  the maximum entry of the matrix product was reduced from 0.35 to  $6 \cdot 10^{-17}$ .

Thus, the algorithm was modified to include there orthogonalization.

#### Algorithm with reorthogonalization

First 3 steps are the same as in the Algorithm with simple orthogonalization.

4. Reorthogonalization.

$$H_1 = Q_F^T \cdot Q_S, B_{S1} = Q_S - Q_F \cdot H_1$$

5. QR decomposition of  $B_{S1}$

$$B_{S1} = Q_{S1} \cdot R_{S1}$$

6. Compute new upper triangle matrix

$$R_{S2} = R_{S1} \cdot H_1$$

7. Solve upper triangle linear system

$$R_{S2} \cdot x_S = Q_{S1}^T \cdot b$$

### 3 Testing Results

Experiments were performed for two data sets:

1. The s-parameters of transmission line obtained by EM simulation. LS systems in the tests correspond with initial poles. The systems are singular at these points.

2. The artificially generated TF with known poles and residues. LS systems in the test correspond with original poles, so the accurate solution must provide zero residual norm. The systems are non-singular.

The results are presented in Table 1, 2 for  $N_f = 200$  and different  $N_p, N_{TF}$ . The prefix at the value of  $N_{TF}$  indicates the data set: transmission line (T) or generated (G). The results of

the Matlab sparse solver and the new solver are presented in the form *Matlab/new = ratio*.

Table 1 presents the CPU time to perform one solving. One can see that new solver allows to reduce CPU time by the factor 50–100 for sufficiently large sizes of LS system. For very small sizes the Matlab solver provides less efforts than the new one but it occurs only in cases with CPU time less than 0.1sec.

Table 2 presents residual norms (LS values) for both solvers. For the generated example norms are given without factor  $10^{-12}$  due to space shortage. Note that LS algorithm minimizes the residual norm, so less value of the norm corresponds to the more accurate solution of the problem. Thus from Table 1 one can conclude that in all cases new solver provides better accuracy. The advantages of new solver increase with increasing the size of the systems.

**Table 1.** CPU Time, sec

$N_{TF}$	$N_p = 10$	$N_p = 20$	$N_p = 40$
T5	.01/.04 = 0.25	.37/.09 = 4.1	1/0.22 = 4.4
T10	0.6/0.09 = 6.8	1.6/0.17 = 9.2	4.8/0.4 = 12
T25	3.4/0.54 = 6.2	20/0.5 = 40	69/1.5 = 46
G6	0.1/0.05 = 2	0.3/0.1 = 3	0.7/0.33 = 2.1
G20	1.9/0.17 = 11.5	5.3/0.47 = 11	21/1 = 21
G30	5.2/0.3 = 17	20/0.95 = 21	96/1.4 = 68

**Table 2.** Residual norm ( $\|Ax - b\|$ )

$N_{TF}$	$N_p = 10$	$N_p = 20$	$N_p = 40$
T5	2/1.5 = 1.4	3.5/3.2 = 1.1	6.9/6.8 = 1.0
T10	3.3/2.3 = 1.45	5.6/5.0 = 1.1	11/0.43 = 25
T25	6.5/5.5 = 1.2	1.3/1.2 = 1.1	26/1.2 = 21
G6	2.4/0.9 = 2.6	11/3.4 = 3.2	15/5.1 = 2.9
G20	6.8/2.1 = 3.2	60/8.0 = 7.5	88/11 = 8.0
G30	17/4.3 = 3.9	111/9 = 12.6	197/21 = 9.3

The comparisons for higher sizes of LS problem were not performed due to insufficient memory in the run of the Matlab sparse solver. A new solver could be run for considerably higher sizes. Thus a new solver essentially reduces memory requirements.

### References

1. B. Gustavsen and A. Semlyen. Rational approximation of frequency domain responses by vector fitting. *IEEE Trans. Power Delivery*, vol. 14, no. 3, pp. 1052–1061, 1999.

# Evaluation of Domain Decomposition Approach for Compact Simulation of On-Chip Coupled Problems

Michal Dobrzynski, Jagoda Plata, and Sebastian Gim

Numerical Methods Laboratory, Faculty of Electrical Engineering, Politehnica University of Bucharest  
Spl. Independentei 313, 060042 Bucharest, Romania ( `d_michal`, `plata`, `seb` )@lmm.pub.ro

**Summary.** Continued device scaling into the nanometer region has given rise to new effects that previously had negligible impact but now present greater challenges to successful design of mixed-signal silicon. This paper evaluates Domain Decomposition strategies for compact simulation of on-chip coupled problems from a computational perspective using the recently completed CHAMELEON-RF software prototype on several standard benchmark structures.

## 1 Introduction

Incessant miniaturization of the transistor according to Moore's Law has lead to generational improvements in microprocessor technology [1]. However, continued scaling of devices into the nanometer region has given rise to new effects that had previously negligible impact but now present challenges to continued scaling. This has resulted in an increased complexity in engineering resources essential for a successful design. The ITRS roadmap suggests extreme scaling of CMOS technology until the 10 nm region and operating frequencies of up to 60 GHz in future generation devices [2]. At such close dimensions, fabrication process variations, substrate noise and EM coupling between circuit components make mixed-signal RF silicon designs extremely challenging.

Because of this, the CHAMELEON-RF project was conceived as a part of an initiative to address these issues [3]. The project is a research platform for the development of prototype tools and methodologies for comprehensive high accuracy modeling of on-chip electromagnetic effects using the Domain Decomposition (DD) approach and the concept of electromagnetic interconnectors or 'hooks'. They are essentially boundary conditions between ElectroMagnetic Circuit Elements (EMCEs), in order to manage the unprecedented complexity faced when designing next generation highly integrated mixed-signal architectures and System on Chip (SoC) applications.

The CHAMELEON-RF nano-EDA research platform incorporates a novel dual Finite Integral Technique (dFIT) EM field simulator with systematic All Level Model Order Reduction to keep

manageable the IC's complexity [4]. The method allows tractable multi-scale parameterized model extraction of coupled structures with the possibility of sensitivity analysis [5]. This approach has advantages over alternative approaches in full 3D field simulators - such as FEM, BEM etc. - which, although enable greater accuracy, are intractable for most practical real world designs.

In this paper, we evaluate the DD strategy for compact simulation of on-chip coupled problems from a computational perspective. By decomposing an intractable simulation domain into distinct domains connected by 'hooks', computational savings can be obtained by simulating non essential domains, such as the substrate or air layers, in just the MagnetoStatic (MS) regime, compared with a Full Wave (FW) simulation. This approach results in state space matrices with a reduced number of Degrees Of Freedom (DoFs).

The remaining sections of this paper are organized as follows. Section 2 presents the key points of the DD approach to manage the design complexity with a user specified accuracy. Validation results from a benchmark test case using the recently completed CHAMELEON-RF software prototype are presented in Section 3. The computational savings of the DD strategy is then demonstrated. The paper is finally concluded in Section 4.

## 2 Domain Decomposition Approach

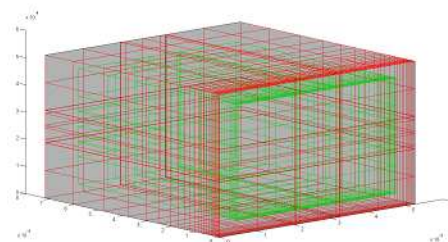


Fig. 1. Air domain

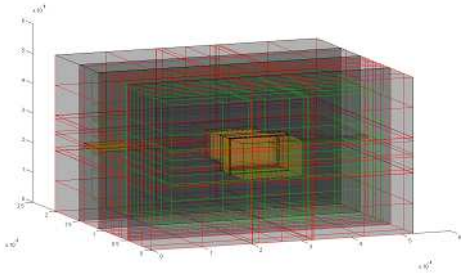


Fig. 2. SiO2 domain

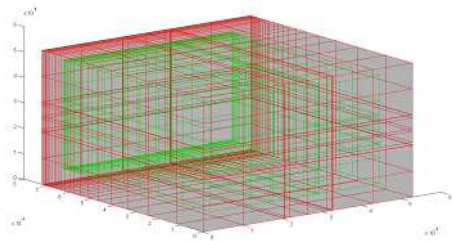


Fig. 3. Substrate domain

### 3 Validation Results

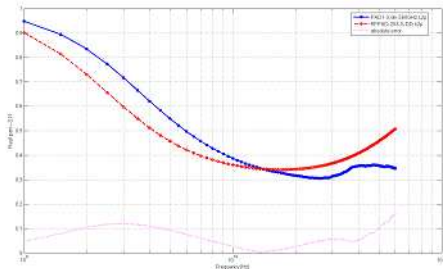


Fig. 4. Parameter S11

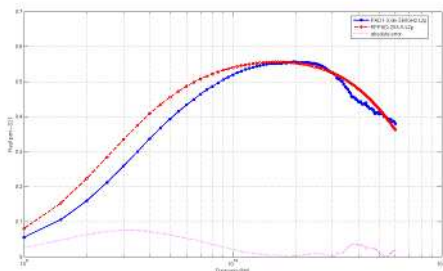


Fig. 5. Parameter S21

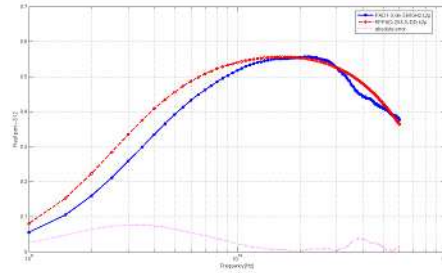


Fig. 6. Parameter S12

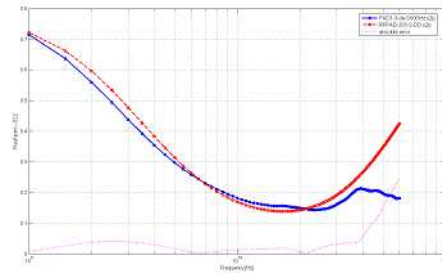


Fig. 7. Parameter S22

### 4 Conclusions

*Acknowledgement.* The authors would like to gratefully acknowledge support and insightful discussion with Prof. Daniel Ioan, Asc. Prof. Gabriela Ciuprina and the LMN Chameleon project team. The authors would also like to acknowledge the financial support offered by the European Commission under the Marie Curie Fellowship programme (FP6/EST3, FP6/ToK4nEDA).

### References

1. E. Mollick, *Establishing Moore's Law*, IEEE Annals of the History of Computing, vol. 28, pp. 62-75, 2006.
2. *ITRS Roadmap*, in [www.itrs.net](http://www.itrs.net).
3. J. Niehof, H. Janssen, and W. Schilders, *Comprehensive High-Accuracy Modeling of Electromagnetic Effects in Complete Nanoscale RF blocks: CHAMELEON RF*, presented at IEEE Workshop on Signal Propagation on Interconnects, 2006.
4. D. Ioan, G. Ciuprina, M. Radulescu, and E. Seebacher, *Compact modeling and fast simulation of on-chip interconnect lines*, IEEE Transactions on Magnetics, vol. 42, pp. 547-550, 2006.
5. D. Ioan, G. Ciuprina, and M. Radulescu, *Theorems of parameter variations applied for the extraction of compact models of on-chip passive structures*, presented at International Symposium on Signals, Circuits and Systems, 2005.

# A Novel Graphical Based Tool for Extraction of Magnetic Reluctances between On-Chip Current Loops

Sebastian Gim, Alexander Vasenev, Diana Mihalache, Alexandra Ștefănescu, and Sebastian Kula

Politehnica University of Bucharest, Electrical Engineering Dept., Numerical Methods Lab., Spl. Independentei 313, 060042, Romania [lmn@lmn.pub.ro](mailto:lmn@lmn.pub.ro)

**Summary.** Continued device scaling into the nanometer region has given rise to new effects that previously had negligible impact but now present greater challenges and unprecedented complexity to designing successful mixed-signal silicon. This paper presents a novel graphical tool for semi automatic extraction of magnetic reluctances between on-chip current loops. The novel graphical tool seamlessly integrates within the workflow of the CHAMELEON-RF software prototype developed.

## 1 Introduction

One of the major challenges in the nano electronic design industry (EDA) is the management of design complexity. As integrated circuits are being scaled into the nanometer scale, more and more functionality can be integrated on-die. However, this greater integration has also led to a number of design challenges, amongst them, the mutual coupling between interconnects, sub-circuits and functional blocks. All these need to be effectively managed by the EDA software in an efficient but intuitive manner to ensure a successful design. A coherent framework and comprehensive workflow model is needed.

There are several reasons to find an optimal procedure to support communication between the various data formats within a framework's workflow model and automating the tasks. The two most pressing reasons are reduction of human effort and elimination of user errors. Furthermore for the effective use of simulation software it is necessary to find a proper way for correct representation and transformation of initial data from schematic parameters and layout to simulation.

In this paper, we present a novel graphical tool and a proposed workflow model for the extraction of magnetic reluctances between on-chip current loops that integrates seamlessly with the Chamy electromagnetic simulator. Based on the principles identified previously, code for a novel graphical tool called Mag-Tris (Magnetic Tetris) was developed in LayoutEditor<sup>TM</sup> and Matlab<sup>TM</sup>. This novel graphical tool that is specially designed for Chamy software [1] is based on Matlab and can

effectively work with Matlab standard files (.mat) and ASCII files as an import format.

A few rules should be observed to solve this task. First, the solution should comply with requirements of Chamy. For example, it must support any Manhattan geometry structure and other principles, defined by the software. Secondly, it must be based on Graphical User Interface (GUI). A designer as the user can easily make modification, see and examine changes. Finally, implementation should be done by using non-commercial general public license.

The remaining sections of this paper are organized as follows. Section 2 describes the key features of Mag-Tris and presents the proposed workflow model and seamless integration with Chamy software. This approach is then applied to extracting the magnetic reluctances between fundamental current loops in a 24 GHz LNA. The results from this extraction process are then presented in Section 3.

## 2 Workflow for Multi-scale Compact Modeling

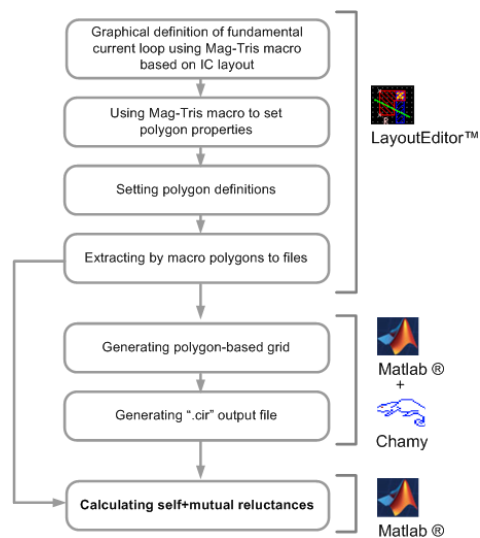


Fig. 1. Dataflow of Mag-Tris

### 3 Calculation of Magnetic Reluctances

The fluxes and magnetic voltages of the magnetic terminals are related by means of the linear relations:

$$\varphi = P v_m \quad (1)$$

where P is the nodal magnetic permeance matrix of magnetic terminals. The matrix P is a symmetric, diagonal dominant and positive defined matrix with positive diagonal entries and negative off-diagonal terms. By expressing voltage between two terminals as potentials difference, the branch reluctances in the complete polygonal topology are obtained

$$\begin{aligned} \varphi_{kj} &= \sum_{j,k=1}^n p_{jk} v_k = \sum_{j,k=1}^n G_{mjk} (v_j - v_k) \\ G_{mkj} &= -p_{kj} > 0, \quad G_{mk0} = \sum_{i=1}^n p_{ki} > 0 \\ R_{mkj} &= 1/G_{mkj}, \quad R_{mk0} = 1/G_{mk0} \end{aligned} \quad (2)$$

The test case consists on a 24GHz Car Radar LNA (Fig. 2). According to the modeling procedure described on short above, first a system of independent fundamental loops has to be identified before computation of magnetic reluctances. After that, in order to model the parasitic induced voltages, a dual magnetic circuit needs to be coupled to the original electrical circuit by means of controlled sources. The demo Chameleon soft-

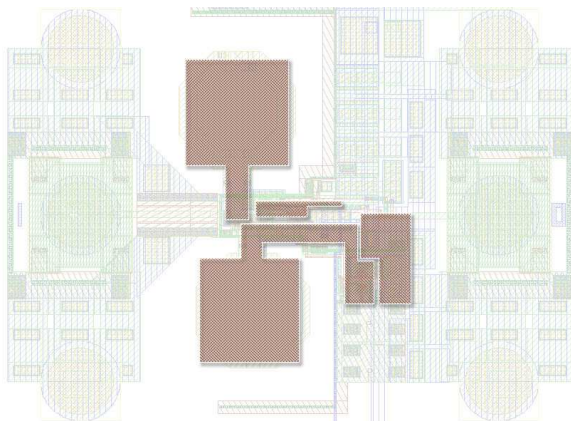


**Fig. 2.** Identified fundamental current loops in a 24 GHz LNA

ware prototype [1] was developed to extract the self and mutual reluctances between the hooks of Manhattan shapes (union of rectangles). The values are summarized in the tables below.

*Acknowledgement.* The authors would like to gratefully acknowledge support and insightful discussion with Prof. Daniel Ioan, Asc.Prof. Gabriela Ciuprina. The authors would also like to acknowledge the financial support offered by the European Commission

Fundamental Loop	Reluctance [1/H]
11	2.40630e+010
22	3.14921e+011
33	4.30807e+010
44	2.29307e+011
12	2.53936e+011
13	3.83304e+010
14	2.00067e+011
23	3.97307e+011
24	1.97317e+012
34	2.76450e+011

**Table 1.** Extracted self and mutual reluctances

under the Marie Curie Fellowship (FP6) programme and also the Romanian Cercetare de Excelenta in CEEEX/eEDA program. The views stated herein reflect only the author's views and the European Commission is not liable for any use that may be made of the information contained.

### References

1. CHAMELEON - RF website: [www.chameleon-rf.org](http://www.chameleon-rf.org)
2. E. Mollick, Establishing Moore's Law *IEEE Annals of the History of Computing* vol. 28, pp. 62-77, 2006.
3. J. Niehoff, H. Janssen and W. Schilders, Comprehensive High - Accuracy Modeling of Electromagnetic Effects in Complete Nanoscale RF blocks: CHAMELEON RF presented at *Signal Propagation on Interconnects, IEEE Workshop, 2006*

# Multiobjective Optimization Applied to Design of PIFA Antennas

Stefan Jakobsson, Björn Andersson, and Fredrik Edelvik

Fraunhofer-Chalmers Research Centre, Chalmers Science Park, SE-412 88 Göteborg, Sweden  
 stefan.jakobsson@fcc.chalmers.se, bjorn.andersson@fcc.chalmers.se,  
 fredrik.edelvik@fcc.chalmers.se

**Summary.** In this paper we apply multiobjective optimization to antenna design. The optimization algorithm is a novel respond surface method based on approximation with radial basis functions. This algorithm is combined with CAD and mesh generation software, electromagnetic solvers and a decision making platform for postprocessing. To demonstrate the procedure we optimize the geometric design and location of PIFA antennas on a ground plane.

## 1 Introduction

In many engineering applications there are often, at least partly, conflicting requirements. For example, for cars it is desirable to have both low fuel consumption and high effect. In antenna design the requirements can be based on S-parameters, functions of the directivity of the antenna, bandwidth, input impedance and/or other characteristics of the antenna.

In a current project, which is a collaboration between the Fraunhofer-Chalmers Centre and the Antenna Research Centre at Ericsson AB, we are developing new efficient optimization algorithms with the purpose of studying communication performance possibilities and limitations for multiple antennas within a limited area, such as a handheld terminal. The antenna elements are so-called printed inverted “F” antenna (PIFA) designs that have low profile, good radiation characteristics and wide bandwidths. This makes them an attractive choice for antenna designs of various wireless systems. In some recent works genetic and evolutionary algorithms have been applied to single objective optimization of PIFAs [3, 4].

In multiobjective optimization some requirements are formulated as objective functions and the ultimate goal is to find all *Pareto optimal solutions*: a solution is Pareto optimal if there is no other solution which is better in all objectives. As in other types of optimization, some requirements may also be formulated as constraints.

We have developed a multiobjective optimization algorithm based on radial basis functions to find an approximation of the *Pareto front* (the set

of Pareto solutions). In this paper the algorithm is demonstrated for optimization of the design of a PIFA antenna on a ground plane. The objective functions that should be minimized are the maximum return loss in a frequency band, the antenna height and the enclosed antenna area. The design parameters describe the geometry and location of the PIFA on the ground plane. The electromagnetic simulations are performed with the MoM solver from the software package efield<sup>®</sup> [1].

In post processing of results from multiobjective optimization it is interesting to analyze the trade-off between the different objectives. The main advantage of multiobjective optimization is that the decision making process takes place when all possibilities and limitations are known. A graphical tool to assist the decision maker in this process will be presented at the conference.

## 2 A multiobjective optimization algorithm

The algorithm, called *qualSolve*, is a respond surface method based on interpolation/approximation with radial basis functions and is described in detail in [2]. In each iteration of the optimization an interpolation/approximation (also called surrogate model) of every objective function is made based on all previous evaluations of the goal functions. By using for example evolutionary algorithms, an approximation of the Pareto front for the surrogate models is made. In the second step, a new evaluation point is chosen such that it maximizes a quality measure. This quality measure is a function both of the quality of the approximation (measured by the distance to an already evaluated point in the parameter space) and the interest to further explore an area of the parameter space. The latter is measured in terms of the distance to the Pareto front for the surrogate models in the objective space. The results of the algorithm are both a finite set of approximate Pareto points and coefficients for RBF expansions of the objective functions that can be

used for further post-processing. This enables the algorithm to use less evaluations of the objective functions compared to genetic algorithms. Since the evaluations of the objective functions involve time-consuming simulations this fact can greatly improve efficiency.

### 3 Results

To demonstrate the performance we perform an optimization of a PIFA antenna element located on a  $100 \times 45 \times 2$  mm ground plane, see Fig.1. For

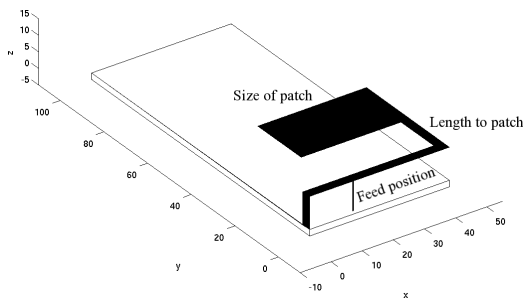


Fig. 1. The PIFA design used for optimization.

this case we have two objective functions which are the enclosed antenna area (convex hull) and the maximum return loss in the frequency interval 700 - 800 MHz. Both objective functions should be minimized. The optimization is carried out with respect to four design parameters: the size of the patch (length and width), the distance to the patch and the position of the feed, see Fig.1. All parameters are subjected to simple box constraints. Simulations are performed using the efield<sup>®</sup> MoM solver for five frequencies in the above given interval. The Pareto front is shown in Fig.2, where it can be clearly seen that these two objectives are conflicting.

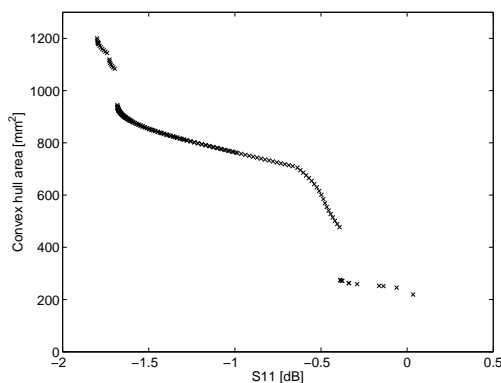


Fig. 2. The Pareto front for the RBF approximations of the maximum return loss in the frequency band and the enclosed antenna area.

This section will be extended with results for cases with more design parameters and also additional objectives such as the antenna height. To be able to change also other parameters of the antenna is clearly needed to e.g. obtain lower return loss.

### 4 Conclusions

A key property of the proposed algorithm is that the result is both a set of approximately Pareto-optimal solutions and also approximations of all objective function as expansions in radial basis function which can be used for further post-processing. This enables the algorithm to use less evaluations of the objective functions compared to e.g. genetic algorithms. Another key aspect is that all numerical simulations contain errors (noise) and to replace interpolations with approximations is a feature of the algorithm to make it more robust. Finally, by avoiding a weight-based trial-and-error strategy, where the objectives are weighted to form a single objective function, the decision of the optimal solution is postponed until all possibilities and limitations are known.

Future work includes to study multiple antennas on the same ground plane. The performance in the frequency band 2500-2700 MHz will also be optimized. Furthermore, the efficiency of the optimization algorithm in finding new evaluation points needs to be improved for cases with many design parameters.

*Acknowledgement.* Financial support for this work has been provided by the Swedish Foundation for Strategic Research (SSF) through the Gothenburg Mathematical Modeling Centre (GMMC).

### References

1. efield<sup>®</sup>. <http://www.efieldsolutions.com>.
2. S. Jakobsson, M. Patriksson, J. Rudholm, and A. Wojciechowski. A method for simulation based optimization using radial basis functions. Submitted for publication.
3. D.Y. Su, D.M. Fu, and Yu D. Genetic algorithms and Method of Moments for the design of pifas. *Progress in Electromagnetics Research Letters*, 1:9–18, 2008.
4. L. Zhan and Y. Rahmat-Samii. Optimization of PIFA-IFA combination in handset antenna designs. *IEEE Trans. on Antennas and Propagation*, 53:1770–1778, 2005.

# Space Mapping with Difference Method for Optimization

N. Serap Şengör and Murat Şimsek

Istanbul Technical University, Electrical and Electronics Engineering Faculty, Maslak, Istanbul, Turkey  
sengorn@itu.edu.tr, simsekmu@itu.edu.tr

**Summary.** The surrogate optimization techniques have to combine the high fidelity of fine models with speed of coarse models. In Space Mapping (SM) techniques, this is achieved by a mapping from the fine model input space to the coarse model input space. Space Mapping with Difference (SM-D) method is a variant of SM and in this work, how SM-D can be used in optimization will be presented.

## 1 Introduction

In Space Mapping (SM) techniques a mapping from the fine model input space to the coarse model input space [1] is constructed to obtain a surrogate model which would lessen the computational burden during design procedure. In Space Mapping with Difference (SM-D) method this mapping is revised by enlarging the dimension of the domain of the SM function,  $P(\cdot)$ , with the fine model output. With this adjustment, the need to evaluate the fine model was reduced and the simulation results obtained for different applications revealed that the extrapolation capability of the models obtained with SM-D were improved [2]. Enlarging the dimension of the SM function  $P(\cdot)$  with the already existing knowledge simplifies the process of constructing the function  $P(\cdot)$ . In previous works on SM-D [2], the SM function is constructed using feedforward Artificial Neural Network (ANN) structures and the method is used only to obtain surrogate models. In this work, in order to reveal the efficiency of the SM-D method and to achieve a simpler structure to be used in optimization processes during design procedure an affine function is constructed instead of ANN. In the next section, the SM-D method will be introduced and in the last section, the method will be used to solve wedge problem [1] and the results will be compared with classical SM, Aggressive SM (ASM) and Linear Inverse SM (LISM) [1, 3, 4].

## 2 Space Mapping with Difference Method

In most of SM techniques as ASM, and SM a mapping,  $P(\cdot)$ , from the fine model input space

to the coarse model input space is constructed as following:

$$x_c = P(x_f) \quad (1)$$

such that

$$R_c(P(x_f)) \approx R_f(x_f) \quad (2)$$

where,  $x_f$ ,  $x_c$ ,  $R_f(\cdot)$  and  $R_c(\cdot)$  are fine and coarse model design parameters and fine and coarse model responses, respectively [1]. As it can be followed from the block diagram given in Fig. 1 in SM-D method  $P_d(\cdot)$  maps fine model output  $R_f(x_f)$  and the fine model design parameter  $x_f$  to the difference between fine and coarse model design parameters  $x_d$  [2]. Thus a mapping from  $x_f$  to  $x_c$  is formed as following:

$$x_c = P_d(R_f(x_f), x_f) + x_f \quad (3)$$

Since the fine model response  $R_f(x_f)$  is already used, using it does not give rise to an extra computational burden. The steps to find the optimum

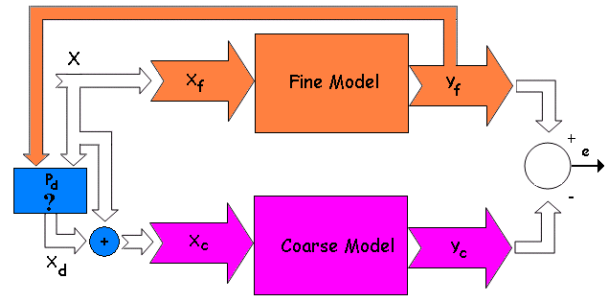


Fig. 1. The block diagram of SM-D method

design parameters of fine model  $\bar{x}_f$  giving rise to optimum fine model response  $\bar{Y}_f$  using coarse model responses  $R_c(\cdot)$  in SM-D method are the following:

- step 1: choose  $Y_c^* = \bar{Y}_f$
- step 2: find  $x_c^*$  from  $x_c^* = \min_{x_c} \|Y_c^* - R_c(x_c)\|$
- step 3: set  $x_f^{(i)} = x_c^*$
- step 4: find  $Y_f^{(i)} = R(x_f^{(i)})$
- step 5: if  $\|Y_f^{(i)} - Y_c^*\| \leq \varepsilon$  then  $\bar{x}_f = x_f^{(i)}$  else go to step 6
- step 6: find  $x_c^{(i)}$  from  $x_c^{(i)} = \min_{x_c} \|Y_f^{(i)} - R_c(x_c)\|$

- step 7: form  $P_d^{(i)} = QD^{-1}$  where  $Q \doteq [x_c \ -x_f]$ ,  $D \doteq [1 \ x_f]^T$
- step 8:  $i = i + 1$
- step 9: set  $x_f^{(i)} = (P_d^{(i)})^{-1}(x_c^*)$  from  $x_f^{(i)} = \min_{x_f} \|x_c^* - P_d(x_f)\|$  and go to step 4

### 3 Simulation Results

In order to demonstrate the efficiency of the SM-D method in optimization a simple problem defined in [1] and given in Fig. 2 is solved with classical SM, LISM, ASM and SM-D and compared with the results obtained with SM-D. In all these techniques linear SM mapping is constructed. The results are summarized in Table.

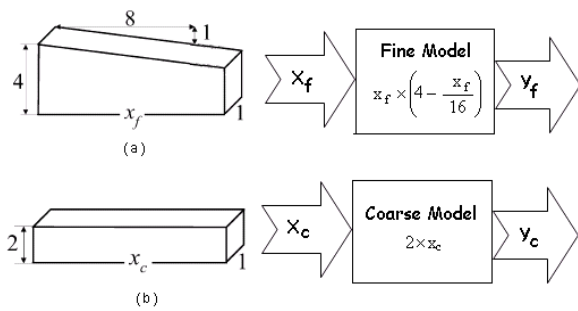


**Fig. 2.** Wedge problem [1]: (a) Fine model (b) Coarse model.

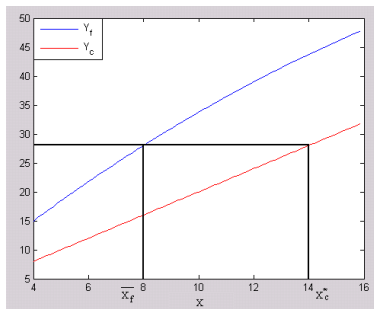


**Fig. 3.** The difference between the fine model and coarse model optimum values.

Since the difference between the fine model and coarse model optimum value is large as shown in Fig. 3, the convergence of SM and LISM methods took longer than ASM and SM-D methods. Even though the results of ASM and SM-D methods are very much alike, ASM method diverge for small  $\varepsilon$  values.

### 4 Conclusions

In this work, SM-D method is utilized for optimization. The simulation results obtained for

**Table 1.** Comparison of SM-D with SM, LISM and ASM

Methods	$\bar{x}_f = 8$	$ \bar{x}_f - x_{opt} $	$\bar{Y}_f = 28$
SM	7.9997	3.32e-004	27.9990
Iteration	123		
LISM	7.9997	3.31e-004	27.9990
Iteration	123		
ASM	8.0002	1.50e-004	28.0005
Iteration	6		
SM-D	7.9997	2.73e-004	27.9992
Iteration	3		

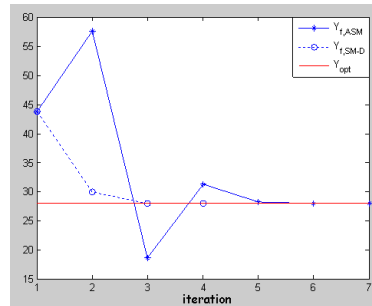


**Fig. 4.** Convergence of ASM and SM-D.

wedge problem shows that the method is efficient compared to classical SM, LISM, ASM. Since  $P_d(\cdot)$  is an affine function, the computational complexity of the method is less than the original SM-D proposed in [2]. The efficiency of the method will be further investigated with different applications.

### References

1. J.W. Bandler, Q.S. Cheng, S.A. Dakroury, S.A.Mohamed, M.H. Bakir, K.Madsen and J. Sondergaard. Space Mapping : The State of the Art. *IEEE Trans. on Microwave Theory and Tech.*, 52:337–361, 2004.
2. M. Simsek and N.S. Sengor. A New Modelling Method Based on Difference between Fine and Coarse Models Using Space Mapping. Abstract Book of 2nd Int. Workshop SMSMEO-06, 64:65, 2006.
3. J.W. Bandler, R.M. Biernacki, S.H. Chen, R.M. Hemmers and K. Madsen. Electromagnetic Optimization Exploiting Aggressive Space Mapping. *IEEE Trans. on Microwave Theory and Tech.*, 43:2847–2882, 1995.
4. J.E. Rayas-Sánchez, F. Lara-Rojo and E. Martinez-Guerrero. A Linear Inverse Space-Mapping (LSIM) Algorithm to Design Linear and Nonlinear RF and Microwave Circuits. *IEEE Trans. on Microwave Theory and Tech.*, 53:960–368, 2005.

# Modification of Space Mapping with Difference Method for Inverse Problems

Murat Şimşek and N. Serap Şengör

Istanbul Technical University, Electrical and Electronics Engineering Faculty, Maslak, Istanbul, Turkey  
simsekmu@itu.edu.tr, sengorn@itu.edu.tr

**Summary.** The surrogate methods have been used to ease the computational burden in different disciplines. In this work, a previously proposed surrogate method, namely, Space Mapping with Difference is modified to solve the inverse problems. The efficiency of the method is demonstrated solving the shape reconstruction of a conducting cylinder.

## 1 Introduction

The distinctive feature of surrogate methods are their capability of combining the computational efficiency of a coarse model with the accuracy of the fine model and in Space Mapping (SM) technique this is provided through a mapping from the fine model input space to the coarse model input space [1]. In Space Mapping with Difference (SM-D) method this mapping has been adjusted by enlarging the dimension of the domain of the mapping with the coarse model output. With this adjustment, the need to evaluate the fine model was reduced and the simulation results obtained for different applications revealed that the extrapolation capability of the models obtained with SM-D were improved [2,3]. In this work, SM-D method is modified for inverse problems and this new method is named Space Mapping with Inverse Difference (SM-ID). In SM-ID, instead of coarse model an inverse coarse model which is generated as a multilayer perceptron is used. The mapping between coarse model and fine model parameter spaces are constructed similar to Linear Inverse Mapping (LISM) algorithm given in [4] but in the proposed method, parameter extraction step is no longer necessary to build an appropriate space mapping function  $P(\cdot)$ . In the next section, the proposed method will be introduced and in the third section, the method will be used to solve shape reconstruction of a conducting cylinder [5].

## 2 Space Mapping with Inverse Difference

In design problems, the main concern is to determine the design parameters  $x_{design}$  which mini-

mize an objective function defined over responses  $R(x_{design})$  of design parameters  $x_{design}$ . In inverse problems, main concern is to determine the some parameters  $x$  of the problem given responses  $R(x)$ . As both problems are synthesis problems the solution is not unique and furthermore for the inverse problems it can be ill-posed.

It has been shown that, SM-D method solves the design problems with efficiency. It is based on forming a mapping between fine and coarse model design parameters  $x_f$  and  $x_c$ , respectively. While forming this mapping, a function  $P_d(\cdot)$  is constructed which maps coarse model output  $R_c(x_f)$  and the fine model design parameter  $x_f$  to the difference between fine and coarse model design parameters  $x_d$  [2,3]. Thus the mapping formed maps  $x_f$  to  $x_c$  via  $P_d(\cdot)$  as following:

$$x_c = P_d(R_c(x_f), x_f) + x_f \quad (1)$$

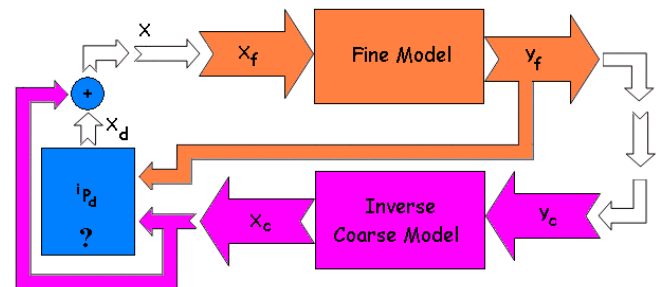


Fig. 1. The block diagram of SM-ID method

As it can be followed from Fig. 1, SM-D method is modified in two ways; first inverse coarse model is used instead of coarse model. In most applications, there will not be possibility of obtaining an inverse coarse model, in such cases using a well-known feedforward neural network structure as multilayer perceptron would be suitable. The second modification is in constructing the SM function  $P(\cdot)$ , as the relation in SM-ID will be the inverse of the relation set up in SM-D. SM function  ${}^iP_d(\cdot)$  will resemble that of LISM algorithm [4] but since inverse coarse model is

used there is no need for parameter extraction step [1, 4] The SM function  ${}^iP_d(\cdot)$  maps  $Y_f$ ,  $x_c$  to  $x_d$  as following:

$$x_f = {}^iP_d(Y_f, x_c) + x_c \quad (2)$$

In this work, the SM function  ${}^iP_d(\cdot)$  is a linear mapping. As  ${}^iP_d(\cdot)$  is linear and since there is no need for parameter extraction the computational burden is decreased compared to other SM methods.

### 3 Simulation Results for Reconstruction of a Conducting Cylinder

The reconstruction of a conducting cylinder problem is considered and the results obtained are compared with results obtained by Artificial Neural Networks (ANN). The inverse coarse model in SM-ID is trained with different number of data, and in the figures the test set results are exposed. The ANN's trained have 20 inputs, nine outputs, where the inputs are the real and imaginary components of scattered electric field obtained at 10 different positions and the outputs are the Fourier series coefficients of the geometrical shape of the conducting cylinder. It can be followed from

**Table 1.** Comparison of SM-ID results with ANN

	Max Error	Mean Error
IANN-50	0.22067	0.06715
SM-ID-50 iteration : 5	0.03762	0.00868
IANN-100	0.11889	0.05266
SM-ID-100 iteration : 4	0.00389	0.00081
IANN-200	0.10386	0.04285

the table and figures that SM-ID results outperforms the ANN results and as the number of data used increases, the iterations needed to construct  ${}^iP_d(\cdot)$  decreases

*Acknowledgement.* The authors thank Necmi Serkan Tezel for introducing the inverse scattering problem.

### References

1. J.W. Bandler, Q.S. Cheng, S.A. Dakroury, S.A.Mohamed, M.H. Bakir, K.Madsen and J. Sondergaard. Space Mapping : The State of the Art.

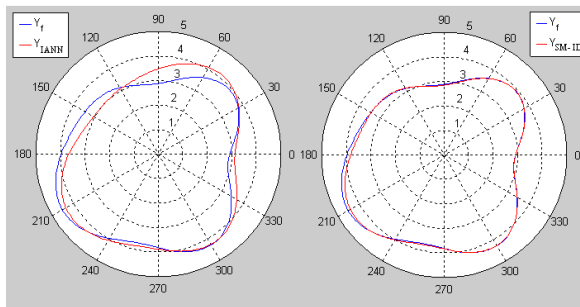


**Fig. 2.** On the left ANN result and on the right SM-ID result is given for 50 data.

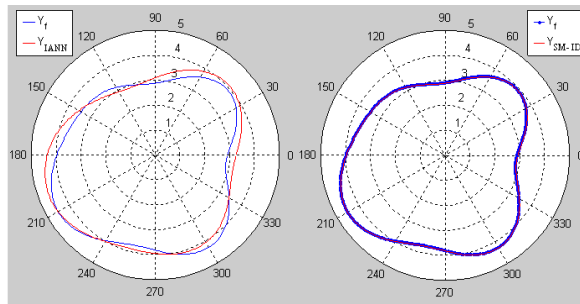


**Fig. 3.** On the left ANN result and on the right SM-ID result is given for 100 data

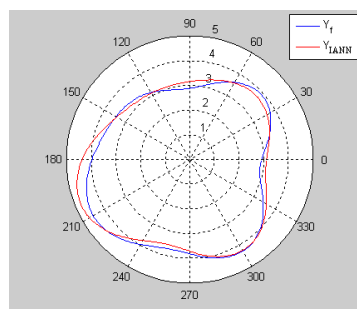


**Fig. 4.** Only the ANN result is given for 200 data as SM-ID fits almost perfectly for 100 data

2. M. Simsek and N.S. Sengor. A New Modelling Method Based on Difference between Fine and Coarse Models Using Space Mapping. Abstract Book of 2nd Int. Workshop SMSMEO-06, 64:65, 2006.
3. M. Simsek. Novel Methods for Surrogate Optimization and Modeling Using Space Mapping Techniques. Ph. D. Thesis Report 2, Istanbul Technical University, 2007.
4. J.E. Rayas-Sánchez, F. Lara-Rojo and E. Martinez-Guerrero. A Linear Inverse Space-Mapping (LSIM) Algorithm to Design Linear and Nonlinear RF and Microwave Circuits. *IEEE Trans. on Microwave Theory and Tech.*, 53:960–368, 2005.
5. N.S. Tezel and C. Şimşek. Neural Network Approach to Shape Reconstruction of a Conducting Cylinder. *Istanbul University, Journal of Electrical and Electronics Eng.*, 7:299–304, 2004.

# Exploiting Model Hierarchy in Semiconductor Design using Manifold-Mapping

D.J.P. Lahaye<sup>1</sup> and C. Drago<sup>2</sup>

<sup>1</sup> DIAM - Delft Institute of Applied Mathematics, Technical University of Delft, Mekelweg 4, 2628 CD Delft, The Netherlands [d.j.p.lahaye@tudelft.nl](mailto:d.j.p.lahaye@tudelft.nl),

<sup>2</sup> Dipartimento di Matematica e Informatica, Università di Catania, Città Universitaria, viale Andrea Doria 6, 95125 Catania, Italy [drago@dmf.unict.it](mailto:drago@dmf.unict.it)

**Summary.** In this work we exploit a model hierarchy for the optimal control of semiconductors using the manifold-mapping technique. Herein the drift diffusion and energy transport models act as coarse and fine model, respectively. The advantage of this approach is that it allows for the efficient optimization of the energy transport model without having to implement its adjoint.

## 1 Introduction

The interest in optimal control for semiconductor design has attracted considerable recent attention in both the engineering and applied mathematics community. A major objective in the design is to improve the current flow over some contacts, for fixed applied voltages, by a slight change of the device doping profile. In most applications the design problem is addressed empirically, on the knowledge and experience of electrical engineer. Although this problem can be clearly tackled by an optimization approach, only recently efforts were made to solve the design problem via optimization techniques. Approaches range from the standard black box optimization methods, which in general have an high computational cost, since they require many solvers of the forward model, to the adjoint method, recently proposed in the field of optimal semiconductor design, which provides good results by drastically reducing the amount of computational efforts. The adjoint model has been proposed and analyzed for the drift-diffusion model. Meanwhile the same approach was extended to the energy-transport model. Comparisons between the new optimal designs with the ones obtained based on the drift diffusion model were presented in [3]. Moreover in [3] the idea to exploit this classical model hierarchy to speed up the convergence of the optimization algorithms by using the space mapping approach was introduced for the first time in the field of optimal control in semiconductor design. In this work we replace

the aggressive space-mapping technique by the recently proposed and equally efficient manifold-mapping variant [2] as it has better theoretical properties.

## 2 Semiconductors Models: Drift Diffusion and Energy Transport

Presently, there is a whole hierarchy of semiconductor models available ranging from microscopic models, like the Boltzmann-Poisson or the Wigner-Poisson model, to macroscopic ones, like the drift diffusion, the energy transport and the hydrodynamic model. The drift diffusion model is the simplest and most popular macroscopic one, widely used in commercial simulation packages as it allows for efficient numerical study of charge transport in many case of practical relevance. The unipolar Drift Diffusion model (DD) consists of continuity equations for electron density  $n$  coupled to Poisson's equation for the electrostatic potential  $V$

$$\begin{aligned} \operatorname{div} J_n &= 0, & J_n &= (\nabla n - n \nabla V) \\ \lambda^2 \Delta V &= n - C \end{aligned}$$

where  $C$  is the doping profile,  $\lambda^2$  the Debye length and  $J_n$  denotes the electron current density. On the other hand, in today semiconductor technology, the miniaturization of devices is more and more progressing. As a consequence the simulation of sub-micron semiconductor devices requires advanced transport models. Because of the presence of very high and rapidly varying electric fields, phenomena occur which cannot be described by means of drift-diffusion model, that does not incorporate energy as a dynamical variable. The energy-transport model takes into account also the thermal effects related to the electron flow through the semiconductor crystal. The dimensionless Stratton's energy transport (ET) model consists of continuity equations for electron density  $n$  and the temperature  $T$ , coupled to Poisson's equation reads

$$\begin{aligned}\operatorname{div} J_n &= 0, & J_n &= -\left(\nabla n - \frac{n}{T} \nabla V\right) \\ \operatorname{div} S &= J_n \cdot \nabla V + W(n, T) \\ S &= -\frac{3}{2} (\nabla(nT) - n \nabla V) \\ \lambda^2 \Delta V &= n - C\end{aligned}$$

where  $J_n$  is the carrier flux density,  $S$  the energy flux density,  $W$  the energy relaxation term  $W(n, T) = -\frac{3}{2} \frac{n(T-1)}{\tau_0}$ .

### 3 The Design Problem

Let  $\bar{C}$  be a given reference doping profile and let  $\Gamma_O$  be a portion of the Ohmic contacts  $\Gamma_D$ , at which we can measure the total density current  $J$ , obtained by solving the DD or ET system. At the contact  $\Gamma_O$  we prescribe a gained current  $I^*$  and allow deviations, in some suitable norm, of the doping profile from  $\bar{C}$  in order to gain this current flow. In other words we intend to minimize cost functionals of the form [3]

$$\frac{1}{2} \left| \int_{\Gamma_O} J_n d\nu - I^* \right|^2 + \frac{\gamma}{2} \int_{\Omega} |\nabla(C - \bar{C})|^2 dx$$

where  $\gamma > 0$  allows to balance the effective cost.  $C$  enters as a source term in the DD and ET models and plays the role of our design variable. The DD and ET models are interpreted as a constraint, to the minimization problem, determining the density current  $J_n$ , by the state variables  $(n, V)$  or  $(n, T, V)$  respectively.

### 4 The Manifold-Mapping Technique

The manifold-mapping technique [2] exploits coarse model information and defines a surrogate optimization problem whose solution do coincide with  $x_f^*$ . The key ingredient is the manifold-mapping function between the coarse and fine model image spaces  $\mathbf{c}(X) \subset \mathbb{R}^m$  and  $\mathbf{f}(X) \subset \mathbb{R}^m$ . This function  $\mathbf{S} : \mathbf{c}(X) \mapsto \mathbf{f}(X)$  maps the point  $\mathbf{c}(\mathbf{x}_f^*)$  to  $\mathbf{f}(\mathbf{x}_f^*)$  and the tangent space of  $\mathbf{c}(X)$  at  $\mathbf{x}_f^*$  to the tangent space of  $\mathbf{f}(X)$  at  $\mathbf{x}_f^*$ . It allows the surrogate model  $\mathbf{S}(\mathbf{c}(\mathbf{x}))$  and the manifold-mapping solution to be defined as follows: find  $\mathbf{x}_{mm}^* \in X$  such that

$$\mathbf{x}_{mm}^* = \operatorname{argmin}_{\mathbf{z} \in X} \|\mathbf{S}(\mathbf{c}(\mathbf{z})) - \mathbf{y}\|. \quad (1)$$

The manifold-mapping function  $\mathbf{S}(\mathbf{x})$  is approximated by a sequence  $\{\mathbf{S}_k(\mathbf{x})\}_{k \geq 1}$  yielding a sequence of iterands  $\{\mathbf{x}_{k,mm}\}_{k \geq 1}$  converging to  $\mathbf{x}_{mm}^*$ . The individual iterands are defined by coarse model optimization: find  $\mathbf{x}_{k,mm}^* \in X$  such that

$$\mathbf{x}_{k,mm} = \operatorname{argmin}_{\mathbf{z} \in X} \|\mathbf{S}_k(\mathbf{c}(\mathbf{z})) - \mathbf{y}\|. \quad (2)$$

At each iteration  $k$ , the construction of  $\mathbf{S}_k$  requires the singular value decomposition of the matrices  $\Delta C_k$  and  $\Delta F_k$  of size  $m \times \min(k, n)$  whose columns span the coarse and fine model tangent space in the current iterand, respectively. Denoting these singular value decompositions by

$$\Delta C_k = U_{k,c} \Sigma_{k,c} V_{k,c}^T \quad \Delta F_k = U_{k,f} \Sigma_{k,f} V_{k,f}^T,$$

we introduce the updated objective  $\mathbf{y}_k$  as

$$\mathbf{y}_k = \mathbf{c}(\mathbf{x}_k) - \left[ \Delta C_k \Delta F_k^\dagger + (I - U_{k,c} U_{k,c}^T) \right] \cdot (\mathbf{f}(\mathbf{x}_k) - \mathbf{y}),$$

where superscript  $\dagger$  denotes the pseudo-inverse. With this notation, the problem (2) can shown be to be asymptotically equivalent to: find  $\mathbf{x}_{k,mm}^* \in X$  such that

$$\mathbf{x}_{k,mm} = \operatorname{argmin}_{\mathbf{z} \in X} \|\mathbf{c}(\mathbf{z}) - \mathbf{y}_k\| \quad (3)$$

By construction  $\mathbf{x}_{mm}^* = x_f^*$ .

### 5 Numerical Results

We test the performance of the MM algorithm for a one-dimensional  $n^+ - n - n^+$  ballistic diode, which is a simple model for the channel of a MOS transistor. We tried to achieve an amplification of the current of 50% for different value of the applied voltage ranging between  $\bar{U} = 0.026$  V and  $\bar{U} = 0.52$  V. The current voltage characteristics (IVC) before and after optimization are shown in Fig. 1.

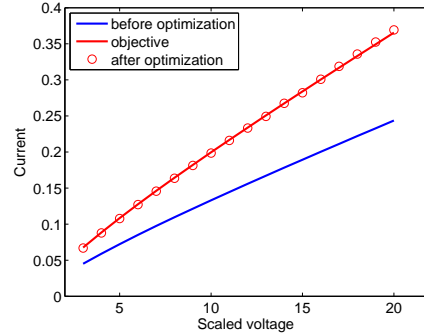


Fig. 1. Resulting IVCs

### References

1. Bandler et al. Space Mapping: The State of the Art *IEEE Trans. on Microwave Theory and Techniques*, 52(1):337–361, 2004
2. Echeverría, D. and Hemker, P. W. Space Mapping and Defect Correction *Comp. Methods in Appl. Math.*, 5(2):107–136, 2005.
3. Drago C. D. and Pinnau, R. Optimal Dopant Profiling based on Energy Transport Semiconductor Models, *Math. Mod. Meth. Appl. Sc.* 18(2):195–214, 2008.

# An *hp*-Adaptive Strategy for the Solution of the Exact Kernel Curved Wire Pocklington Equation

D.J.P. Lahaye

DIAM - Delft Institute of Applied Mathematics  
 Department of Electrical Engineering, Mathematics and Computer Science  
 TU Delft, Mekelweg 4, 2628 CD Delft, The Netherlands  
 d.j.p.lahaye@tudelft.nl

**Summary.** In this paper we introduce an adaptive method for the numerical solution of the Pocklington integro-differential equation with exact kernel for the current induced in a smoothly curved thin wire antenna. The *hp*-adaptive technique is based on the representation of the discrete solution, which is expanded in a piecewise *p*-hierarchical basis. The key element in the strategy is an element-by-element criterion that controls the *h*- or *p*-refinement. Numerical results demonstrate both the simplicity and efficiency of the approach.

## 1 Introduction

In this study we treat electric field scattering from thin curved wire antennas. The current that an incident electrical field induces in the antenna is computed by solving the Pocklington integro-differential equation [4]. In engineering literature the reduced kernel approximation is typically used. However, if very fine meshes are used for the discretization, the ill-posedness of the resulting problem causes spurious oscillations in the numerical solution, which prevents the computation of highly accurate solutions [3, 5]. We therefore treat the computationally more challenging exact kernel model [1].

We consider a smoothly curving, non self-intersecting thin wire antenna of arbitrary shape with total length  $L$ , and circular cross-section with radius  $a$ , where  $a \ll L$ . We denote the arc length variables along the axis and the boundary of the cross-section by  $s$  and  $\theta$ , respectively. Let the symbols  $R$ ,  $\hat{\mathbf{s}}$  and  $\frac{d}{ds}$  represent the distance between two points on the lateral surface of the wire, the unit tangential vector and derivative along the wire, respectively. The wire antenna is assumed to be illuminated by a time-harmonic electrical field plane wave with angular frequency  $\omega$ , wavenumber  $k = \frac{\omega}{c}$  and wavelength  $\lambda = \frac{2\pi}{k}$ . The wavelength is assumed to be large compared with wire radius, i.e.  $a/\lambda \ll 1$ . The tangential component of the incident field will be denoted by  $E_s^{inc}(s, \theta)$ . We furthermore introduce the integration kernel

$$G(s, \theta, s', \theta') = G(R(s, \theta, s', \theta')) = \frac{\exp(-jkR)}{4\pi R},$$

where  $j^2 = -1$ . The Pocklington's integral equation for the current induced in the antenna then reads:

$$\begin{aligned} k^2 \int_{s'} \int_{\theta'} \mathbf{s} \cdot \mathbf{s}' \frac{I(s', \theta')}{2\pi} G(\|\mathbf{r} - \mathbf{z}\|) ds' d\theta' \\ + (\mathbf{s} \cdot \nabla_{\mathbf{r}}) \int_{s'} \int_{\theta'} \frac{\partial}{\partial s'} I(s', \theta') \frac{G(\|\mathbf{r} - \mathbf{z}\|)}{2\pi} ds' d\theta' \\ = -j\omega \epsilon \mathbf{s} \cdot \mathbf{E}^{in}(\mathbf{r}) \end{aligned}$$

The finite element (FE) technique proposed in this paper achieves high accuracy at moderate computational cost by automatic adaption of both the mesh width (*h*-adaptation) and the polynomial degree (*p*-adaptation) of the approximation to the local smoothness of the solution. The discrete solution is expanded in a piecewise hierarchical basis [6], consisting of the standard linear FE shape functions enriched with higher order bubble functions. Apart from the treatment of a smooth arbitrarily curved wire, a new aspect in this work is the element-by-element criterion for *h*- or *p*-refinement. As shown below, this criterion is based on the behaviour of the coefficients of the discrete solution in the hierarchical basis representation.

## 2 The *hp*-Adaptive Strategy

The *hp*-adaptive strategy in this paper relies on an *p*-hierarchical basis and makes use of the fact that for smooth functions the expansion coefficients—on a single element in a piecewise polynomial approximation—are supposed to decrease as a geometric sequence.

This observations lead to the following *hp*-adaptive strategy. On a (non-uniform) mesh we determine in each interval a *p*-hierarchical representation of the solution with a sufficient number of terms. On each interval the convergence of the approximation is studied. If the rate of decrease

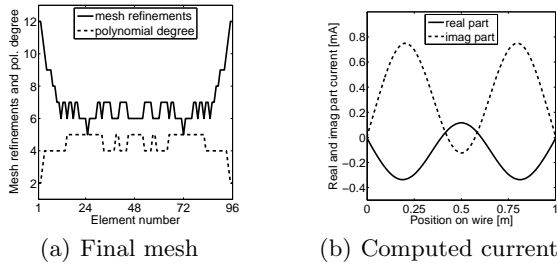


**Fig. 1.** Results for a receiving straight wire antenna. Left: the number of mesh refinement steps and the polynomial degree yielding an  $L^1$ -error smaller than  $TOL = 5e-8$  Am. Right: the real and imaginary part of the computed current.

of the coefficients is fast enough, then the series is truncated such that an a-priori given tolerance criteria is satisfied. If the rate of decrease is not fast enough, then the interval is split into two smaller intervals of equal size and a new approximation is computed. The process will stop after a finite number of iterations, except in those areas where derivatives are unbounded. At such singular locations the process can be stopped by introducing a limit for the minimal allowed mesh-size. Details of the strategy are explained in [2].

### 3 Numerical Results

#### 3.1 Current in Receiving Antenna

In the first experiment, we consider the computation of the current in a straight wire antenna of length  $L = 1$  m and radius  $a = 0.001$  m, induced by a plane wave excitation of frequency  $f = 500$  MHz and propagation vector perpendicular to the axis of the antenna. We use an  $L^1$ -error bound introduced as the stopping criterium in the mesh refinement process. As initial discretization we choose a uniform mesh with 16 second degree elements having in total 33 (i.e.,  $17 + 16$ ) degrees of freedom. Imposing a tolerance  $TOL = 5e-8$  Am, this results in eight adaptive refinement steps and a mesh of 96 elements with 422 degrees of freedom. In Figure 1(a) for the final mesh we plot the number of local mesh refinements and polynomial order. In Figure 1(b) we show the computed current. The mesh shows to have been  $h$ -refined near the end-point singularities and to have been  $p$ -refined where the current is a smooth function.

#### 3.2 Current in Emitting Antenna

This time we consider the computation of the current in an emitting straight antenna. Length and radius are as in the previous example. Now the

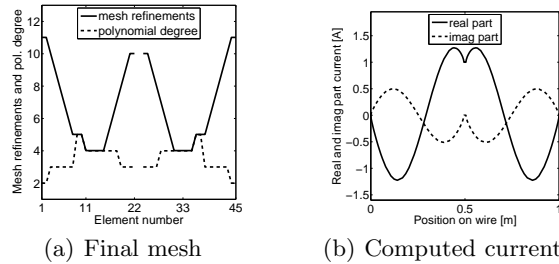


**Fig. 2.** Results for an emitting straight wire antenna. Left: the number of mesh refinement steps and the polynomial degree yielding an  $L^1$ -error smaller than  $TOL = 3e-3$  Am. Right: the real and imaginary part of the computed current.

antenna has a gap of 0.01 m in its middle where a current source of 1 A is impressed. Starting from a piecewise second degree solution on a uniform mesh with eight elements on either side of the gap and imposing a tolerance  $TOL = 1e-3$  Am, seven adaptive refinement steps result in a mesh of 45 elements with 154 degrees of freedom. The final  $hp$ -mesh and computed current are shown in Figure 2. Both the end-point singularities and the singularities at the boundaries of the gap are clearly resolved by low order small elements.

Numerical results for a smoothly curved antenna can be found in [2].

*Acknowledgement.* This research was supported by the Dutch Ministry of Economic Affairs through the project IOP-EMVT 04302.

### References

1. P. J. Davies, D. B. Duncan, and S. A. Funken. Accurate and Efficient Algorithms for Frequency Domain Scattering from a Thin Wire. *J. Computational Physics*, 168:155–183, 2001.
2. P. W. Hemker and P. Lahaye, D. J. An  $hp$ -Adaptive Strategy for the Solution of the Exact Kernel Curved Wire Pocklington Equation. *CMAM*, 8(1):39–59, 2008.
3. B. P. Rynne. The Well-Posedness of the Integral Equations for Thin Wire Antennas. *IMA J. Applied Math.*, 49:35–44, 1992.
4. A. G. Tijhuis, P. Zhongqiu, and A. R. Bretones. Transient Excitation of a Straight-Wire Segment: a New Look to an Old Problem. *IEEE Trans. Antennas Propagat.*, 40(10):1132–1146, 1992.
5. M. C. van Beurden and A. G. Tijhuis. Analysis and Regularization of the Thin-Wire Integral Equation With Reduced Kernel. *IEEE Trans. Antennas Propagat.*, 55(1):120–129, 2007.
6. H. Yserentant. Hierarchical basis. In R.E. O’Malley, editor, *Proceedings of the Second International Conference on Industrial and Applied Mathematics (ICIAM 91)*, pages 256–276, 1992.

# Sensitivity Analysis of Capacitance for a TFT-LCD Pixel

Ta-Ching Yeh, Hsuan-Ming Huang, and Yiming Li<sup>1</sup>

National Chiao Tung University, 1001 Ta-Hsueh Rd., Hsinchu 300, Taiwan <sup>1</sup>yml@faculty.nctu.edu.tw

**Summary.** In this paper, a computational statistics method for sensitivity analysis of capacitance is implemented for a thin-film transistor liquid-crystal display (TFT-LCD) Pixel. Based on 3D TCAD simulation and design of experiment (DOE), we construct capacitances' 2<sup>nd</sup> response surface model (RSM). By this model, we analyze the sensitivity of capacitances with design parameters under Gaussian distribution. This approach is cost effective and has its engineering accuracy, compared with 3D field simulation.

## 1 Introductions

Thin film transistors (TFTs) find wide usage in active matrix liquid crystal displays (LCDs) [1-2]. The basic principle of operation of the LCD panel is to control the transparency of each pixel portion by bus lines to charge the pixel electrode. The structure capacitance of each TFT-LCD pixel plays very important role in designing high quality display panel. However, the capacitance of a pixel is very hard to be analyzed analytically because of the complex geometry structure. In this work, we implement a systematical way to analysis the effect of designing parameters on the structure capacitances of TFT-LCD pixel, as shown in Fig. 1. A computational statistics technique [3] is developed which consists of the 3D TCAD field simulator, the design of experiment (DOE) and the second order response surface model (RSM). By considering the designing parameters as changing factors, listed in Tab. 1, according to the DOE, we construct a RSM for capacitances of the explored TFT-LCD pixel. The RSM highly explains the behavior of capacitances for the investigated TFT-LCD pixel. With Gaussian distribution, the developed model allows us to analysis the sensitivity of capacitances in a TFT-LCD pixel with respect to the aforementioned factors efficiently.

## 2 Computational Technique

The proposed computational statistics methodology that accounts for the characteristic sensitivity is depicted in Fig. 2. A Plackett-Burman design is adopted to screen and determine major

interactions. Based on the results of the screening experiment, parameters in need of further study are identified. With central composite design (CCD) DOE technique, a 3D TCAD simulation is performed to calculate each capacitance for RSM construction. The model adequacy checking is necessary to check the model assumption and accuracy verification which is to examine the values that we are interested in the accuracy of the model in-between our high and low level settings. A 2<sup>nd</sup> order model is then established between capacitances (i.e., responses) and design parameters (i.e., factors). The sensitivity of capacitances then can be explored in a computationally cost-effective way.

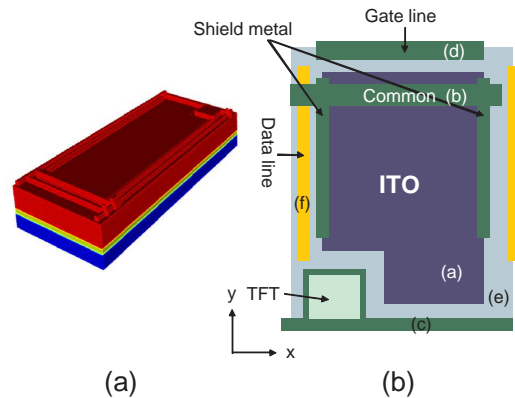


**Fig. 1.** (a) 3D schematic plot of TFT-LCD pixel and (b) a top-view of the structure.

## 3 Results and Discussion

We construct 2<sup>nd</sup> order RSM using 149-runs with CCD for the ten capacitances in the investigated TFT-LCD pixel. Without loss of generality, we partially list a model for  $C_{ac}$  which is the capacitance between part(a) and part(c) in Fig. 1(b)

$$\ln C_{ac} = -0.498 + 0.321A + 0.021B + 0.027C + 0.029D + 0.011E + 0.337G + 0.473J - 0.045GJ + \dots \quad (1)$$

where A to J are designing parameters, as listed in Tab. 1. The model predicted and the TCAD

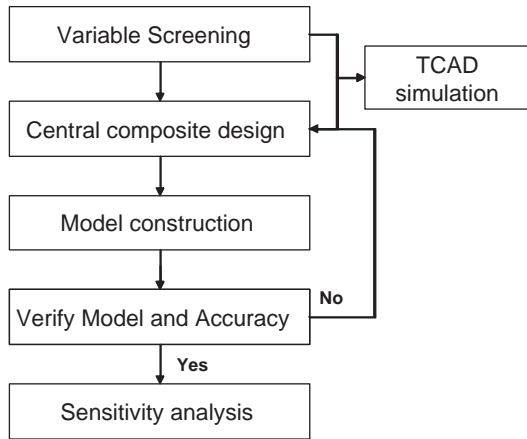


Fig. 2. The computational procedure.

Table 1. The upper and lower bounds of the TFT-LCD designing parameters.

Variable	Parameters	Variation Range(um)
Size Variation		
A	Gate line	[0,10] in y
B	Shield metal(left)	[0,3] in x
C	Shield metal(left)	[0,3] in y
D	Shield metal(right)	[0,3] in x
E	Shield metal(right)	[0,3] in y
F	ITO electrode	[0,5] in x
G	ITO electrode	[0,5] in y
Position Shift		
H	Shield metal(left)	[0,5] in x
I	ITO electrode	[-2,2] in x
J	ITO electrode	[-2,2] in y

Table 2. The R-square of the capacitance models.

Response	R-Square	Response	R-Square
$C_{ab}$	0.9832	$C_{ad}$	0.9701
$C_{ae}$	0.9986	$C_{ac}$	0.9936
$C_{fe}$	0.9935	$C_{bf}$	0.9624
$C_{ce}$	0.9563	$C_{df}$	0.9472
$C_{af}$	0.9938	$C_{bd}$	0.9778

simulated actual result, shown in Fig. 3, validates the accuracy of the constructed model (symbols locate in the line very well). The R-square for this model is 0.9936, and the others are also listed in Tab. 2. Figure 4 is the relationship between  $C_{ac}$  and parameter J, given in Tab. 1, where the other parameters are set to nominal values, and under Gaussian distribution (with more than 1000 trails and  $\sigma$  is determined by process variation), the inset is the estimated standard deviation of  $C_{ac}$  due to the parameter J variations of the examined pixel TFT-LCD. A 0.1051 fF increase of  $\sigma C_{ac}$  when the ITO shift varies from -1.5 um to 1.5 um. The increase of  $\sigma C_{ac}$  is mainly due to relatively large variation of circuit performance when the ITO shift increase in the y direction.

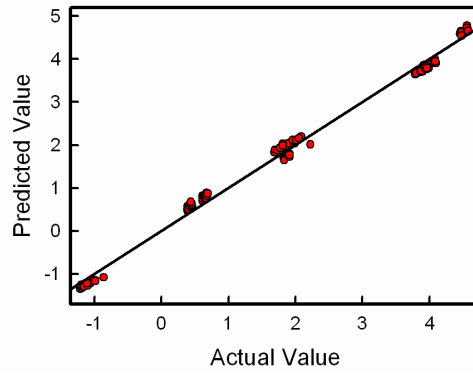


Fig. 3. The model predicted vs. actual result for  $C_{ac}$ .

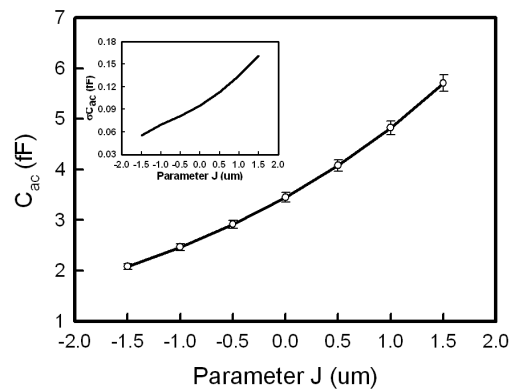


Fig. 4. Plot of  $C_{ac}$  versus J. The inset shows the standard deviation of  $C_{ac}$  with respect to J.

## 4 Conclusions

We have established RSMs for capacitance sensitivity analysis of a TFT-LCD pixel based upon a computational statistics technique. The model could also be used for design optimization.

*Acknowledgement.* This work was supported by Taiwan National Science Council under Contracts NSC-96-2221-E-009-210 and NSC-96-2752-E-009-003-PAE.

## References

1. I.-W. Wu. Polycrystalline silicon thin film transistors for liquid crystal displays. *Solid State Phenom.*, 37-38:553–564, 1994.
2. Y. Li. A Two-Dimensional Thin Film Transistor Simulation Using Adaptive Computing Technique. *Appl. Math. Comput.*, 184:73–85, 2007.
3. Y. Li, Y.-L. Li and S.-M. Yu. Design Optimization of a Current Mirror Amplifier Integrated Circuit Using a Computational Statistics Technique. *Math. Comput. Simul.*, doi:10.1016/j.matcom.2007.11.002, 2008.

---

**Session**

**CM 2**

---



# Numerical Time Integration in Computational Electromagnetics

Galina Benderskaya<sup>1</sup>, Oliver Sterz<sup>1</sup>, Wolfgang Ackermann<sup>2</sup>, and Thomas Weiland<sup>2</sup>

<sup>1</sup> CST GmbH, Bad Nauheimer Str. 19, D-64289 Darmstadt, Germany  
galina.benderskaya@cst.com, oliver.sterz@cst.com

<sup>2</sup> Technische Universität Darmstadt, Institut für Theorie Elektromagnetischer Felder, Schlossgartenstr. 8, D-64289 Darmstadt, Germany  
ackermann@temf.tu-darmstadt.de, thomas.weiland@temf.tu-darmstadt.de

**Summary.** In time domain, mathematical models of various electromagnetic devices operating at low frequencies generally represent a system of first order ordinary differential equations or index 1 differential-algebraic equations. Numerical schemes employed to follow the time evolution of the transient processes fall into explicit and implicit time integration algorithms. In the paper, the types of the implicit time integration are considered and illustrated with the corresponding numerical experiments.

## 1 Introduction

Electromagnetic low frequency time domain modeling can be performed using the regimes of quasistatic approximations or the full set of Maxwell's equations. Naturally, the usage of the full information provided by the Maxwell's equations leads to more accurate numerical simulation results which are, however, accompanied by higher computational costs. Under certain conditions, the quasistatic approximations can be applied which allows to obtain simulation results of comparable accuracy but considerably reduces the computational costs. In Section 2, a classification of the electromagnetic simulation regimes is given. The material highlighted in this paper is focused on the quasistatic electromagnetic formulations which are described with a set of first order ordinary differential equations (ODEs) or index 1 differential-algebraic equations (DAEs). The indispensable spatial discretization is performed e.g., with the Finite Integration Technique (FIT) or the Finite Element Method (FEM). Pros and cons of different time integration methods used to resolve the time dependencies appearing in these formulations are discussed in Section 3. The following Sections 4 and 5 provide a deep insight into implicit time integration methods and discuss the possible problems associated with their implementation. Finally, in the full paper the discussed numerical schemes are illustrated with the test examples in Section 6.

## 2 Quasistatic Approximation or Exact Formulation

Maxwell's equations govern the complete behavior of electromagnetic fields and represent a system of coupled differential equations. As a result, the full spectrum ranging from statics to high frequency can be modeled entirely. This approach allows to obtain precise simulation results but may be equipped with high computational costs. Under certain conditions, however, it is possible to partially omit the time dependencies in the electromagnetic field quantities without losing too much accuracy within the numerical simulations.

Excluding the time derivatives of the electric or magnetic flux density from the system of Maxwell's equations leads to the magneto- or electroquasistatic time domain approximations, respectively. The necessary condition for any quasistatic approximation to be valid is that the time required for an electromagnetic wave to propagate at the velocity  $c = 1/\sqrt{\mu\epsilon}$  over the largest length of the system consisting of a material with permittivity  $\epsilon$  and permeability  $\mu$  is much shorter than the characteristic time constant of the global field variation. In other words, this condition is fulfilled if the time rates of the changes are slow enough so that time delays due to the propagation of the electromagnetic waves can be neglected. The quasistatic approximation regime is further subdivided into electro- and magnetoquasistatic ones depending on the dominant effect [1].

Resolving the space dependencies appearing in the quasistatic formulations using the FIT approach results in the following discrete formulations

$$-\tilde{\mathbf{S}}\mathbf{M}_\epsilon\mathbf{G}\frac{d\phi(t)}{dt} - \tilde{\mathbf{S}}\mathbf{M}_\sigma(\mathbf{G}\phi(t))\mathbf{G}\phi(t) = 0 \quad (1)$$

for the electroquasistatic simulation regime and

$$\mathbf{M}_\sigma\frac{d}{dt}\hat{\mathbf{a}}(t) + \tilde{\mathbf{C}}\mathbf{M}_{\mu^{-1}}(\hat{\mathbf{a}}(t))\mathbf{C}\hat{\mathbf{a}}(t) = \hat{\mathbf{j}}_s(t) \quad (2)$$

for the magnetoquasistatic counterpart. In (1),  $\tilde{\mathbf{S}}$  represents the discrete dual divergence operator, whereas the material parameters are gathered in the discrete permittivity matrix  $\mathbf{M}_\varepsilon$  and the discrete conductivity matrix  $\mathbf{M}_\sigma$ . The matrix  $\mathbf{G}$  describes a discrete gradient operator and the scalar unknowns are represented by the vector of discrete potentials  $\phi$ . Equation (2) is formulated in terms of the discrete curl operators  $\mathbf{C}$  and  $\tilde{\mathbf{C}}$ , the discrete inverse permeability  $\mathbf{M}_{\mu^{-1}}$ , the imposed electrical grid currents  $\tilde{\mathbf{J}}_s(t)$  and the vector  $\tilde{\mathbf{a}}(t)$  of magnetic vector potentials integrated along the primal grid edges.

### 3 Implicit versus Explicit Time Integration

Since in electroquasistatic formulations the permittivity  $\varepsilon$  never vanishes, the matrix  $\tilde{\mathbf{S}}\mathbf{M}_\varepsilon\mathbf{G}$  in (1) is always regular. As a consequence, the electroquasistatic formulation (1) represents a nonlinear ODE system and all available explicit time integration schemes can be applied. If (1), however, becomes stiff implicit time integration methods are more appropriate.

In magnetoquasistatic formulations, the conductivity  $\sigma$  obviously equals zero exactly for those parts of the model which are filled with non-conductive materials. In this case, the diagonal matrix  $\mathbf{M}_\sigma$  contains zero entries and is singular. Then, (2) represents a nonlinear DAE system of index 1 [1]. Such problems are extremely stiff and explicit integration methods will stuck. When encountering stiffness implicit schemes offer a much better choice.

There is another important criterion counting in favor of the implicit time integration schemes when they are applied to treat the time dependencies in parabolic partial differential equations: the stability limit  $\Delta t \leq \mathcal{O}(\Delta x^2)$  put on the size of the time step in the explicit time integration methods implies that an enormous amount of time steps is necessary to follow the evolution of the time process if one reduces the spatial resolution  $\Delta x$  to improve the overall accuracy of the numerical solution [2].

Typically, the electro- and magnetoquasistatic formulations (1) and (2) are written in the following general form

$$\mathbf{M}\frac{d}{dt}\mathbf{x}(t) + \mathbf{K}(\mathbf{x}(t))\mathbf{x}(t) = \mathbf{r}(t) \quad (3)$$

where the corresponding unknowns are composed into a vector  $\mathbf{x}$ . The matrices  $\mathbf{M}$  and  $\mathbf{K}$  are square matrices of real-valued entries and  $t$  is a real-valued variable denoting the time.

## 4 Types of Implicit Time Integration

Numerical time integration methods fall into two categories: those which use only one starting value at each integration step are called *one-step* methods and those which are based on several values of the solution calculated at the previous time instants are called *multistep* methods. In this paper we concentrate only on the one-step methods. Among the most popular one-step implicit time integration schemes are the so called  $\theta$ -method, the Runge-Kutta methods [3] and the Rosenbrock-type methods.

## 5 Adaptive Stepsize Control

*Embedded* implicit Runge-Kutta and Rosenbrock-type methods offer an effective way of estimating the local error of the method. Such integration schemes deliver for each time step a solution  $\mathbf{x}^{(p)}$  of a given order  $p$  and an embedded solution  $\mathbf{x}^{(\hat{p})}$  of a lower order  $\hat{p}$ . The difference between two vectors is used to build an error vector whose norm is then employed to measure the local error for a given time step. The main and the embedded methods share the same coefficient matrix of the Butcher table. Thus, the computation of the embedded solution does not require the solution of a nonlinear system, but just the superposition of the already calculated stage values using merely different weight factors.

## 6 Numerical Simulations

In the full paper, numerous numerical examples demonstrating the application of the implicit adaptive methods to the quasistatic formulations described by (3) calculated using the CST EM STUDIO<sup>TM</sup> software package will be presented.

## References

1. G. Benderskaya. Numerical Methods for Transient Filed-Circuit Coupled Simulations Based on the Finite Integration Technique and a Mixed Circuit Formulation. PhD thesis, Darmstadt University of Technology, Darmstadt, 2007.
2. K.W. Morton, and D.F. Mayers. *Numerical Solutions of Partial Differential Equations*. Cambridge University Press, Cambridge, 2005.
3. A. Nicolet and F. Delincé. Implicit Runge-Kutta Methods for Transient Magnetic Field Computation. *IEEE Trans. Magn.*, 32:3:1405–1408, 1996.

# Co-Simulation of Circuits Refined by 3-D Conductor Models

Sebastian Schöps<sup>1</sup>, Andreas Bartel<sup>1</sup>, Herbert De Gerssem<sup>2</sup>, and Michael Günther<sup>1</sup>

<sup>1</sup> Bergische Universität Wuppertal {schoeps,bartel,guenther}@math.uni-wuppertal.de

<sup>2</sup> Katholieke Universiteit Leuven Herbert.DeGerssem@kuleuven-kortrijk.be

**Summary.** In this paper a coupling approach for the solution of circuits refined by 3-D conductor models is proposed. The circuit is given in terms of the modified nodal analysis and the field is discretized by the finite integration technique. The coupled system is introduced and analyzed; first numerical results are obtained by a co-simulation approach.

## 1 Introduction

Magnetoquasistatic (MQS) field problems naturally occur in circuit analysis. They are commonly solved by either a circuit or a field approach [3]. Any of them may become physically inaccurate or computationally inefficient. Consequentially, *co-simulation*, i.e., the simultaneous use of a circuit and field method in different model parts, is beneficial [2]. Furthermore it provides a natural support for diversifying integration methods and time-stepping rates towards distinct subproblems.

## 2 Electric Circuit

Large circuits are simulated by the modified nodal analysis (MNA) technique (notation from [7])

$$A_C \frac{d}{dt} q + A_R r(A_R^T e, t) + A_L \iota_L + A_V \iota_V + A_I \iota(t) + A_\lambda \iota_\lambda = 0, \quad (1a)$$

$$\frac{d}{dt} \Phi - A_L^T e = 0, \quad (1b)$$

$$A_V^T e - v(t) = 0, \quad (1c)$$

$$q - q_C(A_C^T e, t) = 0, \quad (1d)$$

$$\Phi - \Phi_L(\iota_L, t) = 0, \quad (1e)$$

with incidence matrices  $A$ , node potentials  $e$ , currents through voltage and flux controlled elements  $\iota_V$  and  $\iota_L$ , voltage dependent charges and fluxes  $q$  and  $\Phi$ , voltage dependent resistors  $r$ , voltage and current dependent charge and flux functions  $q_C$  and  $\Phi_L$ , independent current and voltage functions  $\iota$  and  $v$ , controlled voltage sources  $\iota_\lambda$ .

The numerical properties of (1) are well known, e.g. the index of this differential-algebraic equation (DAE) has been shown to equal 1 assuming several topological conditions [6].

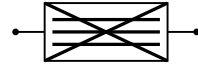


**Fig. 1.** Circuit symbol of a network element with 2 terminals embedded in a field model

## 3 Magnetoquasistatic Field

The finite integration technique (FIT) translates the MQS subset (without displacement) of Maxwell's equations into

$$\begin{aligned} C \bar{e} &= -\frac{d}{dt} \bar{b}, & \tilde{C} \bar{h} &= \bar{j}, \\ \tilde{S} \bar{d} &= q, & S \bar{b} &= 0, \end{aligned} \quad (2)$$

which is accomplished by the material relations

$$\bar{b} = M_\mu \bar{h}, \quad \bar{d} = M_\epsilon \bar{e}, \quad \bar{j} = M_\sigma \bar{e}, \quad (3)$$

with discrete curl operators  $C$  and  $\tilde{C}$ , divergence operators  $S$  and  $\tilde{S}$ , electric and magnetic field strength  $\bar{e}$  and  $\bar{h}$ , source current density, discrete magnetic and electric flux  $\bar{j}$ ,  $\bar{b}$  and  $\bar{d}$ . The material matrices  $M_\mu$ ,  $M_\epsilon$  and  $M_\sigma$  represent the permeabilities, permittivities and conductivities, with  $M_\sigma$  singular in general due to non-conducting regions [4].

A single equation of curl-curl form (4) is obtained from (2)+(3) by algebraic manipulations

$$\tilde{C} M_\nu C \bar{a} + M_\sigma \frac{d}{dt} \bar{a} = \bar{j}, \quad (4)$$

where  $\bar{a}$  denotes the Magnetic Vector Potential (MVP). This is a special index-1 DAE, because it has non-unique solutions. But for the following analysis a gauge can be assumed.

## 4 Coupling

In [5] field models for solid and stranded conductors have been developed for the use in circuits. We use the symbol of Fig. 1 for a ( $n$ -terminal) device of several solid and stranded conductors. In the case where the field model contains multiple current-driven solid and voltage-driven stranded conductors, the field model (4) is excited by

$$\widehat{j} = M_{\sigma} Q_{\text{sol}} u_{\text{sol}} + Q_{\text{str}} i_{\text{str}}, \quad (5)$$

where  $u_{\text{sol}}$  and  $i_{\text{str}}$  are unknowns that are described by the two additional coupling equations

$$G_{\text{sol}} u_{\text{sol}} - Q_{\text{sol}}^T M_{\sigma} \frac{d}{dt} \widehat{a} = i_{\text{sol}}, \quad (6)$$

$$R_{\text{str}} i_{\text{str}} + Q_{\text{str}}^T \frac{d}{dt} \widehat{a} = u_{\text{str}}, \quad (7)$$

where  $Q_{\text{sol}}$ ,  $Q_{\text{str}}$  are coupling matrices,  $u_{\text{sol}}$ ,  $u_{\text{str}}$  denote branch voltages, and  $i_{\text{sol}}$ ,  $i_{\text{str}}$  currents through both conductor types;  $G_{\text{sol}}$  and  $R_{\text{str}}$  denote the solid conductor conductance and the stranded conductor resistance, respectively.

Assuming a regularization we can show that (4)–(7) is still index-1 and that the algebraic part of the MVP vanishes, if the discretization grid is sufficiently fine such that no *smearing* of the two conductor volumes occurs.

Assigning the voltages to differences of node potentials and replacing the controlled current source by the current through the conductors in (1a) yields the coupling conditions

$$u_{\text{sol}} = A_{\text{sol}}^T e, \quad u_{\text{str}} = A_{\text{str}}^T e, \quad i_{\lambda} = \begin{pmatrix} i_{\text{sol}} \\ i_{\text{str}} \end{pmatrix}. \quad (8)$$

Finally the combined system consists of (1), (4)–(8). A simple numerical analysis of this system is present, both for the case of a monolithically solution as for co-simulation. It turns out that the monolithic system is still index-1 and the convergence of the co-simulation is guaranteed according to the results of [1].

## 5 Numerical Experiments

Our software is implemented on top of the COMSON DP<sup>1</sup>. First numerical simulations are obtained for the simple but effective RLC circuit in Fig. 2(a), where the inductance  $L$  is represented by a field model consisting of one stranded and one solid conductor. The field problem has been constructed using the CST EMstudio software package<sup>2</sup>.

The co-simulation converges without any additional iteration of the individual time frames. The computational results are given in the plot Fig. 2(b). They are comparable to the solutions obtained from the other approaches, the monolithic and the plain MNA case. Examination of the time-scales in the co-simulation showed that the adaptive method for the integration of the circuit part used the same step size as the integrator of the field part. This corresponds to the observation that the dynamics in the field equal those

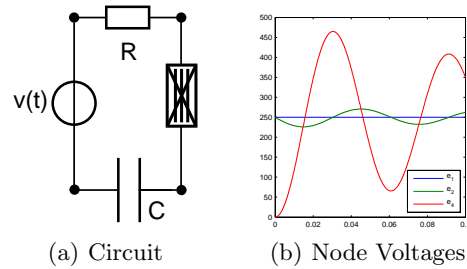


**Fig. 2.** Refined RLC circuit with an inductance represented by a field model and node potentials computed by co-simulation

of the circuit and hence no multi-rate potential is recognizable in this particular example. This is a reasonable result since the circuit has no parts with additional dynamics.

## 6 Conclusions

The monolithic field-circuit coupled system is index-1 and the convergence of the proposed co-simulation approach is guaranteed, as documented by the simulation of a RLC circuit where the inductance is represented by a field model. The co-simulation approach allows for the use of different, existing software packages and enables the application of multi-rate time-stepping schemes.

*Acknowledgement.* This work was partially supported by the European Commission in the framework of the COMSON RTN project.

## References

1. A. Bartel. PDAE Models in Chip Design - Thermal and Semiconductor Problems. PhD thesis, TU München, 2004. VDI Verlag.
2. G. Bedrosian. A new method for coupling finite element field solutions with external circuits and kinematics. *IEEE Trans. Magn.*, 29(2): 1664 – 1668, 1993.
3. G. Benderskaya, H. De Gersem, T. Weiland. Integration over discontinuities in field-circuit coupled simulations with switching elements. *IEEE Trans. Magn.*, 42(4): 1031 – 1034, 2006.
4. M. Clemens, T. Weiland. Discrete electromagnetism with the finite integration technique. *PIER*, 32: 65 – 87, 2001.
5. H. De Gersem, K. Hameyer, T. Weiland. Field-circuit coupled models in electromagnetic simulation. *J. Comp. Appl. Math.*, 168: 125 – 133, 2004.
6. D. Estévez Schwarz, C. Tischendorf. Structural analysis of electric circuits and consequences for MNA. *Int. J. Circ. Theor. Appl.*, 28: 131 – 162, 2000.
7. M. Günther, P. Rentrop. Numerical simulation of electrical circuits. *GAMM-Mitteilungen*, 1/2: 51 – 77, 2000.

<sup>1</sup> [www.comson.org](http://www.comson.org)

<sup>2</sup> [www.cst.com](http://www.cst.com)

# Robust FETI solvers for multiscale elliptic PDEs

Clemens Pechstein<sup>1</sup> and Robert Scheichl<sup>2</sup>

<sup>1</sup> SFB F013, Johannes Kepler University Linz, Austria [clemens.pechstein@numa.uni-linz.ac.at](mailto:clemens.pechstein@numa.uni-linz.ac.at),

<sup>2</sup> Department of Mathematical Sciences, University of Bath, United Kingdom [masrs@bath.ac.uk](mailto:masrs@bath.ac.uk)

**Summary.** FETI methods are efficient parallel domain decomposition solvers for large-scale finite element equations. In this work we investigate the robustness of FETI methods in case of heterogeneous coefficients. Our main application are magnetic field computations where both large jumps and large variation in the reluctivity coefficient may arise. We give theoretical bounds and numerical results.

## 1 Introduction

Finite element tearing and interconnecting (FETI) methods due to Farhat and Roux [1, 7] are parallel solvers for large-scale finite element systems arising from partial differential equations (PDEs). We briefly describe the method. As a model problem we consider the finite element discretization of the Poisson-type problem

$$-\nabla \cdot (\alpha \nabla u) = f \quad (1)$$

in the bounded domain  $\Omega \subset \mathbf{R}^d$ ,  $d = 2$  or  $3$ , subject to suitable boundary conditions. The domain  $\Omega$  is partitioned into  $N$  non-overlapping subdomains  $\Omega_i$ ,  $i = 1, \dots, N$ , such that an effective direct solve of local subdomain problems is possible. The FETI method is a special preconditioned conjugate gradient (CG) method, built from local Dirichlet and Neumann solves, as well as a coarse problem which corresponds to a sparse linear system of dimension  $\mathcal{O}(N)$ . The spectral condition number  $\kappa$  of the preconditioned system can be estimated by

$$\kappa \leq C^*(\alpha) (1 + \log(H/h))^2, \quad (2)$$

where the constant  $C^*(\alpha)$  is independent of the subdomain diameter  $H$ , the mesh parameter  $h$ , and the number  $N$  of subdomains. If  $\alpha$  is (globally) constant, then  $C^*(\alpha) \sim 1$ . The total computational complexity in a parallel scheme is

$$\mathcal{O}((\mathcal{D}(N) + \mathcal{D}(N_{loc})) \log(\varepsilon^{-1}) \sqrt{\kappa}), \quad (3)$$

where  $N_{loc}$  is the maximal number of unknowns per subdomain,  $\mathcal{D}(\cdot)$  is the cost of the direct solver, and  $\varepsilon$  is the desired relative error.

However, in many applications the original system matrix is ill-conditioned due to heterogeneous coefficient distributions. For instance, in

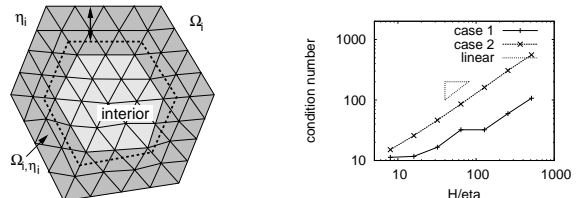


**Fig. 1.** Left: Subdomain boundary layer. Right: Estimated condition numbers for varying  $\eta$ , fixed  $h$ .

magnetic field computations one may have (i) large jumps in the reluctivity coefficient due to different materials, and (ii) smooth but large variation in the same coefficient due to nonlinear effects. We are now interested in the question whether/how the condition number  $\kappa$  of the preconditioned system is affected by this. If the heterogeneities are resolved by the subdomain partition (i. e.,  $\alpha$  constant on each  $\Omega_i$ ), then, using a special diagonal scaling, Klawonn and Widlund [2] proved that  $C^*(\alpha) \sim 1$ . However, in general, using classical proof techniques, we only get

$$C^*(\alpha) \leq C \max_{i=1, \dots, N} \max_{x, y \in \Omega_i} \frac{\alpha(x)}{\alpha(y)}, \quad (4)$$

with  $C$  independent of  $\alpha$ , i. e., the bound is proportional to the maximum local variation of  $\alpha$  on the subdomains. As noticed by several authors [3, 6] this asymptotic bound is in general far too pessimistic, and robustness is observed for many special kinds of coefficient distributions. The aim of the present contribution is to give more theoretical insight on the coefficient-dependency.

## 2 Variation in subdomain interiors

In this section we give a sharper estimate than (4). On each subdomain  $\Omega_i$  with diameter  $H_i$ , we choose a width  $\eta_i \in [h_i, H_i]$  and define the boundary layer  $\Omega_{i, \eta_i}$  by the agglomeration of those finite elements which have distance at most  $\eta_i$  from the boundary, cf. Fig. 1, left. Our new bound reads

$$C^*(\alpha) \leq C \max_{k=1}^N \left( \frac{H_k}{\eta_k} \right)^2 \max_{i=1}^N \max_{x, y \in \Omega_{i, \eta_i}} \frac{\alpha(x)}{\alpha(y)}, \quad (5)$$

i. e., it involves only the variation of  $\alpha$  in the boundary layer  $\Omega_{i, \eta_i}$ . For  $\eta_i \simeq H_i$  we reproduce

the known estimate (4). Again our estimate is robust with respect to large jumps across the subdomain interfaces. However, if  $\alpha$  exhibits large (even arbitrary) variation in the interior  $\Omega_i \setminus \Omega_{i,\eta_i}$  of the subdomains, but varies little in the boundary layers, our new bound (5) is in general far better/sharper than (4). Moreover, if in addition the coefficient is larger in the interior  $\Omega_i \setminus \Omega_{i,\eta_i}$  than in the boundary layer on each subdomain, then the quadratic factor  $(H_i/\eta_i)^2$  reduces to a linear factor  $H_i/\eta_i$ . The detailed analysis will be given in an upcoming paper [5].

Fig. 1, right, shows some numerical results for a two-dimensional example. We set  $\alpha = 10^5$  (Case 1) and  $\alpha = 10^{-5}$  (Case 2) in the subdomain interiors, and  $\alpha = 1$  on the rest. We choose the distance between the “material” jump and the subdomain interfaces to be  $\eta$ , and set  $H/h = 512$ . We see that our asymptotic bound is sharp for Case 1, but still slightly pessimistic for Case 2.

### 3 Boundary layer variation

In the case of nonlinear magnetostatics in two dimensions (transverse magnetic mode), we have to solve

$$-\nabla \cdot [\nu(|\nabla u|)\nabla u] = f, \quad (6)$$

subject to suitable boundary conditions, where  $u$  is the  $z$ -component of the magnetostatic vector potential. The reluctivity  $\nu$  depends nonlinearly on the magnetic flux density  $|\mathbf{B}| = |\nabla u|$ . If we apply Newton’s method to (6), the linearized system in each Newton step is of similar form as (1). However, the variation of the coefficient depends essentially on the variation of  $|\mathbf{B}|$ . Indeed, in many applications  $|\mathbf{B}|$  may vary strongly along subdomain boundaries. Numerical experiments reveal that in this case, our new bound (5) is still too pessimistic: The constant  $C^*(\alpha)$  depends only mildly on the variation of  $\alpha$  near subdomain interfaces. This effect has already been reported in [3, 4].

Large values of  $|\mathbf{B}|$  appear mostly at singularities of  $u$ , e. g., near material corners. Contrary to the usual suggestion to choose subdomain partitions that resolve material interfaces in order to obtain robustness, our new bound (5) suggests that it might be more advantageous to put each peak of  $|\mathbf{B}|$  and thus each material corner into the center of a subdomain. Fig. 2 shows two such examples. In both cases, the coefficient variation is approximately  $7 \times 10^3$  and our FETI solver performs extremely well (Case 1: condition number 8.5, Case 2: condition number 13.7, compared to 8.3 in case of a constant coefficient). In Case 1, the boundary layer variation is small, whereas it is large in Case 2.

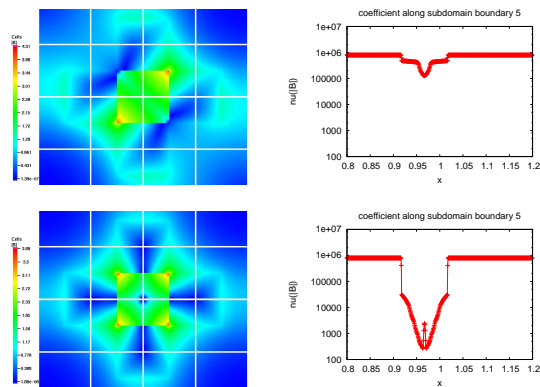


**Fig. 2.** Upper: Case 1. Lower: Case 2. Left:  $|\mathbf{B}|$ -field, subdomain partition. Right: Boundary variation of  $\nu$ .

We are currently trying to extend our analysis to also cover this case and to explain why in many situations even a variation in the boundary layer does not affect the robustness of our FETI solver.

*Acknowledgement.* We would like to thank Ulrich Langer for his encouragement. The first author acknowledges the financial support by the Austrian Science Funds (FWF) under grant SFB F013.

### References

1. C. Farhat and F.-X. Roux. A method of finite element tearing and interconnecting and its parallel solution algorithm. *Int. J. Numer. Meth. Engrg.*, 32:1205–1227, 1991.
2. A. Klawonn and O. B. Widlund. FETI and Neumann-Neumann iterative substructuring methods: connections and new results. *Comm. Pure Appl. Math.*, 54(1):57–90, 2001.
3. U. Langer and C. Pechstein. Coupled finite and boundary element tearing and interconnecting solvers for nonlinear potential problems. *ZAMM Z. Angew. Math. Mech.*, 86(12), 2006.
4. U. Langer and C. Pechstein. Coupled FETI/BETI solvers for nonlinear potential problems in (un)bounded domains. In G. Ciuprina and D. Ioan, editors, *Scientific Computing in Electrical Engineering: The European Consortium for Mathematics in Industry*, Berlin, Heidelberg, 2007. Springer.
5. C. Pechstein and R. Scheichl. Analysis of FETI methods for multiscale elliptic PDEs. (in preparation).
6. D. Rixen and C. Farhat. A simple and efficient extension of a class of substructure based preconditioners to heterogeneous structural mechanics problems. *Internat. J. Numer. Methods Engrg.*, 44:489–516, 1999.
7. A. Toselli and O. B. Widlund. *Domain Decomposition Methods – Algorithms and Theory*, volume 34 of *Springer Series in Computational Mathematics*. Springer, Berlin, Heidelberg, 2005.

# Functional Type A Posteriori Error Estimates for Maxwell's Equations

Antti Hannukainen

Institute of Mathematics, Helsinki University of Technology, P. O. Box 1100, FIN-02015 TKK  
antti.hannukainen@tkk.fi

**Summary.** In this work, we study functional type a posteriori error estimation for eddy-current and time-harmonic approximations of Maxwell's equations. The presented estimates can be applied to any admissible approximation, hence they are not tied to any particular numerical scheme. The behavior of these estimates is numerically tested.

## 1 Introduction

Majority of the existing research on a posteriori error estimates for Maxwell's equations has focused on residual based error estimation techniques (see [1, 5, 8]). Such techniques require the approximate solution  $\tilde{\mathbf{E}}$  to satisfy a certain Galerkin orthogonality property, which in practice means that residual based estimates are applicable only in the context of the finite element methods. In addition, they contain Clément interpolation constants, which are mesh dependent and difficult to estimate sharply (see [2]). Hence, current residual based a posteriori error estimates cannot deliver sharp upper bound for the error and serve only as error indicators.

In this note, we will focus on functional type a posteriori error estimation approach (see [3, 4, 6]), which gives practically computable upper bounds. First functional type error estimates for the eddy-current problem were presented in [7]. Error bound for the time-harmonic problem was presented by the author in the ENUMATH conference. In this talk, we derive an upper bound in both cases and present numerical examples, which verify the effectivity of our approach.

## 2 Model problem

The model problem is : find  $\mathbf{E} \in H_0(\Omega, \text{curl})$  such that

$$(\nabla \times \mathbf{E}, \nabla \times \mathbf{v}) + \beta(\mathbf{E}, \mathbf{v}) = (\mathbf{J}, \mathbf{v}) \quad \forall \mathbf{v} \in H_0(\Omega, \text{curl}), \quad (1)$$

where  $\Omega \subset \mathbb{R}^3$  satisfies sufficient regularity assumptions and  $\mathbf{J} \in L^2(\Omega)$ . The space  $H_0(\Omega, \text{curl})$

denotes the standard Sobolev space with zero boundary condition  $\mathbf{n} \times \mathbf{E} = 0$ .

We study the above problem in two different case,  $\beta \in \mathbb{R}$ ,  $\beta > 0$  and  $\beta \in \mathbb{C}$ ,  $\Re \beta \geq 0$ . For positive parameter values (1) is the weak form of the eddy-current problem in a domain with positive conductivity and PEC boundary conditions. For complex-valued parameters (1) is the time-harmonic approximation of Maxwell's equations in a domain with PEC boundary conditions.

## 3 Error bounds

In the following, we consider some approximation  $\tilde{\mathbf{E}} \in H_0(\Omega, \text{curl})$  for  $\mathbf{E}$  and derive an upper bound for the error  $\mathbf{e} = \mathbf{E} - \tilde{\mathbf{E}}$  in a suitable norm.

An upper bound for the error also yields an estimate for the relative error.

**Lemma 1.** *Let  $\|\cdot\|$  be any norm and  $M$  be an upper-bound to  $\|\mathbf{e}\|^2$ , such that  $M \leq \|\tilde{\mathbf{E}}\|$ . Then there applies*

$$\frac{\|\mathbf{e}\|}{\|\mathbf{E}\|} \leq \frac{M}{\|\tilde{\mathbf{E}}\| - M}.$$

### 3.1 Eddy-current case

In the eddy-current case, the bilinear form is elliptic and induces a natural norm

$$\|\cdot\| := \sqrt{(\nabla \times \cdot, \nabla \times \cdot) + \beta(\cdot, \cdot)},$$

which provides a direct connection between the error and the weak problem. In this norm, we obtain the following error bound.

**Theorem 1.** *Let  $\mathbf{E} \in H_0(\Omega, \text{curl})$  be the solution to (1) with  $\beta > 0$ . For any  $\tilde{\mathbf{E}}, \mathbf{y}^* \in H_0(\Omega, \text{curl})$  there applies*

$$\|\mathbf{e}\|^2 \leq \|\beta^{-1/2}(\mathbf{J} - \beta\tilde{\mathbf{E}} - \nabla \times \mathbf{y}^*)\|^2 + \|\nabla \times \tilde{\mathbf{E}} - \mathbf{y}^*\|^2. \quad (2)$$

This estimate is sharp in the sense that choosing the parameter  $\mathbf{y}^*$  as  $\mathbf{y}^* = \nabla \times \mathbf{E}$  yields equality. One appropriate choice of  $\mathbf{y}^*$  is discussed in Section 4.

### 3.2 Time-harmonic case

In time-harmonic case, the sesquilinear form is not elliptic and does not induce any natural norm. We will follow [5] and measure the error in the  $L^2(\Omega)$  - norm.

**Theorem 2.** *Let  $\mathbf{E} \in H_0(\Omega, \text{curl})$  be the solution to (1) with  $\beta \in C, \Im\beta \geq 0$ . For any  $\tilde{\mathbf{E}}, \mathbf{y}^* \in H_0(\Omega, \text{curl})$  there applies*

$$\|\mathbf{e}\| \leq C(\|\mathbf{J} - \beta\tilde{\mathbf{E}} - \nabla \times \mathbf{y}^*\| + \|\mathbf{y}^* - \nabla \times \tilde{\mathbf{E}}\|).$$

in which the constant  $C > 0$  depends only on the parameter  $\beta$  and the domain.

### 4 Numerical example

The upper-bound for the eddy-current problem is tested in the case  $\Omega = (-1, 1)/[0, 1]$ ,  $\beta = 1$  and  $\mathbf{f} = [1, 1, 1]^T$ . As the domain contains a re-entrant corner at the origin  $(0, 0, 0)$ , a boundary singularity can be expected near this point. Our aim is to study, how well does the upper bound detect the singularity in adaptive refinement process.

The problem (1) was solved using the finite element method with lowest order Nedelec (Whitney) elements on tetrahedral mesh. The adaptive procedure is based on using the elementwise contributions of the upper bound as local error measures.

The parameter  $\mathbf{y}^*$ , required in Theorem 1, was chosen as a minimizer of (2) from the same finite element space  $X_h$  as the approximate solution. The minimizer is obtained by solving the problem : find  $\mathbf{y}^* \in X_h$  such that

$$\begin{aligned} (\beta^{-1}\nabla \times \mathbf{y}^*, \nabla \times \mathbf{v}) + (\mathbf{y}^*, \mathbf{v}) &= (\nabla \times \tilde{\mathbf{u}}, \mathbf{v}) \\ + \left( \beta^{-1/2}(\mathbf{f} - \beta\tilde{\mathbf{u}}), \nabla \times \mathbf{v} \right) &\quad \forall \mathbf{v} \in X_h, \end{aligned}$$

which is also an eddy current problem, solved with the same finite element solver as the original problem.

The results are plotted in Fig. 1. As one can clearly observe, the adaptive refinement based on the presented upper bound improves the convergence rate compared to uniformly refined mesh. This means that the adaptive refinement process can detect the singularity and improve the quality of the approximation. Since the true error is unknown, we have used a reference solution from a very dense mesh to compute estimate for the error.

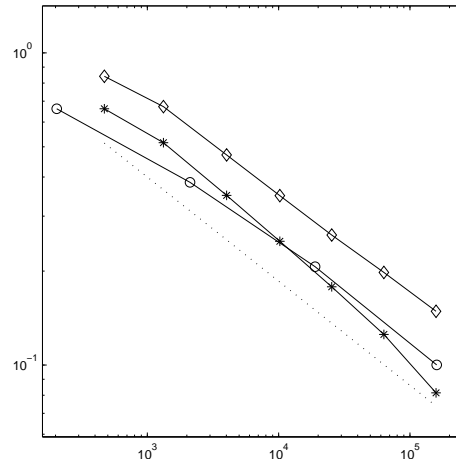


**Fig. 1.** Behavior of the error in adaptive refinement as a function of degrees of freedom. Diamonds denote the estimated error, stars the reference error and circles error in a solution from uniformly refined mesh. The dotted line is the optimal convergence rate  $O(h)$ .

*Acknowledgement.* The author has been supported by the project no. 211512 from the Academy of Finland.

### References

1. R. Beck, R. Hiptmair, R. Hoppe, and B. Wohlmuth. Residual based a-posteriori error estimators for eddy current computation. *Math. Model. Numer. Anal.*, 34(1):159–182, 2000.
2. C. Carstensen and S. A. Funken. Constants in Clément-interpolation error and residual based a posteriori error estimates in finite element methods. *East-West J. Numer. Math.*, 8:153–175, 2000.
3. A. Hannukainen and S. Korotov. Computational technologies for reliable control of global and local errors for linear elliptic type boundary value problems. *JNAIAM*, 2(3–4):157–176, 2007.
4. S. Korotov. Two-sided a posteriori error estimates for linear elliptic problems with mixed boundary conditions. *Appl. Math.*, 52(3):235–249, 2007.
5. P. Monk. A posteriori error indicators for Maxwell’s equations. *Journal of Computational and Applied Mathematics*, 100:173–190, 1998.
6. P. Neittaanmäki and S. Repin. *Reliable Methods for Computer Simulation: Error Control and A Posteriori Error Estimates*. Elsevier, Amsterdam, 2004.
7. S. Repin. Functional a posteriori estimates for the maxwell’s problem. *J. Math. Sci.*, 1:1821–1827, 2007.
8. J. Schöberl. Commuting quasi-interpolation operators for mixed finite elements. *Math. Comp.* (submitted), 2006.

# Large-Scale Atomistic Circuit-Device Coupled Simulation of Intrinsic Fluctuations in Nanoscale Digital and High-Frequency Integrated Circuits

Chih-Hong Hwang, Ta-Ching Yeh, Tien-Yeh Li, and Yiming Li<sup>1</sup>

National Chiao Tung University, 1001 Ta-Hsueh Rd., Hsinchu 300, Taiwan <sup>1</sup>yml@faculty.nctu.edu.tw

**Summary.** Investigation of device variability is crucial for the design of state-of-art nanoscale digital and high-frequency circuits and systems. This study provides a large-scale statistically sound "atomistic" circuit-device coupled simulation approach to exploring the random-dopant-induced characteristic fluctuations in nanoscale CMOS integrated circuits concurrently capturing the discrete-dopant-number- and discrete-dopant-position-induced fluctuations.

## 1 Introduction

As dimension of semiconductor scales down, characteristic fluctuation is more pronounced and become crucial for circuit design. Diverse approaches have recently been reported to study fluctuation-related issues in semiconductor devices and circuit [1, 2]. However, due to the randomness of dopant position in device, the fluctuation of device gate capacitance is nonlinear and hard to be modeled in current compact models [2]. In this study, a large-scale statistically sound circuit-device coupled simulation approach is thus proposed to analyze the discrete-dopant-induced characteristic fluctuations in nanoscale MOSFET circuit. Based on the statistically (totally randomly) generated large-scale doping profiles, the device simulation is performed. In estimation of the circuit fluctuations, to capture the nonlinearity of gate capacitance fluctuation, a circuit-device coupled simulation [5] with discrete dopant distribution is conducted, which concurrently considers the discrete-dopant-number- and discrete-dopant-position-induced fluctuations.

## 2 Simulation Technique

Figure 1 illustrates the developed simulation flow of the proposed approach. To consider the effect of random fluctuation of the number and location of discrete channel dopants in channel region, 758 dopants are randomly generated in a 80 nm<sup>3</sup> cube, in which the equivalent doping concentration is  $1.48 \times 10^{18}$  cm<sup>-3</sup> (the nominal channel doping concentration), as shown in Fig. 1(a). The 80 nm<sup>3</sup> is then partitioned into sub-cubes of 16 nm<sup>3</sup>. The number of dopants may vary from zero to 14, and the average number is six, as shown

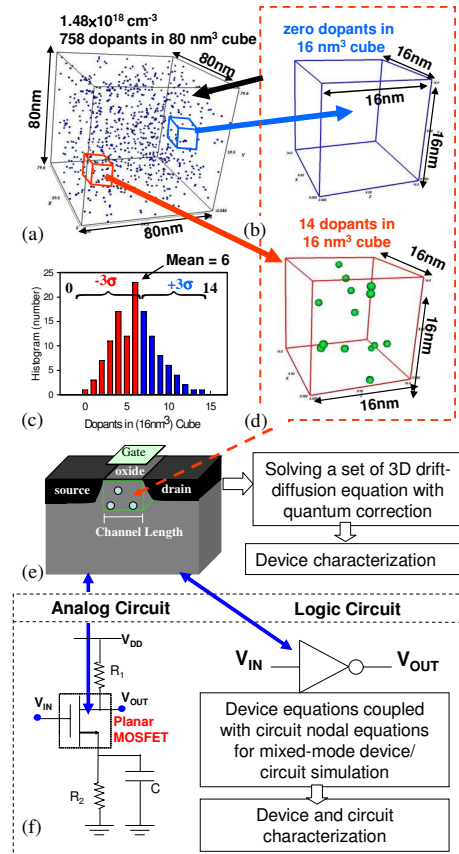


**Fig. 1.** (a) Discrete dopants randomly distributed in the 80 nm<sup>3</sup> cube with the average concentration  $1.48 \times 10^{18}$  cm<sup>-3</sup>. The dopants in sub-cubes of 16 nm<sup>3</sup> may vary from zero to 14 (the average number is six), [(b), (c), and (d)]. The sub-cubes are equivalently mapped into channel region for discrete dopant device and circuit-device coupled simulations as shown in (e) and (f).

in Figs. 1(b), 1(c) and 1(d). These sub-cubes are then equivalently mapped into the channel region of the device for the 3D device simulation, as shown in Fig. 1(e). The device simulation is performed by solving a set of 3D density-gradient equation coupling with drift-diffusion equations [3], which is conducted using a parallel computing system [4]. To investigate the random discrete dopant induced circuit fluctuations, and due to

the lack of reasonable compact model for describing device gate capacitance [1, 2], the aforementioned device equations directly coupled with circuit equations and then solved simultaneously [5]. A common-source amplifier and an inverter are used as the test circuits for high-frequency characteristic and timing variation estimation, as shown in Fig. 1(f). We noted that the proposed simulation technique is statistical sound and computationally cost-effective for random dopant fluctuation characterization.

### 3 Results and Discussion

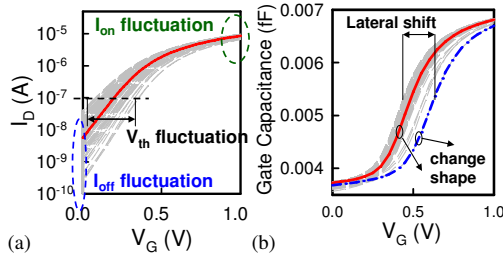


**Fig. 2.** The (a)  $I_D$ - $V_G$  curves (b) and gate capacitance fluctuations of the studied 16-nm-gate planar MOSFET

Figure 2(a) show the  $I_D$ - $V_G$  characteristics of the discrete-dopant-fluctuated 16 nm planar MOSFETs, where the solid line shows the nominal case ( $1.48 \times 10^{18} \text{ cm}^{-3}$  continuously doping concentration), and the dashed lines are random-dopant-fluctuated devices. The fluctuation of DC characteristics are observed. The capacitance-voltage (C-V) characteristics of the discrete-dopant-fluctuated 16 nm planar MOSFETs are investigated in Fig. 2(b). The lateral shift and change of shape for the C-V characteristics are observed. The variation of shape of C-V curves is resulted from the position of discrete dopants in channel and therefore is hard to be described in present compact model [3]. Therefore, to investigate the circuit level characteristic fluctuations, the circuit-device coupled simulation is used for obtaining circuit characteristics. The transition characteristics of the inverter circuit are investigated in Figs. 3(a). The fluctuations of rise time and fall time for digital circuits are observed, where the rise(fall) time is defined as the time required for the output voltage to go from 10%(90%) of the logic "0"("1") level to 90%(10%) of the logic "1"("0"). For the high-frequency characteristic simulation, the high-frequency response are investigated in Fig. 3(b). The fluctuation of high frequency circuit gain, 3dB bandwidth, and unity-gain bandwidth are estimated. Fig. 3(c) summarized the fluctuations of DC, timing, and high-frequency characteristics. The accuracy of timing and stability of frequency characteristics are crucial for the state-of-art circuits and systems using nanoscale transistor.

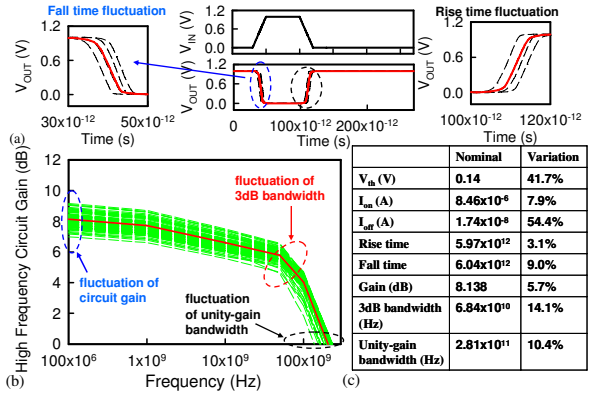


**Fig. 3.** (a) The input and output signal for the studied discrete-dopant-fluctuated 16-nm-gate inverter. (b) the high-frequency response of the common-source circuits. (c) summarized DC, timing, and high-frequency characteristic fluctuations

### 4 Conclusion

In this paper, a large-scale 3D "atomistic" circuit-device coupled simulation approach has been proposed to investigate the random-dopant-induced characteristic fluctuations in nanoscale CMOS digital and high-frequency integrated circuits. The approach successfully estimated the timing and high-frequency characteristics fluctuations. The fluctuation suppression technique may be further verified and developed from the viewpoint of circuit operation. We believe that the proposed approach will benefit the development of nanoscale circuits and systems.

*Acknowledgement.* This work was supported by Taiwan National Science Council under Contract NSC-96-2221-E-009-210, NSC-96-2752-E-009-003-PAE and by the Taiwan Semiconductor Manufacturing Company under a 2007-2008 grant.

### References

1. Y. Li, and C.-H Hwang. Discrete-dopant-induced characteristic fluctuations in 16 nm multiple-gate silicon-on-insulator devices. *J. Appl. Phys.*, 8:084509, 2007.
2. A. Brown and A. Asenov. Capacitance fluctuations in bulk MOSFETs due to random discrete dopants. *J. Comp. Elect.*, DOI:10.1007/s10825-008-0181-y, 2008.
3. S. Odanaka. Multidimensional discretization of the stationary quantum drift-diffusion model for ultrasmall MOSFET structures. *IEEE Trans. Computer-Aided Design Integr. Circuit and Sys.*, 23:837–842, 2004.
4. Y. Li and S.-M. Yu. A Parallel Adaptive Finite Volume Method for Nanoscale Double-gate MOSFETs Simulation *J. Comp. Appl. Math.*, 175:87–99, 2005.
5. T. Grasser, and S. Selberherr. Mixed-mode device simulation. *Microelectronics Journal*, 31:873–881, 2000.

---

## Author Index

- Ackermann, Wolfgang, 195  
 Alì, Giuseppe, 85, 165  
 Andersson, Björn, 181  
 Antoulas, Athanasios C., 79, 161  
 Arkkio, Antero, 57  
  
 Bahls, Christian R., 129  
 Bandlow, Bastian, 9  
 Bartel, Andreas, 165, 197  
 Baumanns, Sascha, 89  
 van Belzen, F., 167  
 Benderskaya, Galina, 195  
 Benner, Peter, 3, 23, 25  
 van Beurden, M.C., 41  
 Blaszczyk, Andreas, 11  
 Brachtendorf, Hans Georg, 103  
 Bruma, Alina, 33, 35  
 Brunk, Markus, 69, 91  
 Bunse-Gerstner, Angelika, 103  
  
 Chauviere, C., 127  
 Christoffersen, Carlos, 97  
 Ciuprina, Gabriela, 15, 43, 45  
 Condon, Marissa, 105, 123  
 Copeland, Dylan, 131  
 Costa, Luis R.J., 47  
 Croon, Jeroen, 93  
 Culpò, Massimiliano, 71, 165  
  
 Dağ, Hasan, 115  
 Dautbegovic, Emira, 141  
 De Gersem, Herbert, 197  
 De Tommasi, Luciano, 93  
 Denk, Georg, 71  
 Dewilde, Patrick, 135  
 Dhaene, Tom, 93  
 Dobrzynski, Michal, 177  
 Drago, C., 187  
  
 Ebrahimi, B.M., 49, 53  
 Edelvik, Fredrik, 181  
 Faiz, Jawad, 49, 53  
  
 de Falco, Carlo, 71, 165  
 Feldmann, Uwe, 95  
 Feng, Lihong, 23  
 Freitag, Josefine, 169  
  
 Ghofrani, M., 49  
 Gim, Sebastian, 177, 179  
 Gjonaj, Erion, 137  
 Gorissen, Dirk, 93  
 Gourary, M.M., 101, 145, 175  
 Grahovski, Georgi G., 123  
 Greiff, Michael, 169  
 Grimberg, Raimond, 33, 35  
 Gu, B., 175  
 Gullapalli, K.K., 101  
 Günther, Michael, 197  
  
 Hannukainen, Antti, 201  
 Harutyunyan, D., 173  
 Herberthson, Magnus, 171  
 Hesthaven, J.S., 127  
 Honkala, Mikko, 99, 117, 119, 157  
 Huang, Hsuan-Ming, 191  
 Hwang, Chih-Hong, 203  
  
 Ilievski, Z., 113  
 Ioan, Daniel, 15, 31, 43, 45, 153  
 Ionutiu, Roxana, 161  
 Islam, M. Jahirul, 57  
 Iwata, Satoru, 143  
  
 Jakobsson, Stefan, 181  
 Jüngel, Ansgar, 69, 91  
  
 Kajiwara, Takahiro, 95  
 Karanko, Ville, 99  
 Khan, M.A., 53  
 Kula, Sebastian, 179  
 Kuo, Yi-Ting, 39  
  
 La Rosa, Salvatore, 83  
 Lahaye, D.J.P., 187, 189  
 Lampe, Siegmars, 103  
  
 Lang, Barbara, 103  
 Langer, Ulrich, 131  
 Lau, Thomas, 137  
 Lefteriu, Sanda, 79  
 Lenaers, Peter, 27  
 Levadoux, David P., 77  
 Li, Tien-Yeh, 203  
 Li, Yiming, 39, 191, 203  
  
 Mascali, Giovanni, 83, 85  
 ter Maten, E.J.W., 21, 113  
 Mathis, Wolfgang, 169  
 Meuris, Peter, 61  
 Michielsen, B.L., 41, 73  
 Miettinen, Pekka, 117, 119, 157  
 Mihalache, Diana, 43, 45, 179  
 Miura-Mattausch, Mitiko, 95  
 Miyake, Masataka, 95  
 Mohaghegh, Kasra, 121  
 Mulvaney, B.J., 101, 145, 175  
 Munz, Claus-Dieter, 37  
  
 Neff, Carsten, 117  
 Neitola, Marko, 111  
 Nikoskinen, Keijo, 47  
  
 Pechstein, Clemens, 199  
 Plata, Jagoda, 177  
 Pöplau, Gisela, 129  
 Pomplun, Jan, 133  
 Preisner, Thomas, 169  
 Pulch, Roland, 85, 147  
 Pusch, David, 131  
  
 Quandt, Martin, 37  
  
 Rahkonen, Timo, 107, 109, 111  
 Rajabi-Sebdani, M., 53  
 Rebican, Mihai, 31  
 Reis, Timo, 159  
 van Rienen, Ursula, 129  
 Romano, Vittorio, 67, 83  
 Römisch, Werner, 149  
 Rommes, Joost, 27, 161

## Author Index

- Roos, Janne, 117, 119, 157  
Rusakov, S.G., 101, 145, 175
- Savin, Adriana, 33, 35  
Scheichl, Robert, 199  
Schilders, W.H.A., 27, 113, 155, 173  
Schmidt, Frank, 133  
Schneider, André, 25  
Schneider, Rudolf, 37  
Schoenmaker, Wim, 61, 173  
Schöps, Sebastian, 197  
Schuhmann, Rolf, 9  
Scordia, C., 67  
Seebacher, Ehrenfried, 43  
Selva, Mónica, 89  
Şengör, N. Serap, 183, 185  
Sheng, Zhifeng, 135  
Sickenberger, Thorsten, 149  
Şimsek, Murat, 183, 185
- Ştefănescu, Alexandra, 15, 45, 179  
Steigmann, Rozina, 33, 35  
Steinbach, Olaf, 13  
Sterz, Oliver, 195  
Striebel, Michael, 21, 121  
Stykel, Tatjana, 159  
Sy, O.O., 41
- Takamatsu, Mizuyo, 143  
Taskinen, Matti, 81  
Tijhuis, A.G., 41  
Tischendorf, Caren, 89, 143
- Udpa, Lalita, 33  
Udpa, S.S., 33  
Ugryumova, M.V., 155  
Ulyanov, S.L., 101, 145, 175
- Vaessen, J.A.H.M., 41  
Valtonen, Martti, 47
- Vasenev, Alexander, 179  
Verhoeven, A., 21  
Voigtmann, Steffen, 71
- Wan, Shan, 19  
Warburton, T., 127  
Weiland, S., 167  
Weiland, Thomas, 137, 195  
Wilcox, L., 127  
Windisch, Markus, 13
- Xu, Tao, 105
- Yeh, Ta-Ching, 191, 203  
Yetkin, E. Fatih, 115  
Ylä-Oijala, Pasi, 81  
Yuferev, Sergey, 7
- Zhang, Q.J., 19  
Zharov, M.M., 101, 145, 175



1. L. Jylhä: Modeling of electrical properties of composites, March 2008.
2. I. Torniainen: Multifrequency studies of gigahertz-peaked spectrum sources and candidates, May 2008.
3. I. Hänninen: Analysis of electromagnetic scattering from anisotropic impedance boundaries, June 2008.
4. J. Roos, L.R.J. Costa (eds.): SCEE 2008 book of abstracts, September 2008.

ISBN 978-951-22-9557-9 (printed)

ISBN 978-951-22-9563-0 (electronic)

<http://lib.tkk.fi/Books/2008/isbn9789512295630.pdf>

urn:nbn:fi:tkk-012356

ISSN 1797-4364 (printed)

ISSN 1797-8467 (electronic)